COMPOSITIONAL ZONING IN KĪLAUEA OLIVINE:

A GEOCHEMICAL TOOL FOR INVESTIGATING MAGMATIC PROCESSES AT HAWAIIAN VOLCANOES

A DISSERTATION SUBMITTED TO THE GRADUATE DIVISION OF
THE UNIVERSITY OF HAWAIʻI AT MĀNOA IN PARTIAL
FULFILLMENT OF THE REQUIREMENTS FOR THE DEGREE OF

DOCTOR OF PHILOSOPHY

IN

GEOLOGY AND GEOPHYSICS

MAY 2017

By

Kendra J. Lynn

Dissertation Committee:

Michael O. Garcia, Chairperson
Thomas Shea
Julia Hammer
Eric Hellebrand
Michael Mottl

DEDICATION

This dissertation is dedicated to my grandfather, *Charles A. Thomas*.

His emotional, intellectual, and financial support have allowed me to chase this dream and make it a reality. He inspired me to travel, be inquisitive, and work hard without expectation of reward. It is my great honor to join him in the line of scientists in our family.

It is ok to risk, to take adventures, to aspire to something
so unimaginable that only you can see it.
- Ann Bancroft

i ka nānā no a ike

By observing we learn.

ACKNOWLEDGEMENTS

I was five years old when I told my parents that I wanted to study volcanoes. The pursuit of this dream would not have been possible without the support of many and I would like to take this opportunity to express my gratitude to those people.

My success would not have been possible without the support of my graduate advisor, Michael Garcia, who allowed me to pursue the topics that fascinated me and provided tremendous support for those endeavors. I am deeply grateful to Thomas Shea, who once taught a diffusion workshop in my theoretical petrology class and has since become an irreplaceable collaborator in my work. Many thanks to Eric Hellebrand and Julia Hammer for being my professors for several classes, serving on all my committees, and providing technical analytical expertise. Finally, I am grateful to Michael Mottl, who served as my outside committee member and provided perspective on my work.

My love for all subjects related to olivine crystals developed from stimulating discussions with Benoît Welsch, who generously provided advice during my research. Don Swanson's vast knowledge of Kīlauea, the Keanakāko'i Tephra, and stories of Pelehonuamea influenced my research questions and bigger picture ideas about explosive eruption periods. The Keanakāko'i Tephra olivine projects were repeatedly supported by Fidel Costa, Gareth Fabbro, Jason Herrin, Dawn Sweeny-Ruth, and the Earth Observatory of Singapore, who welcomed me into their research groups and lab facilities numerous times. My 2015 EAPSI fellowship Singapore 'ohana, and my NTU cohort Brandon Ng, Emil Petkov, Ali and Jason Wu, Olivia Barbee, and Madison Meyers have become lifelong friends after an excellent summer of science, travel, and adventure.

I have cherished the steadfast support and patience of my family as I pursued this dream. Thank you to Mom, Dad, Kyle, Kelsey, Korbin, Lisa, Anna, Benjamin, Bob and Holly Anderson (and Moose and Bailey), and Robina Scaife for all your love and understanding.

I’m so grateful for the GG graduate students, who have shown me that there’s more to life than work. I owe my sanity to Jessica Zaiss for getting me hooked on long distance running, Emily First (i.e. the best officemate ever) for interisland adventures, and Sammie Jacob, my science sister, travel buddy, and dear friend. I would be nothing without the Hawai‘i Ultimate League Association and my Wahine Ultimate ‘ohana, with whom I shared many sunny days and starry nights hucking discs and winning boat races. Thriving friendships have kept me going on the toughest days, and I am thankful to have Cole Hanson, Rick Provost, Laura Gerson, Mark Brown, Sadie Neuman, Heidi Breid, Chelsea Habberstad, Brock Norwood, Paul Tlougan, Kelsey Johnson, Cassie Bly, and Mimi Danicic in my life.

I am especially grateful to Kelly Farhni, who taught me to be like a duck (calm on the surface but paddling like crazy underneath), Jim Woodbury, who said if you’re going to hit a wall you might as well hit it running, and Devon Green, who gave me perspective to remind me that I’m only human. I am indebted to Ruth Oliver for inspiring my scientific mind, and of course, to Steve Allard, who taught me that he/she who sees the most rocks wins.

And finally, my sincerest gratitude to my love, Isaac Ishihara, for all the patience and unending support. Thanks for climbing mountains with me.

This work was supported financially by the National Science Foundation, East Asia and Pacific Summer Institutes, National Research Foundation of Singapore, Fred M. Bullard Endowed Graduate Fellowship, and the Harold T. Stearns Fellowship.

ABSTRACT

Olivine compositions and zoning patterns have been widely used to investigate the evolution of magmas from their source to the Earth’s surface. Modeling the formation of compositional zoning in olivine crystals has been used to retrieve timescales of magma residence, mixing, and transit. This dissertation is composed of three projects that apply diffusion chronometry principles to investigate how zoned olivine phenocrysts record magmatic processes at Hawaiian volcanoes. Olivine phenocrysts from Kīlauea, the most active and thoroughly studied volcano in Hawai‘i, are used to develop a better understanding of how Hawaiian olivine crystals record magmatic histories. This work begins by examining how crustal processes such as magma mixing and diffusive re-equilibration can modify olivine compositions inherited from growth in parental magmas (Chapter 2). Diffusive re-equilibration of Fe-Mg, Mn, and Ni in olivine crystals overprints the chemical relationships inherited during growth, which strongly impacts interpretations about mantle processes and source components. These issues are further complicated by sectioning effects, where small (400 µm along the *c*-axis) olivine crystals are more susceptible to overprinting compared to large (800 µm) crystals. Olivine compositions and zoning patterns are then used to show that magmas during Kīlauea’s explosive Keanakāko‘i Tephra period (1500-1823 C.E.) were mixed and stored in crustal reservoirs for weeks to months prior to eruption (Chapter 3). Fe-Mg disequilibrium between olivine rims and their surrounding glasses show that a late-stage mixing event likely occurred hours to days prior to eruption, but the exact timescale is difficult to quantify using Fe-Mg and Ni diffusion. Lithium, a rapidly diffusing trace element in olivine, is modeled for the first time in a natural volcanic system to quantify this late-

stage, short-duration mixing event (Chapter 4). Lithium zoning in olivine records both growth and diffusion processes that are affected by charge balancing requirements with growth zoning of P. Timescales from modeling diffuse Li zoning range from a few hours to three weeks, but most record short storage durations of four days or less. These timescales correspond to short storage periods after mixing. Thus, Li probably records the final perturbation of a magmatic system prior to eruption.

TABLE OF CONTENTS

LIST OF TABLES

LIST OF FIGURES

LIST OF EQUATIONS

CHAPTER 1

INTRODUCTION

1.1. Dissertation Overview

This dissertation seeks to improve our understanding of the compositional zoning recorded in olivine crystals to investigate the magmatic histories of poorly understood Hawaiian eruptions. Chapter 1 presents a brief geologic background for Hawaiʻi and Kīlauea Volcano, describes Kīlauea's eruptive behavior, and introduces the explosive eruption deposits that are a main focus of this work. This is followed by an overview of the methods including: diffusion theory, relevant equations for diffusion models, experimentally determined element diffusivities, and how diffusion chronometry is applied in volcanic systems. Chapters 2, 3, and 4 were written for publication in peer-reviewed journals. Thus, there is some overlap between the background information presented here in Chapter 1 and individual chapter introductions. This section concludes with an overview of the research presented in Chapters 2, 3, and 4, and summarizes future research considerations presented in Chapter 5.

1.2. Hawaiian Volcanism

As the number of people living on or near Earth's active volcanoes increases, our understanding of volcanic events and their associated hazards is of growing importance (e.g. Wright and Pierson 1992; Trusdell 1995; Poland et al. 2016). Hawaiʻi is home to the most active and best studied volcanoes in the world, serving as a natural laboratory in which scientists seek to better understand Earth's volcanic processes (e.g. Tilling and Dvorak 1993; Tilling et al. 2014; Garcia 2015). The Hawaiian-Emperor seamount chain represents ~81 million years of volcanism (Keller et al. 1995) generated by a relatively low-density upwelling mantle plume that is geochemically heterogeneous (Sleep 1990; Pietruszka and Garcia 1999; Wolfe et al. 2009; Weis et al. 2011; Greene et al. 2013; Pietruszka et al. 2013; Ballmer et al. 2015). The seamounts and islands produced by the plume extend nearly 6,000 km across the northern Pacific Ocean (Figure 1.1; Clague and Dalrymple 1987), a testament to its long-lived productivity.

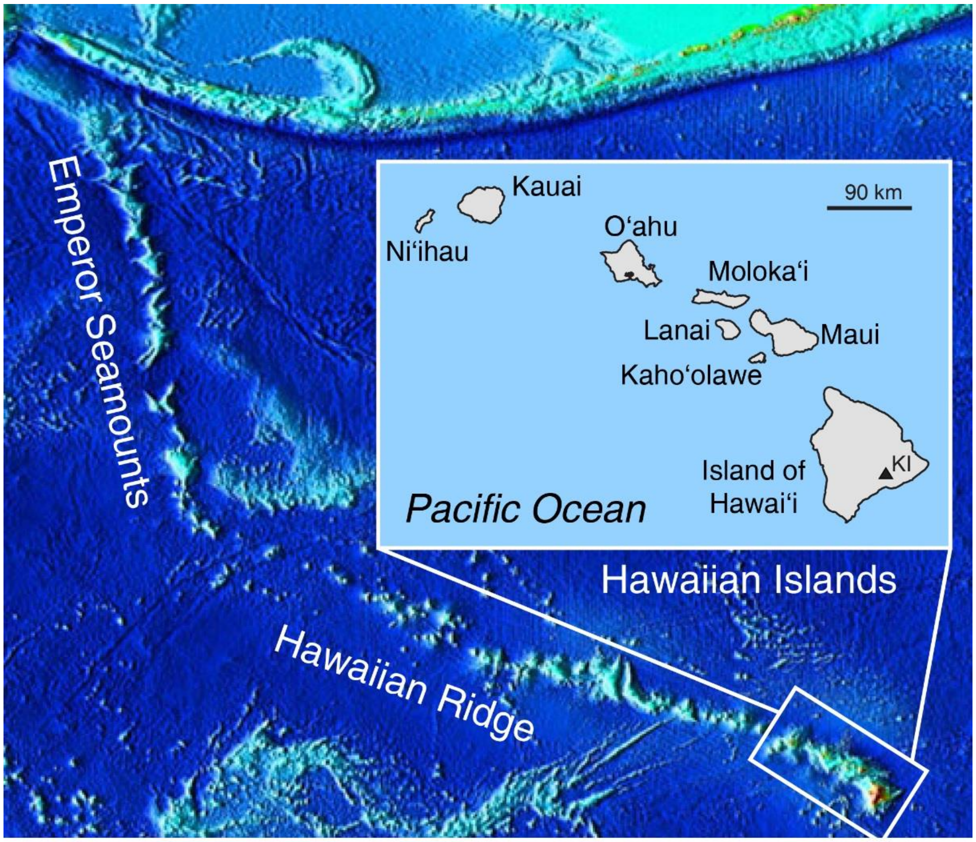

Figure 1.1. Bathymetric map of the northern Pacific Ocean showing the hotspot track of the Hawaiian-Emperor seamount chain and subaerial Hawaiian Islands (inset). Triangle on the Island of Hawai'i marks the summit of Kīlauea Volcano. Base map is from the National Oceanic and Atmospheric Administration ETOPO2v2 database (National Geophysical Data Center, 2006).

Studies of Hawaiian volcanoes and their eruptions have resulted in fundamental discoveries of magmatic and other geologic processes (see overview in Garcia 2015). They have also served as analogue systems for other basaltic ocean islands (e.g. La Réunion, Peltier et al. 2015) as well as extraterrestrial bodies (e.g. Mars; Marlow et al. 2008; Chemtob et al. 2010; Seelos et al. 2010). Volcanic eruptions in Hawaii are monitored for seismic activity (Okamura et al. 1988; Koyanagi et al. 1988; Okubo 1995; Wright and Klein 2008), deformation (Dvorak and Dzurisin 1993; Linde and Sacks 1995; Decker et al. 2008; Poland et al. 2012; Anderson et al. 2015), and the composition of erupted lavas (Garcia and Wolfe 1988; Neal et al. 1988; Garcia et al. 1992; Garcia et al. 1996) and emitted gases (Greenland 1988; Gerlach et al. 2002; Edmonds et al. 2013).

These measurements have led to a basic understanding of shallow plumbing systems in basaltic volcanoes, largely due to the accessibility of frequent effusive eruptions in the past ~100 years (Tilling and Dvorak 1993; Wright and Klein 2014).

However, many questions remain about how and why Hawaiian volcanoes erupt (Poland 2015). Despite the abundance of effusive lava flow producing eruptions in past two centuries, many ash deposits cover parts of the Island of Hawaiʻi and show that Hawaiian volcanoes can also erupt explosively (Powers 1916; Powers 1948; Easton and Garcia 1980; Macdonald et al. 1983). These deposits have been linked to many volcanoes including Mauna Kea, Mauna Loa, and Kīlauea (Powers 1916), but explosive eruptions have rarely occurred in modern times (e.g. 1924; Macdonald et al. 1983). No geophysical or observational records exist to describe this type of behavior, and many aspects of explosive eruptions in Hawaiʻi remain poorly understood.

1.3. Kīlauea Volcano

Kīlauea is the youngest, most active subaerial volcano on the Island of Hawaiʻi (Figure 1.2). It is one of the best studied volcanoes in the world (e.g. Tilling and Dvorak 1993, Garcia 2015) with an extensive geophysical monitoring program (Decker et al. 2008) that

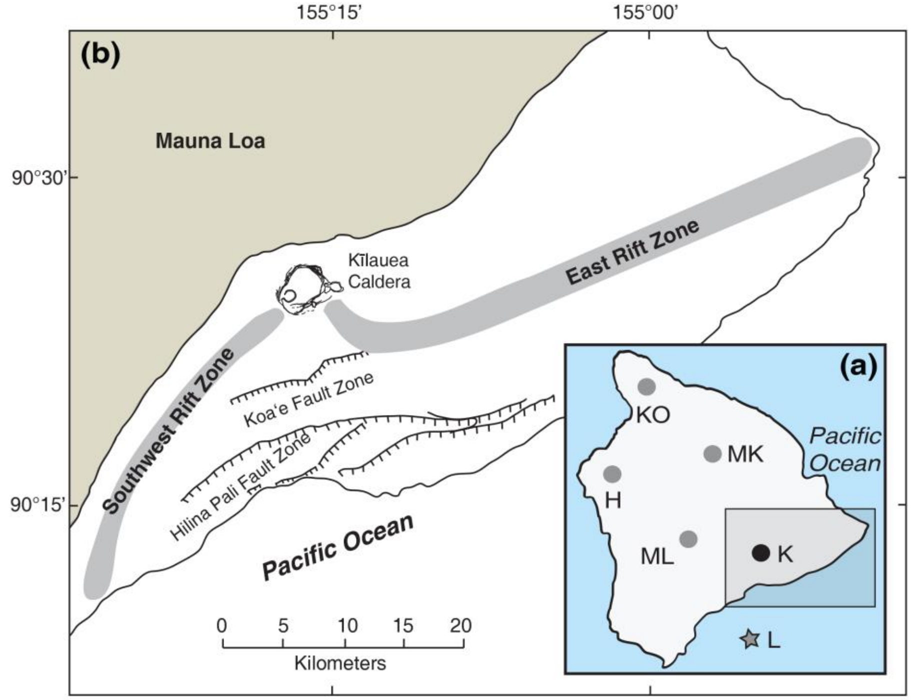

Figure 1.2. (a) The Island of Hawaiʻi, with circles marking the summits of the subaerial volcanoes: Kohala (KO), Hualālai (H), Mauna Kea (MK), Mauna Loa (ML), and Kīlauea (K). The summit of submarine Lōʻihi (L) is marked with a star. **(b)** Simplified cartoon of Kīlauea's major structural features including the summit caldera, rift zones, and major fault systems modified after Holcomb (1987).

has been in place for more than 100 years (Kauhikaua and Poland 2012). Current models suggest that eruptions are sourced from a shallow magmatic plumbing system with at least two geophysically and isotopically distinct magma storage regions since at least 1959: the Halemaʻumaʻu and South Caldera reservoirs (Figure 1.3; Pietruszka et al. 2015). Volcanic eruptions occur at the summit, along the Southwest or East Rift Zones (ERZ), or, rarely, south of the summit caldera in the Koaʻe fault zone (Figure 1.2; Holcomb 1987). Sustained eruptions on the ERZ (e.g. Puʻu ʻŌʻō; 1983 to present) are thought to be supplied by a conduit connected to the summit reservoir system (Figure 1.3). Ascending magmas may partially bypass the deeper South Caldera reservoir (Pietruszka et al. 2015) before being transported to erupt at vents along the rift zone (Figure 1.3).

The geochemical evolution of Hawaiian tholeiitic magmas is primarily controlled by fractional crystallization of only olivine for >100°C below the liquidus (Wright 1971; Montierth et al. 1995). Secondary processes, such as the mixing of magmas in the summit and rift reservoirs, strongly influence the compositions of erupted olivine and their lavas. (e.g. Garcia et al. 1989; Wright and Helz 1996; Shamberger and Garcia 2007). Most summit eruptions have been olivine poor (e.g. as low as 0.2 vol%; Garcia et al. 2003) compared to the weakly to moderately olivine phyric (e.g. Puʻu ʻŌʻō, 1-7 vol%; Garcia et al. 1989; 1992; 1996; 2000; Marske et al. 2008) or rarely strongly olivine phyric (e.g.

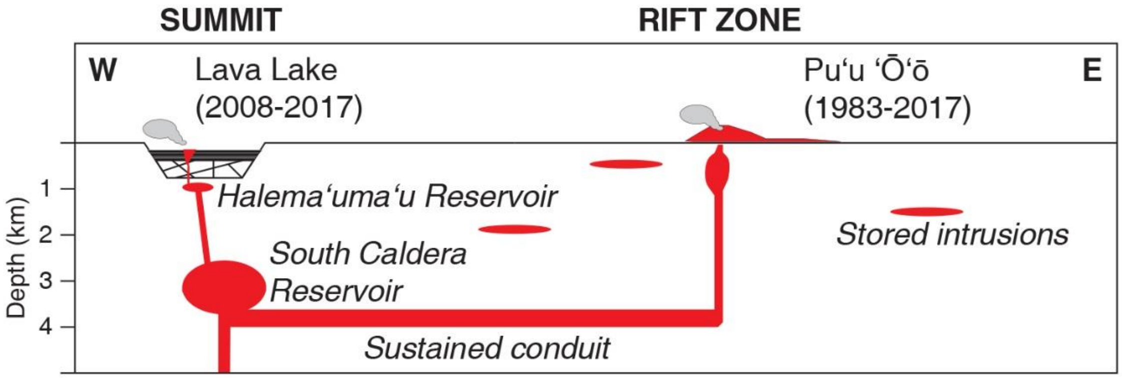

Figure 1.3. Schematic cross section of the modern magmatic plumbing system at Kīlauea (no horizontal scale). It features two summit magma bodies (Halemaʻumaʻu and South Caldera Reservoirs) that have existed since at least 1959 (Pietruszka et al. 2015). The dike that transports magma from the summit reservoir system to the Puʻu ʻŌʻō eruption on the ERZ may be fed from or partially bypass the South Caldera reservoir (Garcia et al. 1996). Modified after Poland et al. (2014) and Pietruszka et al. (2015).

1840 ERZ; 14-30 vol%; Norman and Garcia 1999) eruptions on the rift zones. The presence of olivine in most of Kīlauea's eruptive products make it an ideal tool for investigating magmatic processes to gain insights into the storage and transport histories of ascending magmas.

1.4. Eruptive Cycles

Since the founding of the Hawaiian Volcano Observatory by Thomas Jagger in 1912, observations and geophysical measurements of Kīlauea's eruptions have been used to better understand the behavior of Hawaiian volcanoes. The recorded historical period at Kīlauea began with the arrival of the first western visitors in 1823 (Ellis 1827). Since that time, Kīlauea has been dominated by effusive activity characterized by a sustained summit lava lake and/or lava flows, fissures, and high fountains (Macdonald et al. 1983). The frequency and duration of eruptions, and the inferred magma supply to Kīlauea, has increased dramatically since around 1950 (see Wright and Klein 2014 for overview). An ~2x increase in magma supply in the early 2000's (Poland et al. 2012) culminated in sustained eruptions on both the ERZ and at the summit (beginning in 2008; Wilson et al. 2008) which are ongoing at the time of this writing in 2017 (Figure 1.3).

Kīlauea's eruptive behavior has varied dramatically throughout the Holocene despite the dominantly effusive eruptions that have occurred since 1823. Tephra deposits near the summit caldera record five centuries-long periods of either dominantly explosive or effusive eruptions in the past 2,500 years (Figure 1.4; Swanson et al. 2014). Older deposits suggest that explosive periods may extend back to ~70 ka (Easton and Garcia 1980; Easton 1987). Two episodes of caldera formation in the recent period were followed by long-lived explosive activity (Figure 1.4). The Powers Caldera (~200 C.E.; Powers 1948; Holcomb 1987) was followed by the Uwēkahuna Tephra (ca. 200 BCE to 1000 C.E.; Powers 1916; Dzurisin et al. 1995; Fiske et al. 2009). The modern summit caldera formed around 1470-1510 C.E. and was followed by the Keanakāko‘i Tephra (1500-1823 C.E.; Swanson et al. 2012a). Explosive behavior has occurred for ~60% of this recent period (Figure 1.4), associated with substantial hazards including pyroclastic density currents, tephra falls, and ballistic showers (Decker and Christiansen 1984; Dzurisin et al. 1995; Fiske et al. 2009; Swanson et al. 2012a, 2012b).

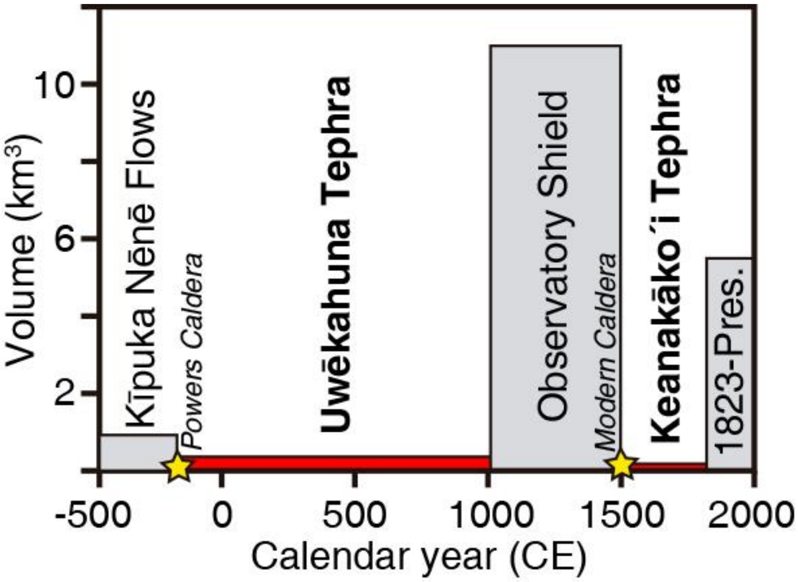

Figure 1.4. Erupted volume (km3) for recent effusive (grey bins) and explosive (red bins) periods in the past 2,500 years at Kīlauea. Yellow stars indicate caldera collapse events (Holcomb 1987; Swanson et al. 2012a). Modified after Swanson et al. (2014).

No records exist to decipher magma storage and transport histories during explosive periods because prolonged explosive activity has not been observed since 1823.

This dissertation investigates the petrology and geochemistry of the most recent explosive deposits to better understand the magmatic processes operating during the Keanakāko‘i Tephra period (KT, 1500-1823 C.E.; Swanson et al. 2012a). The KT was produced by numerous eruptions spanning ~300 years (Figure 1.5). Most of the units are near-summit products of phreatomagmatic eruptions, in which ascending magmas interacted with ground or surface water that drove explosive fragmentation of primarily recycled lithic material (McPhie et al. 1990; Mastin 1997; Mastin et al. 2004). Some units are fallout from high lava fountains or sub-plinian eruptions dominated by juvenile material, and are marker units within the tephra (^{14}C ages from Swanson et al. 2012a; Figure 1.5). These include the Basal Reticulite (1500 C.E.), Layer 6 (1650 C.E.), and Golden and Eastern Pumices (1790-1823 C.E.; the Eastern Pumice has only recently been recognized to overlie the Golden Pumice; Figure 1.5). Only one Kīlauea lava flow (1670-1700 C.E.) has been documented within the KT period; it erupted SW of the summit caldera. Most studies of these deposits have focused on the physical aspects of eruption and deposition (McPhie et al. 1990; Mastin 1997; Mastin et al. 2004; Swanson et al.

2012a, 2012b; May et al. 2015), with limited petrologic and geochemical characterization (Mucek 2012; Sides et al. 2014; Helz et al. 2015; Ferguson et al. 2016).

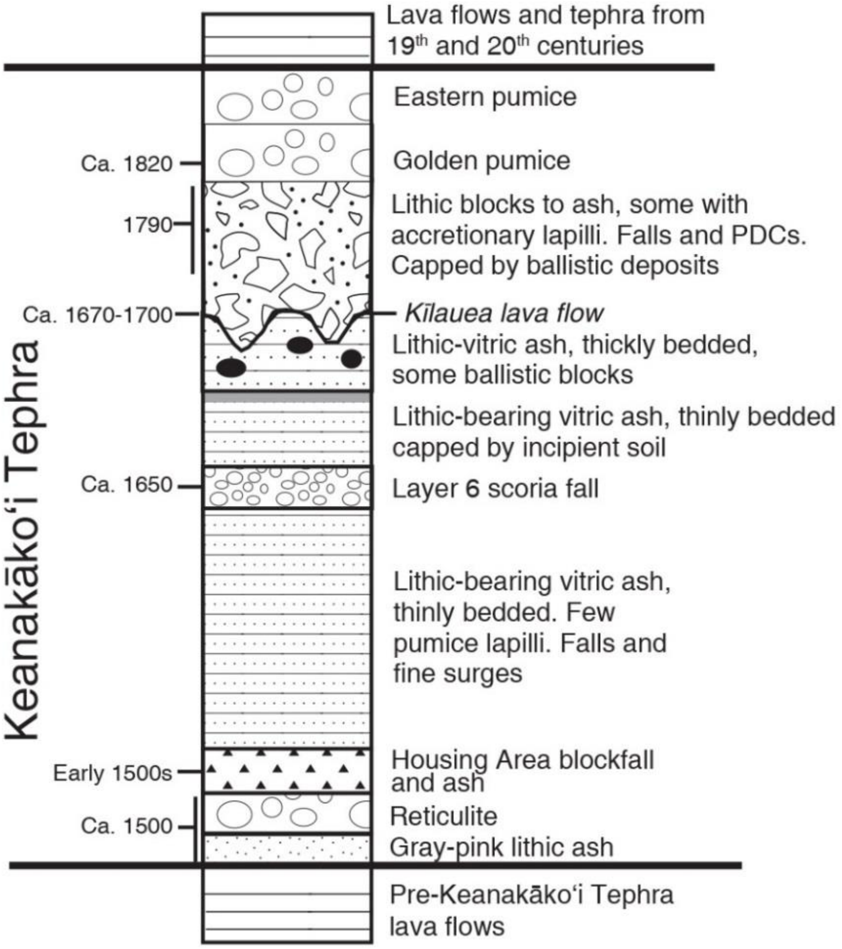

Figure 1.5. Simplified stratigraphic column for the Keanakāko'i Tephra (not to scale; modified after Swanson et al. 2012a). Only the largest erosional unconformity is shown (*Kīlauea Lava Flow*) although many smaller ones occur throughout. All ^{14}C ages are in C.E. (common era).

1.5. Method Overview

Petrologic and geochemical methods are often used to investigate enigmatic prehistoric periods in Hawaiian volcanism (e.g. Hammer et al. 2015). A key component to the success of geochemical studies is a clear understanding of how lavas and their phenocrysts record magmatic processes from their source to the surface (e.g. Thomson and Maclennan 2013; Bouvet de Maisonneuve et al. 2016). This dissertation seeks to provide insights on: (1) the distribution of major, minor, and trace elements in olivine crystals during growth and diffusive re-equilibration, (2) how these distributions record magmatic histories, and (3) how chemical zoning in olivine can be used to investigate magma mixing and storage histories for Kīlauea's explosive periods. The following sections introduce the theory of diffusion in magmatic minerals, present the 1D and 3D diffusion equations used in this dissertation, review experimentally determined element diffusivities, and provide an example of how diffusion chronometry in olivine is applied in volcanic systems.

1.5.1. Diffusion Equations

Chemical diffusion in minerals can be broadly defined as the movement of atoms within a crystal lattice. This movement occurs by random fluxes of ions at all temperatures, and can be associated with gradients in chemical potential throughout the diffusion medium (Zhang 2010). It is analogous to Fourier's law of heat conduction, and the flux of atoms is typically expressed by Fick's first law:

$$\mathrm{J} = -\mathrm{D}\frac{\partial \mathrm{C}}{\partial \mathrm{x}} \tag{1.1}$$

where *J* is the diffusive mass flux, *D* is the diffusion coefficient (i.e. the rate of diffusion, or diffusivity), *C* is the concentration of the chemical species of interest, and *x* is the distance. The flux of atoms (Equation 1.1) through a volume can induce changes in the concentration gradient as a function of time, taking the form of Fick's second law, or the continuity equation (Crank 1975):

$$\frac{\partial \mathrm{C}}{\partial \mathrm{t}} = \frac{\partial}{\partial \mathrm{x}}\left(\mathrm{D}\frac{\partial \mathrm{C}}{\partial \mathrm{x}}\right) \tag{1.2}$$

where *D* is the diffusivity, *C* is concentration, and *x* is the distance as a function of time *t*. Equation 1.2 is applied in Chapter 4 to model 1D gradients of Li, for which the diffusivity is expressed as a simple Arrhenius relation (Dohmen et al. 2010).

However, the diffusivities of some elements (e.g. Fe-Mg, Ni, and Mn) in olivine are dependent on the concentration of a chemical species in the mineral phase. As diffusion changes the concentration gradient of Fe-Mg in the mineral, the relative diffusivity of each of these species will also change as a function of time. This can be incorporated in the 1D diffusion equation (Equation 1.2) to account for changes in *D* as the concentration evolves:

$$\frac{\partial C}{\partial t} = \frac{\partial D}{\partial x}\frac{\partial C}{\partial x} + D\frac{\partial^2 C}{\partial x^2} \tag{1.3}$$

Volume diffusion in three dimensions (expanded from) Equation 1.3 is written (Crank 1975):

$$\frac{\partial C}{\partial t} = \left[\left(\frac{\partial D}{\partial x}\frac{\partial C}{\partial x}+D\frac{\partial^2 C}{\partial x^2}\right)+\left(\frac{\partial D}{\partial y}\frac{\partial C}{\partial y}+D\frac{\partial^2 C}{\partial y^2}\right)+\left(\frac{\partial D}{\partial z}\frac{\partial C}{\partial z}+D\frac{\partial^2 C}{\partial z^2}\right)\right] \tag{1.4}$$

where *x*, *y*, and *z* refer to principal directions in Cartesian coordinates.

To apply the 1D or 3D diffusion equations (Equations 1.3 or 1.4) and model the progressive change of a compositional gradient, we replace the partial derivatives by finite differences, which approximate changes using a forward-time, centered space expression. The finite difference form of the second derivative of Equation 1.3 for diffusion in 1D is:

$$C_{i,\, j+1} = \frac{D\Delta t}{\Delta x^2}(D_{i+1}\text{-}D_i)(C_{i+1}\text{-}C_i) + D_i\left(C_{i+1,j}\text{-}2C_{i,j}+C_{i\text{-}1,j}\right) \tag{1.5}$$

where *i* is distance along *x* and *j* is time. Equation 1.5 is the form used in the program DIPRA (Girona and Costa 2013) and numerical diffusion simulations in Chapter 3.

The drawback of using finite-difference derivatives for the time-dependent diffusion equation is that both the time and space intervals over which the model is applied are coupled and limited by each other. For example, higher spatial resolution models (e.g. smaller *x*) require a smaller increment of time to be used in forward iterations, thus increasing the total iterations needed to achieve good model fit. The balance between distance (*x*) and the size of the time step (*t*) is expressed by the stability criterion, *R*:

$$R = \frac{D\Delta t}{\Delta x^2} \tag{1.6}$$

where D is diffusivity (as above), Δt is the time increment for each iteration, and Δx is the spacing between two points in the model. The stability criterion R (Equation 1.6) must be < 0.5 for 1D applications, and this condition must be satisfied for all diffusing species when multiple elements with different D are modeled. The same finite-difference concepts apply for diffusion in 3D:

$$\begin{aligned} C_{i,\, j+1} = \frac{D\Delta t}{\Delta x^2}\Big\{&\big[\big(D_{i+1,x}-D_{i,x}\big)\big(C_{i+1,x}-C_{i,x}\big)+D_{i,x}\big(C_{i+1,j,x}-2C_{i,j,x}+C_{i-1,j,x}\big)\big] \\ &+\big[\big(D_{i+1,y}-D_{i,y}\big)\big(C_{i+1,y}-C_{i,y}\big)+D_{i,y}\big(C_{i+1,j,y}-2C_{i,j,y}+C_{i-1,j,y}\big)\big] \\ &+\big[\big(D_{i+1,z}-D_{i,z}\big)\big(C_{i+1,z}-C_{i,z}\big)+D_{i,z}\big(C_{i+1,j,z}-2C_{i,j,z}+C_{i-1,j,z}\big)\big]\Big\} \end{aligned} \tag{1.7}$$

where the stability criterion R (Equation 1.6) must be < 0.166. Chapter 2 uses Equation 1.7 for 3D numerical models of Fe-Mg, Ni, and Mn diffusion modified after the methods outlined in Shea et al. (2015a).

1.5.2. Diffusivity Equations

This dissertation focuses on olivine, an orthorhombic mineral with varying rates of diffusion for many elements along the three crystallographic axes *a*, *b*, and *c* (Chakraborty 1997). This anisotropy is described by the diffusivity tensor (Zhang 2010):

$$D = \begin{bmatrix} D_a & 0 & 0 \\ 0 & D_b & 0 \\ 0 & 0 & D_c \end{bmatrix} \tag{1.8}$$

which corresponds to Cartesian directions as $D_x = D_a$, $D_y = D_b$, and $D_z = D_c$.

Diffusion anisotropy occurs because the M1 octahedral polyhedral in the crystal structure form a continuous chain along [001] (i.e. the *c*-axis), whereas the M2 octahedral polyhedral are not organized in any direction (Chakraborty 2010). For commonly used major and minor elements in olivine (e.g. Fe, Mg, Ni, Mn; Dohmen and Chakraborty

2007a, 2007b; Petry et al. 2004; Holzapfel et al. 2007), diffusion along the *c*-axis occurs approximately six times faster than the *a*- or *b*-axes (e.g. Chakraborty 1997):

$$D_a = D_b = \frac{1}{6} D_c \tag{1.9}$$

The relative contributions from each of the axes along any 1D analytical traverse can be modeled if the axis orientations within a 2D olivine section are known (Costa and Chakraborty 2004). A diffusivity factor is required to account for the relative rate differences in different directions:

$$D_{traverse} = D_a^i(\cos\alpha)^2 + D_b^i(\cos\beta)^2 + D_c^i(\cos\gamma)^2 \tag{1.10}$$

where *i* is the element of interest and α, β, and γ are the angles between the 1D traverse and the *a*-, *b*-, and *c*-axes of the olivine, respectively (Costa and Chakraborty 2004). Axis orientations are determined using electron backscatter diffraction (EBSD; see Prior et al. 1999 for detailed methods) and the angles α, β, and γ are calculated using lower hemisphere projections in *Stereonet9*© (Cardozo and Allmendinger 2013).

1.5.3. Experimentally determined diffusivities

Using diffusive re-equilibration to study magmatic processes requires good constraints on elemental diffusivities. Early experimental determination of diffusivities in olivine [$(MgFe)_2SiO_4$] focused on the exchange reaction between Fe^{2+} and Mg^{2+} (Buening and Busek 1973; Misener 1974; Chakraborty 1997; Dohmen and Chakraborty 2007a, 2007b; Table 1.1). Advances in analytical and experimental techniques throughout the past few decades have allowed the additional determination of minor element diffusivities (Mn, Ni, and Ca; Table 1.1). The diffusivities of Fe, Mg, Ni, and Mn are applied in the models presented in Chapter 2, and Fe, Mg, and Ni are used in Chapter 3. The diffusivities of some trace elements in olivine have only recently been characterized (e.g. Be, Li, Ti, H; Dohmen et al. 2010; Cherniak and Liang 2014; Jollands et al. 2016a, 2016b, 2016c). Lithium diffuses up to an order of magnitude faster than Fe-Mg (Table 1.1.), providing a new opportunity to investigate rapidly occurring volcanic processes. The diffusivity of Li along the *c*-axis in olivine is represented by a simple Arrhenius equation and is used in models presented in Chapter 4.

Table. 1.1. Currently accepted, experimentally determined diffusivities for commonly used major and minor elements in olivine.

Element	Diffusivity Expression (m^2/s)	Reference
Fe, Mg Mn	$D_c=10^{-9.21}\left(\frac{f_{O2}}{10^{-7}}\right)^{\frac{1}{6}}10^{3(X_{Fe}-0.1)}\exp\left(\frac{-201000+(P-10^5)(7x10^{-6})}{RT}\right)$	Dohmen and Chakraborty 2007a, 2007b Holzapfel et al. 2007
Ni	$D_c=3.84x10^{-9}\left(\frac{f_{O2}}{10^{-6}}\right)^{\frac{1}{4.25}}10^{1.5(X_{Fe}-0.1)}\exp\left(\frac{-220000+(P-10^5)(7x10^{-6})}{RT}\right)$	Petry et al. 2004
Ca	$D_a=16.59x10^{-12}\left(\frac{f_{O2}}{10^{-7}}\right)^{\frac{1}{3.2}}\exp\left(\frac{-19300\pm11000}{RT}\right)$	Coogan et al. 2005
	$D_b=34.67x10^{-12}\left(\frac{f_{O2}}{10^{-7}}\right)^{\frac{1}{3.2}}\exp\left(\frac{-201000\pm10000}{RT}\right)$	
	$D_c=95.49x10^{-12}\left(\frac{f_{O2}}{10^{-7}}\right)^{\frac{1}{3.2}}\exp\left(\frac{-207000\pm8000}{RT}\right)$	
Li	$D_c=10^{-5.92(\pm1.0)-1.2847x\frac{10^4}{T}}$	Dohmen et al. 2010

Note(s): Expressions for Fe, Mg, Mn, and Ni are concentration dependent and follow the anisotropic relationship in Equation 1.9. Ca is anisotropic with different diffusivities along each axis. f_{O2} is oxygen fugacity (pascals), P is pressure (pascals), T is temperature (Kelvin), and R is the gas constant (8.314 J/mol/K). The effects of P and f_{O2} on Li diffusivity have not yet been determined.

1.5.4. Diffusion chronometry in volcanic systems

Diffusion chronometry is an increasingly popular technique that is significantly advancing our understanding of volcanic systems and magmatic processes (Rosen 2016). Compositional gradients in olivine develop due to the diffusive re-equilibration between an overgrowth rim of different composition compared to the olivine core (Figure 1.6) or re-equilibration of the olivine with a surrounding magma of contrasting composition (Figure 1.7). The formation of the compositional gradient is directly related to the duration at which the crystal was held at a given temperature, pressure, and oxygen fugacity (Costa et al. 2008).

At Kīlauea, the P, T, and f_{O2} conditions are thought to be well understood (Helz and Thornber 1987; Poland et al. 2014; Moussalam et al. 2016; Helz et al. 2017). Petrologic constraints are used to infer initial concentration distributions (Figure 1.7b) used in diffusion models. If the above properties are well-known for a magmatic system, timescales of storage after mixing events can be calculated with confidence using the

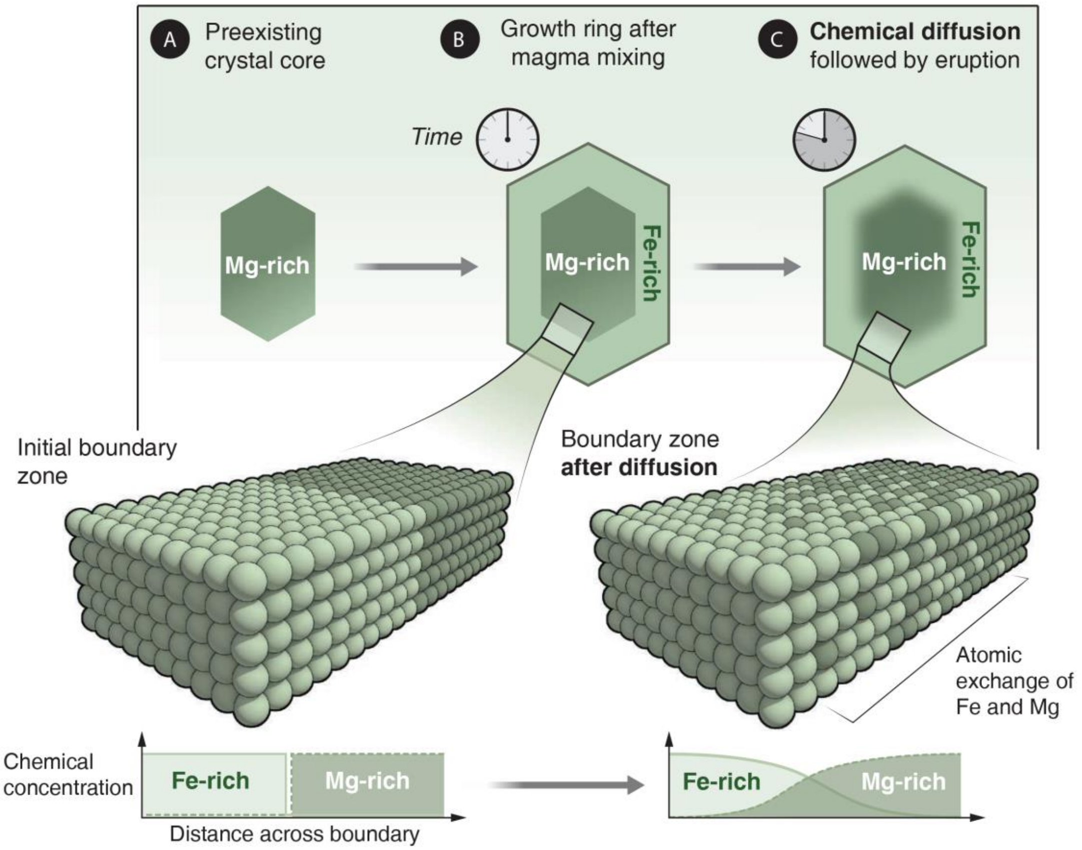

Figure 1.6. Schematic showing the process of diffusion in the case of an olivine overgrowth rim (modified after Rosen 2016). **(a)** An initially Mg-rich olivine core is homogeneous in composition. **(b)** After magma mixing, an outer rim of comparatively Fe-rich olivine grows around the homogeneous Mg-rich core. **(c)** The olivine is stored at magmatic temperatures for some length of time over which atomic exchange of Fe and Mg relax the boundary between the initial core and overgrowth rim, creating smoothed compositional profiles.

experimentally determined diffusivities for different chemical species in olivine crystals (Table 1.1). Recent studies have also highlighted how the random orientation of crystals in natural samples usually results in off-center and oblique 2D olivine sections (Shea et al. 2015a). These section types usually exhibit merging diffusion fronts that can strongly influence the timescales retrieved from diffusion models (Shea et al. 2015a). Thus, sections taken near the core and perpendicular to a crystallographic axis (Figure 1.7a) are most likely to show symmetrical concentration gradients that are suitable for modeling.

Diffusion models are run using intrinsic properties (P, T, f_{O2}), the orientation of the crystallographic axes (determined by EBSD), known diffusivities of elements of interest (Table 1.1) and the 1D or 3D diffusion equations (see section 1.5.1). The progressive evolution of the concentration profile from the initial boundary conditions

(Figure 1.7b) is tracked until a profile is obtained that matches the measured analytical traverse in the natural sample (see Costa et al. 2008 for detailed methods; Figure 1.7c). The exercise should be repeated for many elements measured along the analytical traverse (Fe-Mg with Ni, Mn, Ca) to retrieve robust timescales associated with magmatic processes (e.g. Costa and Dungan 2005; Cooper and Kent 2014), crystal residence times in magmatic reservoirs (e.g. Kahl et al. 2011, 2013), and even magma ascent rates (Ruprecht and Plank 2013).

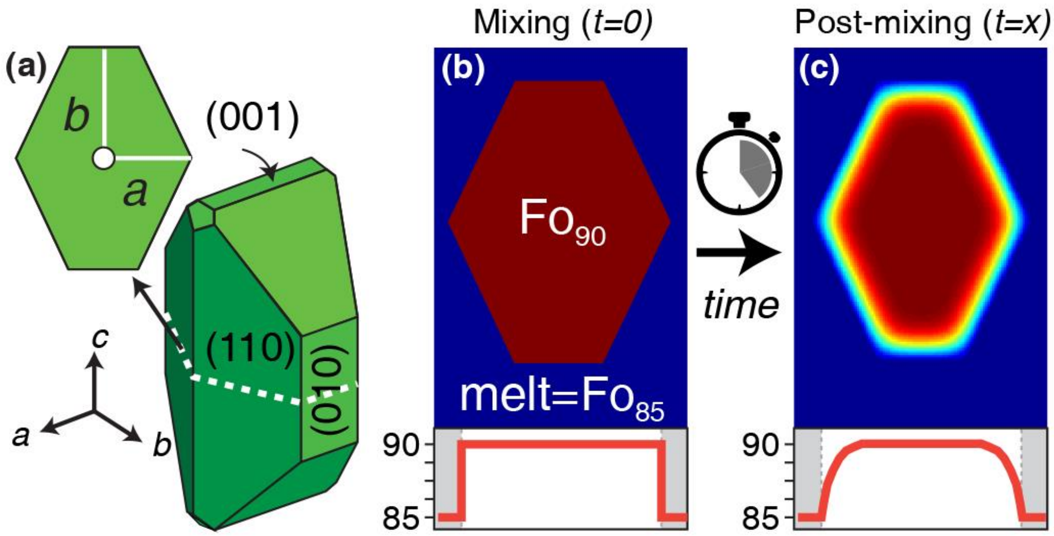

Figure 1.7. Schematic illustration of the process of diffusion after mixing. **(a)** Three-dimensional schematic of euhedral olivine crystal with crystallographic orientation and crystal faces. Dashed white line marks the location of the two-dimensional section perpendicular to the *c*-axis. **(b)** An initially homogeneous Fo_{90} olivine is mixed with a magma in Fe-Mg equilibrium with Fo_{85}. Compositional profile across the middle of the crystal (red line) shows initially sharp boundaries between the olivine and surrounding melt. **(c)** The same olivine section post-mixing after time *x* has passed. Diffusive re-equilibration of the olivine with its surrounding melt has resulted in a smoothed compositional gradient from the olivine rim toward its core.

1.6. Structure of the Dissertation

The research presented in this dissertation begins by investigating how crustal magmatic processes (e.g. fractional crystallization, magma mixing, diffusive re-equilibration) influence the compositions of Hawaiian olivine phenocrysts inherited from growth. Chapter 2 resolves inter- and intra-volcano variations in Hawaiian olivine Ni content through investigations of (1) variations in parental magma composition (specifically SiO_2 and Ni) and subsequent fractional crystallization paths, (2) shallow Fo-NiO trends created by magma mixing, and (3) diffusive re-equilibration, which can overprint compositions inherited from growth and strongly influence estimates of mantle source composition.

In Chapters 3 and 4, growth vs. diffusion insights from Chapter 2 are used to investigate magma storage and transport histories of prehistoric explosive eruptions at Kīlauea Volcano. Olivine from the Keanakāko‘i Tephra period (KT; 1500-1823 C.E.) are used to investigate whether magmas ascended rapidly from depth, bypassing storage in crustal reservoirs (Sides et al. 2014). Most olivine populations are derived from mixing of mantle-derived recharge and up to three stored reservoir components. We model the diffusive re-equilibration of Fe-Mg and Ni in olivine to show that KT magmas experienced at least two mixing events and were stored for weeks to years before eruption, contrary to previous interpretations of rapid ascent (Sides et al. 2014). Thin (5-20 µm) rims with minor Fe-Mg zoning (< 1 %) suggests that a late-stage mixing event may have occurred shortly before eruption.

Chapter 4 presents a new method for quantifying the timing of the late-stage mixing suggested by Fe-Mg zoning in KT olivine rims. High precision measurements (± 0.08 ppm) of Li concentrations in a subset of the olivine crystals are used with other trace elements (Na, Al, P, and Cr) to: (1) explore how Li records growth and diffusion, (2) examine the potential anisotropic nature of Li diffusion, and (3) quantify the timing of late-stage mixing in KT eruptions. The timescales of storage are then used to revise the model for crustal magmatic processes in Kīlauea’s KT period.

Finally, Chapter 5 summarizes the conclusions of this dissertation, weaving them into a broader context linked to beneficial future work that focuses on both geologic applications and experimental constraints on olivine.

CHAPTER 2

NICKEL VARIABILITY IN HAWAIIAN OLIVINE: EVALUATING THE RELATIVE CONTRIBUTIONS FROM MANTLE AND CRUSTAL PROCESSES

Published as:

Lynn, K.J., Shea, T., and Garcia, M.O. (2017), Nickel variability in Hawaiian olivine: Evaluating the relative contributions from mantle and crustal processes. American Mineralogist, 102, 507-518. doi: 10.2138/am-2017-5763.

2.1. Abstract

Olivine in Hawaiian tholeiitic lavas have high NiO at given forsterite (Fo) contents (e.g. 0.25-0.60 wt % at Fo_{88}) compared to MORB (e.g. 0.10-0.28 wt% at Fo_{88}). This difference is commonly related to source variables such as depth and temperature of melting, and/or lithology. Hawaiian olivine NiO contents are also highly variable and can range from 0.25-0.60 wt% at a given Fo. Here we examine the effects of crustal processes (fractional crystallization, magma mixing, diffusive re-equilibration) on the Ni content in olivine from Hawaiian basalts. Olivine compositions for five major Hawaiian volcanoes can be subdivided at $\geq Fo_{88}$ into high-Ni (0.25-0.60 wt% NiO; Koʻolau, Mauna Loa, and Mauna Kea) and low-Ni (0.25-0.45 wt% NiO; Kīlauea and Lōʻihi), groups that are unrelated to major isotopic trends (e.g. Loa and Kea). Within each group, individual volcanoes show up to 2.5x variation in olivine NiO contents at a given Fo. Whole-rock Ni contents from Koʻolau, Mauna Loa, Mauna Kea, and Kīlauea lavas overlap significantly and do not correlate with differences in olivine NiO contents. However, inter-volcano variations in parental melt polymerization (NBO/T) and nickel partition coefficients ($D_{Ni}^{ol/melt}$), caused by variable melt SiO_2, correlate with observed differences in olivine NiO at Fo_{90}, indicating that an olivine-free source lithology does not produce the inter-volcano groups. Additionally, large intra-volcano variations in olivine NiO can occur with minimal variation in lava SiO_2 and NBO/T. Minor variations in parental melt NiO contents (0.09-0.11 wt%) account for the observed range of NiO in $\geq Fo_{88}$ olivine. High precision electron microprobe analyses of olivine from Kīlauea eruptions (1500-2010 C.E.) show that the primary controls on $< Fo_{88}$ olivine NiO contents are fractional crystallization, magma mixing, and diffusive re-equilibration. Core-rim transects of normally zoned olivine crystals reveal marked differences in Fo and NiO zoning patterns that cannot be related solely to fractional crystallization. These Fo-NiO profiles usually occur in olivine with $< Fo_{88}$ and are common in mixed magmas, although they are not restricted to lavas with obvious petrographic signs of mixing. 3D numerical diffusion models show that diffusive re-equilibration decouples the growth zoning signatures of faster diffusing Fe-Mg (Fo) from the somewhat slower Ni. This diffusive 'decoupling' overprints the chemical relationships of Fe-Mg, Ni, and Mn inherited from crystal growth and influences the calculated fraction of pyroxenite-derived melt (Xpx). Sections of numerical olivine that have been affected by diffusive re-equilibration indicate that larger phenocrysts (800 μm along *c*-axis) are > 50% more likely to preserve original Xpx compared to smaller phenocrysts (400 μm along *c*-axis) which rarely (6%) recover original Xpx. Sections that are parallel or sub-parallel to the *c*-axis and/or pass near the core of the crystal best preserve growth signatures. Thus, diffusive re-equilibration, crystal size, and sectioning effects can strongly influence the characterization of mantle source lithologies for Hawaiian volcanoes.

Keywords: Olivine, nickel, Kīlauea, Hawai'i, magma mixing, diffusion, pyroxenite

2.2. Introduction

Hawaiian olivine from tholeiitic basalts are enriched in Ni compared to those from mid-ocean ridge basalts (MORB) at a given forsterite content (Figure 2.1). This enrichment is a feature that has received much attention, with diverse interpretations (source and crustal) regarding its origin (e.g. Hart and Davis 1978; Sobolev et al. 2005; Wang and Gaetani 2008; Herzberg et al. 2013). One hypothesis advocates that high-Ni parental liquids are produced from olivine-free pyroxenite (i.e. secondary pyroxenite, formed from the reaction of partial melts of eclogite with peridotite; Sobolev et al. 2005;

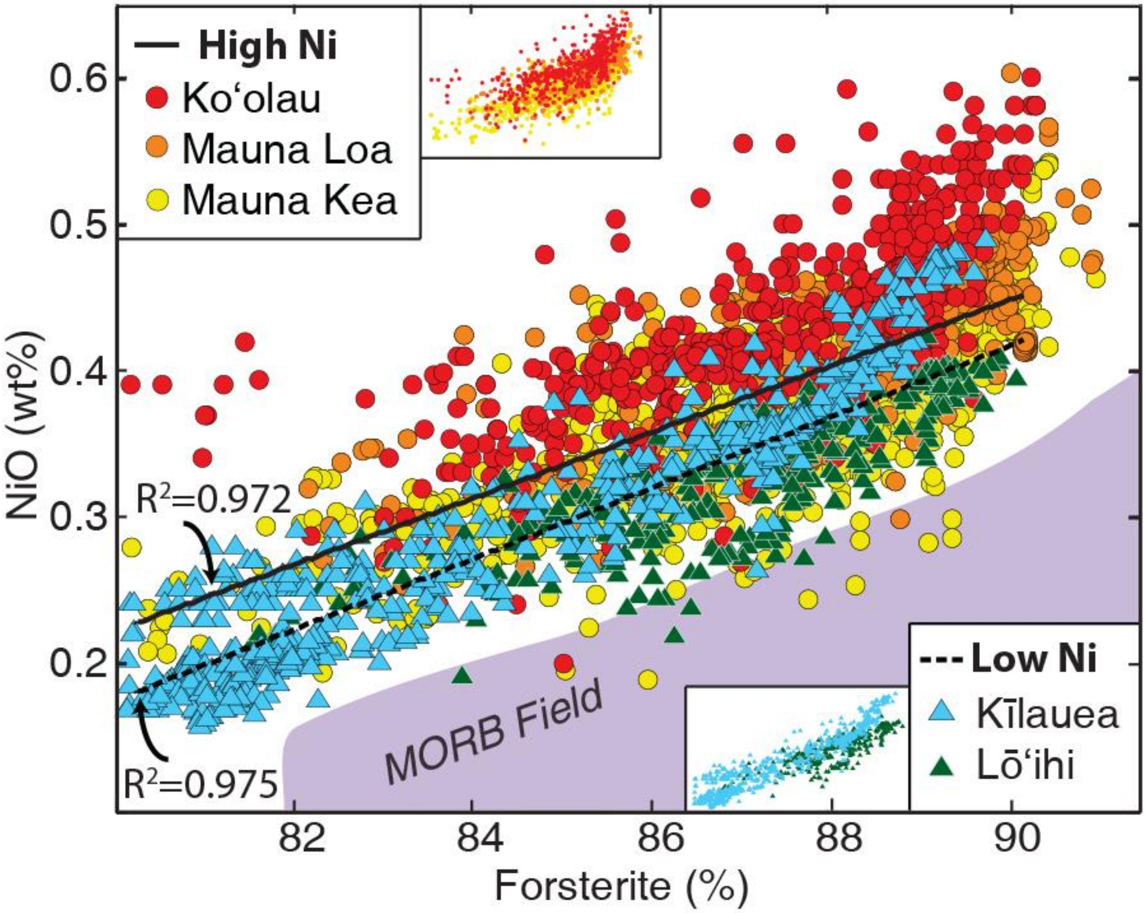

Figure 2.1. Forsterite (%) vs. NiO (wt%) for olivine from Ko‘olau, Mauna Loa, Mauna Kea, Lō‘ihi, and Kīlauea lavas. The data can be separated into high-Ni (warm colors) and low-Ni volcano groups (cool colors). Linear regressions for high- (solid line) and low-Ni (dashed line) groups with R^2 values. Olivine from the high-Ni volcanoes have a wider range in NiO at a given Fo compared to the low-Ni volcanoes (inset figures). Ko‘olau olivine are from Garcia (2002) and Sobolev et al. (2007), Mauna Loa, Mauna Kea, and Lō‘ihi are from Sobolev et al. (2007). Kīlauea data are from this study and Sobolev et al. (2007). MORB field (purple) from Sobolev et al. (2007).

Herzberg 2006; Sobolev et al. 2007). Alternatively, somewhat more siliceous magmas can influence olivine compositions because they cause higher partition coefficients for nickel in olivine (e.g. $D_{Ni}^{ol/melt}$=12.5-22.5 for eclogite melt compared to 7.5-12.5 for basaltic melts; Wang and Gaetani 2008), alleviating the need for a multi-stage process to form an olivine-free pyroxenite hybrid source component. Differences in melting and crystallization temperatures can also strongly influence $D_{Ni}^{ol/melt}$ (Hart and Davis 1978; Kinzler et al. 1990; Matzen et al. 2013) but are unlikely to affect Hawaiian olivine Ni variability because: (1) the age of the oceanic crust under the Hawaiian Islands is 85-95 Myr so decreasing plate age would have a minimal effect on the plate thickness (i.e.

melting T) for this relatively old oceanic crust (Parsons and Sclater 1977; Müller et al. 2008), (2) the difference in melting temperature between major Hawaiian volcanoes is small (< 60 °C; Putirka et al. 2011), and (3) variations in crystallization temperature between Hawaiian volcanoes probably do not produce resolvable variations in olivine Ni content (Matzen et al. 2013).

Crustal magmatic processes can also have a significant influence on olivine compositions (e.g. Herzberg et al. 2014, 2016). Fractional crystallization has been shown to strongly affect $D_{Ni}^{ol/melt}$ as a result of changing melt composition, producing steep olivine Fo-NiO trends at high Fo that are distinct from shallower trends associated with batch or equilibrium crystallization (Hart and Davis 1978; Beattie et al. 1991; Wang and Gaetani 2008). Magma mixing and diffusive re-equilibration, important processes in Hawaiian magmas, control the composition of erupted magma and element zoning in olivine (e.g. Wright and Fiske 1971; Yang et al. 1999). Diffusive re-equilibration occurs relatively rapidly at basaltic temperatures (Chakraborty 2010 and references therein) and produces shallow linear trends that broaden the NiO variability at a given Fo (Wang and Gaetani 2008). Determining the contributions of these processes to the overall NiO variability in Hawaiian olivine is essential for distinguishing the influence of crustal and mantle processes on the degree of olivine NiO enrichment.

Hawaiʻi is the ideal location to study the relative effects of mantle and crustal processes on the NiO content in olivine because: (1) there are good constraints on the lithosphere and crustal thickness (e.g. Parsons and Sclater 1977; Li et al. 2004), (2) the generation and evolution of mafic magmas has been extensively examined (e.g. Yoder and Tilley 1962; Green and Ringwood 1967; Wright and Fiske 1971; Eggins 1992; Takahashi and Nakajima 2002) and (3) most Hawaiian tholeiites are mineralogically simple with only olivine as a phenocrystic phase (e.g. Wright 1971; Garcia et al. 1989). Thus, the complications of multi-phase crystallization can generally be avoided (e.g. Shorttle and Maclennan 2011). There is also a wealth of published data on olivine and host lavas for many of the major Hawaiian volcanoes (Figure 2.2) allowing comparisons of lava and mineral chemistry (e.g. Garcia et al. 1995; Sobolev et al. 2007; Putirka et al. 2011).

The Ni contents of Hawaiian olivine are examined here from two perspectives: variations between major volcanoes (Figure 2.2) and variations observed for individual volcanoes. First, the parental melt and olivine compositions from five Hawaiian shield volcanoes (Koʻolau, Mauna Loa, Mauna Kea, Kīlauea, and Lōʻihi) are compared. Calculations of melt polymerization (Mysen et al. 1985) and $D_{Ni}^{ol/melt}$ (e.g. Wang and Gaetani 2008) are used to divide these volcanoes into high- and low-Ni groups that are dominantly controlled by parental melt compositions. Second, variations in melt and olivine compositions within one volcano (Kīlauea) are examined in samples for which magmatic conditions can be well constrained. Minor variations in parental melt NiO contents (0.09-0.11 wt%) account for the range of NiO contents for $\geq Fo_{88}$ olivine crystals. Much of the Ni variation for $< Fo_{88}$ olivine in Kīlauea lavas can be explained by shallow magmatic processes (principally storage, crystallization, and mixing), wherein diffusive re-equilibration can have a significant impact on the chemical relationships inherited by growth.

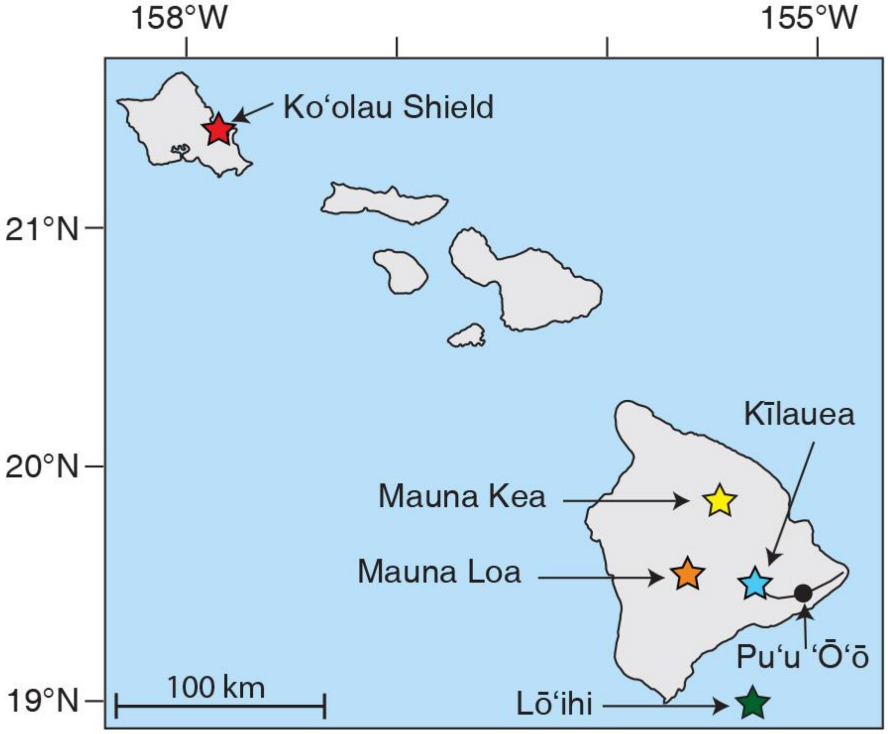

Figure 2.2. Map of the Hawaiian Islands showing the summit locations of the high-Ni (Koʻolau Shield, Mauna Loa, and Mauna Kea) and low-Ni (Kīlauea and Lōʻihi) volcanoes. Stars indicate the location of volcano summits, color coordinated to match Figure 2.1. The Puʻu ʻŌʻō eruption (black dot) is located 20 km southeast of Kīlauea's summit along its East Rift Zone (curved line).

2.3. Samples and Methods

Modal mineralogy for 14 samples from the long-lived, ongoing Puʻu ʻŌʻō eruption (Figure 2.2), upper east rift zone (ERZ; not including Puʻu ʻŌʻō), and summit eruptions were determined using 300 counts per sample (excluding vesicles) for phenocrysts (> 0.5 mm), microphenocrysts (0.1-0.5 mm), and matrix (glass and small crystals < 0.1 mm). The Kīlauea lavas and tephra used for this study are glassy and weakly to moderately olivine-phyric, with 1-7 vol. % phenocrysts and/or microphenocrysts (Table 2.1). Olivine is almost always the only phenocryst in these samples, usually with rare equant spinel inclusions < 0.1 mm in diameter. Puʻu ʻŌʻō lavas erupted between 1990 and 2010 are less olivine-phyric than those erupted earlier. Clinopyroxene and plagioclase phenocrysts are absent or rare (< 1.5 vol. %; Table 2.1) in Puʻu ʻŌʻō lavas. When present, they occur as microlites (< 0.1 mm) or rarely as microphenocrysts in lavas erupted from 2006-2010. The groundmass of all samples is typically light brown glass or black cryptocrystalline matrix. Most Kīlauea samples were collected in a molten state and quenched with water

Table 2.1. Representative modes for Kīlauea lavas (volume %), based on 300 (vesicle-free) counts/sample. Phenocrysts (ph, > 0.5 mm), microphenocrysts (mph, 0.1-0.5 mm), matrix (< 0.1 mm).

Location[a]	Eruption Date	Whole-rock MgO (wt%)[b]	Olivine		Cpx		Plag		Matrix
			ph	mph	ph	mph	ph	mph	
U	13-Jun-69	9.43	-	2.3	-	-	-	-	97.7
S	Aug 1971	10.01	-	0.3	-	-	-	-	99.7
P[c]	16-Aug-83	7.77	2.7	1.0	-	0.7	-	*[d]	95.6
P[c]	7-Sep-83	7.94	3.0	0.3	-	-	-	-	96.7
P[c]	18-Oct-87	8.11	1.0	3.0	-	-	-	-	96.0
P	20-July-90	9.04	5.7	-	-	-	-	-	94.3
P	5-Oct-92	7.93	-	4.7	-	-	-	-	95.3
P	18-May-94	7.61	0.3	2.7	-	0.3	-	-	96.7
P	22-Aug-96	8.23	0.7	2.7	-	-	-	-	96.7
P	13-Feb-99	7.41	-	1.7	-	-	-	-	98.3
P	4-Aug-00	8.29	0.3	4.3	-	-	-	-	95.3
P	12-Mar-03	7.62	1.3	5.0	-	0.3	-	-	93.3
P	17-Jun-07	8.53	-	2.0	-	*	-	-	98.0
P	6-Mar-10	7.18	-	0.7	-	0.7	-	0.7	97.9

Note(s): [a]Locations – S: Summit, 1971A-2 from Garcia et al. (2003), U: Upper East Rift Zone (rift zone eruptions not including Puʻu ʻŌʻō), this sample is from Mauna Ulu, P: Puʻu ʻŌʻō eruption; [b] for bulk compositions see Greene et al. (2013) and Garcia et al. (2003); [c] indicates samples with textural evidence of mixing (e.g. normal and reverse zoning of olivine) [d] * denotes phases that were observed but not counted.

to minimize post-eruption crystallization. Sample numbers (e.g. 4-Aug-00) refer to the date it was collected in a molten state. Episodes (Ep.) 1-12 from the Puʻu ʻŌʻō eruption were selected for detailed olivine analyses because magma mixing was documented as a dominant process throughout that time period (e.g. Garcia et al. 1992).

High precision olivine analyses were made using a five spectrometer JEOL Hyperprobe JXA-8500F at the University of Hawaiʻi. Compositions were determined for 519 olivine crystals (Tables 2.2 and A2) from Kīlauea lavas that span a wide compositional range (whole-rock MgO 7.0-10.1 wt%). Olivine spot analyses were done using a 20 kV accelerating voltage and a 200 nA beam current with a diameter of 10 μm. Peak counting times for analyses that included Mn (used for calculating percent pyroxenite in the melt) were 100 s for Si, Mg, Ca and Ni, 60 s for Mn, and 30 s for Fe. A more efficient routine without Mn and with shorter peak counting times (40-60 s for Si, Fe, Ni, Mg and Ca) was used for core-rim traverses. Backgrounds for all analyses were measured on both sides of the peak for half the peak counting times. Traverses in olivine were made using a 2 μm beam diameter and a 5 μm spacing and were oriented perpendicular to well-formed crystal faces away from corner locations to reduce sectioning effects on zoning patterns (Pearce 1984; Shea et al. 2015a).

Standards were San Carlos olivine (USNM 111312/444; Jarosewich et al. 1980) for Si, Fe and Mg, a synthetic nickel-oxide for Ni, Verma garnet for Mn and Kakanui Augite (USNM 122142; Jarosewich et al. 1980) for Ca. Two sigma relative precision for analyses, based on repeated analysis of San Carlos olivine, are 0.68 wt% for SiO_2, 0.38 wt% for MgO, 0.15 wt% for FeO, 0.008 wt% for NiO, 0.004 wt% for MnO, and 0.006 wt% for CaO (for analyses that included Mn) and 0.78 wt% for SiO_2, 0.44 wt% for MgO, 0.13 wt% for FeO, and 0.02 wt% for NiO and CaO (for analyses that did not include Mn). X-ray intensities were converted to concentrations using standard ZAF corrections (Armstrong 1988). Analyses with totals < 99.0 wt% or > 100.5 wt% were rejected. Each olivine data point represents an average (reported in Table 2.2 and Appendix Table A3) of two to three analyses at the center of the crystal determined by observation of geometry and intensity of zoning in BSE images. Olivine datasets for shield stage tholeiitic basalts from the literature (Garcia 2002; Sobolev et al. 2007) were filtered for analysis quality (e.g. > 99.0 wt% and < 100.5 wt%).

2.4. Results

Kīlauea olivine cores have a wide range in NiO at a given Fo (e.g. 0.29-0.42 wt% at Fo_{87}; Figure 2.3 and Table 2.2). Olivine from Pu‘u ‘Ō‘ō samples can be divided into two groups: higher Ni for Ep. 1-12 and lower Ni for Ep. 48-58 olivine. Most Pu‘u ‘Ō‘ō Ep. 1-12 olivine crystals have core forsterite compositions that are too high to be in equilibrium with their host-rock Mg-number (Mg# = [Mg/(Mg+Fe^{2+}) x 100]; Figure 2.4). Some lavas with an Mg# of 59-60 have olivine compositions that plot both above and below the

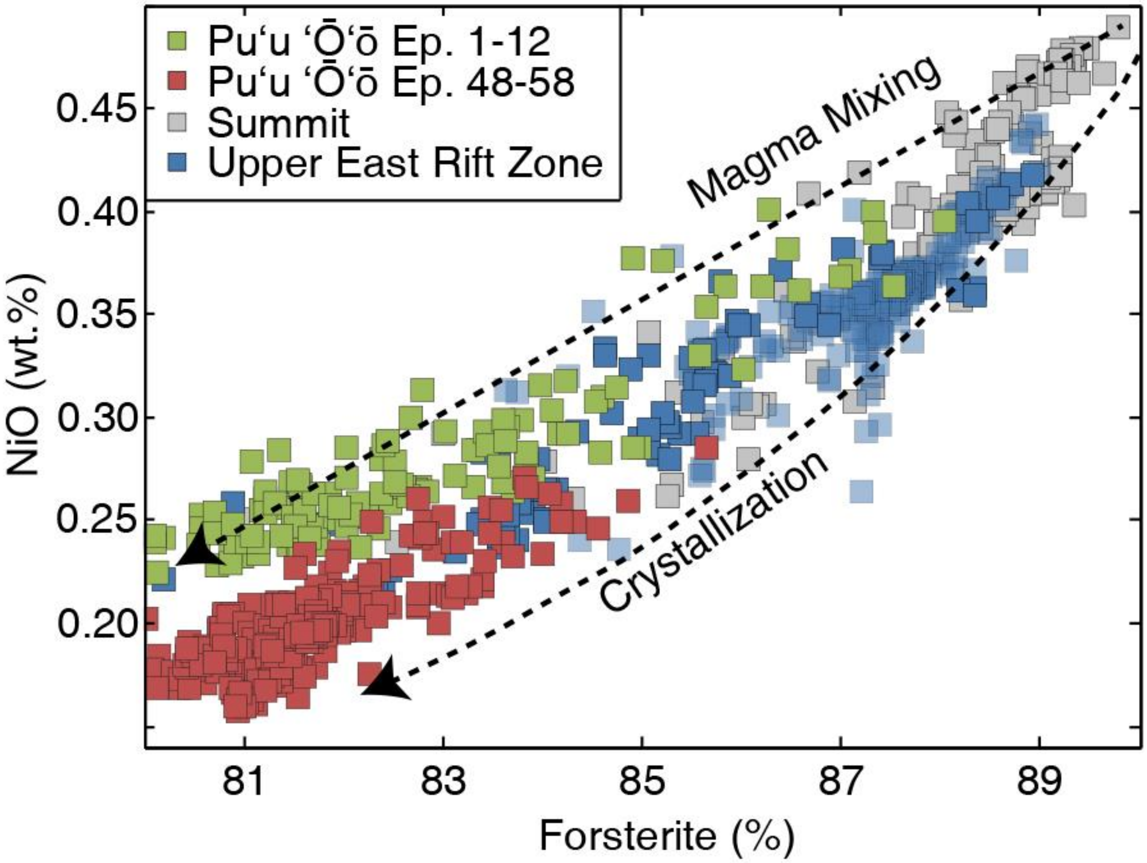

Figure 2.3. Forsterite (Fo%) vs. NiO (wt%) for Kīlauea olivine core compositions. Episode (Ep.) 1-12 (n=8 samples) Pu‘u ‘Ō‘ō olivine cover a period of magma mixing. Later Pu‘u ‘Ō‘ō Ep. 48-58 (n=31) olivine are from lavas that lack obvious petrographic signs of mixing. See Appendix A for specific samples and episodes. Vectors denote the evolution of olivine compositions during progressive crystallization and magma mixing (after Wang and Gaetani 2008). Upper ERZ includes historical rift zone eruptions (n=4), not including Pu‘u ‘Ō‘ō. Summit eruptions are from 1500-1971 (n=6). Light blue squares are data from Sobolev et al. 2007.

Table 2.2. Representative microprobe analyses for olivine from historical Kīlauea lavas. Oxides are in wt%. Full dataset can be found in Appendix A.2.

Sample	SiO$_2$	FeO[a]	NiO	MnO	MgO	CaO	Total	Fo[b]	Sample	SiO$_2$	FeO[a]	NiO	MnO	MgO	CaO	Total	Fo[b]
13-Jun 1969[c]	40.05	13.55	0.32	-	45.65	0.20	99.8	85.7	**18-Oct 1987**	39.47	16.25	0.21	0.228	43.76	0.22	100.1	82.8
	39.86	13.49	0.32	-	45.56	0.20	99.4	85.8		39.64	15.70	0.23	0.22	44.35	0.22	100.4	83.4
	39.71	13.95	0.30	-	45.28	0.21	99.4	85.3		39.42	17.10	0.20	0.24	43.14	0.23	100.3	81.8
	39.80	13.70	0.32	-	45.43	0.22	99.5	85.5		39.33	17.07	0.20	0.24	43.12	0.25	100.2	81.8
	39.77	13.60	0.32	-	45.56	0.22	99.5	85.7		39.28	17.22	0.20	0.24	43.12	0.25	100.3	81.7
	39.80	13.61	0.32	-	45.48	0.22	99.4	85.6		39.32	17.13	0.20	0.24	43.27	0.24	100.4	81.8
Aug 1971[d]	40.44	11.70	0.38	-	47.67	0.19	100.4	87.9		39.27	17.53	0.19	0.25	42.75	0.25	100.2	81.3
	40.40	10.93	0.41	-	48.54	0.18	100.5	88.1		39.31	17.14	0.19	0.24	42.73	0.24	99.8	81.6
	40.45	11.53	0.40	-	47.97	0.18	100.5	88.8		40.06	13.63	0.29	0.19	45.62	0.21	100.0	85.6
	40.21	12.95	0.34	-	46.57	0.19	100.2	86.5	**20-Jul 1990**	39.27	17.09	0.21	0.24	43.02	0.23	100.1	81.8
	40.29	11.96	0.40	-	46.57	0.19	100.2	86.5		39.16	17.22	0.21	0.24	43.00	0.22	100.1	81.7
	40.12	13.20	0.31	-	46.08	0.20	99.9	86.2		39.15	17.23	0.20	0.24	43.03	0.22	100.1	81.7
	39.84	14.01	0.26	-	45.44	0.21	99.8	85.3		39.01	17.10	0.21	0.24	42.89	0.23	99.7	81.7
	40.02	13.32	0.30	-	45.94	0.21	99.8	86.0		39.08	17.15	0.20	0.24	42.79	0.24	99.7	81.7
	40.07	13.29	0.31	-	46.09	0.20	100.0	86.1		39.21	17.14	0.20	0.24	42.70	0.31	99.8	81.6
	40.01	13.66	0.30	-	45.58	0.21	99.8	85.6		39.17	17.25	0.21	0.24	43.02	0.21	100.1	81.6
	40.18	10.80	0.41	-	48.31	0.18	99.9	88.9		39.15	17.27	0.20	0.24	42.79	0.24	99.9	81.5
	40.22	10.79	0.41	-	48.43	0.19	100.0	88.9	**4-Aug 2000**	39.14	17.17	0.19	0.23	43.33	0.23	100.3	81.8
7-Sep 1983	39.42	13.69	0.33	0.19	45.55	0.21	99.4	85.6		39.32	17.23	0.18	0.23	43.22	0.23	100.4	81.7
	39.61	14.43	0.29	0.19	45.54	0.23	100.3	84.9		39.29	17.39	0.18	0.24	43.14	0.24	100.5	81.6
	39.20	14.56	0.28	0.20	44.83	0.24	99.3	84.6		39.13	17.40	0.18	0.24	42.87	0.23	100.1	81.5
	39.45	15.24	0.32	0.20	44.84	0.24	100.3	84.0		39.07	17.41	0.17	0.24	42.75	0.24	99.9	81.4
	39.41	15.37	0.28	0.20	44.69	0.24	100.2	83.8		39.15	17.55	0.17	0.24	42.91	0.24	100.3	81.3
	39.31	15.52	0.30	0.20	44.43	0.23	100.0	83.6		39.16	17.58	0.18	0.24	42.89	0.24	100.3	81.3
	39.39	15.72	0.29	0.21	44.44	0.24	100.3	83.5		39.23	17.68	0.17	0.24	42.65	0.24	100.2	81.1
	39.08	16.19	0.27	0.22	43.64	0.22	99.7	82.8		38.64	18.75	0.16	0.25	41.87	0.26	99.9	79.9
	38.97	16.53	0.28	0.22	43.36	0.23	99.6	82.4	**6-Mar 2010**	39.45	17.94	0.19	0.23	41.41	0.21	99.4	80.5
	39.18	16.94	0.25	0.22	43.35	0.25	100.2	82.0		39.74	17.90	0.18	0.23	41.44	0.25	99.7	80.5
	39.09	17.27	0.26	0.22	43.25	0.24	100.3	81.7		39.68	18.04	0.17	0.23	41.40	0.27	99.8	80.4
	38.95	17.27	0.24	0.23	42.89	0.24	99.8	81.6		39.74	18.03	0.18	0.23	41.59	0.25	100.0	80.4
	39.19	17.34	0.25	0.22	43.19	0.23	100.4	81.6		39.56	18.02	0.17	0.23	41.34	0.25	99.6	80.4
	38.89	17.33	0.24	0.23	42.68	0.22	99.6	81.5		39.71	18.14	0.18	0.23	41.47	0.25	100.0	80.3
	38.83	17.72	0.23	0.24	42.35	0.21	99.6	81.0		39.72	18.25	0.17	0.24	41.26	0.26	99.9	80.1
	38.93	17.94	0.25	0.23	42.59	0.23	100.2	80.9		39.48	18.39	0.17	0.24	41.11	0.26	99.7	80.0
	38.81	17.93	0.23	0.24	42.16	0.22	99.6	80.7		39.34	19.27	0.15	0.25	39.97	0.30	99.3	78.7

Note(s): [a]FeO reported as total iron; [b]Fo (forsterite) = [Mg/(Mg+Fe) x 100]; [c]Mauna Ulu; [d]1971A-2 from Garcia et al. (2003).

equilibrium field (e.g. Ep. 1-12; Figure 2.4). These lavas have bimodal olivine Fo populations with both normally and reversely zoned crystals, consistent with the inferred history of magma mixing for these episodes (e.g. Garcia et al. 1992). Olivine crystals from Ep. 48-58, a period when the lavas have no obvious petrographic signs of mixing (except Ep. 54, not shown here; Garcia et al. 2000; Thornber et al. 2003) are either in equilibrium with their whole-rock Mg# or are more magnesian than their host whole-rock would suggest at equilibrium (dashed black lines; Figure 2.4). These olivine crystals are normally zoned and may reflect delayed fractionation (Maaløe et al. 1988) indicating a simpler magmatic history compared to Ep. 1-12 samples.

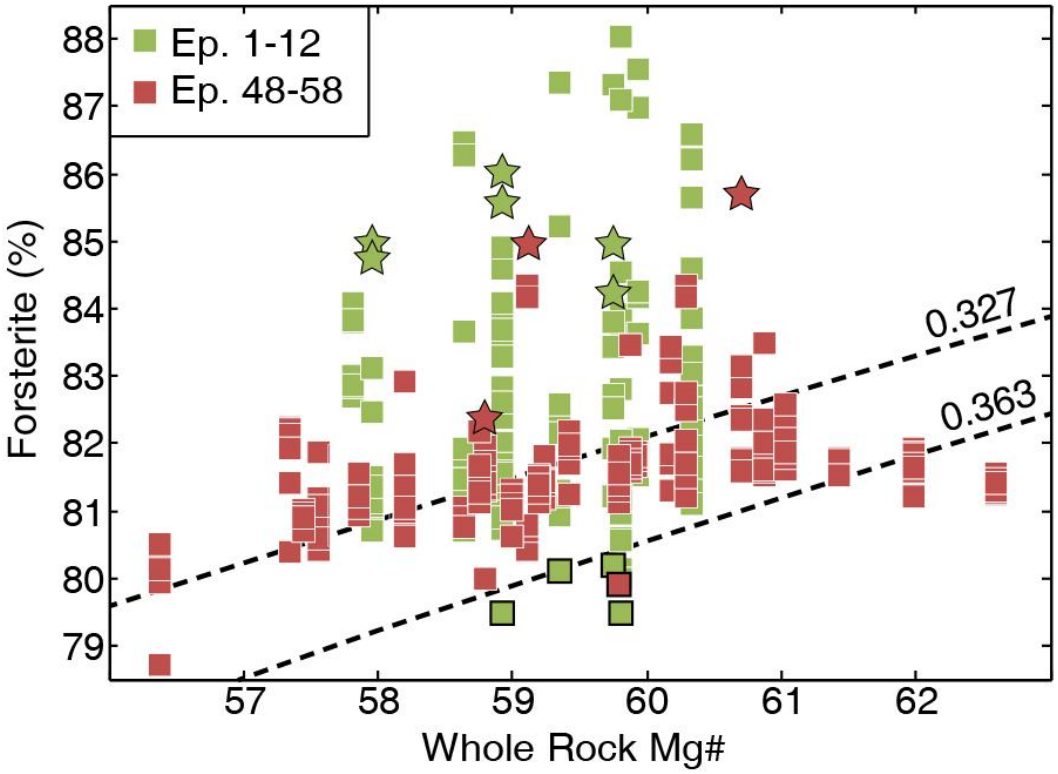

Figure 2.4. Representative whole-rock Mg-numbers [Mg/(Mg+Fe2+) x 100] plotted against olivine core forsterite contents for Kīlauea lavas. The Mg# is calculated assuming 90% of the total iron is Fe^{2+}, based on iron titration measurements of Kīlauea lavas (e.g. Moore and Ault 1965; Byers et al. 1985; Rhodes and Vollinger 2005). The dashed lines denote the shallow pressure (1 atm) equilibrium field for basaltic magma ($Kd^{ol/melt}_{Fe\text{-}Mg} = 0.345 \pm 0.018$ at 2σ; Matzen et al. 2011). Higher Mg# samples (e.g. 62.0-62.5) that dominantly plot below the equilibrium field have probably experienced olivine accumulation, whereas samples above the field represent non-equilibrium olivines from mixed magmas or delayed fractionation. Stars indicate examples of olivine with decoupled Fo-NiO zoning profiles, whereas squares with black outlined boxes indicate core compositions of reversely zoned crystals. For each sample, 5-12 olivine crystals were analyzed (similar Fo contents appear stacked; see Appendix A for analyses).

Core-rim transects of Kīlauea olivine crystals reveal two distinct Fo and NiO zoning patterns. Typically, olivine in equilibrium with their whole-rock Mg# have simple normal zoning profiles (e.g. Pearce 1984), where Fo and NiO co-vary and have similar concentration plateaus followed by similar decreases toward the rim (‘coupled’ profile, Figure 2.5). Some Kīlauea olivine crystals have distinctly different Fo and NiO zoning morphologies with a wider NiO plateau in their core compared to Fo (‘decoupled’ profile, Figure 2.5), similar to those observed by Nakamura (1995). Decoupled crystals are found throughout the Pu‘u ‘Ō‘ō eruption and always have Fo compositions above the equilibrium field with respect to their whole-rock Mg# (Figure 2.4), suggesting that decoupling is a feature of olivine crystals that are from mixed magmas.

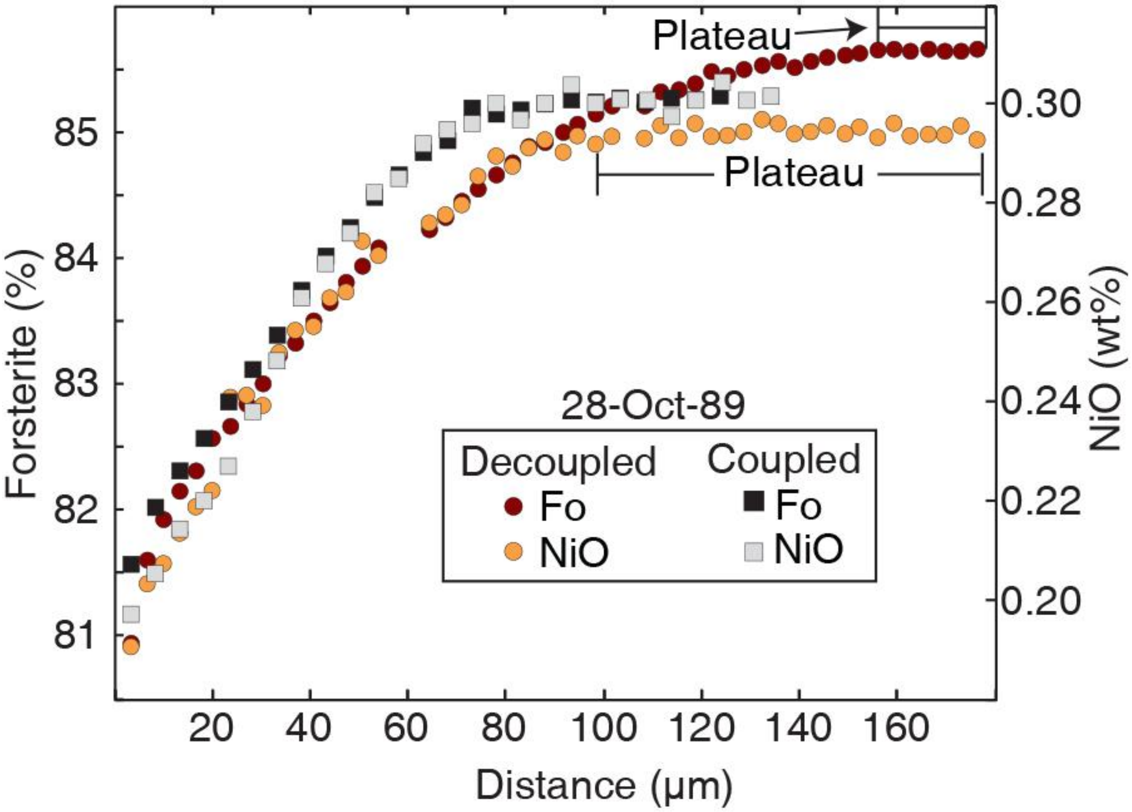

Figure 2.5. Examples of two Fo (%) and NiO (wt%) profiles from the same sample (28-Oct-89) that are similar in size and composition. Plateaus are regions where the composition (e.g. Fo or NiO) does not vary outside the analytical error. The sample name corresponds to the date it was collected during the Pu‘u ‘Ō‘ō eruption. Spot analyses with low totals due to cracks or spinel inclusions were removed and appear as gaps in otherwise regularly spaced analyses. Errors for all analyses are smaller than the symbol size.

2.5. Discussion

The origin of Ni-rich olivine in Hawaiian lavas is controversial. An olivine-free pyroxenite and/or eclogite source has been invoked to explain the high Ni contents (e.g. Sobolev et al. 2007; Wang and Gaetani 2008). Previous studies focused primarily on mantle processes for generating the Ni-enriched, Makapuʻu (Koʻolau) olivine (e.g. 0.60 wt% NiO at > Fo_{88}; Figure 2.1). The goal here is to examine other potential causes for the observed NiO differences in olivine between five Hawaiian volcanoes (inter-volcano variability) and at individual volcanoes (intra-volcano variability) in order to evaluate the relative contributions of mantle and crustal processes. First, inter-volcano variability is explored through investigations of parental melt composition, $D_{Ni}^{ol/melt}$, and the NiO contents of primitive olivine. Intra-volcano variations are examined using high precision analyses of olivine to assess the influence of crustal processes such as crystallization, magma mixing, and diffusive re-equilibration on interpretations of mantle source lithology.

2.5.1. Inter-volcano Ni variability

The wide range of Hawaiian olivine composition can be subdivided into two groups based on the average NiO at a given Fo (Figure 2.1, regression lines). Olivine in lavas from Koʻolau, Mauna Kea, and Mauna Loa form a broad, crescent shaped Fo-NiO field (upper insert; Fig 1) with a 0.25-0.60 wt% range in Ni at Fo_{88} (high-Ni group). Olivine from Kīlauea and Lōʻihi lavas form flatter Fo-NiO trends (lower insert, Figure 2.1) with a narrower range in NiO (0.27-0.43 wt% at Fo_{88}; low-Ni group). The division of the high- and low-Ni volcano groups is likely unrelated to parental liquid Ni content, as there is no systematic difference in whole-rock Ni between lavas from different Hawaiian volcanoes for a large range of MgO (Figure 2.6a). Evolved lavas (< 7.0 wt% MgO) were not considered in this study to avoid the complicating effects of multi-phase fractionation (e.g. Shorttle and Maclennan 2011). Lavas with MgO >10.5 wt% are likely affected by olivine accumulation (e.g. Hart and Davis 1978; Garcia 1996; Rhodes et al. 2012), although are similar to parental melt compositions (e.g. Putirka et al. 2011).

Koʻolau, Mauna Loa, and Mauna Kea lavas have whole-rock Ni that lie on both sides of the Hart and Davis (1978) line and overlap considerably with 20th and 21st

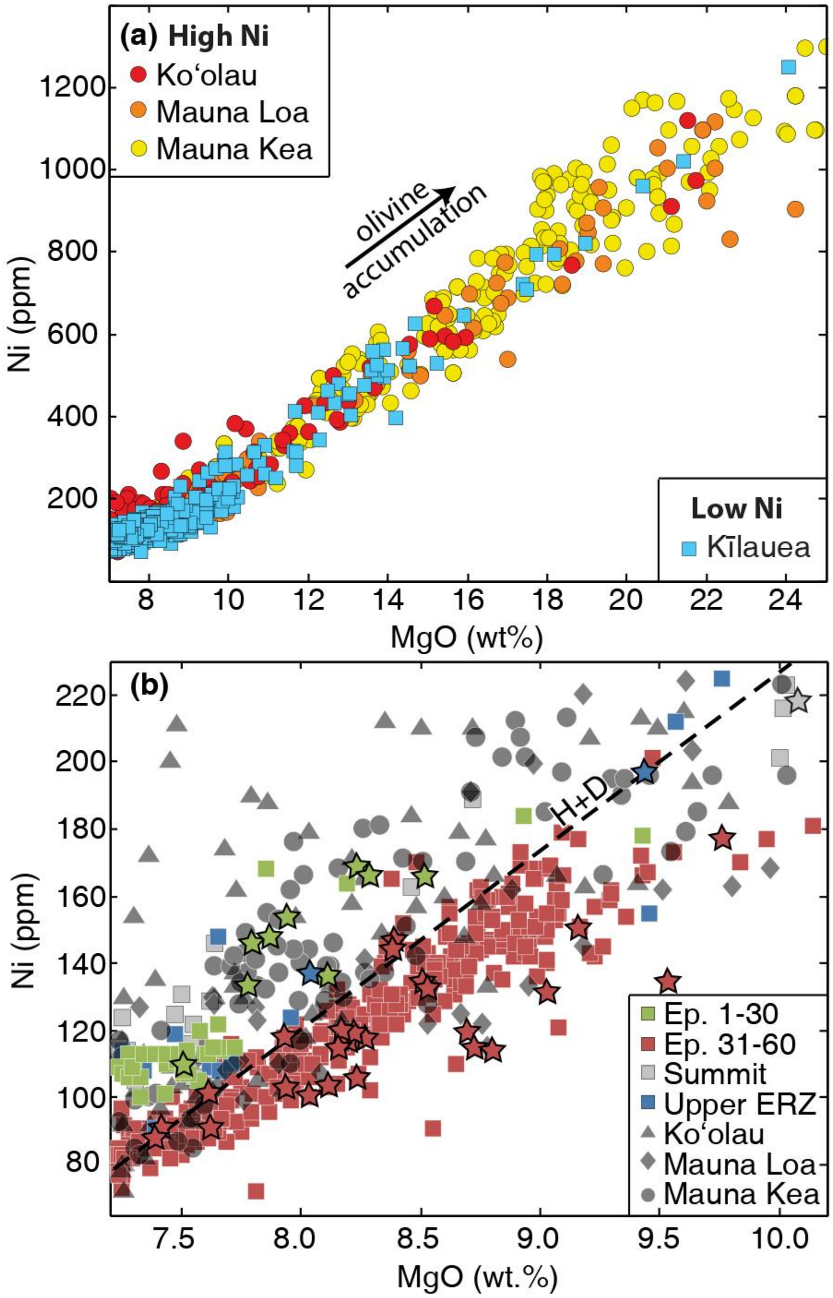

Figure 2.6. **(a)** Whole-rock MgO vs. Ni for Hawaiian volcanoes. All samples were analyzed in the same facility (University of Massachusetts) to avoid inter-laboratory differences. **(b)** Pu‘u ‘Ō‘ō samples are subdivided into early, mixed lavas from episodes (Ep.) 1-30 (Shamberger and Garcia 2007), and later unmixed samples (Ep. 31-60; minus Ep. 54). Dashed line (H+D) represents Kīlauea trend from Hart and Davis (1978). The line separates most early, mixed Ep. 1-30 Pu‘u ‘Ō‘ō lavas from later unmixed Ep. 31-60 lavas. Symbols with dark outlines indicate Kīlauea samples used for olivine analyses in this study. Data are from Pietruszka and Garcia 1999, Marske et al. 2007, Garcia et al. 2003, Greene et al. 2013, Marske et al. unpublished, and this study (Appendix A Table A1) for Kīlauea, Rhodes 1995, Rhodes and Hart 1995 for Mauna Loa, Rhodes et al. 2012 for Mauna Kea, and Frey et al. 1994, Jackson et al. 1999, and Haskins and Garcia 2004 for Ko‘olau.

century Kīlauea samples (Figure 2.6a). However, olivine from these volcanoes display significant differences in maximum NiO contents (e.g. up to 0.22 wt%) at Fo_{88} (Figure 2.1). This issue was highlighted by Rhodes et al. (2012), who showed that there is no relationship between the olivine NiO contents and the SiO_2 contents of lavas from Mauna Loa and Mauna Kea (even for lavas with 30 wt% MgO), contrary to what would be expected if the source for the parental melts were an olivine-free pyroxenite hybrid. Furthermore, there is considerable Ni variation at a given MgO content for peridotites (e.g. 1200-3200 ppm Ni at 40% MgO; Rhodes et al. 2012), and when coupled with current uncertainties in estimating the partitioning of Ni between olivine and melt, melting of peridotite could account for Ni and SiO_2 variability observed in Hawaiian basalts (Putirka et al. 2011; Rhodes et al. 2012).

2.5.1.1. Influence of parental melt composition on $D_{Ni}^{ol/melt}$***.*** Lavas from the low-Ni group volcanoes (Kīlauea and Lō‘ihi) have 1-5 wt% lower SiO_2 than those from the high-Ni group at the same MgO contents (Ko‘olau, Mauna Loa, and Mauna Kea; e.g. Garcia et al. 1989; Rhodes et al. 1989; Frey et al. 1994). Variations in SiO_2 in Hawaiian basalts have been explained by variable degrees of melting of eclogite and/or peridotite (e.g. Takahashi and Nakajima 2002; Putirka et al. 2011; Rhodes et al. 2012). Experimental studies have also shown that Ni partitioning increases significantly with increasing melt polymerization (higher SiO_2), yielding high NiO olivine in more siliceous melts (e.g. Hart and Davis 1978; Wang and Gaetani 2008). The increase in $D_{Ni}^{ol/melt}$ with increasing SiO_2 is hyperbolic (Wang and Gaetani 2008). Thus, the small observed differences in parental melt SiO_2 (1-5 wt%) may potentially affect $D_{Ni}^{ol/melt}$ significantly. The magnitude of this effect is evaluated below.

Parental melt compositions (Table 2.3) for each volcano were calculated by incremental addition of olivine in equilibrium with the melt until added olivine reached Fo_{91} (the maximum Fo measured in Hawaiian lavas; Garcia et al. 1995), an approach that was used by Putirka et al. (2011) to estimate Hawaiian parental magma compositions. Parental melt NiO values of 0.09 wt% and 0.11 wt% NiO (i.e. 707-864 ppm Ni, expressed as elemental concentration) were used, similar to the parental Ni contents suggested by Sobolev et al. (2005) and Putirka et al. (2011). A pressure of 1 GPa and a starting temperature of 1450 °C were determined with MELTS (Ghiorso and Sack 1995; Asimow and Ghiorso 1998) and used in the model runs. The ratio of non-bridging oxygen to tetrahedrally-coordinated cations (NBO/T; Mysen et al. 1985) was calculated to approximate the degree of polymerization for each parental melt composition along its fractional crystallization trend. These ratios were used to calculate the Ni partition coefficient of Wang and Gaetani (2008), which is sensitive to variations in SiO_2, a major component of NBO/T.

Table 2.3. Parental melt compositions, calculated to be in equilibrium with Fo_{91} olivine, used in fractional crystallization models. NBO/T and $\mathbf{D_{Ni}^{ol/melt}}$ are reported for Fo_{91} olivine compositions.

Oxide (wt%)	**Lōʻihi**[a]	**Kīlauea**[b]	**Mauna Kea**[c] **(Low-Si)**	**Mauna Kea**[c] **(High-Si)**	**Mauna Loa**[d]	**Koʻolau**[e]
SiO_2	46.62	47.54	46.42	48.68	48.3	50.18
TiO_2	1.88	1.64	1.88	1.84	1.55	1.59
Al_2O_3	9.96	9.24	9.96	10.15	9.91	9.98
Cr_2O_3	0.20	0.20	0.20	0.20	0.20	0.05
FeO	11.50	11.43	11.50	10.50	10.92	10.87
MnO	0.16	0.16	0.16	0.16	0.17	0.13
MgO	19.21	19.73	19.14	17.25	18.01	17.60
CaO	8.66	7.64	8.16	8.52	7.47	6.23
Na_2O	1.69	1.57	1.71	1.67	1.55	1.97
K_2O	0.34	0.30	0.27	0.29	0.25	0.43
P_2O_5	0.14	0.16	0.15	0.15	0.16	0.20
NiO[f]	0.11 or 0.09	0.11 or 0.09	0.11 or 0.09	0.11 or 0.09	0.11 or 0.09	0.11 or 0.09
% ol. add.	9.7	-	5.6	4.0	1.9	6.7
NBO/T	1.66	1.61	1.61	1.45	1.45	1.36
$D_{Ni}^{ol/melt}$	4.3	4.25	4.25	4.0	4.0	3.8

Note(s): [a]Garcia et al. 1993; [b]Matzen et al. 2011, no olivine addition because parental composition as already in equilibrium with Fo_{91}; [c]Stolper et al. 2004; [d]Rhodes 2015; [e]Norman and Garcia 1999; [f]Imposed NiO concentration for all parental compositions (similar to Sobolev et al. 2005, Putirka et al. 2011).

The Koʻolau parental magma had the lowest calculated NBO/T for Fo_{91} olivine (1.36), the Mauna Loa and high-SiO_2 Mauna Kea parental magmas are intermediate (1.45), and Kīlauea and low-SiO_2 Mauna Kea (1.61) and Lōʻihi (1.66; Figure 2.7a) are the highest. These NBO/T values equate to $D_{Ni}^{ol/melt}$ values (using the equation of Wang and Gaetani 2008) of 4.3 (Koʻolau), 4.25 (Mauna Loa and high-SiO_2 Mauna Kea), 4.0 (low-SiO_2 Mauna Kea, Kīlauea) and 3.8 (Lōʻihi; Figure 2.7b) for the crystallization of primitive olivine (e.g. Fo_{90}). Olivine compositions were calculated along a liquid line of

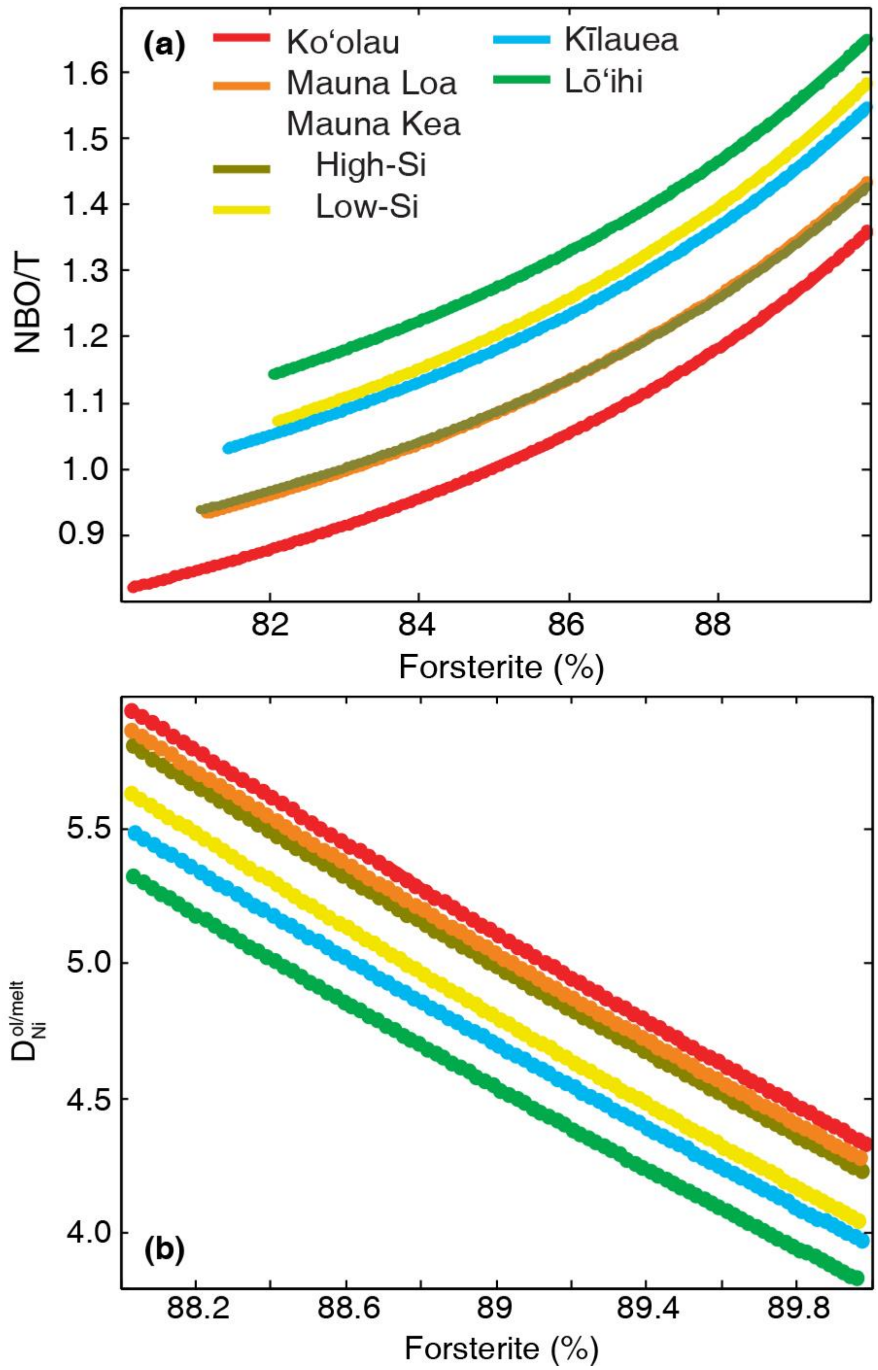

Figure 2.7. (a) NBO/T in standard fractional crystallization models of parental melt compositions for Ko‘olau, Mauna Loa, Mauna Kea (high- and low- SiO2), Kīlauea, and Lō‘ihi starting at 1450 °C until ~35 vol.% olivine is crystallized (producing variable final % forsterite due to small variations in parental composition and $D_{Mg}^{ol/melt}$). **(b)** The changing $D_{Ni}^{ol/melt}$ from Wang and Gaetani (2008), which is sensitive to variations in NBO/T, along fractional crystallization trends for primitive olivine at each volcano.

descent from each volcano's parental magma using both the $D_{Ni}^{ol/melt}$ and $Kd_{Fe\text{-}Mg}^{ol/melt}$ of Wang and Gaetani (2008; Figure 2.8a). The resulting olivine crystallization paths were also compared to crystallization models that used the $D_{Ni}^{ol/melt}$ from Matzen et al. (2013) with $D_{Mg}^{ol/melt}$ calculated from Putirka (2008) and a constant $Kd_{Fe\text{-}Mg}^{ol/melt}$ of 0.32 (Figure 2.8b). Previous partitioning approaches (e.g. Hart and Davis 1978; Kinzler et al. 1990; Beattie et al. 1991; Toplis 2005; Li and Ripley 2010; Putirka et al. 2011) have been thoroughly compared and discussed in both Wang and Gaetani (2008) and Matzen et al. (2013). Incorporation of the melt composition dependent $Kd_{Fe\text{-}Mg}^{ol/melt}$ expression of Toplis (2005) showed no difference in olivine compositions > Fo_{88} (see Appendix A).

Both models reproduce the relative NiO enrichment of primitive olivine compositions between volcanoes, with Koʻolau olivine having the highest NiO and Lōʻihi olivine the lowest. The Wang and Gaetani (2008) model reproduces the steep Fo-NiO trends for > Fo_{88} olivine compositions better than Matzen et al. (2013), although the NiO contents of Fo_{90} olivine are better matched by the Matzen et al. (2013) approach. Regardless of the partitioning models used, the relative inter-volcano differences are reproduced independent of variations in parental melt Ni content (Figure 2.8). This is consistent with the interpretations of Rhodes et al. (2012) who also compared the partitioning models of Beattie et al. (1991) and Putirka et al. (2011). Models from parental magmas with 0.11 wt% NiO provide a good match the highest compositions observed for each volcano, whereas parental magmas with 0.09 wt% NiO reproduce the lower Ni trends (Figure 2.8). Thus, minor variations in parental melt Ni contents account for the range of NiO contents for ≥ Fo_{88} olivine.

2.5.2. Intra-volcano Ni variability

Variations in olivine composition within Kīlauea volcano and its long-lived (34-year) Puʻu ʻŌʻō eruption provide additional insight into the mantle and crustal processes that control Ni concentrations in Hawaiian basalts. There is substantial variation in whole-rock Ni among weakly olivine phyric Kīlauea basalts at a given MgO concentration (e.g. 75 ppm variability at 9.5 wt% MgO; Figure 2.6b). A wide range is also observed for lavas from a single eruption (e.g. Puʻu ʻŌʻō, 60 ppm or 20% relative to median at 9.0 wt% MgO; Figure 2.6b). Lavas erupted at the summit and east rift zone (including Ep. 1-

30 of the Puʻu ʻŌʻō eruption) almost always lie above the Hart and Davis (1978) line with higher whole-rock Ni compared to lavas erupted from 1988-2010 (Puʻu ʻŌʻō Ep. 31-60; Figure 2.6b). Despite the differences in whole-rock Ni, olivine from Ep. 48-58 lavas overlap with summit and east rift zone compositions (Figure 2.3). Olivine compositions from Ep. 1-12 are somewhat elevated in Ni at < Fo_{85} but also overlap with summit and east rift zone analyses (Figure 2.3). These observations show that melt Ni contents do not correlate with olivine compositions, suggesting that other processes are affecting the NiO content of < Fo_{88} olivine in Kīlauea magmas. Below, the effects of fractional crystallization, magma mixing, and diffusive re-equilibration on olivine Ni contents in Kīlauea lavas are examined.

2.5.2.1. Crystallization. The olivine Fo-NiO trends for Kīlauea lavas (Figure 2.3) can be partly explained by fractional crystallization (Hart and Davis 1978; Wang and Gaetani 2008), which rapidly depletes Ni from the melt and produces steep, positive Fo-NiO trends for early crystallizing olivine from parental liquids (e.g. Kīlauea summit and ERZ olivine; Figure 2.3). These observations are consistent with many studies that have identified olivine fractionation as a dominant crustal process at Kīlauea and other Hawaiian volcanoes (e.g. Powers 1955; Wright 1971; Garcia 2002). Delayed fractionation, where magmas undergo extensive cooling and crystallization before fractionation takes place (Maaløe et al. 1988), may account for the range of Fo contents exhibited by many Kīlauea lavas and the presence of olivine with more primitive compositions than predicted (Figure 2.4).

The high- and low-Ni volcano groups can also be reproduced via fractional crystallization models from parental magmas with the same NiO contents (Figure 2.8). The changing $D_{Ni}^{ol/melt}$ during fractional crystallization (as a function of changing melt composition) creates Fo-NiO trends that are shallower than those observed for < Fo_{88} olivine at all volcanoes, suggesting that other processes control the compositions of these more evolved olivine. Mauna Kea compositions span the two Ni groups with the high-Si parental melt producing olivine similar to the highest NiO observed, and the low-Si parental melt forming lower NiO olivine (Figure 2.8). This accounts for some of the wide range of olivine NiO contents observed for Mauna Kea at Fo_{90}. As discussed above,

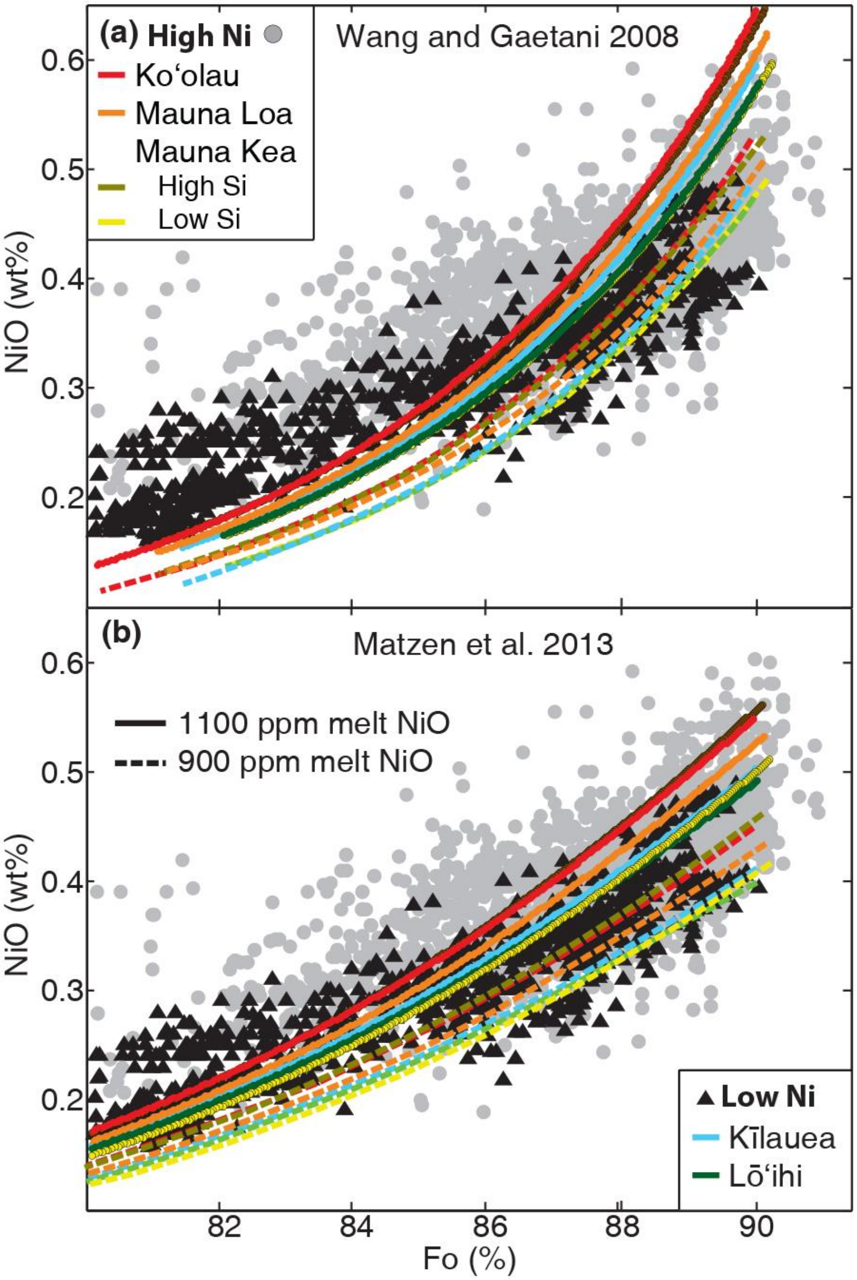

Figure 2.8. Olivine forsterite (%) vs. NiO (wt%) for fractional crystallization models at 1 GPa using **(a)** Wang and Gaetani (2008) and **(b)** Matzen et al. (2013) using parental melt compositions from Table 2.3. High- (grey) and low-Ni (black) volcano groups as in Figure 2.1. Solid lines represent models run for parental melts with 0.11 wt% NiO; dashed lines for parental melts with 0.09 wt% NiO.

slight variations in the parental melt Ni contents (e.g. 0.09-0.11 wt% NiO) can additionally explain the observed range of olivine NiO contents at ≥ Fo_{88} for each volcano (Figure 2.8).

2.5.2.2. Magma mixing. The high-NiO olivine from the mixed Ep.1-12 of the Puʻu ʻŌʻō eruption define a somewhat shallower Fo-NiO trend compared to Ep. 48-58 (Figure 2.3). If the compositions of these olivine were controlled by the higher whole-rock Ni of their host lavas and subsequent fractional crystallization, the trend should be parallel to and elevated above the later Ep. 48-58 olivine. This divergence in observed Fo-NiO trends requires that some other process is involved. Many of the Ep. 1-12 olivine are out of equilibrium with their whole-rock Mg#, have decoupled Fo-NiO profiles, and are from lavas that contain both normally and reversely zoned olivine crystals (Figure 2.4 and 2.5). These features are indicative of magma mixing, which agrees with previous interpretations based on whole-rock geochemistry (e.g. Garcia et al. 1989, 1992). The Ep. 1-12 mixing trend is generated as olivine crystallizes from and diffusively re-equilibrates with the mixed magmas (Wang and Gaetani 2008). Olivine crystals that have undergone protracted diffusive re-equilibration have higher Ni at a given Fo compared to olivine compositions produced by fractional crystallization (e.g. Ep. 1-12 vs. 48-58 of Puʻu ʻŌʻō; Figure 2.3). The effect of this relative Ni enrichment is more pronounced for evolved compositions (e.g. Fo_{80-85}, Figure 2.3).

The fractional crystallization models (Figure 2.8) generated < Fo_{85} olivine with lower Ni than is observed in the natural dataset. The natural olivine compositions are probably affected by magma mixing (Figure 2.3) and/or other processes, which causes the Fo-NiO trend to become shallower than the fractional crystallization only trends produced by the models (Figure 2.8). Mixing of relatively more primitive and more evolved melts produced by fractional crystallization with variable $D_{Ni}^{ol/melt}$ contributes to a broad crescent-shaped Fo-NiO field for Koʻolau, Mauna Loa, and Mauna Kea (upper insert; Figure 2.1) due to the relatively high NiO in primitive olivine equilibrating with more evolved compositions. A lower NiO content for ≥ Fo_{88} olivine at Kīlauea and Lōʻihi leads to a narrower range of compositions that mix and produce the more limited Ni array (lower insert, Figure 2.1).

2.5.2.3. Diffusive re-equilibration. The extent of diffusive re-equilibration of individual chemical species is largely dependent on (1) the relative diffusivities of the cations (e.g. $D_{Fe\text{-}Mg} \approx D_{Mn} > D_{Ni} > D_{Ca}$; Chakraborty 2010 and references therein) and (2) the contrast in element concentration between the olivine and the surrounding melt. To quantify the development of elemental decoupling by diffusion, numerical models were used to simulate diffusive re-equilibration of Fo and Ni in olivine. A concentration dependent, 3D diffusion equation (three spatial dimensions *x*, *y*, and *z* in addition to time *t*) was implemented following the methods described in Shea et al. (2015a) to allow Fe-Mg and Ni to diffuse simultaneously. The olivine+melt model had dimensions of 221 x 221 x 221 voxels with each voxel being 4 x 4 x 4 µm. The olivine has a dimension of 201 voxels along the *c*-axis, 123 voxels along the *b*-axis, and 94 voxels along the *a*-axis (Figure 2.9). The resulting olivine is ~800 x 500 x 375 µm, comparable to the size of larger olivine in Kīlauea lavas (e.g. Vinet and Higgins 2011). The volume of melt around the crystal,

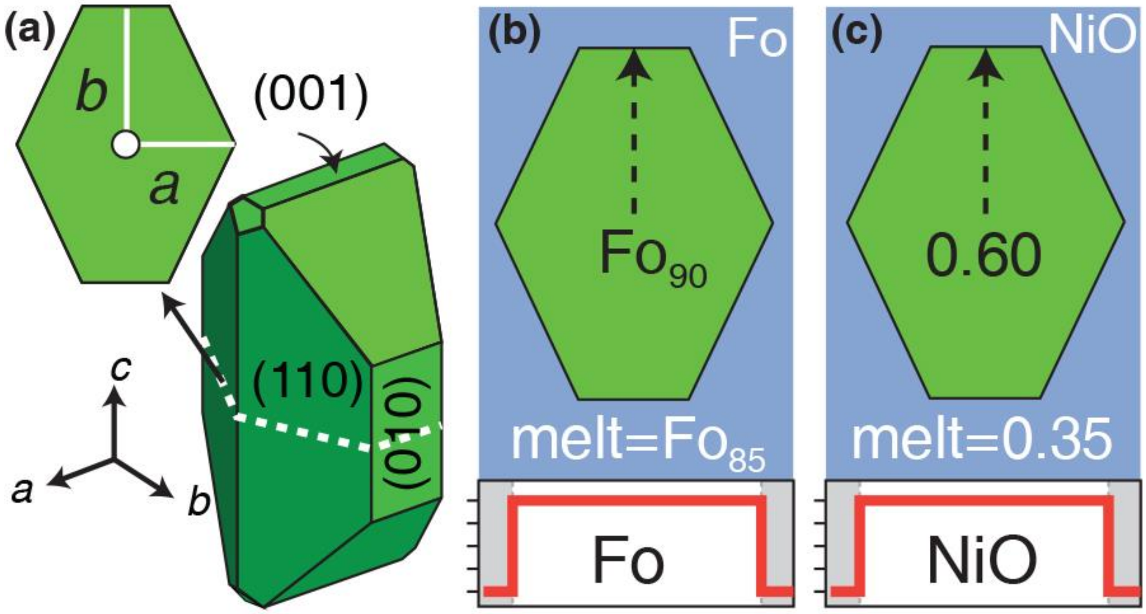

Figure 2.9. (a) 3D numerical olivine model showing 2D section (dashed white line) taken perpendicular to the *c*-axis [001]. **(b and c)** Initial crystal (black text) and melt (white text) compositions used in models. Melt forsterite is equivalent to a melt Mg# in equilibrium with Fo_{85} olivine. Melt and olivine NiO concentrations reported as wt%. Rim-to-rim concentration profile (bottom red lines) indicates sharp boundary between crystal and melt before diffusion has occurred. Black dashed line marks location of profile selection along [010] (*b*-axis) after diffusive re-equilibration with the surrounding melt.

although limited in the model, was an infinite reservoir for diffusing species and as such an infinite boundary condition. Magmatic conditions appropriate for Kīlauea were used, including a pressure of 85 MPa (within the depth range for Kīlauea's summit reservoir, 2-5 km; Cervelli and Miklius 2003; Poland et al. 2014) assuming a crustal density of 2.9 kg/km^3. The oxygen fugacity was set at ΔQFM -1 (Rhodes and Vollinger 2005) and temperature was held constant at 1200 °C, which is appropriate for a Kīlauea magma with 9.25 wt% MgO based on the experimental work of Helz and Thornber (1987). Model runs simulated diffusive re-equilibration for 1 and 2 years, which are within the 0.5-8 years magma residence time estimate for historical Kīlauea lavas (Pietruszka et al. 2015). Diffusivities for Fe-Mg and Ni were taken from Dohmen and Chakraborty (2007) and Chakraborty (2010) respectively. Olivine models were sectioned perpendicular to the *c*-axis through the core of the crystal, and core-rim profiles were sampled along the *b*-axis (Figure 2.9).

Variations in the extent of diffusion between chemical species are described by % re-equilibration (req), which is used to normalize the absolute concentration change of each element and allow their direct comparison (Equation 2.1),

$$\%\ \text{req} = \frac{(C_{\text{initial}} - C_{\text{measured}})}{(C_{\text{initial}} - C_{\text{equilibrium}})} * 100 \tag{2.1}$$

where $C_{initial}$ is the composition of olivine inherited from crystal growth before the onset of diffusion, $C_{measured}$ is the measured composition of the olivine after diffusion, and $C_{equilibrium}$ is the composition of the surrounding melt (expressed as the Fo content of an olivine in Fe-Mg equilibrium with the melt; Figure 2.10a). NiO and Fo contents were chosen based on natural compositions from the high-Fo end of the Hawaiian olivine dataset (Figure 2.1). The numerical olivine had C_{initial} of Fo_{90} and 0.60 wt% NiO and $C_{\text{equilibrium}}$ of Fo_{85} and 0.35 wt% NiO (Figure 2.9).

The model results show that the decoupled Fo-NiO profiles associated with magma mixing at Kīlauea are produced by diffusion (Figure 2.10a). The decoupling is caused by the slower diffusion of Ni compared to Fe-Mg, as shown by Dohmen and Chakraborty (2007) and Petry et al. (2004). The faster diffusion of Fe-Mg in olivine produces shorter core plateau lengths for Fo than NiO in the same crystal (e.g. Figure 2.5

and 2.10a). Although Ni diffusivity can vary with melt SiO_2 (Zhukova et al. 2014a), this effect is negligible for Hawaiian lavas given their small observed ranges in melt SiO_2 (1-5 wt%; see Appendix A). High-Fo olivine mixed with fractionated basaltic melt produces olivine with normal zoning, in which olivine crystals re-equilibrate to more Fe rich, Mg poor (e.g. lower Fo) and Ni poor compositions (Figure 2.5 and 2.10a). With time, olivine crystals develop lower Fo at a faster rate than the decrease of Ni, resulting in compositions that would not be expected from fractional crystallization alone (e.g. Nakamura 1995). The penetration distance and degree of diffusive re-equilibration in the olivine increases with time (Figure 2.10b). Thus, olivine compositions that have been affected by diffusive re-equilibration probably do not preserve chemical relationships inherited from crystal growth.

2.5.3. Characterizing source lithology using olivine composition

Olivine major and minor elements have been used to calculate the weight fraction of pyroxenite derived melt in the source (Xpx; Sobolev et al. 2005, 2007; Gurenko et al. 2010). A potential flaw in this method is the use of element ratios (e.g. Li and Ripley 2010) which can be affected by crustal processes. To more fully characterize the extent to which crustal processes affect estimates of source lithology, we examined the influence of diffusive re-equilibration on the calculated pyroxenite content in both natural olivine and numerical model olivine crystals.

Decoupling of Fo and NiO in olivine (Figure 2.10b) may modify the recorded fraction of pyroxenite derived melt (Xpx) because concentrations of Ni, Mn, FeO, and MgO are used to make these calculations (e.g. Sobolev et al. 2005) as in this example (Gurenko et al. 2010; Equation 2.2):

$$X_{px} = 6.70\text{E-}04 \times \text{Ni} \times \frac{\text{FeO}}{\text{MgO}} - 1.332\text{E-}02 \times \frac{\text{Mn}}{\text{FeO}} + 1.524 \qquad (2.2)$$

As a high-Fo olivine becomes normally zoned, FeO increases as MgO decreases, resulting in an increase in the FeO/MgO ratio (Equation 2.2). This increase has a larger impact on calculated pyroxenite than the decrease of Ni during diffusion due to (1) the

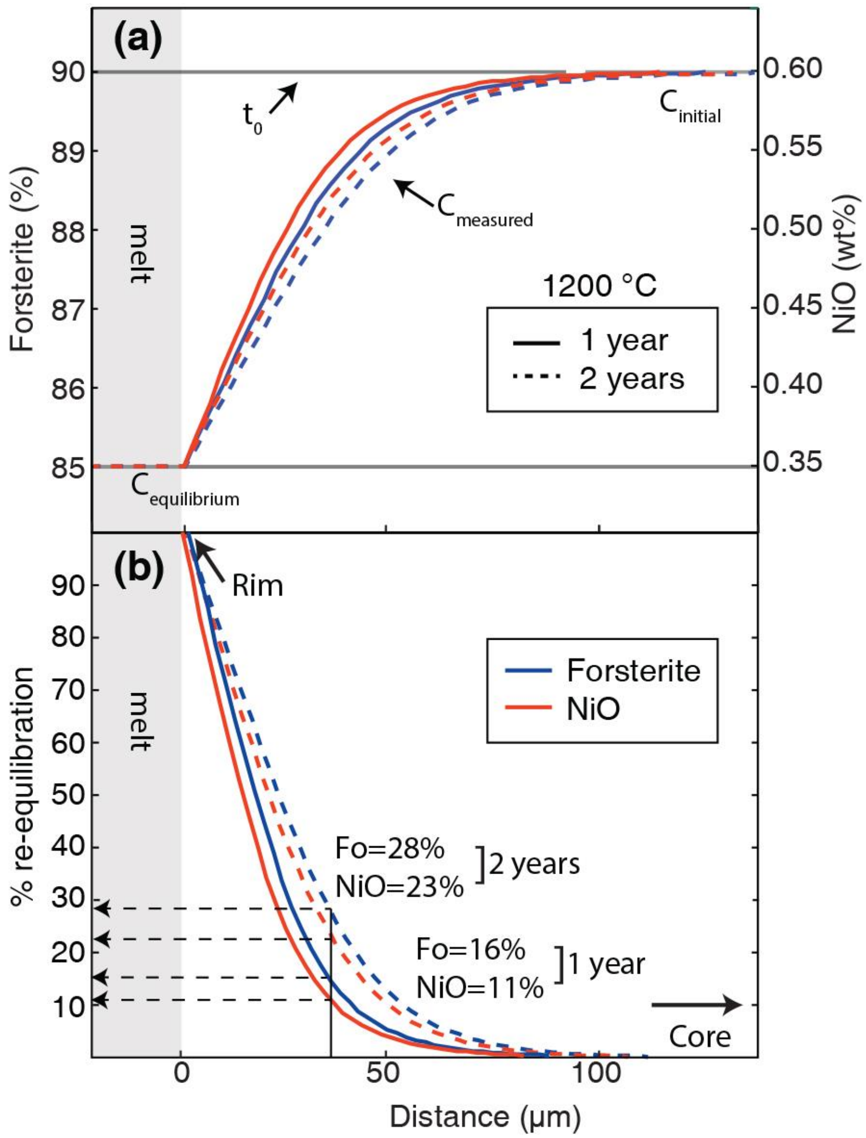

Figure 2.10. Results from numerical olivine diffusion models. **(a)** Forsterite (blue) and NiO (red) profiles along the *b*-axis in the olivine section. Solid line is one year of diffusion and dashed line is two years of diffusion. Cinitial and Cequilibrium values labeled for starting crystal and surrounding melt compositions as in Figure 2.9. **(b)** Results of % re-equilibration calculation (Equation 2.1) using Cinitial, Cequilibrium, and Cmeasured (zoning profiles from panel a). In this ideal section through the crystal's center, the core retains $C_{initial}$ after diffusion has occurred.

slower diffusivity of Ni and (2) the amplifying effect of increasing FeO while simultaneously decreasing MgO. Olivine from Kīlauea can be strongly zoned in Fo (e.g. 78-86.5%; Figure 2.11a) with complex growth and diffusion histories. From the core of the example olivine to its rim, diffusive re-equilibration of Fe-Mg, Ni, and Mn increased

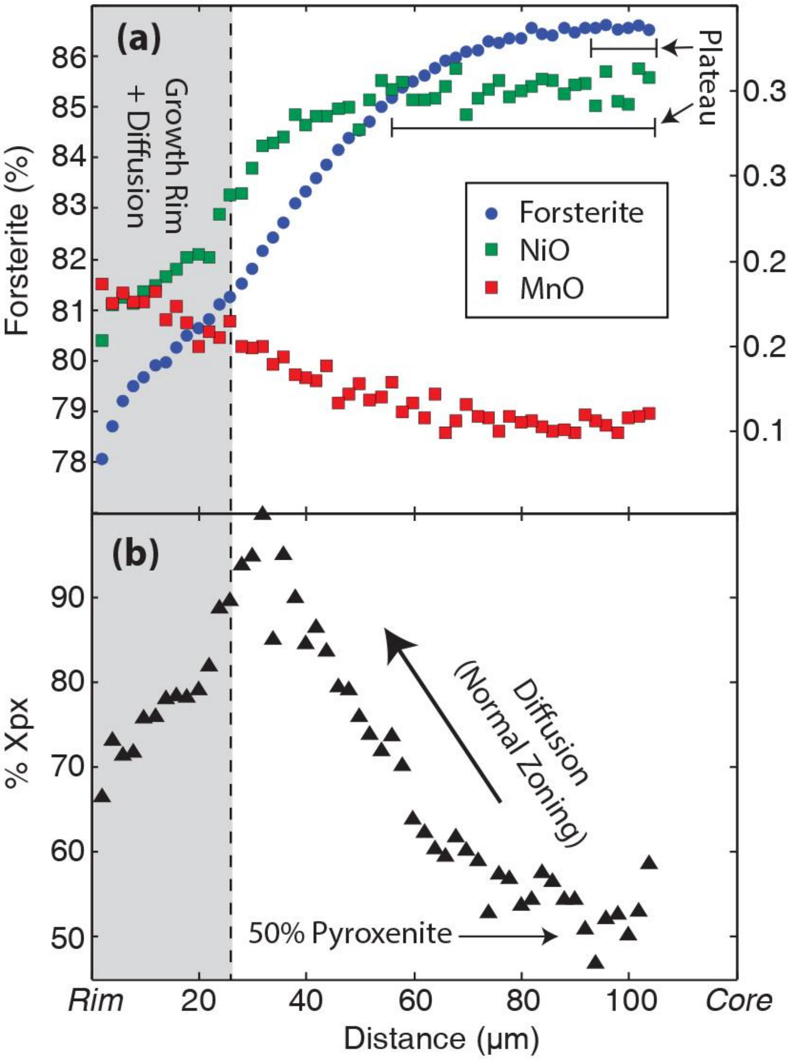

Figure 2.11. (a) Normally zoned and decoupled Kīlauea olivine (1670 C.E. summit lava flow) with complex rim zoning influenced by growth and diffusion (evident in multiple changes in slope for Fo; see Appendix A for analyses) and **(b)** calculated pyroxenite (Gurenko et al. 2010) of the profile from the core plateau to the rim. Scatter in the % Xpx calculated for the core region is due to analytical variability in minor elements (panel a).

the calculated pyroxenite fraction from ~50% to 100% (Figure 2.11b) and then decreased again to ~67%. This natural example suggests that diffusive re-equilibration can significantly raise and/or lower the measured pyroxenite component (by at least 50%), creating significant spread in the inferred lithology of the mantle source region.

To determine whether diffusive re-equilibration strongly affects olivine core compositions, we compared numerical olivine models of different sizes (along their *c*-axis): 800 μm ("large", consistent with antecryst sizes in Kīlauea lavas; e.g. Vinet and

Higgens 2011) and 400 µm ("small", a size that is common in many Kīlauea lavas, especially those from Pu'u 'Ō'ō; Table 2.1). Models simulated two years of diffusion at 1200 °C for Fe-Mg (Fo), NiO, and MnO. Crystal ($C_{initial}$) and melt ($C_{equilibrium}$) compositions of $Fo_{initial} = 90$, $NiO_{initial} = 0.60$ wt%, $MnO_{initial} = 0.13$ wt% , $Fo_{equilibrium} = 82$, $NiO_{equilibrium} = 0.25$ wt%, and $MnO_{equilibrium} = 0.23$ wt% were used. Numerical olivine crystals from both models were randomly sliced 250 times, the Ni and Mn (ppm) and FeO and MgO (wt%) core compositions in each crystal section were "measured" (see Appendix A), and the results were used to calculate the weight fraction of pyroxenite-derived melt using Equation 2.2 (Gurekno et al. 2010).

The model sections of the large olivine had an average composition of $Fo_{88.8}$ compared to the original Fo_{90}. About 60% of the sections returned original Xpx within ±1% of the original value (e.g. 76-78% Xpx). The section types most likely to retain original compositions were oriented parallel or sub-parallel to the *c*-axis and/or near to the core of the crystal (Figure 2.12). In contrast, the small model thin section had an average of Fo_{86} and only 6% recovered the original Xpx within ±1%. The small olivine had sections with core compositions that were on average more re-equilibrated (e.g. 50% re-equilibration) compared the large crystal (13% re-equilibration). In both models, the calculated Xpx ranged up to 87-89%, more than 10% higher than the 77% Xpx from the original composition. The small crystal also had a considerable range of Xpx below the original value (minimum was 67%), indicating that these highly re-equilibrated sections reflect the Xpx of the more evolved surrounding melt, not the initial crystal composition. Strikingly, sections from the small crystal taken near to the core and parallel or sub-parallel to the *c*-axis rarely recovered initial Xpx. These example models indicate that at least a 20% range in Xpx is recoverable if the olivine have been affected by diffusive re-equilibration, and the natural example (Figure 2.11b) suggests even greater variability is possible if the compositional difference between the phenocryst and surround melt is more significant.

Regardless of crystal size, sectioning a natural olivine phenocryst parallel or sub-parallel to the *c*-axis is statistically rare due to its relatively elongate geometry (Figure 2.9). Crystals are more likely to be sectioned in some manner sub-perpendicular to the *c*-axis (Figure 2.12, see also Appendix Figure A2.2). Larger crystals should generally be

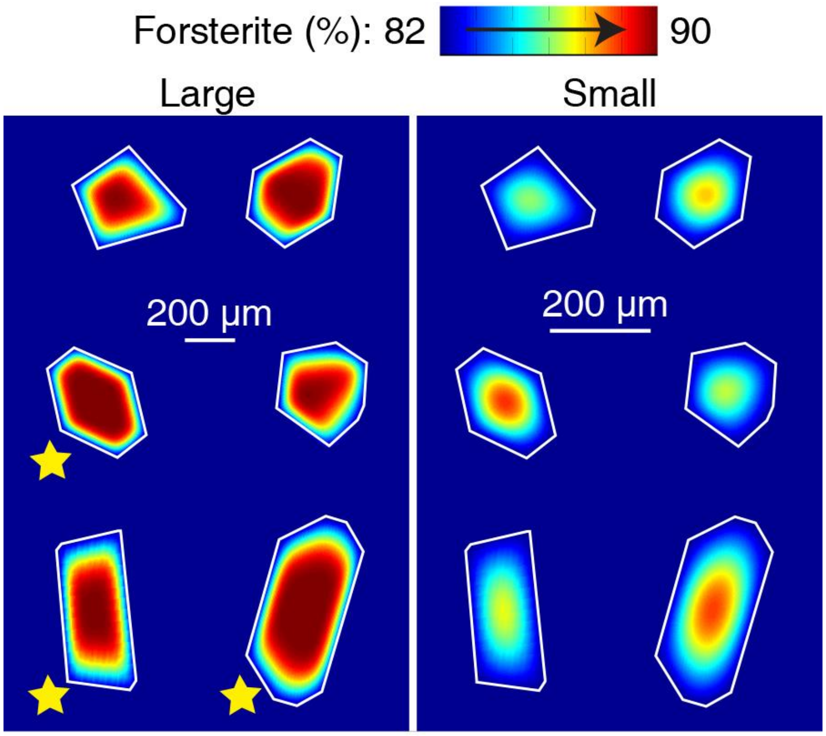

Figure 2.12. Examples of numerical “thin sections” for large (800 µm; left) and small (400 µm; right) olivine diffusion models (full dataset can be found in Appendix A). The small model was scaled up 2x to provide direct comparison with the large model. Thin white line marks the crystal margins within the melt (blue background). Yellow stars next to sections from the large model indicate preservation of initial compositions and recovery of original % Xpx values. Each section is either (1) near the crystal’s core and/or (2) sectioned parallel or sub-parallel to the *c*-axis.

more reliable for using olivine compositions to infer characteristics about source componentry. The core compositions of these larger crystals are, however, decoupled and compromised after ~6 years of diffusive re-equilibration based on model conditions described above. These storage timescales are not unreasonable, considering recent estimates of magma storage within Kīlauea range from 0.5-8 years (Pietruszka et al. 2015). Thus, some knowledge of the storage histories of olivine cargo is required if using their compositions to investigate mantle processes.

2.6. Implications

This study highlights the complexities associated with the modifying effects of crustal processes and inferring characteristics about mantle source lithologies. In light of the numerous hypotheses regarding the origin of Hawaiian basalts, our study clearly illustrates that crustal processes are a significant factor in contributing to these diverse interpretations. Even parental melt characteristics (e.g. SiO_2), which are inherited during melt generation, can strongly control $D_{Ni}^{ol/melt}$ and the compositions of primitive olivine. New modeling investigations presented here provide evidence that subsequent diffusive re-equilibration of Fe-Mg, Mn, and Ni in olivine can rapidly overprint the chemical relationships inherited during growth, thereby strongly affecting the calculated pyroxenite component and inducing 20-50% (or more) variability. The numerical olivine may provide minimum constraints, as the mixing end member compositions could vary substantially and greater differences in melt Mg# would induce greater extents of diffusive re-equilibration and elemental decoupling.

The effects of diffusion on olivine composition are further complicated by random sectioning of crystals. In natural samples, ideal sections are rare (e.g. Pearce 1984; Figure 2.12). The vast majority of olivine in a typical thin section are cut off center and oblique to principle axes (Shea et al. 2015a). Diffusive re-equilibration will substantially modify the FeO/MgO, Ni, and Mn/FeO in these sections due to the different diffusivities of these elements. Thus, olivine crystals of moderate size that grow and are stored in the crust for a few years are unlikely to preserve their original crystallization history. These effects are significant for smaller crystals (e.g. < 0.5 mm along *c*-axis), which should be avoided in estimating the composition of the source components. Large, high Fo (≥ 88) olivine crystals are likely less affected by a few years of diffusive re-equilibration if sectioned near or through the crystal core and are more appropriate for analyses that will be used to characterize mantle processes if there are good constraints on magma storage and transport histories. Furthermore, large crystals like those found in picrites are more likely to retain growth compositions after a few years of diffusive re-equilibration and are potentially more reliable indicators of source lithology in Hawaiian lavas (although some sense of their storage histories are required).

Our results raise concerns regarding the use of olivine major and minor elements to characterize source lithologies for Hawaiian volcanoes and suggest that their olivine compositions can be unreliable records of mantle source. This work emphasizes how rapidly olivine compositions are compromised in relatively high temperature basaltic systems, particularly when the inherent complexities of natural samples are considered. Due to numerous variables (e.g. diffusion duration, crystal size, heterogeneous vs.

homogeneous populations) these numerical examples represent a simple case scenario, and suggest that diffusion could have a significant influence on interpretations drawn from olivine major and minor element compositions.

2.7. Acknowledgements

The authors acknowledge Keith Putirka, Benoît Welsh, and Dawn Sweeny-Ruth for fruitful discussions on olivine growth and compositional zoning, Mike Vollinger for XRF analyses, Eric Hellebrand for assistance with EPMA analyses, Jared Marske for unpublished East Rift Zone XRF data, and Garrett Ito for access to the Department of Geology and Geophysics, Geophysics and Tectonics Division’s computer cluster for diffusion modeling. We thank Claude Herzberg and Andrew Matzen for their helpful formal reviews, and Bruce Watson for editorial handling. The comments from the GG616 Scientific Writing class are also appreciated. This work is supported by NSF Grants EAR1118741 and EAR13347915 to MG, EAR1321890 to TS, the Fred M. Bullard Foundation and the University of Hawai‘i Graduate Student Organization to KL. This is School of Ocean and Earth Science Technology (SOEST) contribution number 9392.

CHAPTER 3

TIMESCALES OF MIXING AND STORAGE FOR KEANAKĀKO‘I TEPHRA MAGMAS (1500-1823 C.E.), KĪLAUEA VOLCANO, HAWAI‘I

Submitted for review as:

Lynn, K.J., Garcia, M.O., Shea, T., Costa, F., and Swanson, D.A. (in review) Timescales of mixing and storage for Keanakāko‘i Tephra magmas (1500-1823 C.E.), Kīlauea Volcano, Hawai‘i. Submitted to Contributions to Mineralogy and Petrology.

3.1. Abstract

The last 2,500 years of activity at Kīlauea Volcano (Hawai‘i) have been characterized by centuries-long periods dominated by either effusive or explosive eruptions. The most recent period of explosive activity, the Keanakāko‘i Tephra (KT; 1500-1823 C.E.) occurred after the collapse of the summit caldera (1470-1510 C.E.). Previous studies suggest that KT magmas may have ascended rapidly to the surface, bypassing storage in crustal reservoirs. The rapid ascent hypothesis is tested here using chemical zoning in olivine crystals to determine the timescales of magmatic processes and storage in the KT period. Olivine forsterite (Fo; [Mg/(Mg+Fe) x 100]) core and rim populations are used to identify melt components in the reservoir system. Primitive ($\geq$ Fo_{88}) cores occur throughout the KT; they originated from mantle-derived mafic recharge magmas that were first mixed and stored in a deep crustal reservoir. Bimodal olivine populations ($\geq$ Fo_{88} and Fo_{83-84}) record repeated mixing of these recharge magmas and more differentiated reservoir components shallower in the system. MELTS models show that liquidus olivine is unstable at depths below the crust. Thus, calculated timescales likely record mixing and storage within the crust and do not reflect deeper processes occurring in the mantle, as was previously suggested for other Kīlauea eruptions. Modeling of Fe-Mg and Ni zoning patterns (normal, reverse, complex) reveal that KT magmas were mixed and stored for many weeks to several years before eruption, contrary to previous interpretations of rapid ascent and no storage. Complexly-zoned crystals also have thin rims (5-20 μm) that are out of Fe-Mg equilibrium with surrounding melt. Numerical diffusion models suggest that these reversal rims formed within a few hours to a few days, indicating that an additional, late-stage mixing event may have occurred shortly prior to eruption.

Keywords: Hawaiʻi, Kīlauea, magma storage, olivine, diffusion

3.2. Introduction

Kīlauea (Hawaiʻi) is one of the best-studied volcanoes in the world (Tilling and Dvorak 1993; Garcia 2015), yet it has centuries-long periods of poorly understood explosive eruptions that may date back to ~70 ka (Easton and Garcia 1980; Easton 1987). The last 2,500 years have included five major periods characterized by either dominantly effusive or explosive eruptions (Swanson et al. 2014). The most recent transition from an effusive to an explosive period was marked by caldera collapse, an event that can have significant impacts on the structure of the shallow magmatic reservoir system (Corbi et al. 2015), magmatic processes (e.g. fractional crystallization vs. magma mixing), and the geochemistry of erupted material (Gavrilenko et al. 2016). Explosive activity at Kīlauea ended shortly before western missionaries first visited in 1823 (Ellis 1827), and the only historical records of these eruptions are translations of Hawaiian oral tradition (Swanson 2008). Thus, little is known about the magmatic processes operating in the crustal reservoir system during pre-historic (i.e. pre-1823) explosive periods.

The Keanakākoʻi Tephra (KT; 1500-1823 C.E.) is Kīlauea's most recent explosive period. It began during or just after the formation of the modern summit caldera (1470-1510 C.E.; Swanson et al. 2012a) and is Kīlauea's best exposed and most thoroughly studied tephra sequence (McPhie et al. 1990; Mastin 1997; Mastin et al. 2004; Swanson et al. 2012a, 2012b, 2014, 2015; Helz et al. 2015). Vent locations for KT eruptions were probably geographically widespread across Kīlauea's summit region (Swanson et al. 2006; Swanson et al. 2012b; May et al. 2015). The explosive nature of KT eruptions is thought to result from rapid injection of magma into a deep crater wet with ground or surface water, causing extensive magma-water interactions (e.g. McPhie et al. 1990; Mastin 1997; Mastin et al. 2004). Olivine-hosted melt inclusions with inferred high volatile contents have led to the interpretation that KT magmas ascended rapidly from depth, bypassing crustal reservoirs to erupt explosively at the surface (Sides et al. 2014). Heterogeneous, high-MgO glasses (e.g. 6.5-11.0 wt%; Helz et al. 2015) in several KT units were also interpreted to reflect inefficient mixing and little or no storage in the shallow reservoir system (Helz et al. 2014, 2015). To date, the mixing histories and the duration of crustal residence for KT magmas remain poorly known.

The rapid ascent hypothesis is tested here by determining the mixing histories and quantifying the durations from storage to eruption for KT magmas. Chemical zoning in olivine phenocrysts provides a means to investigate the timing and duration of magma storage at shallow levels in volcanic systems (e.g. Costa and Dungan 2005). Diffusive re-homogenization of compositional differences in olivine can be modeled to extract timescales that record the interval between magma mixing events and eruption (e.g. Costa et al. 2008 and references therein). The KT sequence is ideal for investigations of Kīlauea's prehistoric crustal reservoir system because; (1) the tephras have glasses with heterogeneous MgO contents, indicating inefficient mixing of magmas (Swanson et al. 2014; Helz et al. 2015) and (2) olivine with adhering glass is present in almost all eruption deposits containing juvenile material.

The magmatic histories of eight KT units are investigated here utilizing; (1) olivine core compositions, (2) modeling of diffusive re-equilibration of Fe-Mg and Ni in chemically-zoned olivine, and (3) Fe-Mg disequilibrium between olivine rims and adhering glass. The melt components in which olivine phenocrysts grew (e.g. within mafic recharge magmas or relatively evolved stored magmas) are determined from core composition populations. Distributions of olivine rim compositions are used to infer the magma composition in which crystals were stored prior to eruption. Zoning of Fe-Mg and Ni in these crystals provide timescales associated with mixing before eruption. Together, these characteristics are used to revise the current understanding of storage histories for KT magmas and characterize Kīlauea's prehistoric magma plumbing system after the collapse of the summit caldera.

3.3. Sample description and preparation

The Keanakākoʻi Tephra includes deposits from explosive phreatomagmatic and phreatic eruptions, high lava fountains, and one effusive lava flow (McPhie et al. 1990; Swanson et al. 2012a). Eight units with juvenile material spanning the entire KT period (1500-1823 C.E.) were included in this study (cf. Table 3.1 for brief unit descriptions). Six sites around Kīlauea's summit caldera were used for sampling the KT sequence since no single locality exposes a complete section (Figure 3.1a, 3.1b). Marker units (C^{14} dates from Swanson et al. 2012a) include the Basal Reticulite (~1500 C.E.), the Layer 6 Scoria (~1650 C.E.), the Circumferential Lava Flow (1670-1700 C.E.), and the Golden and Eastern Pumices (1790-1823 C.E.; Figure 3.1c). The Circumferential Lava Flow is unusual because it erupted from a caldera boundary fault at least 2.5 km south of the vents for the explosive eruptions within the caldera (Figure 3.1). Two pumice-rich layers found between the Basal Reticulite and the Layer 6 Scoria are from 1500-1650 C.E. (here called units 7 and 11), and one pumice-rich layer between the Layer 6 Scoria and the Circumferential Lava Flow is from 1650-1670 C.E (unit 20; Figure 3.1c).

Tephra samples were cleaned, gently crushed, and sieved into 0.5-1.0 mm and 1.0-1.65 mm size fractions. Olivine is almost always the only phenocrystic phase in these samples, and contains equant spinel inclusions (< 0.1 mm). Olivine phenocrysts with obvious crystal faces (Figure 3.2) and adhering glass were handpicked from both size fractions using a binocular microscope so that both crystal rim and glass compositions could be measured. Individual crystals were carefully mounted in epoxy in a 1" round plug to ensure that they were ground and polished perpendicular to a principle crystallographic axis down to the crystal core. This method minimized off-center and

Table 3.1. Keanakākoʻi Tephra samples examined in this study.

Sample Name	Age[1] (C.E.)	Deposit Type[1, 2]
Eastern Pumice[3]	1790-1823	Pumice fall deposit
Golden Pumice	1790-1823	Pumice fall deposit
Circumferential Flow (CLF)	1670-1700	Lava flow, erupted SW of summit caldera
Unit 20	1650-1670	Lithic-bearing vitric ash, thinly bedded
Layer 6	~1650	Scoria fall
Unit 11 Unit 7	1500-1650	Lithic-bearing vitric ash, thinly bedded, falls and fine surges
Basal Reticulite	~1500	Reticulite fall deposit

[1]Swanson et al. (2012a); [2]Sharp et al. (1987); [3]Since the publication of Swanson et al. (2012a), the Eastern Pumice has been identified and it overlies the Golden Pumice.

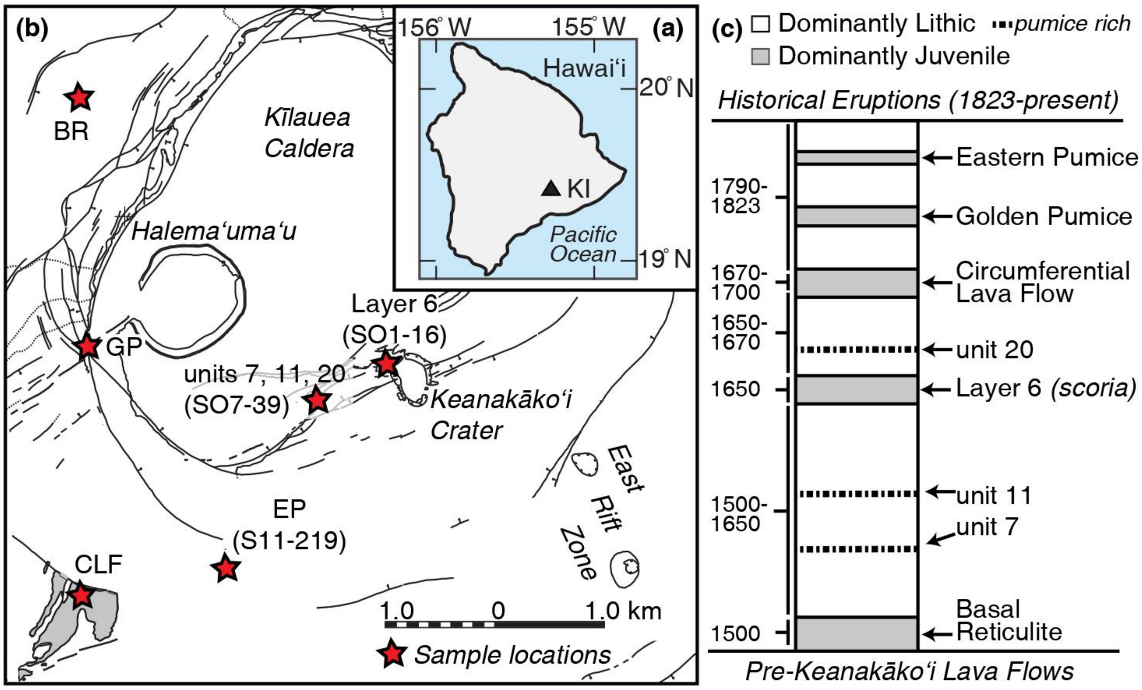

Figure 3.1. (a) The Island of Hawaiʻi, with black triangle identifying Kīlauea's summit. **(b)** Simplified summit map of Kīlauea Caldera with major faults and structural boundaries (modified after Neal and Lockwood 2003). Red stars indicate locations for the KT samples used in this study. Basal Reticulite (BR), units 7, 11, and 20 (SO7-39), Layer 6 (SO1-16), Circumferential Lava Flow (CLF; filled in grey), Eastern Pumice (EP; S11-219), and Golden Pumice (GP). **(c)** Simplified stratigraphic column for the Keanakākoʻi Tephra (modified after Swanson et al. 2012; note: since that paper was published, Eastern Pumice has been found to overlie Golden Pumice). White units are phreatomagmatic eruptions with dominantly lithic material whereas grey denotes deposits of primarily juvenile material. Dashed lines show juvenile-rich phreatomagmatic units selected for this study. (For all references to color in figure captions, the reader is referred to the web version of this article).

highly oblique sections, which can introduce significant error in diffusion timescale estimates (Shea et al. 2015a). Glassy samples from the Circumferential Lava Flow were made into standard polished thin sections.

3.4. Methods

3.4.1. Electron Probe Micro-Analysis (EPMA)

Major and minor element analyses of olivine were made at the University of Hawaiʻi (UH) and Nanyang Technological University (NTU) using JXA-8500F and JXA-8530F JEOL Hyperprobes, respectively. Crystals were catalogued by zoning type (e.g. normal, reverse, complex) using backscatter electron (BSE) images to define populations within each eruption. Cores (i.e. at the geometric center of the 2D olivine crystal section) from

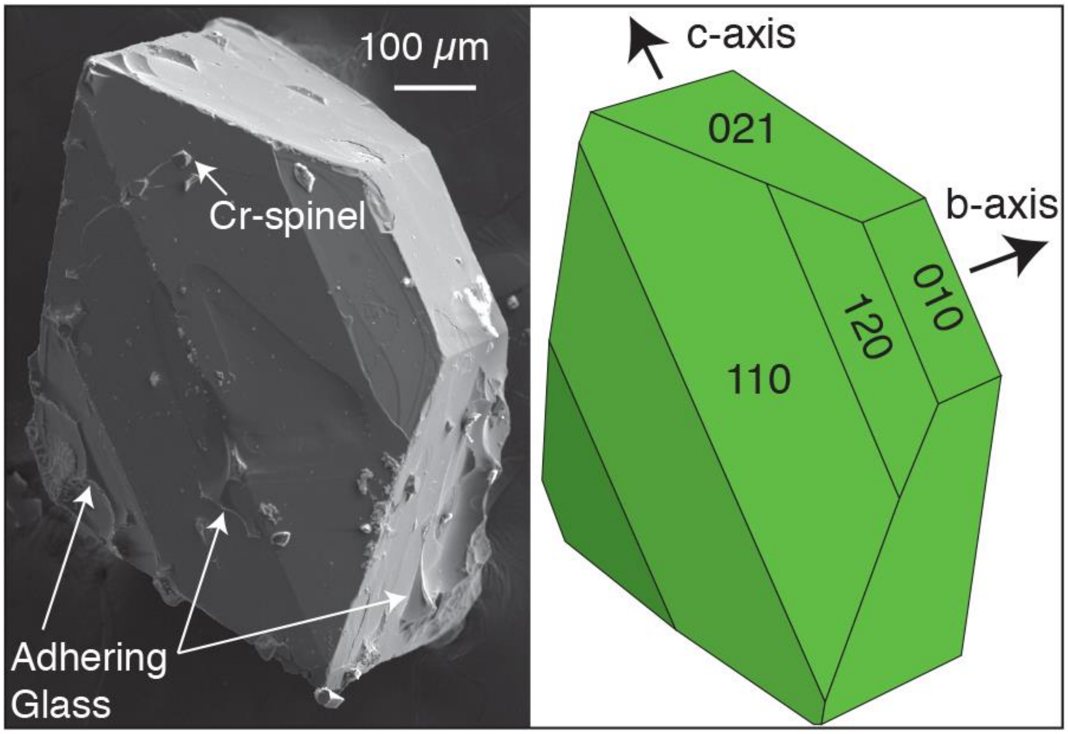

Figure 3.2. Secondary electron image of a typical euhedral olivine crystal observed in KT deposits (left). Adhering glass was removed from this crystal using a HF acid bath for imaging (see Appendix B). Schematic (right) shows crystal faces and orientation of crystallographic axes.

424 olivine crystals were analyzed at UH using a 20 kV accelerating voltage and 10 μm beam with a 200 nA current. The same conditions with a 1 μm beam were used to measure profiles with 3-10 μm spacing across 62 olivine crystals with concentration gradients previously identified in BSE images (10-11 per sample for units 7, 11, and 20, Layer 6, and Golden and Eastern Pumices). BSE images allowed selection of olivine crystals with symmetric concentration gradients and clear grayscale plateaus at the cores. Each traverse was oriented perpendicular to a well-formed crystal face avoiding corners to minimize the effects of merging diffusion fronts (Shea et al. 2015a). Traverses were selected only for crystal faces with adhering glass to ensure the precise measurement of a crystal rim composition within 5 μm of the olivine-glass boundary. Peak counting times were 60 s for Si, Fe, Mg, Ca, and Ni, and backgrounds for all analyses were measured on each side of the peaks for 30 s. Standards, measured routinely to monitor for instrumental drift, were San Carlos olivine (USNM 111312/444; Jarosewich et al. 1980) for Si, Fe and Mg, a synthetic nickel-oxide for Ni, and Kakanui Augite (USNM 122142; Jarosewich et al. 1980) for Ca. Two-sigma relative precision, based on repeated analyses of San Carlos

olivine, are 0.26 wt% for SiO_2, 0.32 wt% for MgO, 0.06 wt% for FeO, 0.002 wt% for NiO, and 0.001 wt% for CaO.

Additional core-rim zoning profiles were measured at NTU for olivine crystals from the Basal Reticulite (n=11) and the Circumferential Lava Flow (n=8), yielding a total of 81 profiles from unique crystals for this study. Analytical conditions were a 15 kV accelerating voltage and 40 nA current with a focused beam and 2-3 µm spacing. Peak counting times were 20 s for Si, Mg, and Fe, 60 s for Mn, and 90 s for Ni and Ca. The mean atomic number background intensity data were calibrated and continuum absorption corrected for Si ka, Mg ka, Fe ka, Mn ka, Ni ka, and Ca ka (Donovan and Tingle 1996). Astimex reference standards for analyses were olivine (#134) for Si, Fe, Mg, and Ni, rhodonite (#139) for Mn, and diopside (#121) for Ca. Two-sigma relative precision for analyses are within 0.68 wt% for SiO_2, 0.38 wt% for MgO, 0.15 wt% for FeO, and 0.008 wt% for NiO, MnO, and CaO. For all measurements, X-ray intensities were converted to concentrations using standard ZAF corrections (Armstrong 1988). Analyses with totals < 99.0 wt% and > 100.5 wt% and/or cation totals < 2.98 or > 3.02 were rejected.

3.4.2. Electron Backscatter Diffraction (EBSD)

The orientation of the crystallographic axes in olivine crystals are necessary to correct for diffusion anisotropy (e.g. Costa and Chakraborty 2004). Crystal orientations for all 81 olivine sections were determined using a HKL Nordlys EBSD detector on a JEOL JSM-5900LV scanning electron microscope at UH. Additional polishing with a 50-70 nm colloidal silica suspension for four hours on a vibratory polisher improved the quality of electron backscatter diffraction patterns (EBSPs). Measurements were taken using a 70° sample tilt, 25 kV accelerating voltage, and a minimized working distance (generally 12-15 mm). Grids of 10 x 10 points spaced at least 10 µm apart achieved mean angular deviation values of < 1°. The EBSPs were processed using the HKL Technology *Channel 5* software package, and axis locations were output into lower hemisphere stereographic projections (see Prior et al. 1999 for EBSD technique details). Crystallographic orientation was the same within individual grains over areas of 100-1000 μm^2, consistent with a juvenile magmatic origin for the phenocrysts (e.g. antecrysts are commonly deformed; Helz 1987; Clague and Denlinger 2004). The angles α, β, and γ between the measured electron probe traverse and the crystallographic *a*-, *b*-, and *c-axes*, respectively (Costa and Chakraborty 2004), were calculated using *Stereonet 9*© (Cardozo and Allmendinger 2013).

3.4.3. Diffusion Modeling

Geochemical profiles of Fe-Mg and Ni from EPMA traverses were modeled using the program DIPRA (Girona and Costa 2013), which numerically solves the one-dimensional concentration-dependent diffusion equation to obtain timescales. The program incorporates diffusion coefficients for Fe-Mg from Dohmen and Chakraborty (2007a, 2007b) and Ni from Petry et al. (2004). Anisotropy-corrected diffusivities were calculated by DIPRA for each traverse based on the angles between the analytical profile and the *a*-, *b*-, and *c-axes* measured by EBSD (α, β, and γ respectively; Costa and Chakraborty 2004). Initial boundary conditions were determined based on the compositions of clear core plateaus (C_i) and the melt composition calculated to be in equilibrium with the measured olivine rim or inferred rim in complex zoning patterns (C_o). DIPRA models provided best-fit results along with uncertainties that are based on estimated analytical, temperature, and oxygen fugacity precision (Girona and Costa 2013). The intrinsic properties required as inputs in DIPRA (e.g. T, P, f_{O2}) are well known for Kīlauea magmas. Temperature was calculated using the Kīlauea MgO thermometer (Helz and Thornber 1987) and the inferred melt MgO in equilibrium (Matzen et al. 2011) with the olivine rim boundary condition (C_o). This value is akin to a magma temperature for storage and diffusion. Oxygen fugacity conditions ~QFM were chosen based on the findings of Moussallam et al. (2016), Helz et al. (2017) and Davis et al. (2017). We used a pressure of 85 MPa, which approximates the depth of the modern South Caldera reservoir (~3.5 km; Cervelli and Miklius, 2003; Poland et al. 2014) and provides one possible crustal storage depth for magmas during the KT period.

3.5. Results

Olivine cores in KT samples have Fo contents with consistently primitive modes (≥ Fo_{88}, Figure 3.3, see also Table 3.2 and Appendix B). Early (1500-1650 C.E.) KT units also have heterogeneous olivine Fo contents (e.g. 80-90) with diverse population distributions (Figure 3.3). Olivine cores from 1650-1670 C.E. (Layer 6 and unit 20) show bimodal distributions of ≥ Fo_{88} and intermediate compositions (modal peaks at Fo_{82-85}; Figure 3.3). The two populations can also be discriminated by their morphologies. Olivine crystals with ≥ Fo_{88} are typically > 0.5 mm across, euhedral, and lack Cr-spinel and melt inclusions (Figure 3.4a). In contrast, Fo_{82-85} olivine crystals are smaller (e.g. 0.1-0.5 mm across) and generally have skeletal morphologies with abundant Cr-spinel and melt inclusions (Figure 3.4b). The Fo distribution corresponding to Layer 6 is strongly bimodal, with an isolated high Fo peak, and a broad intermediate mode (Figure 3.3). The primitive Fo mode in unit 20 is wider and the distribution has a smaller, secondary intermediate peak. Olivine core compositions late in the KT (Circumferential Lava Flow, Golden Pumice, Eastern Pumice; 1670-1823 C.E.) have broad distributions of primitive

Table 3.2. Representative olivine core and rim compositions for dominant modes in individual eruption populations (e.g. Figure 3.3). Two modes are reported for bimodal distributions. Full dataset can be found in Appendix B.

Oxide	**Basal Reticulite**		**unit 7**		**unit 11**		**Layer 6 (mode 1)**	
(wt%)	*Core*	*Rim*	*Core*	*Rim*	*Core*	*Rim*	*Core*	*Rim*
SiO_2	39.7	39.1	40.2	40.0	40.3	40.3	40.3	39.9
FeO	10.6	12.7	10.8	12.1	10.9	12.8	10.7	12.2
MgO	48.8	46.6	48.7	47.5	48.2	46.1	48.6	46.8
NiO	0.47	0.39	0.46	0.41	0.48	0.37	0.45	0.40
CaO	0.20	0.22	0.20	0.22	0.20	0.24	0.19	0.23
Total	99.8	99.0	100.4	100.2	100.1	99.8	100.2	99.5
Fo (%)*	89.1	86.8	89.0	87.5	88.7	86.5	89.0	87.2
Oxide	**Layer 6 (mode 2)**		**unit 20 (mode 1)**		**unit 20 (mode 2)**		**CLF (mode 1)**	
(wt%)	*Core*	*Rim*	*Core*	*Rim*	*Core*	*Rim*	*Core*	*Rim*
SiO_2	38.9	39.1	39.4	41.2	40.3	40.5	40.6	39.2
FeO	15.8	16.6	11.2	11.8	15.9	14.1	12.4	35.7
MgO	44.4	43.6	47.9	46.4	43.7	45.3	46.1	24.2
NiO	0.24	0.22	0.42	0.40	0.30	0.29	0.36	0.20
CaO	0.22	0.24	0.19	0.22	0.19	0.25	0.19	0.25
Total	99.6	99.8	99.1	100.0	100.4	100.4	99.7	99.5
Fo (%)	83.4	82.4	88.4	87.5	83.0	85.1	86.9	77.3
Oxide	**CLF (mode 2)**		**CLF (evolved)**		**Eastern Pumice**		**Golden Pumice**	
(wt%)	*Core*	*Rim*	*Core*	*Rim*	*Rim*	*Core*	*Core*	*Rim*
SiO_2	40.3	39.6	39.3	39.1	39.7	40.3	39.6	39.7
FeO	15.0	18.7	20.0	21.1	11.9	15.0	18.7	11.9
MgO	44.0	41.2	39.9	39.2	47.9	44.3	40.3	47.9
NiO	0.26	0.22	0.21	0.18	0.37	0.26	0.21	0.37
CaO	0.19	0.21	0.24	0.24	0.24	0.19	0.24	0.24
Total	99.8	99.9	99.7	99.8	100.1	100.1	99.1	100.1
Fo (%)	84.0	79.7	78.6	77.5	87.8	84.0	79.3	87.8

* Fo, forsterite = [Mg/(Mg+Fe) x 100]

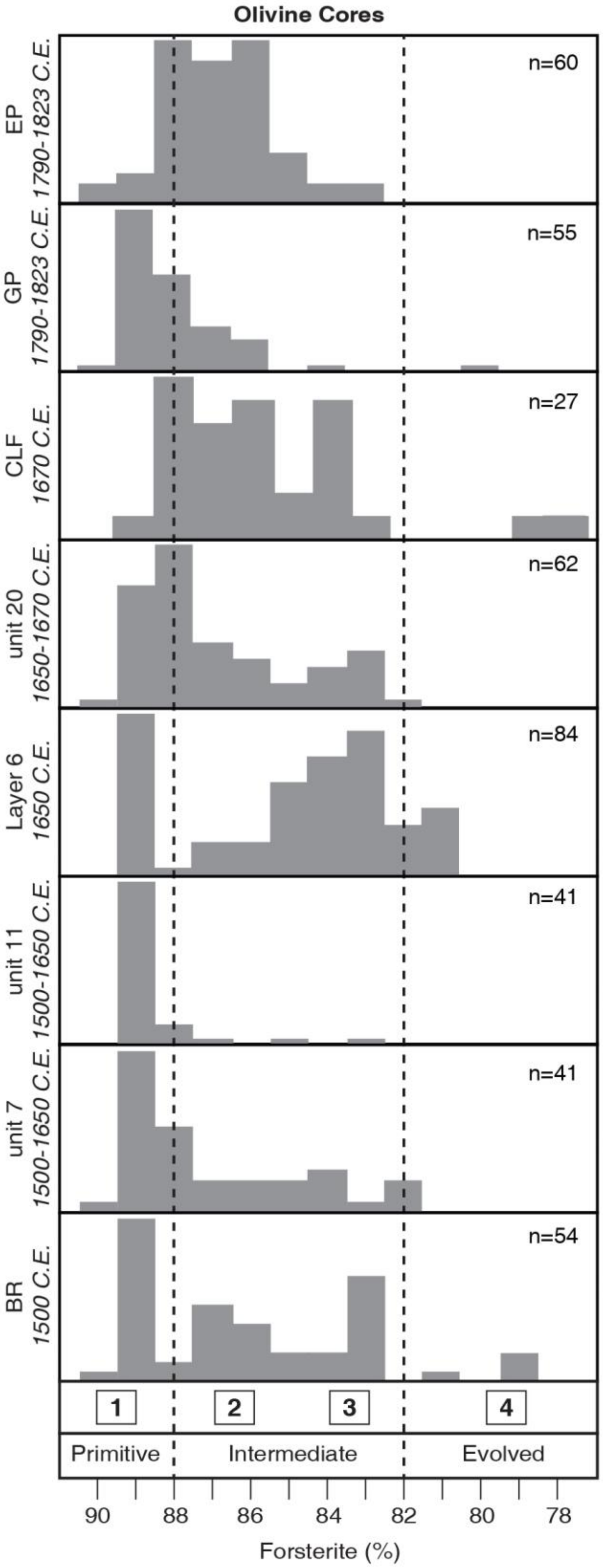

Figure 3.3. Core Fo contents for olivine populations measured within each eruption presented in stratigraphic order from bottom to top. Bins span a 1 mol% range of Fo. All histograms are normalized to 1 (no y-axis scale) to allow direct comparison. [#] denotes olivine populations within each eruption in order of decreasing Fo content.

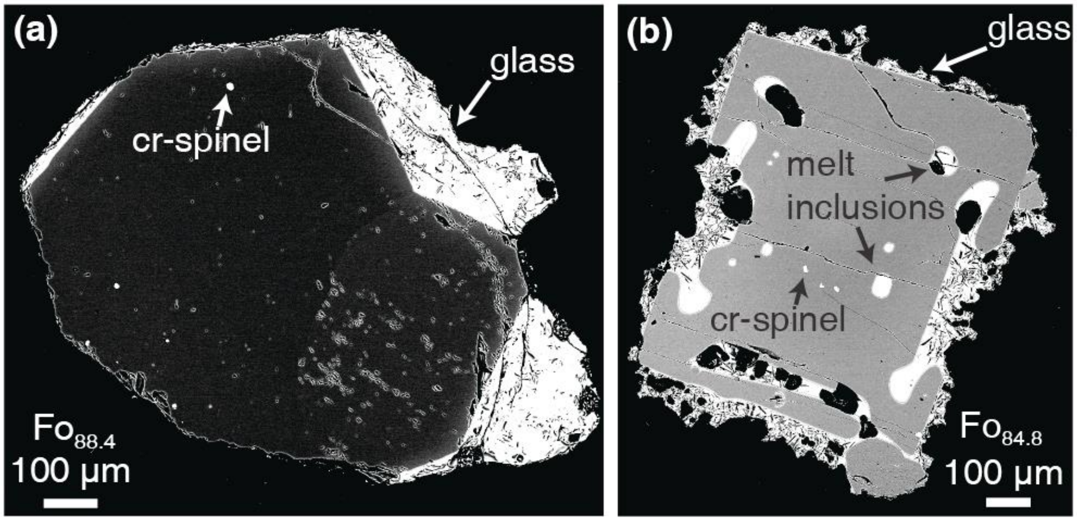

Figure 3.4. Backscatter electron images highlighting textural differences between olivine crystals from the **(a)** primitive (≥ Fo_{88}; grey marks on olivine are pits from polishing) and **(b)** lower-Fo (e.g. Fo_{82-85}) populations from the histograms shown in Figure 3.3. The primitive olivine crystals generally have well-formed faces and rare Cr-spinel or melt inclusions. The lower-Fo olivine crystals have skeletal morphologies with abundant Cr-spinel and melt inclusions.

to intermediate populations (Fo_{83-90}; Figure 3.3). The Circumferential Lava Flow is unusual in that it also has a population of evolved (< Fo_{82}) olivine core compositions.

Olivine rims within 5 µm of the crystal-melt boundary generally have Fo values that are too high to be in Fe-Mg equilibrium with their adhering glass Mg-number (Mg# = [Mg/(Mg+Fe^{2+}) x 100]; assuming 90% of the total iron is Fe^{2+} based on iron titration measurements of Kīlauea lavas; Moore and Ault 1965; Byers et al. 1985; see Appendix B for glass analyses; Figure 3.5). The units 7 and 20 have a bimodal population of olivine cores that are zoned toward unique intermediate rim compositions, providing clear evidence for re-equilibration within a hybrid melt composition after mixing. Fe-Mg disequilibrium between olivine rims and adhering glasses, despite systematic zoning in units 7 and 20, indicate that the olivine crystals may have experienced late-stage, rapid disequilibrium growth (Shea et al. 2015b) and/or limited diffusive re-equilibration with the melt that carried them to the surface. The heterogeneity of matrix glass Mg# in KT tephra deposits within individual eruptions was also observed by Mucek (2012) and Helz et al. (2014, 2015).

The core-to-rim transects for all 81 olivine crystals highlight the diversity of zoning patterns, which are here interpreted to result from diffusive re-equilibration (e.g. are smoothed). Forsterite profiles are subdivided into four types, in which NiO zoning mimics Fo zoning. Most olivine crystals have normal zoning ($Fo_{core} > Fo_{rim}$; Figure 3.6a) with primitive core plateaus ($\geq Fo_{88}$) that decrease 1-5 mol% Fo towards the rim. Reversely-zoned olivine crystals ($Fo_{core} < Fo_{rim}$; Figure 3.6b) have low-Fo cores (e.g. 82) and are relatively rare in KT deposits. These crystals typically have a 1-6 mol% change in Fo between the core and the rim. 'Complex' zoning patterns are classified as: (1) hook (Figure 3.6c), which are mostly normally zoned but have 5-20 µm reversely zoned rims, and (2) shoulder (Figure 3.6d), which are mostly reversely zoned with 5-20 µm of normal zoning at the rim. Hook profiles generally have steep normal zoning from primitive Fo_{88} to < Fo_{80} (Figure 3.6c), indicating the mixing of recharge magmas with a low-Mg melt.

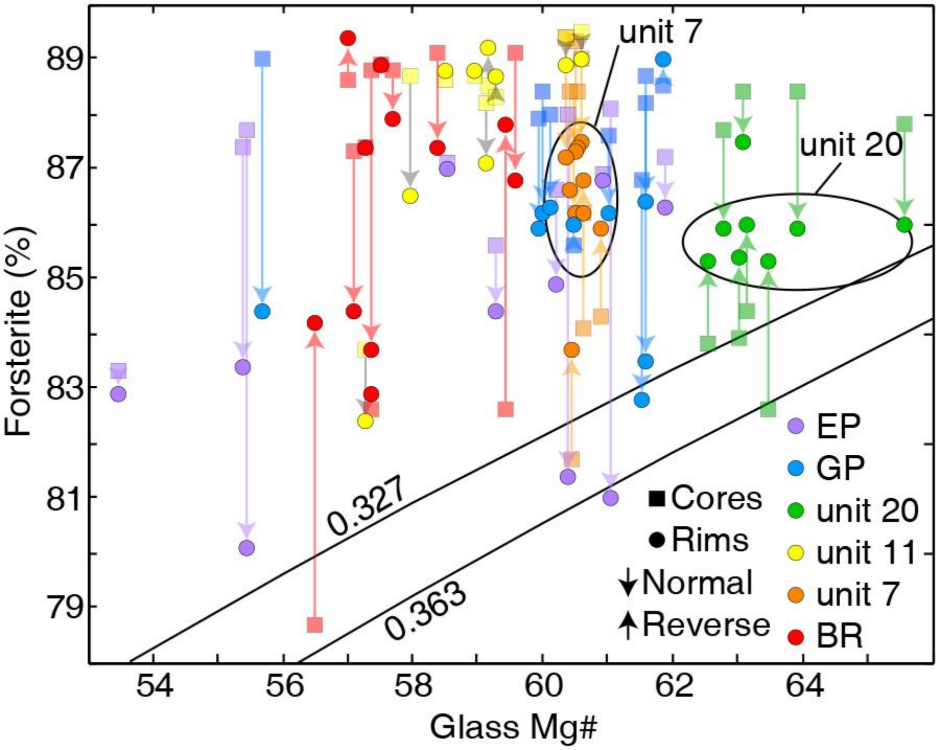

Figure 3.5. Glass Mg-numbers [Mg/(Mg+Fe2+) x 100] plotted against KT olivine core (squares) and rim (circles) forsterite contents (no data for Layer 6 or Circumferential Lava Flow due to microlite rich matrix). The Mg# is calculated assuming 90% of the total iron is Fe^{2+}, based on iron titration measurements of Kīlauea lavas (e.g. Moore and Ault 1965; Byers et al. 1985; Rhodes and Vollinger 2005). Arrows point in the direction of zoning toward the olivine rim (e.g. down denotes normal zoning, up denotes reverse zoning). The solid lines mark the shallow pressure (1 atm) equilibrium field for basaltic magma (Fe/Mg $K_d = 0.343 \pm 0.008$; Matzen et al. 2011). Most olivine cores and rims plot above the field and represent non-equilibrium compositions. Samples with bimodal core populations zoned toward similar rim compositions (circled data) suggest that the rims record a hybrid mixing component that is out of Fe-Mg equilibrium with the melts that carried the olivine crystals to the surface.

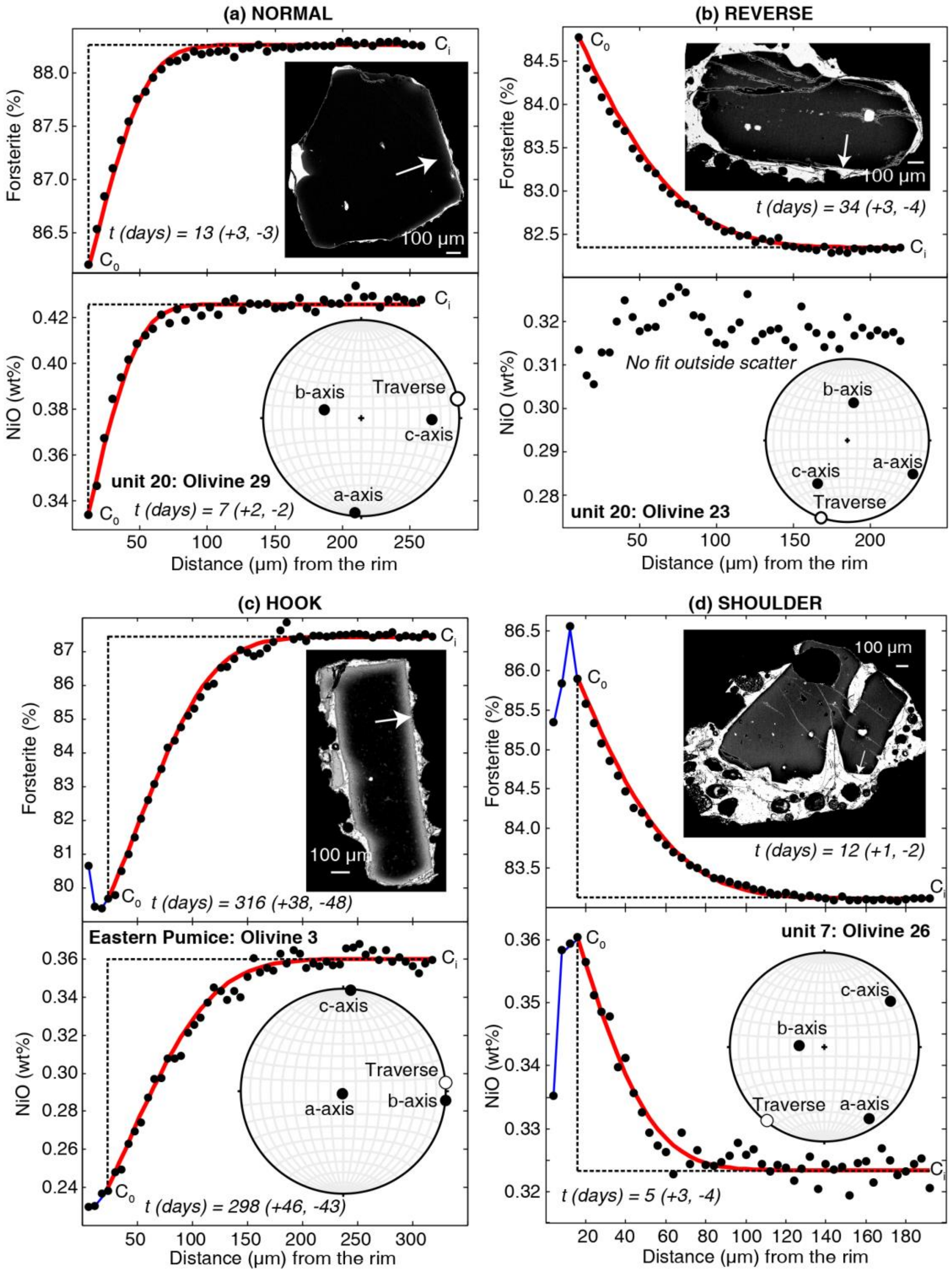

Figure 3.6. Rim (left; x = 0) to core (right) zoning profiles are divided into **(a)** normal, **(b)** reverse, **(c)** hook, or **(d)** shoulder types based on the change in concentration between the core and the rim. BSE images and lower hemisphere projections illustrate the location of the analytical traverse and orientation of the crystallographic axes. Red lines show best-fit results from diffusion models with calculated timescales (Table 3.3). Blue lines in hook and shoulder profiles highlight an additional mixing event followed by limited diffusive re-equilibration that cannot be easily fit by diffusion models.

Hook and shoulder profiles do not always preserve compositional reversals in NiO (e.g. Figure 3.6c).

Diffusion timescales - calculated for only the larger zoned regions in hook and shoulder profiles (Figure 3.6c and 3.6d) - obtained from modeling Fe-Mg and NiO profiles in KT olivine crystals vary from a few days to about two years (n=123; Table 3.3). They do not systematically correlate with zoning type, core Fo content, or stratigraphic order. Most (65%) calculated timescales record less than three months of storage and diffusive re-equilibration (Figure 3.7a). The shortest timescales record

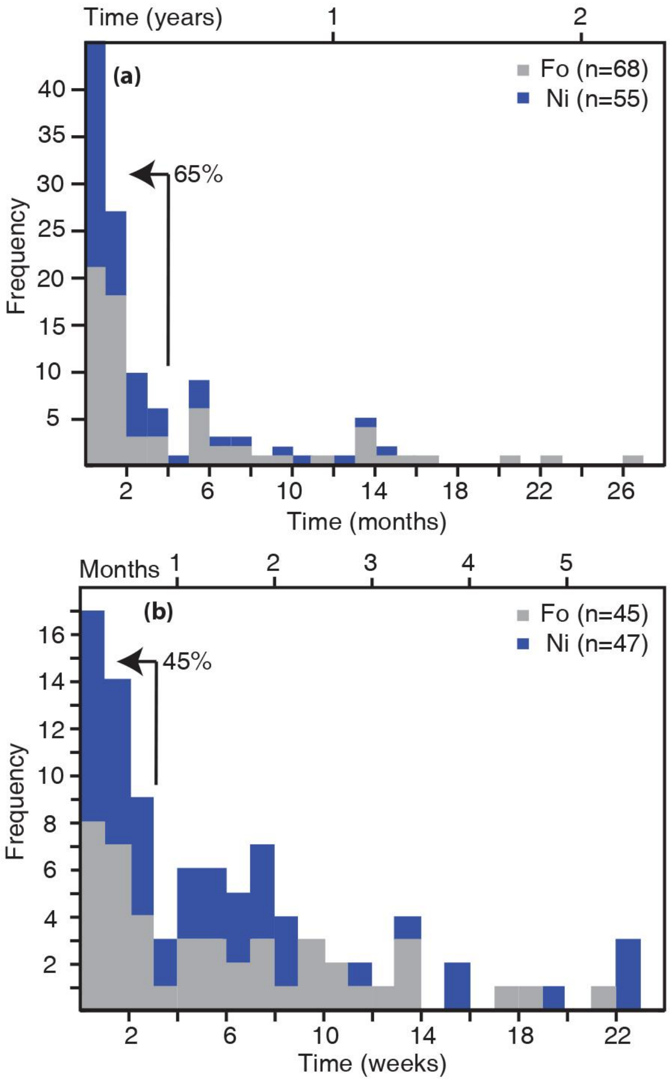

Figure 3.7. Histograms showing the range and frequency of timescales retrieved from modeling Fo (n=68) and NiO (n=55) profiles in KT olivine crystals. **(a)** Bins represent one month. **(b)** Bins represent one week for timescales from 0-6 months.

Table 3.3. Calculated time (days) obtained by modeling the diffusion of Fe-Mg and Ni in olivine crystals.

Sample	Ol.	T(°C)	α	β	γ	Elem.	C_i	C_o	t (days)	Δ (-)	Δ (+)
BR	5	1307	44	86	46	Fo	88.7	86.8	0.6	0.4	0.2
						Ni	0.443	0.400	0.5	0.2	0.3
	7	1245	32	59	88	Fo	82.0	82.3	3.1	3.4	206
						Ni	0.295	0.275	13	10	7
	9	1307	88	60	30	Fo	91.1	90.1	38	10	10
						Ni	0.450	0.423	9	1	1
	12	1307	89	31	57	Fo	86.9	88.2	73	9	8
						Ni	0.395	0.425	18	4	5
	15	1307	16	79	78	Fo	88.8	84	0.2	0.2	0.4
						Ni	0.440	0.290	0.2	0.3	0.1
	16	1245	86	64	26	Fo	86.9	84.8	46	11	6
						Ni	0.4	0.34	35	5	12
	17	1307	18	73	89	Fo	88.2	88.7	209	22	24
						Ni	0.425	0.444	6	4	1
	21	1245	82	17	72	Fo	88.5	88.0	467	56	86
						Ni	0.438	0.415	163	34	32
	28	1245	82	8	83	Fo	78.0	83.5	78	16	16
						Ni	0.270	0.300	31	7	4
U7	1	1281	17	80	77	Fo	89.0	87.0	10	4	3
						Ni	0.457	0.408	8	6	2
	8	1281	5	87	87	Fo	84.4	86.2	10	3	4
						Ni	0.297	0.341	2	1	1
	12	1281	19	72	89	Fo	88.3	87.1	41	18	15
						Ni	0.417	0.387	17	14	14
	14	1245	70	21	82	Fo	86.2	87.5	295	40	60
						Ni	0.350	0.375	58	46	24
	17	1245	65	26	83	Fo	86.2	84.7	634	93	96
						Ni	0.332	0.316	401	353	781
	20	1281	56	40	74	Fo	89.3	86.9	42	5	6
						Ni	0.463	0.377	7	3	2
	26	1281	85	74	16	Fo	83.1	85.8	12	1	2
						Ni	0.323	0.36	5	3	4
	28	1281	72	64	32	Fo	89.4	87.6	4	1	0.5
						Ni	0.460	0.406	2	2	1
	29	1281	77	16	81	Fo	88.3	87.0	190	60	58
						Ni	0.418	0.380	65	29	33
U11	4	1275	23	72	78	Fo	83.7	82.9	434	201	69
						Ni	0.297	0.263	60	11	32
	6	1291	21	68	84	Fo	88.7	89.4	149	60	99
						Ni	0.450	0.460	39	39	262
	7	1291	78	32	61	Fo	88.4	86.9	97	20	27
						Ni	0.389	0.344	145	9	8
	9	1291	33	59	75	Fo	89.7	88.2	30	7	5
						Ni	0.436	0.355	17	4	2
	14	1291	75	59	35	Fo	88.7	89.27	2	1.5	1
						Ni	-	-	-	-	-
	19	1291	47	41	85	Fo	89.5	89.2	37	31	43
						Ni	-	-	-	-	-
	25	1291	56	78	89	Fo	88.9	89.4	444	261	459
						Ni	-	-	-	-	-
	34	1291	43	84	47	Fo	88.6	89.3	197	82	286
						Ni	-	-	-	-	-
L6	4	1197	77	56	37	Fo	85.2	81.3	443	50	56
						Ni	0.332	0.210	361	45	57

Sample	**Ol.**	**T(°C)**	**α**	**β**	**γ**	**Elem.**	**C_i**	**C_o**	**t (days)**	**Δ (-)**	**Δ (+)**
	6	1197	85	21	68	Fo	84.6	84.5	831	129	153
						Ni	0.272	0.212	190	52	34
	8	1263	46	44	88	Fo	81.6	82.7	11	3	4
						Ni	-	-	-	-	-
	20	1263	86	90	4	Fo	89.1	87.9	93	17	18
						Ni	0.457	0.415	61	7	10
	24	1197	90	1	89	Fo	88.0	81.2	708	79	94
						Ni	0.433	0.210	421	58	58
	30	1263	9	84	81	Fo	88.7	84.5	3	3	2
						Ni	0.457	0.270	3	3	1
	34	1263	8	83	87	Fo	89.2	87.5	66	26	26
						Ni	0.473	0.425	37	9	14
U20	9	1275	34	58	77	Fo	83.7	84.6	56	18	15
						Ni	-	-	-	-	-
	17	1275	86	88	5	Fo	86.5	85.2	50	17	15
						Ni	0.391	0.323	26	5	5
	18	1275	29	69	70	Fo	86.5	87.6	16	4	4
						Ni	0.323	0.340	1	1	1
	23	1275	82	52	39	Fo	82.3	84.7	34	3	4
						Ni	-	-	-	-	-
	29	1275	75	61	31	Fo	88.3	86.2	13	3	3
						Ni	0.427	0.335	7	2	2
	34	1275	42	81	49	Fo	87.9	88.3	189	11	120
						Ni	0.390	0.420	230	44	32
	35	1275	34	60	75	Fo	83.8	84.6	75	13	20
						Ni	-	-	-	-	-
	36	1275	88	10	81	Fo	87.9	86.9	243	33	58
						Ni	-	-	-	-	-
CLF	14_18	1180	22	71	82	Fo	78.8	80.0	129	18	24
						Ni	0.195	0.230	63	20	12
	14_21	1139	77	15	86	Fo	77.7	79.2	490	72	70
						Ni	0.185	0.220	167	39	43
	14_22	1188	35	56	85	Fo	87.0	77.3	67	11	11
						Ni	0.370	0.200	49	7	9
	16_9	1189	29	85	61	Fo	83.3	84.8	17	8	8
						Ni	0.195	0.175	47	11	10
	16_11	1188	37	63	68	Fo	84.0	84.9	9	5	11
						Ni	-	-	-	-	-
	16_3	1139	73	14	87	Fo	85.6	81.5	6	5	1
						Ni	-	-	-	-	-
	16_7	1188	72	57	38	Fo	84.0	84.9	12	2	2
						Ni	-	-	-	-	-
GP	6	1275	31	90	59	Fo	88.5	89.1	226	115	93
						Ni	0.428	0.441	115	106	315
	12	1237	78	65	28	Fo	89.3	83.4	20	5	5
						Ni	0.450	0.252	12	2	2
	20	1275	41	71	87	Fo	88.9	86.5	193	39	44
						Ni	0.438	0.360	30	7	4
	22	1275	28	70	71	Fo	88.3	86.0	209	29	36
						Ni	0.432	0.320	114	21	15
	23	1275	43	75	50	Fo	86.8	88.1	14	6	16
						Ni	0.390	0.420	10	5	19
	27	1275	89	16	75	Fo	88.4	86.3	385	88	89
						Ni	0.43	0.31	60	8	18
	30	1275	79	64	26	Fo	88.3	86.0	257	40	46

Sample	**Ol.**	**T(°C)**	**α**	**β**	**γ**	**Elem.**	**C_i**	**C_o**	**t (days)**	**Δ (-)**	**Δ (+)**
						Ni	0.435	0.340	163	37	24
	31	1275	55	81	36	Fo	88.7	86.1	121	13	13
						Ni	0.413	0.350	24	7	11
	32	1237	26	78	66	Fo	88.2	79.7	427	48	57
						Ni	0.410	0.275	101	13	17
	34	1237	29	60	83	Fo	88.5	81.7	217	41	32
						Ni	0.425	0.325	54	9	13
	36	1275	28	66	80	Fo	85.1	86.2	67	26	44
						Ni	0.285	0.325	66	29	15
EP	3	1237	81	10	89	Fo	87.5	79.9	316	38	48
						Ni	0.360	0.245	298	46	43
	5	1275	85	84	7	Fo	87.1	87.7	26	9	6
						Ni	0.370	0.388	34	10	109
	6	1237	80	58	34	Fo	87.1	85.8	4	3	1
						Ni	0.360	0.335	2	2	2
	13	1237	84	63	27	Fo	86.5	87.2	524	116	229
						Ni	0.335	0.355	321	183	40
	15	1237	81	48	44	Fo	87.7	81.4	91	12	11
						Ni	0.365	0.255	0.89	0.19	0.17
	19	1237	61	34	73	Fo	87.8	81.5	31	8	7
						Ni	0.377	0.310	17	8	7
	23	1237	90	74	15	Fo	83.3	84.6	49	6	7
						Ni	-	-	-	-	-
	27	1237	83	77	14	Fo	87.3	82.8	85	10	10
						Ni	0.350	0.240	51	8	8
	30	1237	18	73	88	Fo	87.3	86.5	49	29	19
						Ni	0.355	0.330	14	15	23

Unit abbreviations are the same as in Figure 3.1. All olivine profiles were modeled using P = 85 MPa and f_{O2} = QFM. The angles between the analytical traverse and the *a*-, *b*-, and *c*-axes are reported as α, β, and γ, respectively (Costa and Chakraborty 2004). C_i is the initial crystal composition (e.g. core concentration plateau) and C_o the olivine rim boundary condition. Δ(-) and Δ(+) are the errors on the time calculated by DIPRA (Girona and Costa 2013) after the anisotropy correction. They account for temperature uncertainties (± 10°C) and model fit within analytical uncertainty (Fo = ± 0.1 mol%; Ni = ± 0.008 wt%). A dash represents zoning profiles for which no timescales could be calculated due to small changes in concentration.

mixing and subsequent storage on the order of 1-3 weeks (45%; Figure 3.7b). These timescales demonstrate that KT magmas were mixed and stored for significant durations at magmatic temperatures before eruption, contrary to previous interpretations of little to no storage during rapid ascent (e.g. Sides et al. 2014). Compositional reversals in hook and shoulder profiles (blue lines; Figure 3.6) have limited spatial resolution (defined by 3-6 points), a small change element concentration (~1% for Fo, < 0.03 wt% for NiO), and many are only recorded by Fo and not NiO. These zoning features were difficult to fit with sufficient precision using diffusion models, and timescales were not retrieved for this additional mixing event.

3.6. Discussion

The diversity and complexity of olivine populations and their zoning patterns are evaluated below to better understand the mixing and storage histories of magma that fed the KT eruptions. The compositions of olivine cores are used to infer the magmatic environment in which they grew (e.g. mafic recharge or relatively evolved storage melts), whereas olivine zoning patterns and rim compositions are used to characterize magmatic environment(s) in which they resided prior to eruption (e.g. Kahl et al. 2011, 2013). The olivine population, zoning pattern, and rim composition data are combined with timescale information to provide a new perspective on mixing histories, storage timescales, and magma ascent for the KT period. The interpretations are used to propose a new model for Kīlauea’s prehistoric magmatic plumbing system following the collapse of the summit caldera.

3.6.1. Depths of olivine crystallization and storage

The maximum depth at which zoned crystals might record magma storage was investigated by determining the P-T conditions at which the primitive ($\geq Fo_{88}$) KT olivine crystallized. Rhyolite-MELTS (Gualda et al. 2012; Ghiorso and Gualda 2015) was used to establish where olivine crystallization was stable in ascending KT magmas. A 15 wt% MgO glass with 0.4 wt% H_2O (Clague et al. 1995) was crystallized at different pressures using oxygen fugacities at the Quartz-Fayalite-Magnetite oxygen reaction buffer (between QFM-1 and QFM+1) to consider the possible range of f_{O2} proposed for Hawaiian volcanoes (Rhodes and Vollinger 2005; Moussallam et al. 2016; Helz et al. 2017; Davis et al. 2017). This starting composition was selected because it is in Fe-Mg equilibrium with Fo_{88-90} olivine over the range of f_{O2} considered, similar to the dominantly primitive modes found in KT deposits (~40% of all KT olivine are $\geq Fo_{88}$; Figure 3.3).

Liquidus olivine with Fo_{88-90} composition crystallizes at temperatures ~1380-1400°C and pressures 0.4-0.5 GPa over the range of f_{O2} considered (Figure 3.8). Olivine is not stable at greater pressures and orthopyroxene becomes the liquidus phase, consistent with previous experimental work on Hawaiian tholeiites (e.g. Eggins 1991; Wagner and Grove 1998). The corresponding crystallization depths are ~15-18 km, assuming a crustal density of 2.3 g/cm^3 for depths up to 1 km and 2.9 g/cm^3 for depths > 1 km (Kilburn 2015; Figure 3.8). If uncertainties in f_{O2} and depth constraints are taken into account, liquidus olivine crystallization occurs at a maximum depth near to or just below the Moho (~16 km; Hill and Zucca 1987; Figure 3.8). Thus, calculated timescales for KT olivine document magma mixing and storage within the crust, perhaps in the volcanic edifice (< 10 km; Cayol et al. 2000; Montgomery-Brown et al. 2015; Figure 3.8). Diffusion timescales for the KT period are probably not related to a deeper

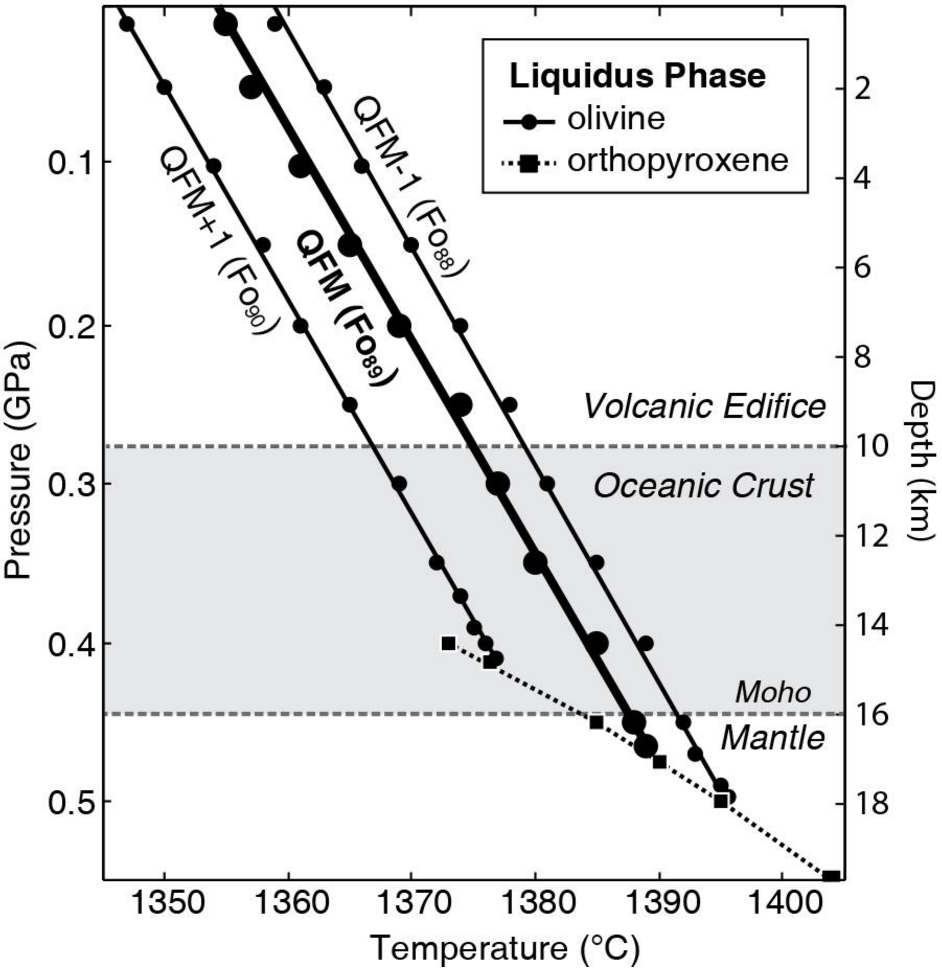

Figure 3.8. MELTS derived phase diagram identifying liquidus phases for crystallization of a 15 wt% MgO glass composition with 0.4 wt% H2O (Clague et al. 1995) at QFM (Moussallam et al. 2016; Helz et al. 2017; Davis et al. 2017), QFM-1 (Rhodes and Vollinger 2005), and QFM+1 (Davis et al. 2017). Nodes represent pressures where MELTS models were run to determine the liquidus phase. Depth-pressure equivalents were calculated assuming a density of 2.3 g/cm^3 for the first 1 km, and 2.9 g/cm^3 for depths >1 km. The resulting geostatic gradient is ~28 MPa/km for Kīlauea's crustal edifice. The boundary between Kīlauea and the oceanic crust is from Cayol et al. (2000) and Montgomery-Brown et al. (2015), whereas the base of the oceanic crust is from Hill and Zucca (1987).

magmatic history (e.g. ascent through the mantle), as has been suggested for other Kīlauea eruptions (Rae et al. 2016).

3.6.2. The Prehistoric Crustal Reservoir System

3.6.2.1. Melt Components. The presence of reverse and complex compositional zoning patterns in KT olivine indicate that they were unlikely to be produced only by crystal growth (e.g. Costa et al. 2008). Thus, KT olivine crystals preserve both the timing of magma mixing in crustal reservoirs and compositional information about the mixing end members. Four different melt components can be identified from KT olivine based on compositions and zoning patterns:

1) Normal and shoulder type zoning occur in high-Fo (e.g. ≥ Fo_{88}) olivine crystals (Figure 3.3, 3.6a and 3.6c) that grew and were mixed in mantle-derived recharge melt components.
2) Olivine cores and rims with intermediate Fo (Fo_{85-88}; Figure 3.6b, 3.6d) grew in or are the result of diffusive re-equilibration within a hybrid melt component that was produced by mixing of recharge and stored magmas.
3) Reversely-zoned crystals with lower Fo cores (Fo_{80-84}; Figure 3.6b) formed within shallower crustal storage reservoirs containing relatively evolved melts produced by fractional crystallization.
4) Strong normal zoning (Fo_{87-88} to < $Fo_{80;}$ Figure 3.6c) in hook profiles was produced by mixing and diffusive re-equilibration with a stored low-Mg# melt component. Evolved olivine cores are also present in early eruption olivine populations (Figure 3.3).

3.6.2.2. Early Eruptions (1500-1670 C.E.). The types of olivine zoning patterns found within products of individual eruptions can be used to characterize the mixing and storage histories with many melt components. Olivine populations in early KT eruptions (1500-1650 C.E.) have a wide distribution of core compositions (e.g. Fo_{78-90}) dominated by primitive Fo (e.g. Fo_{87-89}; Figure 3.3, 3.9a). Normal and shoulder type zoning profiles with ≥ Fo_{88} core plateaus are most common, suggesting that most of the olivine from these units (30-90%; Figure 3.3) crystallized from mantle-derived recharge magmas (melt component [1]; Figure 3.10a).

Some shoulder profiles have reverse zoning to > Fo_{88}, and one remarkable crystal is reversely zoned up to $Fo_{90.5}$ (Figure 3.9a). These zoning patterns are interpreted to form from mixing between mantle-derived recharge magmas in a lower crustal reservoir, perhaps at the transition between the volcanic edifice and oceanic crust (8-10 km; Cayol et al. 2000, Montgomery-Brown et al. 2015). Deep crustal storage regions have previously been inferred in Kīlauea's modern plumbing system to explain a lack of earthquake hypocentral locations (Ryan 1988; Denlinger 1997) and a zone of anomalously low velocity material (Lin et al. 2014). The compositions and zoning patterns found in KT olivine crystals may provide the first geochemical evidence of such a deep crustal mixing reservoir for ascending recharge magmas.

Many eruptions early in the KT period also incorporated more evolved olivine crystals (Figure 3.3, 3.9a), which generally have reverse- or hook-style profiles of intermediate and low-Fo composition (e.g. Fo_{82-88}). The zoning patterns are diverse with variable profile lengths (10-150 µm) and generally show limited variation in Fo (e.g. 1-4 mol%; Figure 3.5). This diversity, in addition to heterogeneous glass MgO contents in many KT units (e.g. 7.0-11.0 wt%; Helz et al. 2015) suggests that ascending magmas may have sampled many pockets of stored magmas at different depths (melt components [2], [3], and [4]; Figure 3.10a). The vent locations for KT eruptions are inferred to be widespread across Kīlauea's summit region (e.g. Swanson et al. 2006; Swanson et al. 2012b; May et al. 2015) and ascending magmas could have sampled magma pockets distributed beneath the summit caldera, perhaps as a system of stacked sills (which are structurally favorable after caldera collapse; Corbi et al. 2015). This interpretation is consistent with the range of olivine compositions, zoning patterns, and glass MgO contents found in early KT eruptions (Figure 3.9a).

Normally- and reversely-zoned olivine crystals from units 7 and 20 (Figure 3.9b) define a 'post-mixing' magma storage region where the populations were partially re-equilibrated together (Figure 3.10a). Recharge olivine with ≥ Fo_{88} cores from melt component [1] mixed with stored reservoir magma (melt component [3]), generating normally zoned crystals with ≥ Fo_{88} plateaus and reversely zoned crystals with Fo_{82-85}

plateaus. The populations (reservoir and recharge) were likely stored together because their zoning patterns span similar distances (~200 μm) toward a broadly similar intermediate rim composition (Fo_{85-87}; Figure 3.9b). Complex patterns indicate that the stored reservoir component may have contained many generations of olivine crystals that record more than one mixing event. Olivine rims with Fo_{85-87} reflect the composition of

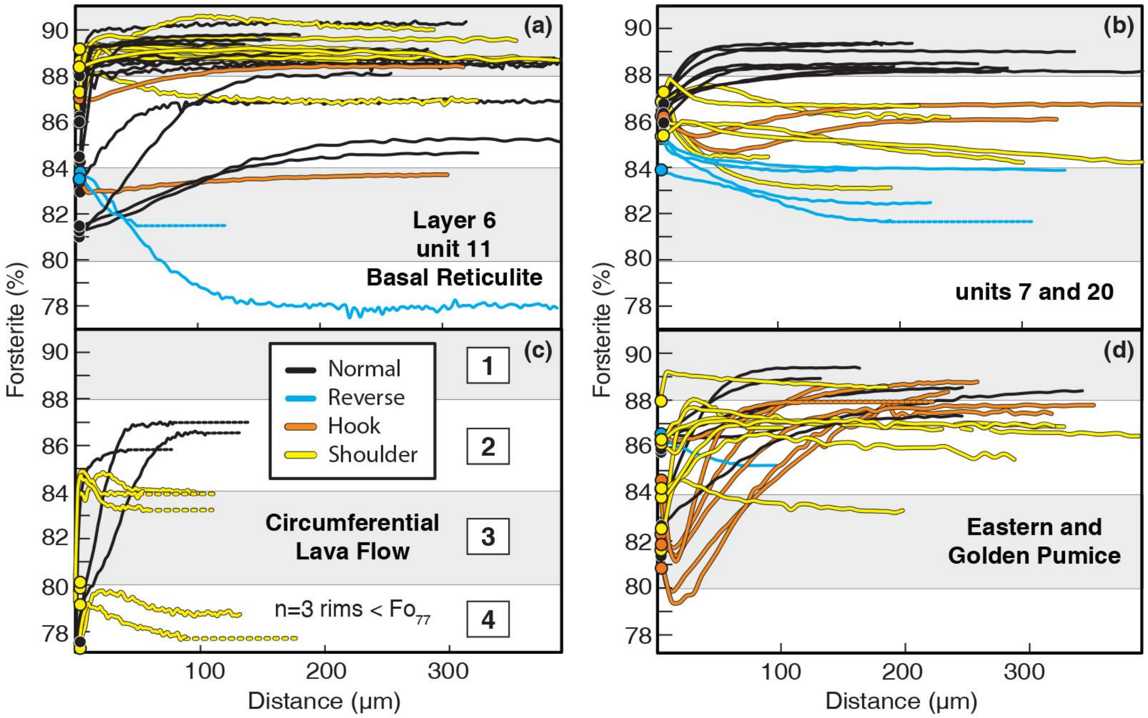

Figure 3.9. Olivine forsterite profiles grouped to highlight similar zoning behavior found in multiple samples. Scales are the same in all panels for comparison. Grey horizontal regions in each panel help highlight olivine populations as identified in Figure 3.3. **(a)** Most olivine in the first half of the KT (Basal Reticulite, unit 11, Layer 6) are normally-zoned with ≥ Fo_{88} cores that grew from mantle-derived recharge magmas (melt component [1]). The heterogeneity in core and rim Fo suggests sampling of multiple pockets of more evolved magmas (melt components [2] and [3]). **(b)** Examples of eruptions with systematic zoning profiles indicative of storage in a reservoir. Almost all profiles are zoned toward a relatively narrow range of rim compositions ($Fo_{85-87.5}$) that probably reflect the hybrid composition (melt component [2]) produced by mixing of recharge and reservoir components (melt components [1] and [3]). **(c)** The Circumferential Lava Flow is unique in that it has three core Fo populations, all with evolved rims (≤ Fo_{80}) that record the influence of a low-Mg# magma (melt component [4]). Dashed lines in the Circumferential Lava Flow panel represent inferred core plateaus based on the similarity between the measured core composition and the end of the geochemical profile. **(d)** The youngest KT samples (Eastern and Golden Pumice) have mostly complexly zoned olivine profiles. They record mixing of recharge and reservoir components with a low-Mg# melt (component [4]), which induced dramatic normal zoning patterns from Fo_{87-88} cores to as low as Fo_{79-80} in the hooks. A final mixing event with a higher-MgO magma produced normal and reverse zoning in shoulder and hook profiles, respectively.

the hybrid magma created by mixing (e.g. Kahl et al. 2011, 2013; melt component [2]; Figure 3.10a). These eruptions show that at least one shallow storage region in Kīlauea's prehistoric plumbing system may have been repeatedly sampled by ascending KT magmas (Figure 3.10a).

3.6.2.3. Late Eruptions (1670-1823 C.E.). Olivine from later KT eruptions (Circumferential Lava Flow, Golden and Eastern Pumices; ~1670-1823 C.E.) also record mixing with a distinct low-Mg# melt component that was not sampled before this period (Figure 3.10b). The Circumferential Lava Flow (1670-1700 C.E.; Figure 3.9c) preserves three populations of olivine (melt components [2], [3], and [4]) that have either normal or shoulder zoning profiles, with $< Fo_{88}$ cores (Figure 3.3) zoned toward $< Fo_{80}$ rims (Figure 3.9c). Mixing with a higher MgO magma generated the initial reverse zoning in shoulder profiles (Figure 3.9c). A second mixing event with the low-Mg# melt induced normal zoning (1-8 mol% change in Fo) in the outer 5-20 µm of the rim. Olivine rims with $< Fo_{80}$ in the Circumferential Lava Flow (Figure 3.9c) preserve a low-Mg# melt signature not observed in eruptions prior to 1670-1700 C.E. This low Mg# component is also recorded in Golden and Eastern Pumices, which have hook type profiles that decrease to $< Fo_{82,}$ with many recording $< Fo_{80}$ (Figure 3.9d). Hook profiles suggest that high-Fo olivine crystals from the recharge component ([1]) were initially mixed with the low Mg# melt (component [4]), developing 200-300 µm wide normal zoning with 1-10% change in Fo between the core and rim (Figure 3.9d). A second mixing event with a more mafic melt (perhaps another intrusion of component [1] or stored reservoir melt components [2] and [3]) induced reverse zoning (1-3% Fo) in the thin 5-20 µm wide rims.

The presence of a low-Mg# melt component late in the reservoir system is also supported by the evolved nature of juvenile material from the 1790 C.E. phreatomagmatic eruption, in which glasses can have as low as 3.4 wt% MgO (Mucek 2012; Swanson et al. 2014). Incorporation of this low-Mg# melt component in erupted magmas from 1670 to 1823 C.E. can explain the large width of zoned regions in olivine (due to contrasts in melt Mg#) and the $< Fo_{80}$ compositions of rims (Circumferential Lava Flow) and hooks (Golden and Eastern Pumices). The low Mg# melt suggests that some recharge magmas may have intruded but did not erupt early in the KT period (Figure

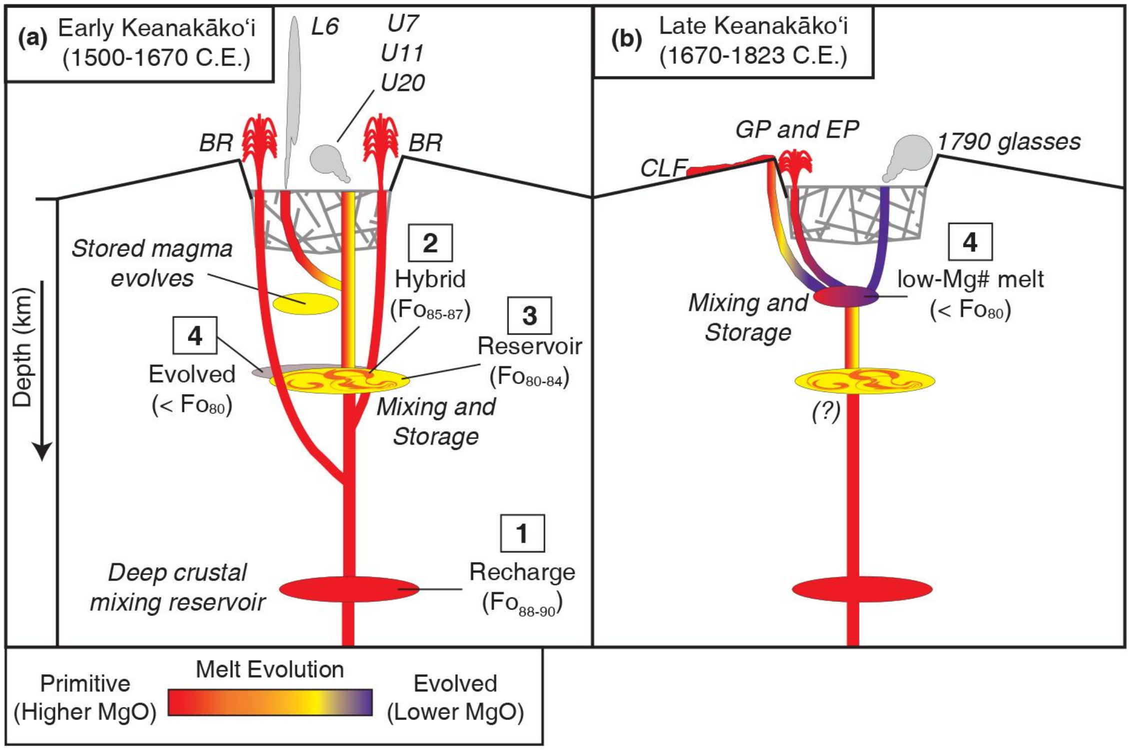

Figure 3.10. Simplified cross sections of Kīlauea's summit region depicting the inferred prehistoric plumbing system with crustal mixing and storage regions (not to scale). The stippled region represents caldera collapse breccia infill. Melt component numbers are the same as in Figures 3 and 9. The KT is divided into two stages: **(a)** Early eruptions (1500-1670 C.E.) are dominated by mantle-derived recharge magmas (component [1]). Some eruptions are inferred to intersect multiple pockets of magma, producing bimodal and/or heterogeneous olivine populations (components [2], [3], and [4]). Vent locations for the KT period are distributed throughout Kīlauea's summit region (Swanson et al. 2006, 2012b; May et al. 2015), consistent with the interpretation that ascending magmas intersected different pockets of melt. **(b)** Late in the KT (1670-1823 C.E.), magmas intersected a low Mg# stored melt (component [4]) that strongly influenced the glass (e.g. 1790 eruption; Mucek et al. 2012; Swanson et al. 2014) and olivine compositions. Olivine with hook type zoning were first stored with the low-Mg# melt component, generating strong normal zoning from Fo_{87-88} to < Fo_{80}. A second influx of higher MgO melt generated the thin reversely zoned rims.

3.10a). Subsequent storage, cooling, and fractional crystallization of the magma resulted in its relatively evolved composition. Alternatively, the low-Mg# component could be a pocket of magma left over from caldera collapse that would have remained isolated and evolved for ~200 years.

3.6.2.4. Late-stage mixing? Hook and shoulder olivine zoning patterns indicate that some KT magmas were mixed at least twice before eruption. The timing of the later mixing event is difficult to quantify with diffusion models due to the limited spatial resolution (3-

6 points using 3-5 µm spacing) and small changes in concentration (~1% for Fo, < 0.03 wt% for NiO; Figure 3.6c and 3.6d). Furthermore, hook and shoulder profiles are typically seen in Fo transects, but not NiO (Figure 3.6c). Olivine rims in the hook and shoulder profiles are also out of Fe-Mg equilibrium with their surrounding glass (Figure 3.5). This disequilibrium is especially surprising for samples with bimodal olivine populations that are zoned toward the same rim compositions (e.g. units 7 and 20; Figure 3.5, 3.9b), and it suggests that the hybrid melt component from storage may be unrelated to the melts which carried the olivine to the surface.

The thin rims of hook and shoulder profiles may have grown rapidly under disequilibrium conditions (e.g. Shea et al. 2015b) and/or experienced limited diffusive re-equilibration with their surrounding melt. Therefore, the second mixing event recorded by these rims probably occurred shortly before eruption. Using numerical diffusion models to simulate the formation of the observed thin rims, we can provide a maximum constraint on how long olivine crystals may have resided within the melt that carried them to the surface. The calculated Fo content of olivine in Fe-Mg equilibrium with the adhering glass compositions (i.e. the region within the equilibrium field; Figure 3.5) can be treated as a boundary condition to determine how long it would take for diffusion to create the outer 5-20 µm observed in the thin rims of hook and shoulder profiles. These numerical models solve the one-dimensional diffusion equation (see Chakraborty et al. 2010 and references therein) and use P, T, and f_{O2} conditions appropriate for each eruption (Table 3.3). Model results predict that the 5-20 µm wide olivine rims could have formed by diffusion in a few hours to a few days after mixing (Figure 3.11). Thus, olivine crystals must have resided within the melts that carried them to the surface for at most a few days before eruption. This brief storage time implies ascent shortly after mixing, but the duration is difficult to constrain using the measured profiles and remains unknown.

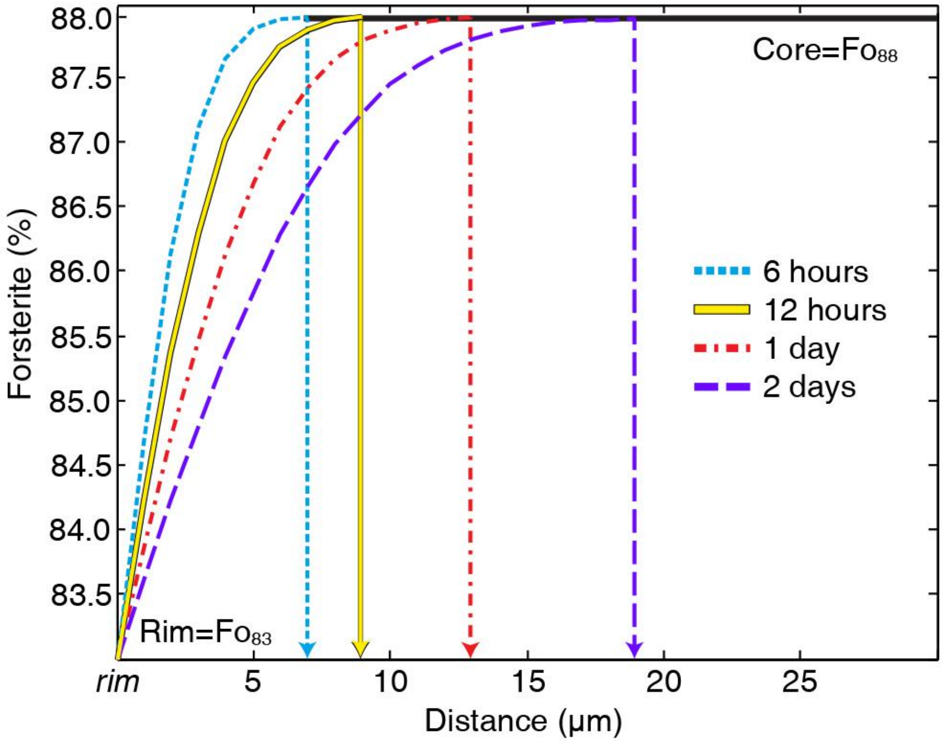

Figure 3.11. Numerical model simulating diffusion over timescales of 6 hours to 2 days. Initial core (Fo$_{88}$) and rim (Fo$_{83}$) boundary conditions and intrinsic properties (1200°C, 85 MPa, f_{O2} at the QFM buffer) were the same for all models. Colored arrows mark the distance at which diffusion has progressed into the core of the olivine crystal. With typical spacing of 3-8 μm for analytical profiles in natural olivine crystals, diffusion profiles 0-20 μm in length are poorly resolved (only 2-6 points) and cannot be accurately modeled for timescales.

3.7. Conclusions

Mixing and diffusive re-equilibration were key processes controlling Keanakāko‘i Tephra olivine compositions and zoning patterns. Olivine crystals preserve a history of mixing and subsequent storage for weeks to years before eruption, indicating that ascending KT magmas could not have bypassed storage in crustal reservoirs, as was previously suggested. Glass and olivine compositions provide a framework for characterizing the evolution of magma mixing and storage in Kīlauea’s prehistoric crustal reservoir system:

1) MELTS modeling suggests that liquidus olivine is only stable at < 0.45 GPa under QFM conditions, near to the base of the oceanic crust (~16 km). This is consistent with experimental studies, and suggests that mixing and storage probably occurred within the crust. Thus, timescales from KT olivine do not record deeper processes such as ascent from the mantle as was previously suggested for other Kīlauea eruptions.

2) The dominantly normally zoned high-Fo (≥ 88) olivine populations that occur throughout the ~300 years of the KT represent persistent recharge of mantle-derived magmas into the shallow reservoir system (melt component [1]). Shoulder type profiles with reverse zoning to Fo_{88} or above may provide the first geochemical evidence for mixing and storage within a deep crustal reservoir at Kīlauea.
3) Early in the KT (1500-1670 C.E.), eruptions were dominated by recharge magmas that sampled a spatially and compositionally heterogeneous crustal reservoir system (melt components [2], [3] and [4]). Bimodal olivine populations with normal and reverse zoning toward intermediate rim compositions illustrate the establishment of at least one storage region with a hybrid-mixing composition (melt component [3]) that was repeatedly sampled throughout the KT period.
4) A low-Mg# melt (component [4]) incorporated late in the KT (1670-1823 C.E.) contributed evolved olivine cores and rims in the Circumferential Lava Flow and generated the dramatic normal zoning profiles to $< \mathrm{Fo}_{80}$ in the Golden and Eastern Pumices. This interpretation is consistent with low-MgO glasses measured in juvenile material from the 1790 phreatomagmatic eruption.
5) Timescales ranging from a few weeks to several years from Fe-Mg and Ni zoning in olivine demonstrate that recharge magmas were mixed and stored with relatively evolved reservoir melts. This contrasts with previous interpretations of rapid ascent and little or no storage (e.g. Sides et al. 2014).
6) Late-stage mixing suggested by hook and shoulder zoning in olivine crystals throughout the KT may have occurred a few hours to several days before eruption.

3.8. Acknowledgements

The authors thank Jason Herrin (NTU) and Eric Hellebrand (UH) for support during electron microprobe analyses, Caroline Caplan and Julia Hammer for guidance in electron backscatter diffraction, and Eileen Chen, Scott Milleson, and Valerie Finlayson for assistance with sample preparation. This work was supported by the National Science Foundation (NSF) East Asia and Pacific Summer Institutes grant OISE1513668 in collaboration with the Research Foundation of Singapore, and the Harold T. Stearns Fellowship and the Fred M. Bullard Graduate Fellowship from UH to KL. Additional support was provided by NSF grants EAR1347915 and EAR1449744 to MG, EAR1321890 to TS, and a Singapore Ministry of Education grant (MoE2014-T2-2-041) to FC.

CHAPTER 4

LITHIUM ZONING IN OLIVINE: DECIPHERING GROWTH VS. DIFFUSION SIGNATURES AT KĪLAUEA VOLCANO, HAWAIʻI

In preparation for publication as:

Lynn, K.J., Shea, T., Garcia, M.O., and Costa, F. Lithium zoning in olivine: Deciphering growth vs. diffusion signatures to document late-stage mixing at Kīlauea Volcano, Hawaiʻi. To be submitted to *Contributions to Mineralogy and Petrology*.

4.1. Abstract

Late-stage, short duration (e.g. hours to days) magmatic processes in basaltic systems are challenging to quantify using major and minor element zoning in olivine. Lithium, a monovalent cation that diffuses about an order of magnitude faster than Fe-Mg, provides a promising means to access these short timescales. Precisely oriented and sectioned euhedral olivine crystals from Kīlauea Volcano provide a unique opportunity to investigate Li zoning in olivine. Here we present laser ablation ICPMS analytical transects of Li, Na, Al, P, and Cr to better understand how Li zoning records crystal growth versus diffusion and determine its capacity as a geospeedometer. Lithium concentration gradients have two key styles. First, most crystals have smoothed diffusion profiles 10-300 µm in length that are normally or reversely zoned and are inversely correlated with Fe-Mg zoning. Normal and reverse zoning indicates that diffusion profiles were not generated by degassing of Li from the melt and instead were generated by magma mixing and diffusive re-equilibration. Analytical transects along two crystallographic axes show no evidence for Li diffusion anisotropy. Second, Li occasionally forms enrichment peaks 10-30 µm wide that always correlate with P and are interpreted to record crystal growth. The relationship between Li and Na, Al, and Cr is highly variable, indicating that Li behavior during growth may only be dependent on P. We suggest that Li enrichment features result from charge balancing P during rapid growth. Lithium and P are coupled during subsequent diffusion and enrichment features are preserved due to the slow diffusivity of P. Modeling of Li diffusion profiles results in timescales that are generally less than four days but can range up to three weeks within individual eruptions. The short durations are interpreted to represent the timing of a late-stage intrusion of recharge magma, which may have contributed to the remobilization of stored reservoir magmas. Thus, Li diffusion records the last major event occurring in a reservoir prior to eruption.

Keywords: lithium zoning, olivine, diffusion, Kīlauea, Hawaiʻi

4.2. Introduction

Quantifying the rates of rapidly occurring, late-stage processes before volcanic eruptions is crucial for understanding the final stages of magma ascent and fragmentation (e.g. Charlier et al. 2012; Lloyd et al. 2014). In basaltic systems, olivine crystals typically record a complex history of crystallization over a range of pressures and temperatures (e.g. Wright 1971; Yang et al. 1999; Thompson and Maclennan 2013; Bouvet de Maisonneuve et al. 2016), magma mixing and diffusive re-equilibration (e.g. Costa and Dungan 2005; Shea et al. 2015b; Hartley et al. 2016; Lynn et al. 2017), and/or crustal contamination (Garcia et al. 1998; 2008). Timescales of weeks to decades associated with mixing and storage are routinely determined by modeling diffusion-controlled concentration gradients of major and minor elements in olivine (e.g. Costa and Dungan 2005; Kahl et al. 2011, 2013). Recent advances in analytical techniques have accessed late-stage syneruptive processes (e.g. decompression and ascent) by modeling the diffusion of volatiles from mineral-hosted melt embayments, but these features are rare and datasets are extremely limited (Humphreys et al. 2008; Lloyd et al. 2014; Ferguson et al. 2016). Thus, characterizing the final hours to days prior to eruption in basaltic systems remains a major challenge for modern petrology.

Rapidly diffusing elements in minerals can capture short timescale information associated with late-stage magmatic processes. Lithium diffuses up to an order of magnitude faster (Dohmen et al. 2010; Spandler and O’Neill 2010) than traditionally used major and minor elements in olivine (e.g. Fe-Mg, Mn, Ni, Ca; Petry et al. 2004;

Coogan et al. 2005; Dohmen and Chakraborty 2007a; Holzapfel et al. 2007; Figure 4.1). Modeling Li concentration gradients 5-300 μm in length can access timescales associated with magma mixing and storage that range from a few hours to a few months (Figure 4.1). However, three key complexities affect Li in basaltic systems: (1) it is weakly volatile in basaltic melts and can partition into a vapor phase (Edmonds 2015), (2) it may form charge-coupling relationships with other elements during crystal growth (e.g. Woodland et al. 2004; Milman-Barris et al. 2008; Grant and Wood 2010; Spandler and O'Neill 2010; Tomascak et al. 2016), and (3) growth coupling may influence Li behavior during subsequent diffusive re-equilibration (Spandler and O'Neill 2010).

Lithium is moderately incompatible in olivine (Brenan et al. 1998; McDade et al. 2003; Grant and Wood 2010; Spandler and O'Neill 2010) and behaves similarly to the

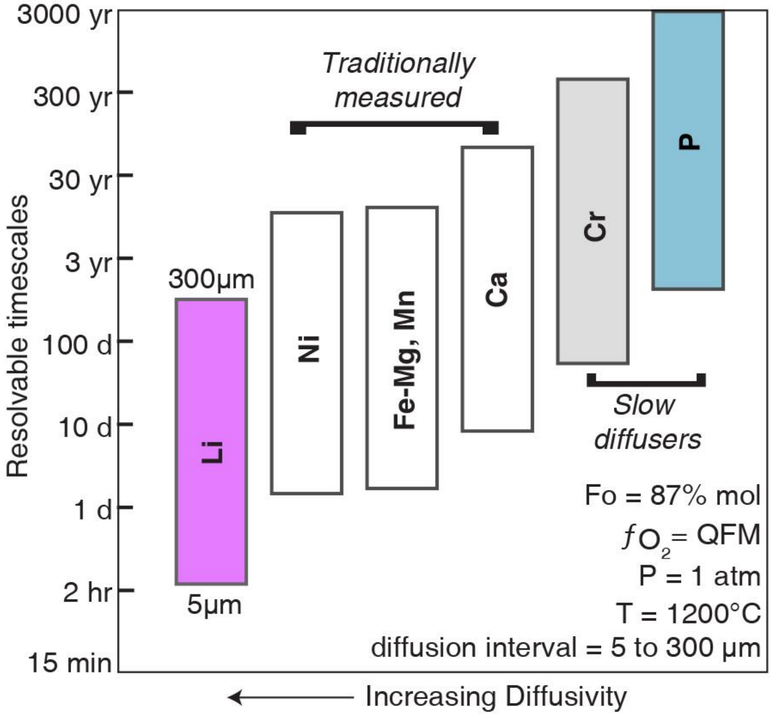

Figure 4.1. Timescale ranges that can be resolved with diffusion distances of 5-300 μm for various elements in olivine. Li is a rapidly diffusing trace element (pink box; Dohmen et al. 2010), whereas major and minor elements like Ni (Petry et al. 2004), Fe-Mg (Dohmen and Chakraborty 2007a, 2007b), Mn (Holzapfel et al. 2007), and Ca (all clear boxes; Coogan et al. 2005) have intermediate diffusivities and are traditionally used in olivine diffusion studies. Cr (grey box; Ito and Ganguly 2006), and P (blue box; Watson et al. 2015) are slowly diffusing trace elements. (For all references to color in figure captions, the reader is referred to the web version of this article).

light to middle rare Earth elements during melting, magma mixing, and crystal fractionation (Ryan and Langmuir 1987; Edmonds 2015). During olivine crystallization, Li may charge balance other trace element impurities that are incorporated during rapid crystal growth (e.g. P, Al, Cr; Milman-Barris et al. 2008; Mallmann et al. 2009). One hypothesis advocates that monovalent cations (e.g. Li) occupy octahedrally coordinated sites to charge balance P substitution in tetrahedrally coordinated sites (Woodland et al. 2004; Milman-Barris et al. 2008; Mallmann et al. 2009):

$$^{IV}Si^{4+} + {}^{VI}Mg^{2+} = {}^{IV}P^{5+} + {}^{VI}(Li^{+}, Na^{+}, H^{+}) \tag{4.1}$$

where *IV* denotes coordination in a tetrahedral site and *VI* denotes coordination in an octahedral site. Equation 4.1 suggests that the concentrations of Li incorporated in olivine during growth may be strongly dependent on the incorporation of P. Dendritic or hopper morphologies (Donaldson 1976) preserved by P-rich zones reflect rapid growth where the slow diffusion of 3+ and 5+ ions in the surrounding melt leads to the formation of boundary layers (e.g. Watson and Muller 2009) that are incorporated in the crystal structure (Albarede and Bottinga 1972; Faure et al. 2003a, 2003b; Faure and Schiano 2005; Milman-Barris et al. 2008; Welsch et al. 2013, 2014). Thus, P zoning serves as a blueprint of crystal growth that can be used to determine if Li is preferentially incorporated during rapid growth processes.

However, P impurities may be balanced by Li (Equation 4.1) or by a combination of 3+ ions and vacancies in octahedral sites (Milman-Barris et al. 2008; Mallmann et al. 2009):

$$^{IV}Si^{4+} + 2{}^{VI}M^{2+} = {}^{IV}P^{5+} + {}^{VI}R^{3+} + {}^{VI}[\ ] \tag{4.2}$$

where $^{VI}M^{2+}$ refers to a divalent cation in an octahedral site (e.g. Fe^{2+}, Mg^{2+}), $^{IV}R^{3+}$ refers to a trivalent cation in a tetrahedral site (e.g. Al^{3+}, Cr^{3+}, and Fe^{3+}) and $^{VI}[\ ]$ represents an octahedral site vacancy. Equation 4.2 is one example of substitution reactions that have been proposed to charge balance the incorporation of P (e.g. Agrell et al. 1998; Boesenberg et al. 2004) and 3+ ions in olivine (Bershov et al. 1983; Mass et al. 1995).

Multiple substitutions involving P occur during growth (e.g. Mallmann et al. 2009), so Li partitioning may also rely on the incorporation of other trace elements.

Growth relationships between coupled elements in olivine are modified by diffusion and can become decoupled depending on the ease with which a given species can diffuse (e.g. Fe-Mg and Ni; Lynn et al. 2017). Phosphorus is one of the slowest diffusing elements in olivine (Watson et al. 2015) and may have a significant effect on the diffusion of elements that charge balance it in the crystal structure (e.g. Li). Coupled diffusion between trace elements is rare and has only been documented in doped experimental studies (e.g. Na and Cr; Spandler and O’Neill 2010), and so its role in olivine crystals with natural concentrations of trace elements is poorly known. Few studies have used concentrations of Li or other trace elements consistent with those found in natural basaltic systems. Thus, examining suites of elements with variable diffusivities is essential to determine if charge-balancing reactions affect the diffusion of Li.

Here, we seek to evaluate the capacity of Li zoning to resolve late-stage magmatic processes by documenting its behavior in basaltic melts and related olivine crystals. The dominantly explosive eruptions of the Keanakākoʻi Tephra (KT, 1500-1823 C.E.; Swanson et al. 2012a) at Kīlauea Volcano are ideal for investigating Li behavior because: (1) olivine crystals are euhedral, allowing them to be carefully oriented for sectioning, (2) the longer-term (weeks to years) magmatic histories were previously characterized by modeling forsterite (Fo; [Mg/(Mg+Fe) x 100]) and Ni zoning (Lynn et al. in review; t_1 in Figure 4.2), and (3) many KT olivine crystals have 5-20 µm outer rims with minor variations in Fo (< 1%) and NiO (< 0.01 wt%) that are difficult to fit with diffusion models (t_2 in Figure 4.2). These thin rims indicate that a late-stage mixing event occurred within a few days prior to eruption (Lynn et al. in review). Therefore, KT olivine crystals provide an excellent opportunity to test Li as a geospeedometer to extract short timescales from natural crystals.

In this work, we used high-precision laser ablation inductively coupled plasma mass spectrometry (LA-ICPMS) to measure Li, as well as other elements that display a range of behaviors during crystal growth and diffusive re-equilibration (Na, Al, P, and Cr). As shown by Equation 4.1 and 4.2, these elements are important to understand Li behavior in olivine. We characterized and mapped the distribution of these elements in

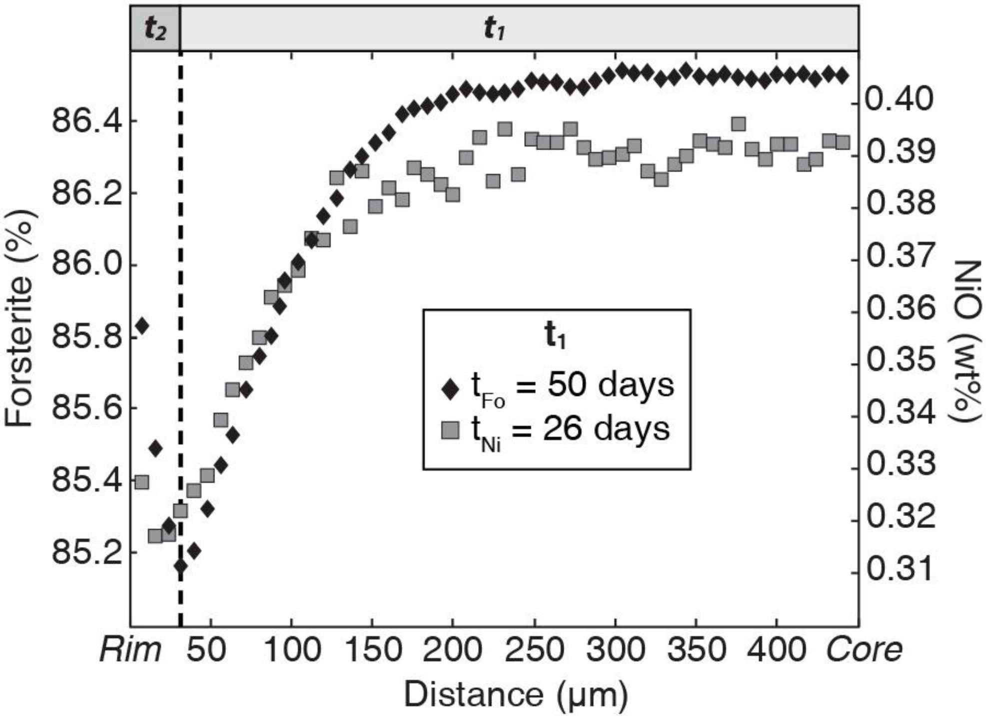

Figure 4.2. Example of Fe-Mg, and Ni "hook" style zoning in rims of KT olivine (Lynn et al. in review). Diffusion modeling of Fo and Ni between 30 and 450 µm from the rim yields storage timescales of 1-2 months (t_1). The compositional reversal in the hook feature (0-30 µm) cannot be fit by diffusion models due to the limited spatial extent and change in concentration. Thus, t_2 is unknown, but indicates that a late-stage mixing event may have occurred shortly before eruption.

KT olivine crystals to explore diffusion and growth signatures in Li zoning and examine the potential anisotropic nature of Li diffusion. Correlations between the different elements are used to investigate how charge-coupling of fast and slow diffusing species (Figure 4.1) preserve a blueprint of growth that is not erased by subsequent diffusive re-equilibration. Smooth Li gradients extending 10-300 µm from olivine rims are modeled to provide essential constraints on late-stage, short duration magma mixing events indicated by near-rim Fo zoning. The timescales of storage are then used to revise the model for crustal magmatic processes during the KT period.

4.3. Methods

4.3.1. Sample Selection and Preparation

A subset of euhedral olivine crystals was selected from the KT eruptions studied by Lynn et al. (in review), including phreatomagmatic units 7, 11, and 20 (U7, U11, and U20), and the marker units Basal Reticulite (BR), Layer 6 (L6), and Golden and Eastern Pumices (GP and EP, respectively; see Swanson et al. 2012a for sample descriptions). Sections through KT olivine crystals are almost always perpendicular to the *a*- or *b*-axes, with the *c*-axis in the plane of the section. This careful orientation aids in extracting analytical profiles that are parallel to principle crystallographic axes, minimizing 3D effects on diffusion timescales derived from 1D modeling (e.g. Shea et al. 2015a).

4.3.2. Electron Backscatter Diffraction (EBSD)

Crystal orientations were determined using the HKL Nordlys EBSD detector on the JEOL JSM-5900LV scanning electron microscope at the University of Hawaiʻi (UH). Additional polishing with a 50-70 nm colloidal silica suspension for four hours on a vibratory polisher improved the quality of electron backscatter diffraction patterns (EBSPs). Measurements were made using a 70° sample tilt, 25 kV accelerating voltage, and a working distance of 16-17 mm. Grids of 10 x 10 points spaced at least 10 µm apart achieved average mean angular deviation values of < 1°. The EBSPs were processed using the HKL Technology *Channel 5* software package and axis locations were output into lower hemisphere stereographic projections using *Steroenet9*$^{©}$ (Cardozo and Allmendinger 2013).

4.3.3. Electron Probe Micro-Analyses (EPMA)

X-ray maps of Al, P, and Cr in olivine were obtained using the JEOL JXA-8500F Hyperprobe at UH. Maps were collected using a 15 kV accelerating voltage and a 300-500 nA beam current, with dwell times between 100 and 200 ms/pixel. Fe-Mg zoning was characterized by backscatter electron (BSE) images and core-to-rim analytical traverses with 5-10 µm spacing, acquired using the methods outlined in Lynn et al. (in review). Two-sigma analytical precision for repeated measurements of San Carlos olivine are 0.35 wt% for SiO_2, 0.06 wt% for FeO, 0.10 wt% for MgO, 0.003 wt% for NiO, and 0.006 wt% for CaO.

4.3.4. Laser Ablation Inductively Coupled Plasma Mass Spectrometry (LA-ICPMS)

Trace element analyses were acquired at the Earth Observatory of Singapore (Nanyang Technological University) using a Photon Machines Analyte G2 excimer laser connected to an iCAP Q ICPMS in an Ar-He atmosphere. Machine settings were optimized to reduce oxide production and interferences by achieving a ThO^+ signal intensity of < 0.6% of the Th^+ signal. The laser was run at 70% output and 8 Hz with constant voltage and 240 shot count. For all analyses, 20 seconds of background signal (laser off) were acquired followed by 40 seconds of ablation signal (laser on). Data reduction in Iolite© removed the first and last three seconds of counts for each analysis before converting counts to concentrations. The NIST 612 silicate glass was used as an internal standard, and NIST 610 and USGS BCR-2G were run as unknowns. The three standards were analyzed in between each olivine transect for instrumental drift corrections during data reduction. Their values were compared to the GeoReM database preferred values (Jochum et al. 2011, 2016) to assess data reduction quality.

Isotopes of ^{7}Li, ^{23}Na, ^{27}Al, ^{29}Si, ^{31}P, and ^{52}Cr were measured for 32 transects in 26 olivine crystals using 10 x 50 µm individual spots oriented with the long length parallel to the crystal-melt boundary. Spot sizes were chosen to maximize ablation volume, while minimizing the homogenization of zoning patterns (only 10 µm wide in the direction of the traverse). An 11 µm spacing was used to avoid overlap, resulting in 1 µm spacing in between individual spot analyses. Two transects measured perpendicular to each other were completed for six olivine crystals to check for Li diffusion anisotropy. The internal reference isotope ^{29}Si was used to convert raw counts to concentrations based on the EPMA measurements of SiO_2 in olivine (taken from Lynn et al. in review). Average 2σ error for analyses of unknowns were 0.07 ppm for Li, 3 ppm for Na, 6 ppm for Al, 10 ppm for P, and 9 ppm for Cr. Analytical precision for repeated measurements of NIST 612 glass are 0.83 ppm for Li (2% relative to preferred GeoReM value), 1291 ppm for Na (1.3%), 178 ppm for Al (1.7%), 6 ppm for P (12%), and 1.7 ppm for Cr (5%).

4.3.5. Diffusion Modeling

Lithium concentration gradients deemed suitable for chemical diffusion work were modeled using the one-dimensional form of Fick's Second Law:

$$\frac{\partial C}{\partial t} = \frac{\partial}{\partial x}\left(D\frac{\partial C}{\partial x}\right) \quad (4.3)$$

where *C* is concentration, *t* is time, *D* is the diffusion coefficient, and *x* is distance (Crank 1975). The diffusivity of Li (D_{Li}) parallel to the *c*-axis can be calculated using the approximate Arrhenius relation (Dohmen et al. 2010):

$$\log(D_{\mathrm{Li}}) = -5.92(\pm 1.0) - 1.2847 \times \frac{10^4}{T(K)} \quad (4.4)$$

where *T* is the temperature in Kelvin. This expression is appropriate for diffusion in olivine containing 1-10 ppm Li and temperatures between 800 and 1200°C (Dohmen et al. 2010). Temperatures were obtained using the inferred melt Mg# in equilibrium with olivine rim Fo contents ($\mathrm{Kd}^{\mathrm{ol/melt}}_{\mathrm{Fe\text{-}Mg}} = 0.343 \pm 0.018$; Matzen et al. 2011) and the Kīlauea glass MgO thermometer (Helz and Thornber 1987). Lithium concentration gradients were modeled using Equation 4.3 and 4.4 to retrieve timescales corresponding to the last thermal and/or chemical perturbation experienced by the host magma. Initial boundary conditions were determined based on the compositions of olivine cores (C_i, the Li content of the crystal before thermodynamic perturbation) and crystal rims (C_o), which are inferred to reflect diffusion with the host melt after perturbation.

4.4. Results

Lithium concentration gradients in KT olivine crystals can be divided into two styles. The prevailing style of Li zoning is a gradual increase or decrease of 0.2-1.6 ppm Li across a smooth 10-300 µm gradient that is amenable to diffusion modeling (Figure 4.3). Lithium zoning is normal ($\mathrm{Li}_{\mathrm{core}} > \mathrm{Li}_{\mathrm{rim}}$; Figure 4.3) or reverse ($\mathrm{Li}_{\mathrm{core}} < \mathrm{Li}_{\mathrm{rim}}$; Figure 4.4) and typically inversely correlated with Fo zoning. In cases where two profiles were measured perpendicular to one another and parallel to different crystallographic axes, no resolvable differences in Li concentration gradient lengths are observed (Figure 4.4). Diffuse gradients of Li are generally not correlated with gradients in other trace elements (Figure 4.3 and 4.4).

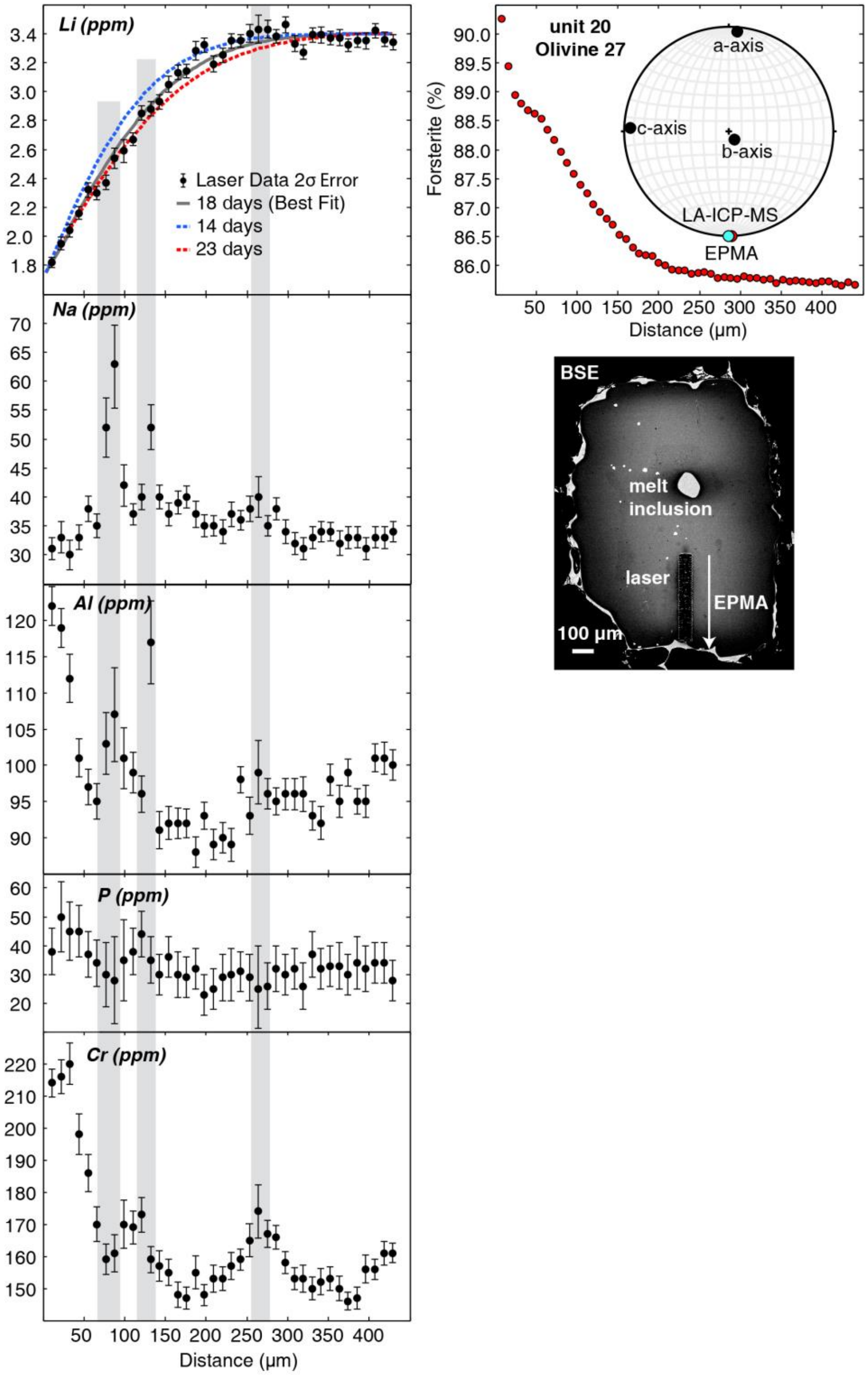

Figure 4.3. Trace element profiles for an Olivine 27 from phreatomagmatic unit 20 (1650-1670 C.E.) with a normally zoned Li rim. Location of crystallographic axes and analytical traverses are marked in lower hemisphere projection and BSE image. Trace element data include 2σ error bars. Lithium is normally zoned, ranging from 1.8-3.4 ppm over 250 μm. Lithium does not correlate with enrichment peaks of other trace elements (grey shading). Diffusion modeling results include a best-fit (grey solid line), minimum (blue dashed line), and maximum (red dashed line) within error bars.

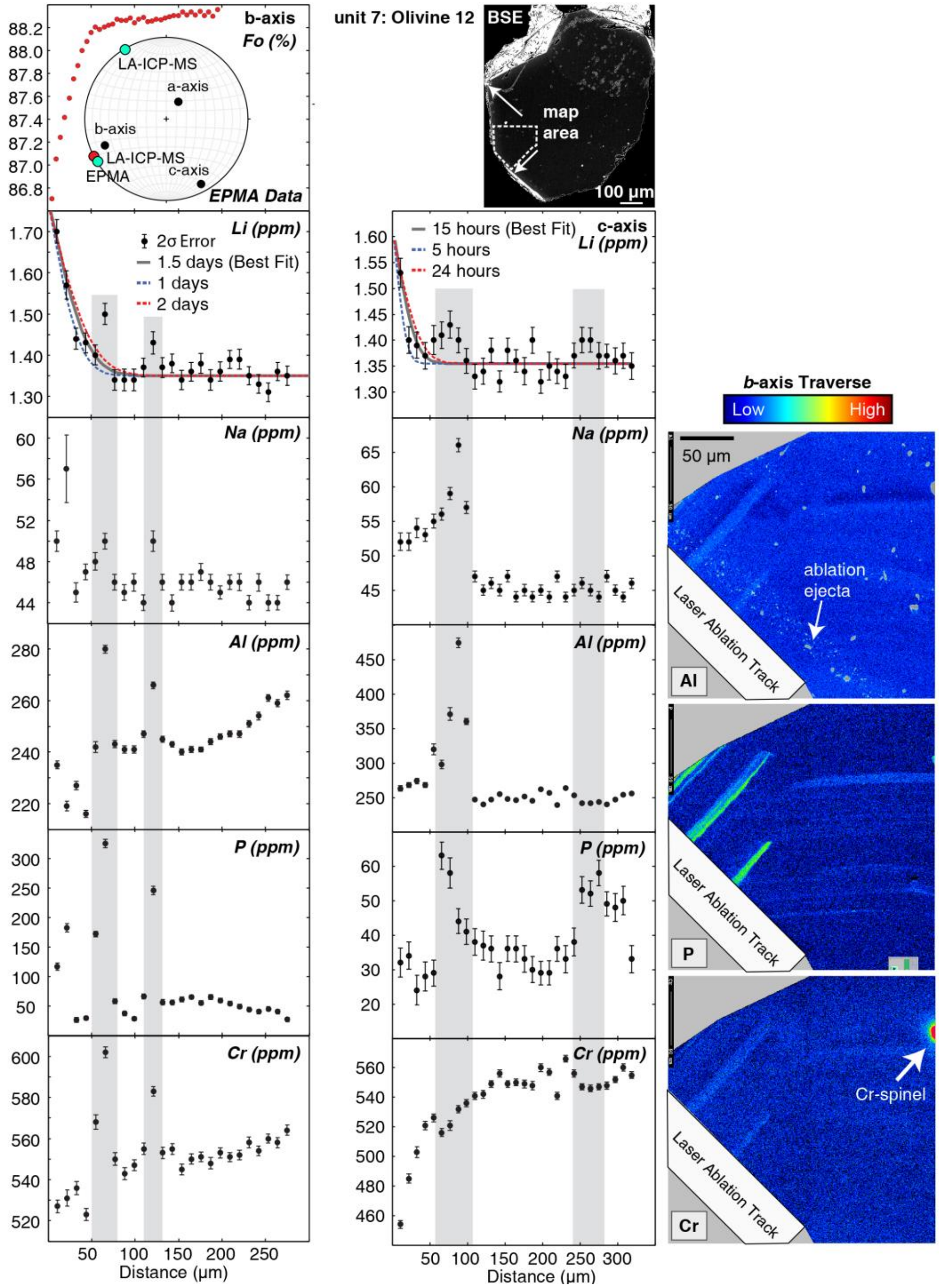

Figure 4.4. Trace element profiles for an olivine from phreatomagmatic unit 7 with reversely zoned Li rims. Location of crystallographic axes and analytical traverses are marked in lower hemisphere projection and BSE image (Fo profile and EBSD from Lynn et al. in review). EPMA X-ray map area marked by white dashed line. Trace element data include 2σ error bars. Greyed out regions in Al map are ablation ejecta with adhering aluminosilicate polishing grit. Grey bars correlate zones of enrichment or depletion across many trace elements. Lithium is reversely zoned and diffusion modeling results include best-fit (grey solid line) minimum (blue dashed line), and maximum (red dashed line) timescales within the error bars.

Occasionally, Li is complexly zoned and positively correlated with Na, Al, P, and/or Cr within discrete regions of crystal interiors (Figure 4.4). In some cases, 10-30 µm wide zones of Li enrichment exist adjacent to or within diffuse rims (e.g. reverse and complex zoning in Figure 4.4). When Li preserves enrichment peak features, they are correlated with strong spikes in P concentration (10’s to 100’s of ppm) relative to low-P regions in the profile (e.g. Figure 4.4). Li enrichment peaks have an inconsistent relationship with other trace elements (e.g. Na, Al, Cr). Only about half (46%) of the analytical profiles examined in this study have correlated Li, P, Na, Al, and Cr zoning in discrete enrichment peak regions (Figure 4.4). Lithium profiles in the other half of the dataset do not preserve enrichment peaks. In these cases, P is decoupled from Al (Figure 4.3 and 4.5) and the two are inversely correlated over broad regions (10’s to 100’s of µm; *b*-axis profile in Figure 4.5 and Appendix C). When P is low in abundance (i.e. a few 10’s of ppm) and nearly nonzoned (e.g. < 10 ppm range outside error) Li appears to preserve diffuse profiles only (Figure 4.3) whereas enrichments peaks of Na, Al, and Cr are strongly correlated.

In rare cases (2 of 26 crystals in this study), Li has no diffuse zoning in olivine rims. Instead, it is complex and generally mimics P (Figure 4.5). In the Layer 6 olivine transects (Figure 4.5), Na and Al are coupled along the *c*-axis but preserve a zoning pattern that is different from Li and P. Along the *b*-axis, Al and Na do not correlate well, and neither corresponds to the zoning observed in Li and P. There are different concentrations of Fe-Mg, Al, and Cr between the crystal’s core and rim, which are also distinct in the P map (oscillatory zoning in the core, no zoning in the rim; Figure 4.5). Phosphorus and Al also exhibit pronounced sector zoning, with sectors parallel to the *b*-axis poorer in P and somewhat richer in Al. The boundary between the core and the rim is smooth for Fe-Mg (BSE image), which diffuses quickly compared to Cr, Al, and P (Figure 4.1). The boundary is comparatively more distinct for Cr, Al, and finally P (Figure 4.5 maps and transects), which is the slowest diffusing species among those examined here (Watson et al. 2015; Figure 4.1). Strong diffusion anisotropy is observed across the boundary between the core and rim when comparing Cr from the *b*- and *c*-axes (Figure 4.5), consistent with previous studies (Petry et al. 2004; Ito and Ganguly 2006).

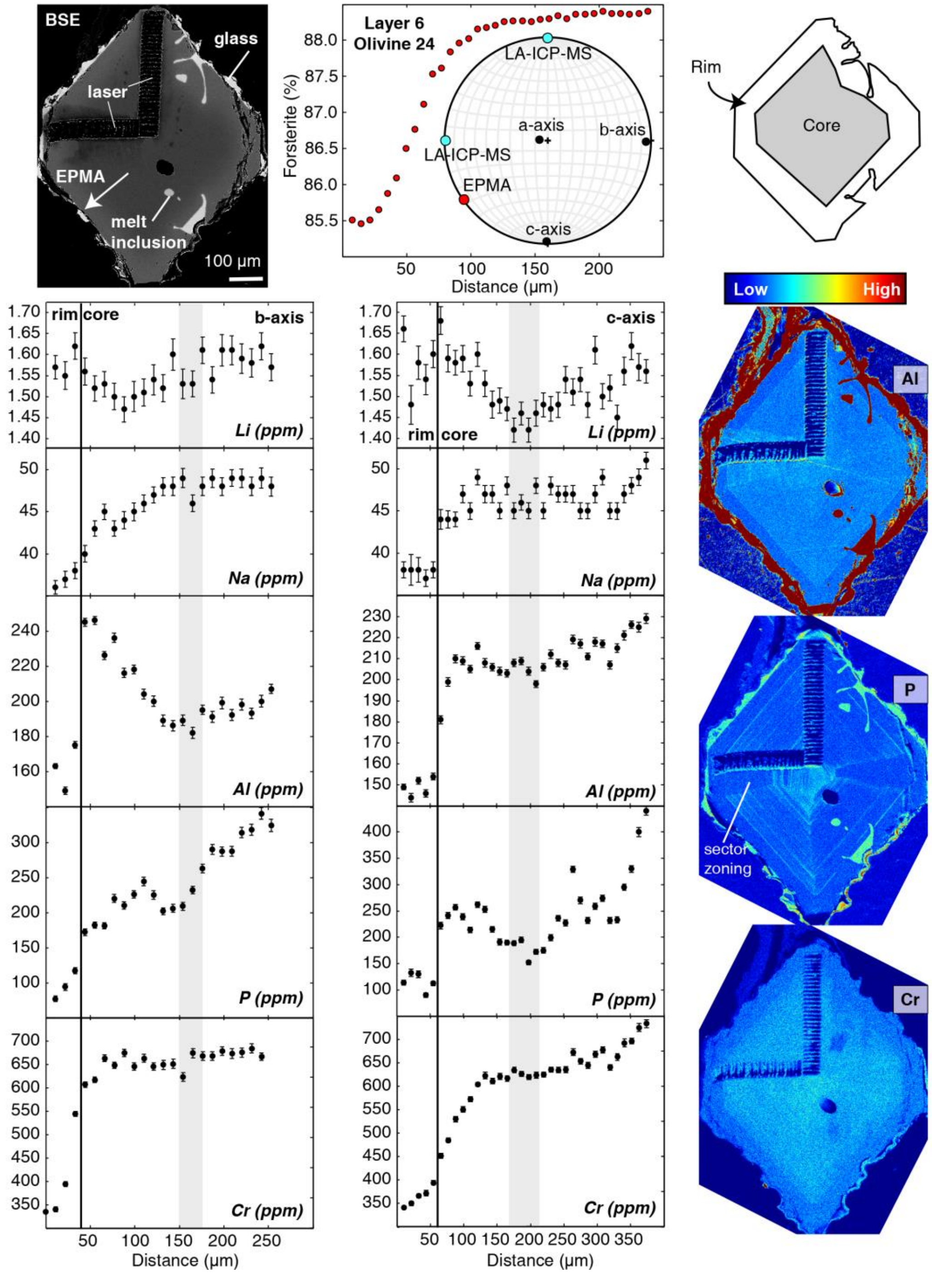

Figure 4.5. Trace element profiles for an olivine from Layer 6 (1650 C.E.) with distinct core and rim regions (boundary marked by solid black line ~50 µm from rim in analytical profile data). Location of crystallographic axes and analytical traverses are marked in lower hemisphere projection and BSE image. Trace element data include 2σ error bars. Lithium zoning mimics P and does not correlate well with other trace elements. Al and Cr record two stages of growth in different melt environments. Phosphorus also records the two growth stages, where the inner core stage has fine-scale P-rich bands and the outer rim stage does not. Anisotropic diffusive re-equilibration of Cr between the two stages is evident when comparing *b*- and *c*-axis transects (e.g. boundary between the core and rim is smoother for the *c*-axis compared to the *b*-axis).

No diffusion between the two growth stages is apparent for Li and it mimics P zoning only.

Lithium zoning behavior in cores and rims can also be distinguished by examining the relationship of P versus Li (Figure 4.6). Diffuse normally or reversely zoned crystal rims (Figure 4.3 and 4.4) have different trends in P versus Li compared to enrichment peaks (Figure 4.4) and complexly zoned crystals (Figure 4.5). Normally zoned diffuse rims have a significant decrease in Li compared to relatively little variation in P, creating a downward trajectory (unit 20 Olivine 35; Figure 4.6). Reversely zoned diffuse rims display the same behavior but increase in Li to form an upward trajectory (unit 7 Olivine 12; Figure 4.6). The core regions of these crystals have minimal variation in both components, forming small clusters in P versus Li space (Figure 4.6). Enrichment

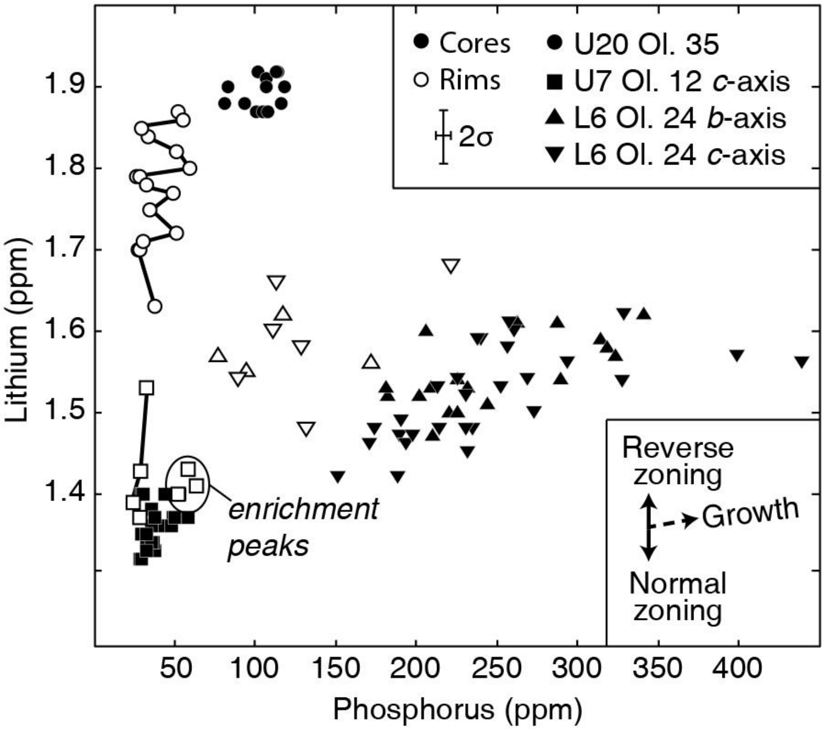

Figure 4.6. Phosphorus (ppm) vs. lithium (ppm) in olivine transects with 2σ error bars shown in the upper right. Core (filled symbols) and rim (open symbols) data have variable behavior related to their zoning patterns. Solid lines connect diffuse rim profiles. Rim data that trend upward away from their core (U7 Ol. 12; Figure 4.4) have reversely zoned Li with minimal variation in P. Rim data that trend downward away from their core (U20 Ol. 35) have normally zoned Li with minimal variation in P. Note that enrichment peak rim data plot similar to the rest of the profile's core data. The Layer 6 Olivine 24 (Figure 4.5) has core and rim regions along both the *b*- and *c*-axes profiles with scattered data fields.

peaks, which are proximal to the diffuse rims in Figure 4.4, behave similarly to the core regions. Both the core and rim in the Layer 6 complexly zoned olivine crystal have considerable scatter owing to a relatively large variation in P compared to Li (Figure 4.6) and the behavior is unlike that observed for the diffuse normally and reversely zoned rims.

Timescales retrieved by modeling diffuse Li rims (using Equation 4.3 and 4.4) from 28 KT olivine transects vary from a few hours to three weeks (Table 4.1). There is no correlation between timescale duration and zoning type (normal vs. reverse), olivine core or rim Fo content, or stratigraphic order of eruptive units (Table 4.1). Most

Table 4.1. Calculated times (days) obtained by modelling the chemical diffusion of Li in olivine crystals.

Unit	Ol.*	Core Fo	T(°C)	Li C_i	Li C_o	Zoning Type	t (days)	(-)	(+)
BR	10_1	86.9	1245	1.41	1.71	R	8	6	12
	10_2	86.9	1245	1.60	1.80	R	0.25	0.05	0.75
	12	87.4	1263	1.50	1.25	N	2	1.5	4
	28	78.8	1245	5.20	2.50	N	8	7	17
U7	12_1	88.4	1245	1.35	1.75	R	1.5	0.5	0.5
	12_2	88.4	1245	1.35	1.69	R	0.6	0.4	0.4
	20	87.3	1245	1.42	1.57	R	2	1	3
	28_1	89.4	1245	1.35	1.45	R	2.5	2	7.5
	28_1	89.4	1245	1.32	1.45	R	1.5	0.25	4.5
U11	1	88.7	1275	1.30	1.59	R	3	2.75	9
	6	88.5	1275	1.50	1.10	N	1	0.75	6
L6	21	89.2	1197	1.20	1.60	R	3	2.5	13
	26	86.8	1197	1.25	1.80	R	18	13	-
U20	7	87.6	1263	1.80	1.36	N	10	9.9	-
	18	86.4	1263	1.85	1.57	N	2.5	1.75	4.5
	21	77.0	1263	1.90	2.80	R	22	10	18
	23	82.6	1263	2.40	1.67	N	6	4	6
	27	79.2	1263	3.40	1.75	N	18	4	5
	29	88.4	1263	1.52	1.61	R	2	1.5	6
	35_1	83.9	1263	1.90	1.60	N	9	5	11
	35_2	83.9	1263	2.00	1.60	N	3	1	17
GP	4	88.7	1237	1.37	1.50	R	2	1.9	6
	32	88.2	1237	1.50	2.20	R	14	6	6
	34	88.3	1237	1.40	2.15	R	10	5	14
EP	3	87.5	1237	1.55	2.05	R	4	3.5	6
	15	85.1	1237	1.63	1.50	N	20	15	50
	18	85.6	1237	2.10	1.60	N	2.5	1.75	4.5
	19	88.1	1237	1.40	2.00	R	1.5	0.75	2.5

Note(s): Fo contents and zoning from Lynn et al. (in review). Lithium zoning types are either N (normal) or R (reverse). All reported timescales are best-fit results within analytical precision and scatter. Initial boundary conditions for the core (C_i) and rim (C_o) are reported in ppm. (-) and (+) represent the errors calculated by finding the minimum and maximum fits by visual inspection of the scatter in the data. A dash under (+) notes profiles in which scatter outliers make it difficult to determine the maximum timescale error. * denotes olivine sample number, and profile number within the olivine where appropriate (e.g. 10_1 and 10_2).

timescales (61%) are less than four days, and rarely more than one week (Figure 4.7). These calculated timescales are nevertheless subject to relatively large errors (average is -60% and +220% relative to best fit value; Table 4.1) due to analytical uncertainty as well as limitations associated with relatively low sampling density (1 spot per 11 µm). Thus, all timescales are presented with minimum, maximum, and best fit results to individual profiles (e.g. 1.5 ± 0.5 days; Figure 4.4 and Table 4.1). Lithium timescales are generally shorter than those retrieved from traditionally measured major and minor elements (Fe-Mg and Ni; upper inset Figure 4.7), suggesting that they record a separate perturbation event.

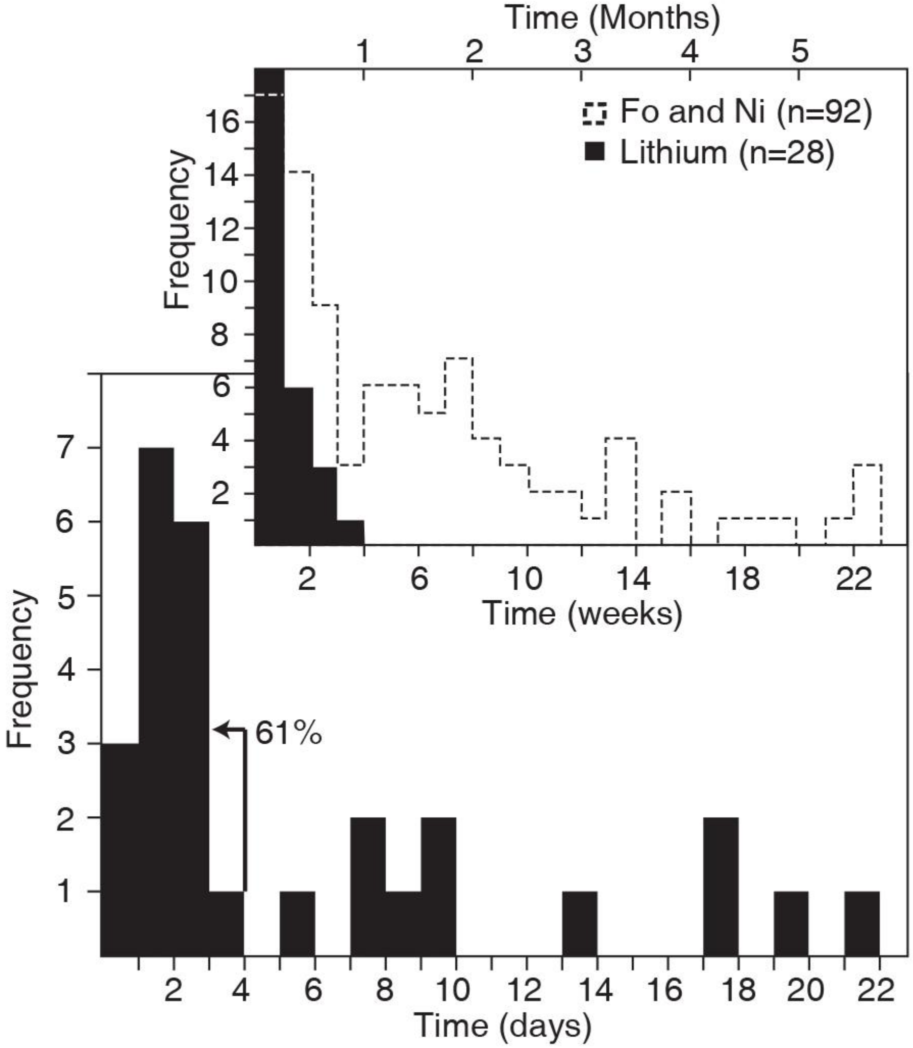

Figure 4.7. Histograms showing the distribution of Li timescales retrieved from diffusion modelling. Upper inset has Li with Fo and Ni timescales (Lynn et al. in review) for comparison in 1-week bins. Lower histogram shows only Li timescales in 1-day bins, where 61% of all timescales are < 4 days.

4.5 Discussion

Zoning of Li, Na, Al, P, and Cr profiles are used in the following sections to resolve how different zoning styles of Li record magmatic processes. First, we consider the potential effects of shallow Li degassing on diffusion profiles. Lithium profiles are then compared to the blueprint of growth recorded chiefly by P zoning (Milman-Barris et al. 2008; Welsch et al. 2013; 2014) and the relationship of P versus Li is used to distinguish growth and diffusion zoning in Li profiles. Olivine transects are also used to determine how growth induced charge-balancing relationships may impact the diffusion of Li and its application as a geospeedometer. Finally, the effects of Li diffusion anisotropy are considered and timescales obtained from modeling of Li diffusion profiles are used to present a new model for the late-stage mixing, storage, and transport histories of KT magmas.

4.5.1. Behavior of Li in magmas

Lithium can enter a fluid phase or degas as felsic magmas reach low pressures (< 22 MPa; Charlier et al. 2012), resulting in diffusion profiles that are consistently zoned in the same direction due to a universal shift in the surrounding melt Li content (Charlier et al. 2012). Lithium is weakly volatile in basaltic melts (Edmonds 2015) as well. Previous studies have suggested that the final ascent of KT magmas began from shallow storage regions near 1.5-2 km depth (< 60 MPa; Ferguson et al. 2016). If shallow degassing strongly affected the Li contents of KT magmas, we would expect that all Li concentration gradients in olivine crystals would be similarly zoned as a result of diffusive exchange with a Li-poor melt.

There are both normally and reversely zoned Li gradients in KT olivine from individual eruptions (Table 4.1), demonstrating that the zoning was not produced by simple fractionation during growth (Costa et al. 2008) or a universal degassing of Li from the melt (Charlier et al. 2012). Weak degassing of Li ($D_{Li}^{vapor/melt}$; ~ 0.1; Edmonds 2015) was inferred to occur in evolved, relatively water-rich basaltic melts based on olivine-hosted melt inclusions with < Fo_{82} core compositions (Sides et al. 2014). Most KT olivine crystals (75%; Lynn et al. in review) have ≥ Fo_{85} cores, and associated high-MgO glasses (up to 11 wt%; Helz et al. 2015) imply high temperatures (up to 1235°C; Helz and Thornber 1987) in a magmatic environment that would not promote degassing (Edmonds 2015). Furthermore, Li melt concentrations are expected to increase with decreasing MgO as a result of its moderate incompatibility in olivine during fractional crystallization (Brenan et al. 1998; McDade et al. 2003; Grant and Wood 2010; Spandler and O'Neill 2010). We suggest that mixing of melts with variable Li contents generated by fractional crystallization produces the diffusion profiles and Li loss via degassing is unlikely.

4.5.2. Lithium zoning in olivine

4.5.2.1. Complex charge coupling of Li during crystal growth. In this study, Li enrichment peaks are uncommon but always positively correlated with P, consistent with the proposed charge balancing substitution reaction in Equation 4.1. This relationship suggests that Li enrichment peaks are growth features. Enrichment peak correlations generally occur for P concentrations that are 10's to 100's of ppm higher than low-P regions (Figure 4.4 and 4.5). In low-P regions (a few 10's of ppm), Li zoning does not correlate with P zoning (Figure 4.4). However, P-rich zones produced by rapid growth are generally ≤ 10 μm wide (Figure 4.4 and 4.5; see also Welsch et al. 2013, 2014) and are therefore susceptible to homogenization with surrounding low-P regions due to the spatial limitations of the analytical method (10 x 50 μm). Thus, the measured Li and P concentrations in enrichment peaks are probably somewhat lower than the true concentrations of thin enrichment features. Weak correlations between Li and P (e.g. Figure 4.4 *c*-axis transect) may result from homogenization of spatially limited enrichment zones.

The broadly positive correlation of P and Li in growth-dominated profiles (Figure 4.4 enrichment peaks and Figure 4.6) is generated due to melt boundary layers with increased 3+ and 5+ cation concentrations. Such boundary layers often show P and Al enrichment near the crystal-melt interface (Milman-Barris et al. 2008; Shea et al. 2015b). Increased Li concentrations in boundary layers could lead to Li enrichments as P is incorporated into olivine crystals due to local partitioning constraints during rapid growth (Tomascak et al. 2016). The increasing concentration of Li in boundary layers and the coupled substitution in Equation 4.1 explain the coupling of Li and P in regions dominated by crystal growth. However, the vastly lower concentration of Li compared with P in P-rich areas indicates that the role of Li in charge balancing P is minor compared with other mechanisms (Mallmann et al. 2009; see also Appendix C). Thus, although P may influence Li incorporation during rapid crystal growth, ${}^{VI}Li^{+}$ does significantly satisfy the charge balancing requirements of P^{5+} substituting for ${}^{IV}Si^{4+}$ in olivine crystals.

The behavior of Li during growth appears to be dependent only on P, despite the clear relationships observed between P and other monovalent and trivalent cations (e.g. Figure 4.4; Woodland et al. 2004; Milman-Barris et al. 2008; Mallmann et al. 2009). In KT olivine crystals, analytical transects and X-ray element maps show that Na, Al, and Cr have inconsistent relationships with P and vary dramatically in both their abundance and zoning pattern morphology (Figure 4.3 and 4.5). In the case of no P zoning, Li preserves diffusive re-equilibration whereas Na, Al, and Cr have complementary enrichment peak zoning (Figure 4.3). Furthermore, coupled Li and P in crystals that preserve only growth have a different zoning pattern than coupled Na, Al, and Cr (Figure 4.5). We propose that the variable behavior of Na, Al, and Cr independent of P can be explained by a coupled substitution modified after Bershov et al. (1983) and Mass et al. (1995):

$${}^{IV}Si^{4+} + 3\,{}^{VI}M^{2+} = {}^{IV}Al^{3+} + 2\,{}^{VI}Cr^{3+} + {}^{VI}Na^{+} \qquad (4.5)$$

Simultaneous implementation of Equation 4.1 and 4.5 during growth explain enrichment correlations of all elements (Li, Na, Al, P, and Cr), while allowing correlated Li and P to be independent of correlated Na, Al, and Cr. Contrasting zoning of Na, Al, and Cr compared to Li and P may depend on growth conditions, the availability of these elements within local boundary layers, and/or many substitution mechanisms (Bershov et al. 1983; Mass et al. 1995; Agrell et al. 1998; Gaister et al. 2003; Boesenberg et al. 2004; Papike et al. 2005). The diffusive coupling of Na and Cr (Spandler and O'Neill 2010) can further complicate these relationships, decoupling their concentration gradients from Al and modifying the relationship expected from growth (*b*-axis profile; Figure 4.5).

Zoning patterns of P and Al can also be inversely correlated (Figure 4.5 and Appendix C). This behavior is consistent with the added complication of sector zoning in olivine, which is Al-rich (Pack and Palme 2003; Milman-Barris et al. 2008) and P-poor (Figure 4.5; McCanta et al. 2008; Milman-Barris et al. 2008). These observations indicate that trace element zoning relationships are strongly dependent on the 3D structure of the olivine crystal during growth (sector, rapid skeletal, slow ripening; Welsch et al. 2014), and sectioning through heterogeneously distributed zoning can complicate the trace element relationships observed in 1D profiles (e.g. Shea et al. 2015a). Thus, many different charge balancing reactions may be needed to explain deviant behavior of trace elements within individual 1D transects in this study (as was observed for Al, Cr, and P in 2D maps by Milman-Barris et al. 2008). However, Li is consistently correlated only with P zoning in KT olivine, and we suggest that its behavior is not dependent on Na, Al, or Cr because any correlations observed can be explained by a common relationship with P (e.g. Equation 4.2).

4.5.2.2. Preserving growth features within Li diffusion profiles. Lithium diffusion profiles 10-300 μm from olivine rims can coexist with well-defined enrichment peaks that consistently correlate with enrichments of P many 10’s to 100’s of ppm higher than low-P regions (Figure 4.4). Phosphorus enrichment features are inferred to represent sampling of a dendritic or hopper zoning morphology generated during rapid growth (Donaldson 1976). Thus, Li peaks are subject to charge balancing conditions (e.g., Equation 4.2), and are apparently not easily overprinted by diffusive re-equilibration. At typical magmatic temperatures (> 800°C), octahedrally coordinated Mg sites appear to host Li (Dohmen et al. 2010). During growth, Li^+ ions are required to satisfy charge imbalances created by P^{5+} occupying tetrahedral sites (Woodland et al. 2004; Mallmann et al. 2009). Coupled elements that charge balance each other within crystal lattices are also susceptible to sharing coupled fluxes during diffusive re-equilibration (Lasaga 1979). We suggest that Li^+ ions in the ^{VI}M sites are mobilized during diffusion, but the charge balancing needs of $^{IV}P^{5+}$ must remain satisfied and some of the Li^+ ions must maintain occupancy in $^{VI}M^{2+}$ sites.

However, zones of P enrichment are usually not volumetrically significant (Welsch et al. 2014; Figure 4.8a). Most of the olivine crystal is low in P due to ripening under slower growth conditions that do not promote the formation of trace element-rich boundary layers (Welsch et al. 2013; Figure 4.8a). Thin (10-30 µm) enrichment peaks of Li and P in 1D profiles may only be removed at the rate of the slowest diffusing element (P; Watson et al. 2015), and rapidly diffusing Li is locally bound to maintain charge balancing (Figure 4.4 and 4.8c). This coupled diffusion phenomenon has also been invoked to explain other correlated zoning in olivine (e.g., P and Cr; Milman-Barris et al. 2008). In slow-growth regions that have P concentrations of only a few 10's of ppm (e.g., Figure 4.3), Li may not be affected by coupling-dependent charge balancing, leaving it free to diffuse through ^{VI}M sites (Figure 4.8c). This is consistent with trace element transects through regions without skeletal P zoning where the Li profile is dominantly controlled by diffusion (Figure 4.3 and 4.8b). Even if core regions preserve complex growth zoning (e.g., enrichment peaks), diffuse rims show the most change in Li concentration with minimal variation in P (Figure 4.6). Thus, despite charge-balancing behavior that may locally couple Li to P, Li can still be used as a geospeedometer to investigate the timescales of magmatic processes.

4.5.3. Lithium geospeedometry

4.5.3.1. Diffusion Anisotropy? Some trace elements are known to diffuse anisotropically along the three principal crystallographic axes in olivine (Ca, Coogan et al. 2005; Na, Spandler and O'Neill 2010; Be, Jollands et al. 2016a). The difference in diffusivity along each axis is generally minor for trace elements (Spandler and O'Neill 2010), unlike the 6x faster rates for Fe-Mg, Mn, and Ni along the *c*-axis (Petry et al. 2004; Dohmen and Chakraborty 2007a, 2007b; Holzapfel et al. 2007). In olivine crystals where two profiles were collected perpendicular to each other (e.g., *b*- and *c*-axes; Figure 4.4), no correlation was found between crystallographic axis and the extent of Li diffusion. Thus, Li does not have strong anisotropy between its axes, and/or limitations in the spatial and analytical precision of laser ablation profiles cannot resolve anisotropic differences. Applying the Arrhenius relation for D_{Li} (Equation 4.4) to all Li diffusion profiles is acceptable considering the precision of analyses and current constraints on its anisotropy.

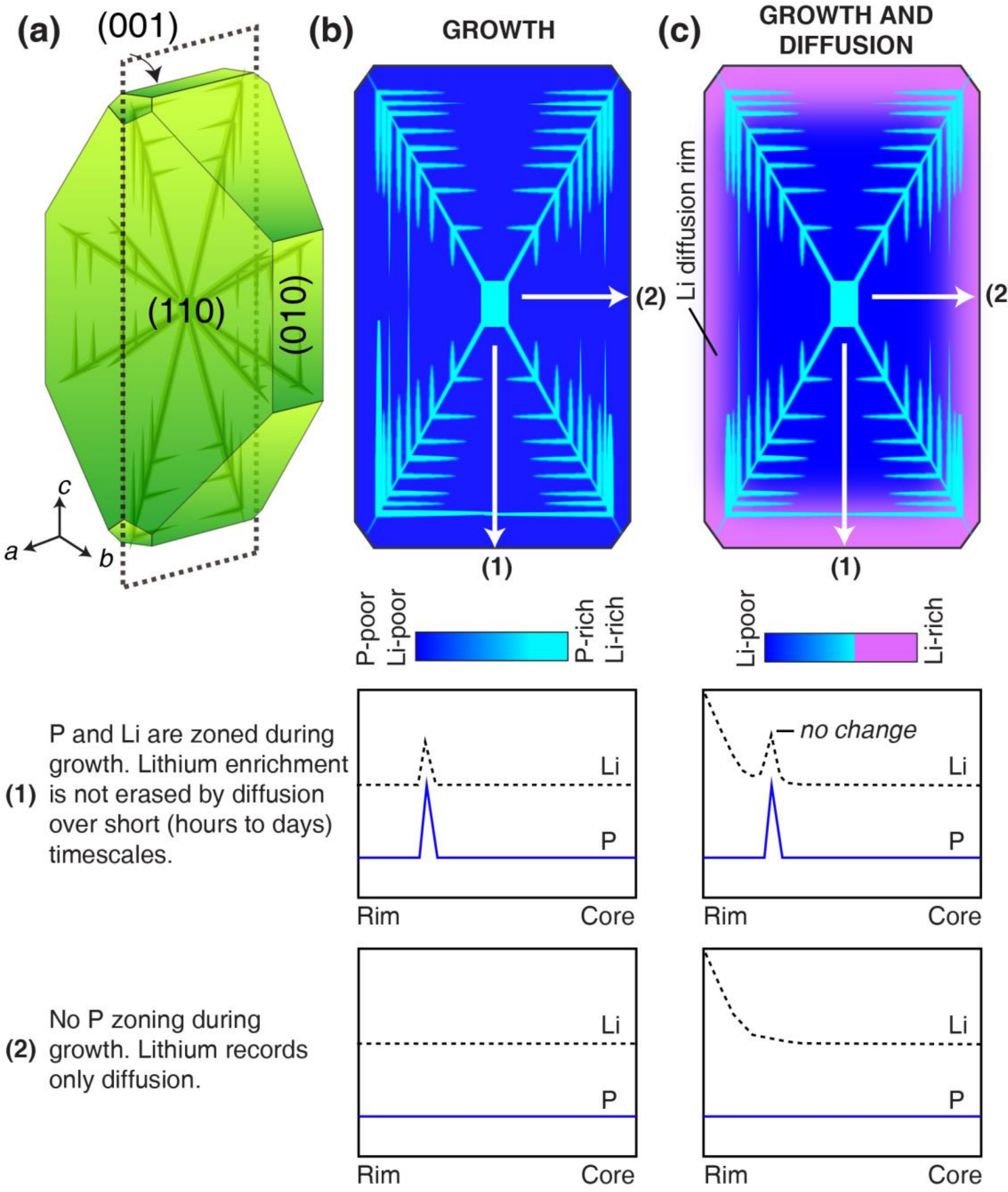

Figure 4.8. Schematic illustration of Li behavior and zoning resulting from growth and diffusion. **(a)** Euhedral olivine crystal with volumetrically small interior skeletal structure (as proposed by Welsch et al. 2013, 2014). Dashed line marks the plane of section perpendicular to the *b*-axis. **(b)** Growth-only zoning of Li- and P-rich skeleton from an early phase of rapid growth (Donaldson 1976) surrounded by Li- and P-poor compositions from later slow ripening. White lines mark the locations of compositional profiles presented below the section. Transects 1 and 2 have complementary Li and P zoning after crystal growth. **(c)** Zoning generated by growth and diffusion of Li (pink rim). Transect 1 has a diffusive rim with no change to the Li enrichment peak. Transect 2 shows Li diffusion only in the absence of growth-related initial zoning. P is unchanged throughout due to its slow diffusivity (Watson et al. 2015) and short time elapsed (hours to days) in the scenario.

4.5.3.2. Magma Mixing and Storage Histories. Zoning of Fo and Ni in KT olivine crystals shows that mantle-derived recharge magmas were mixed at least once and then stored for weeks to months in crustal reservoirs (Lynn et al. in review; Figure 4.9a). These older mixing events are probably not preserved by Li because its rapid diffusion (Dohmen et al 2010) results in the complete re-equilibration of olivine crystals < 1 mm in

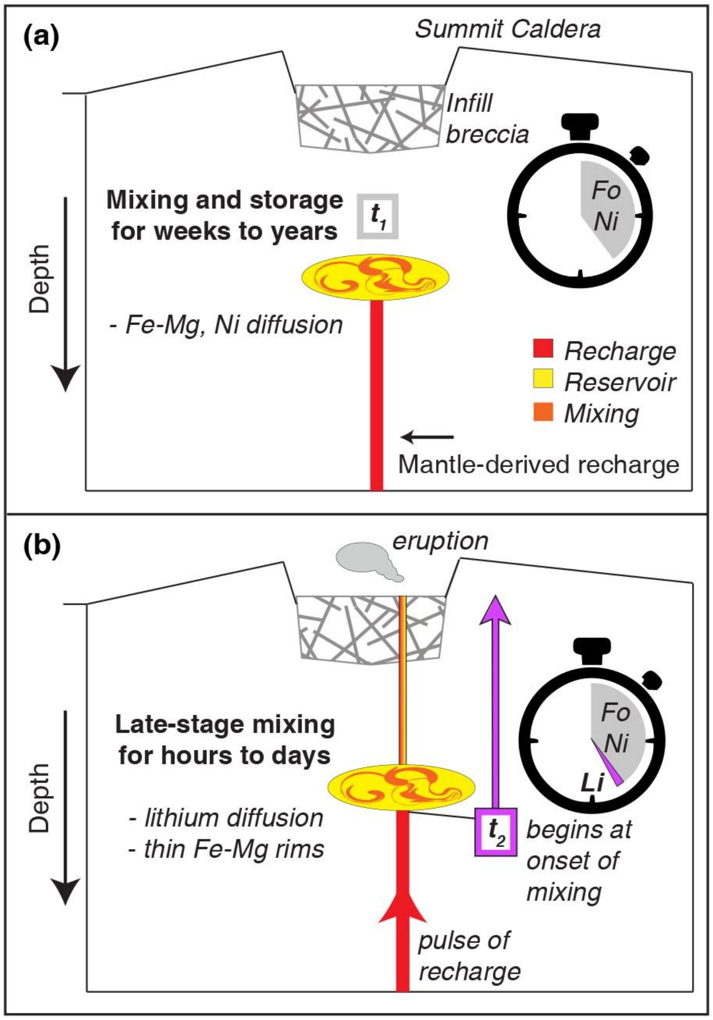

Figure 4.9. Simplified schematic of Kīlauea's plumbing system (not to scale) illustrating magmatic processes for the KT period, modified after Lynn et al. (in review). **(a)** Major and minor elements record early mixing and storage events (t_1). Mantle-derived recharge magmas (red) intersect stored reservoir magma (yellow), producing hybrid compositions (orange). The storage time after mixing (weeks to years; grey on stopwatch) is recorded in Fe-Mg and Ni zoning (Lynn et al. in review) **(b)** Recharge magma intrudes reservoir magma and is generally stored for < 4 days (t_2) before eruption. This is reflected in lithium diffusion profiles (pink on stopwatch) and thin Fe-Mg rims (Lynn et al. in review).

diameter after storage of a few months to a year at temperatures near 1200 °C (Tomascak et al. 2016). Best-fit models of Li diffusion profiles yield timescales that are generally < 4 days (Figure 4.7). This is consistent with Fo zoning in olivine rims (t_2 in Figure 4.2) that suggests the olivine crystals resided within their host melt for a few hours to days prior to eruption (Lynn et al. in review). The Li zoning is interpreted here to record late-stage mixing of MgO-rich recharge magma with more evolved reservoir magma shortly prior to eruption (Figure 4.9b), an event which may have contributed to the remobilization of stored reservoir components. Mixing of these endmembers has been previously invoked to explain heterogeneous glass MgO contents (Mucek 2012; Helz et al. 2015) and olivine populations (Lynn et al. in review) in many of the KT units. Thus, Li zoning probably records the last major event occurring in a reservoir prior to eruption.

4.6. Conclusions

Carefully oriented and sectioned Kīlauea olivine crystals provide a unique opportunity to explore how Li records magmatic processes. The trace element profiles in this study show that:

(1) Lithium concentration gradients in KT olivine have two key styles: (1) Broad diffuse profiles 10-300 µm in length and (2) complex zoning of enrichment peaks 10-30 µm wide.

(2) Diffusion profiles are likely not a result of Li degassing from KT melts because both normal and reverse Li zoning profiles are found in olivine in addition to thin (10-30 µm) rims zoned in Fo.

(3) When Li profiles preserve enrichment peaks, they are always positively correlated with P and are indicative of crystal growth. The relationship of P and Li with other trace elements (Na, Al, Cr) is highly variable due to a complex interplay of growth and diffusion processes. While Li may be correlated with many elements, Li is only dependent on P during growth.

(4) The preservation of Li enrichment peaks within diffusion profiles is a consequence of Li maintaining growth-induced charge-balancing coupled to P. Lithium enrichment features are not easily erased, due to their coupled diffusion and the slow diffusivity of P.

(5) Most timescales from modeling Li diffusion in KT olivine are < 4 days and record a short storage duration after intrusion of recharge magma into stored reservoir magmas, an event which may have contributed to their remobilization. This is consistent with the short storage durations inferred for thinly zoned Fo rims (e.g. t_2 in Figure 4.2) in Lynn et al. (in review). Thus, Li zoning records the last major event occurring in a reservoir prior to magma ascent and eruption.

4.7. Acknowledgements

The authors thank Gareth Fabbro for assistance with LA-ICPMS analyses, Eric Hellebrand with EPMA, Caroline Caplan and Julia Hammer with EBSD, Don Swanson with sample collection, Eileen Chen with sample preparation, and Benoît Welsch for fruitful discussions on olivine zoning. This work was supported by the Fred M. Bullard Graduate Fellowship (UH) and the National Science Foundation (NSF) East Asia and Pacific Summer Institutes grant OISE1513668 to K.J. Lynn. Additional support was provided by NSF grants EAR1347915 and EAR1449744 to M. Garcia, EAR1321890 to T. Shea, and a Singapore Ministry of Education grant (MoE2014-T2-2-041) to F. Costa.

CHAPTER 5

CONCLUSIONS

5.1. Overview

The results presented in this dissertation demonstrate how olivine phenocrysts record magmatic processes (Chapters 2 and 4) and how compositional gradients can be used to better understand magmatic histories during periods of dominantly explosive volcanism at Hawaiian volcanoes (Chapters 3 and 4). The research described in Chapter 2 shows that through careful attention to olivine sectioning, the relative effects of mantle vs. crustal processes can identified so that olivine compositions can be applied appropriately in petrologic and geochemical studies. Chapters 3 and 4 utilize careful sectioning and orientation of euhedral olivine crystals to characterize the magma storage and transport histories during periods of dominantly explosive eruptive behavior at Kīlauea. The careful sample preparation utilized in these studies is needed for a robust examination of how magma mixing and storage histories are recorded by many elements during crystal growth and diffusive re-equilibration in olivine.

5.2. Avenues of Future Research

The research endeavors presented here have stimulated numerous questions that fall beyond the scope of this dissertation. Utilizing Hawaiian olivine compositions to investigate the magmatic histories of explosive eruption periods has highlighted the need for research that will focus on understanding the long-term (e.g. centuries to millennia) geochemical and petrologic evolution of Kīlauea’s eruptive cycles. Olivine compositions and zoning patterns in Chapters 3 and 4 also underlined the need for better constraints on crystal growth rates, trace element charge balancing reactions, and Li diffusivity in olivine. An experimental approach investigating these aspects is necessary to better delineate the relative effects of crystal growth and multi-species diffusion. Potential directions for further work include expanding on current projects as well as applications to new research topics and other eruption periods at Kīlauea. Specific avenues for future research in both geologic and experimental contexts are outlined below.

5.2.1. Increased temporal resolution of the Keanakāko‘i Tephra study

Large sections of explosive deposits on Kīlauea have previously been interpreted to reflect the general evolution of a single eruption over days to months (e.g. Decker and Christiansen 1984; McPhie et al. 1990; Mastin 1997, Neal and Lockwood 2003). Recent careful work on the Keanakāko‘i Tephra revealed that it was actually produced by numerous eruptions throughout a 300-year period (Swanson et al. 2012a). The research in Chapters 3 and 4 focused primarily on the Keanakāko‘i Tephra's marker units, which are fall deposits or lava flows with dominantly juvenile material. We examine only three thin (cm scale) pumice-rich layers within the massively bedded portions of the tephra inferred to have been produced by phreatomagmatic explosions over 170 years.

While our samples span the entire 300-yr period, more work is needed to expand our temporal resolution within these massively bedded deposits and better represent the phreatomagmatic eruptions. Increased sampling of pumice-rich beds throughout the earlier part of the Keanakāko‘i Tephra following the detailed sampling of Mucek (2012) would permit more detailed interpretations on the temporal evolution of the plumbing system, a task that is difficult at present. Additional sampling would also provide better insight into the effects of caldera collapse on the crustal reservoir system and potentially describe its rate of recovery toward the modern-day sustained eruptions (see section 1.4). As field mapping of the Keanakāko‘i Tephra deposits continues, thin, primarily juvenile deposits are being recognized through the period between 1790 and 1823 C.E. (D.A. Swanson, personal communication). Petrologic and geochemical investigations of these units will be necessary to build on our understanding of the Keanakāko‘i Tephra period and shed light on the transition between dominantly explosive and dominantly effusive periods.

5.2.2. Examining older explosive deposits at Kīlauea

The recognition of centuries-long explosive-effusive eruption cycles at Kīlauea (Swanson et al. 2014) has underlined the lack of studies on explosive eruption deposits. Although recent efforts have mapped the deposits, dated their formation, and shed light on their physical eruption mechanisms (e.g. Fiske et al. 2009; Swanson et al. 2012a, 2012b, 2014), the petrologic and geochemical aspects of the deposits remain little investigated.

The contributions made by Chapters 3 and 4 in this dissertation show that mantle-derived recharge magmas entering Kīlauea's magmatic plumbing system have complex mixing and storage histories. This research also raises many questions: (1) Are all explosive eruption deposits petrologically and geochemically similar throughout Kīlauea's history? (2) What are the controls on the lower eruption rates and lower magmatic flux during explosive periods, and can they be characterized geochemically? (3) Do complex magma storage and transport histories characterize eruptions in other explosive periods? To investigate these questions and better understand Kīlauea's long-term (centuries to millennia) behavior, future studies must investigate older explosive deposits.

The Uwēkahuna Tephra (B.C. 200–1000 C.E.; Swanson et al. 2014) is the second most recent explosive period at Kīlauea. It consists of a series of basaltic surge and fall deposits that were emplaced during two or more eruptive episodes (Dzurisin et al. 1995). A detailed study of olivine compositions, zoning patterns, and adhering glasses in the Uwēkahuna Tephra, similar to the one undertaken here in Chapters 3 and 4 for the Keanakāko'i Tephra, is needed to understand if explosive periods share similar petrologic and geochemical records. The Kulanaokuaiki Tephra member (400-1000 C.E.; Fiske et al. 2009) is a well-defined period within the Uwēkahuna Tephra that should be examined with a high sampling resolution in numerous localities across Kīlauea. Additional research efforts should concentrate on geochemical characterization of the older explosive deposits preserved in the Hilina Pali fault scarp (up to ~70 ka; Easton and Garcia 1980). Samples should be prepared as described in Chapter 3, with careful attention to euhedral olivine selection, orientation perpendicular to the *a*- or *b*-axes, and sectioning near to crystal cores to ensure robust timescale results.

5.2.3. Lithium as a new geospeedometer in basaltic systems

The work presented in Chapter 4 shows that Li diffusion in olivine is a potentially powerful tool to investigate the histories of magma mixing and ascent in basaltic systems. This application is most useful when individual olivine crystals can be carefully mounted and sectioned, allowing preferential measurements along the *c*-axis (the only direction along which D_{Li} has been characterized; Dohmen et al. 2010). Lithium diffusion has the capacity to characterize the timing of late-stage processes occurring hours to days before eruption. Studies of Li diffusion in olivine could be applied to older explosive deposits at Kīlauea (e.g. the Uwēkahuna Tephra) to learn if late-stage mixing occurs throughout explosive eruptive cycles. Lithium geospeedometry may also be useful in other basaltic systems with explosive eruptions and/or rapidly quenched tephra deposits (e.g. Réunion; Ort et al. 2016).

Diffusion data are best constrained when similar timescales can be retrieved from multiple elements, as is often done in studies which use traditionally measured elements such as Fe-Mg, Mn, Ni, and Ca (e.g. Costa and Dungan 2005; Kahl et al. 2011). To better understand late-stage short duration processes, it would be advantageous for future studies to also measure and model other rapidly diffusing trace elements such as Be and H (Jollands et al. 2016a, 2016b). Other insights may be gained from modeling the diffusion of volatile species in olivine-hosted melt embayments (e.g. Ferguson et al. 2016), for which current datasets are rare and extremely limited.

5.2.4. Quantifying olivine growth rates

The thin Fe-Mg rims in Keanakāko‘i Tephra olivine may represent a combination of rapid disequilibrium crystal growth and diffusion over timescales of a few days or less. One reason why they are poorly fit by diffusion models is that moving boundary conditions may be needed to accurately simulate both growth and diffusive re-equilibration. A dynamic model is difficult to apply because the growth rates of olivine (Jambon et al. 1992), particularly under disequilibrium conditions, are poorly understood. Experimental determination of olivine growth behavior under a range of cooling rates and other thermodynamic conditions (e.g. T, P, f_{O2}) would allow for better discrimination between growth and diffusion signatures recorded by olivine compositions. It would also support the development of dynamic models that could consider simultaneous growth and diffusion.

5.2.5. Defining charge balancing relationships in olivine

Chapter 4 discusses charge-balancing equations that have been previously invoked to explain the observed correlations between multiple trace elements in the KT olivine crystals. However, much of the experimental work has been completed with doped concentrations (wt% abundances; Spandler and O'Neill 2010) of trace elements, and the results may not be representative of the coupling behavior in natural samples. If the relative abundances of trace elements preserved in zoned regions of rapidly grown olivine can be shown to correlate to conditions surrounding growth (e.g. *T*, *P*, cooling rate), slowly diffusing elements (e.g. P, Al; Zhukova et al. 2014b; Watson et al. 2015; McCarty and Stebbins 2017) in natural crystals could potentially be used to advance investigations of magmatic histories (as suggested by Milman-Barris et al. 2008). Understanding coupling relationships between trace elements will also shed light on the ongoing challenge of distinguishing between zoning created by crystal growth vs. diffusive re-equilibration (e.g. Shea et al. 2015b). This distinction is complicated by numerous types of zoning (e.g. rapid growth, sector, slow ripening) being reflected in 1D analytical profiles, requiring more than one charge balancing reaction to explain complex relationships.

5.2.6. Increased constraints on Li diffusion in olivine

Although Dohmen et al. (2010) provide a detailed examination of Li diffusion in olivine, additional experiments are needed to characterize and quantify its potential diffusion anisotropy. This was unresolvable at the 10 μm spatial resolution of the LA-ICP-MS method in Chapter 4. Future applications of Li diffusion in olivine would benefit from higher resolution analyses, which could be achieved by measurements with nanoSIMS (secondary ion mass spectrometry). The research advances in Chapter 4 were possible because the olivine crystals were precisely oriented and sectioned so that Li was measured parallel to crystallographic axes, reducing errors associated with 3D diffusion not reflected in a 1D analytical profile (Shea et al. 2015a). This generally cannot be achieved in natural samples (e.g. thin sections), which increases errors associated with an unknown degree of diffusion anisotropy. In most natural samples for which careful orientation is not possible, quantifying D_{Li} for all the principle axes is necessary to retrieve robust interpretations of Li timescales.

APPENDIX A

Supporting Information for
NICKEL VARIABILITY IN HAWAIIAN OLIVINE: EVALUATING THE RELATIVE CONTRIBUTIONS FROM MANTLE AND CRUSTAL PROCESSES

A1. Introduction

This supporting file contains all content that appears as Supplementary Tables or other Supplementary Material published with Chapter 2: Lynn et al. (2017). All data that appear in the publication's electronic resource are provided below, including XRF analyses (Table A1) and examples of standards (Table A2), the full dataset of olivine compositions (Table A3), the electron microprobe core-to-rim traverse through a zoned olivine presented in Figure 2.11 (Table A4 and Figure A1), microprobe glass analyses and $a\mathrm{SiO_2}$ sensitive D_{Ni} calculations (Table A5), and numerical model olivine compositions with calculated fraction of pyroxenite (Table A6 and Figure A3).

A2. Methods and Results

A2.1. XRF Analyses

Some Puʻu ʻŌʻō lavas were re-analyzed to investigate anomalous whole-rock Ni measurements (Table A1). Major and trace (Y, Sr, Rb, Nb, Zr, Ni, Cr, V, Zn, Ce, Ba, and La) whole-rock analyses were made using X-ray fluorescence (XRF) methods at the University of Massachusetts (see Rhodes and Vollinger 2004). All XRF analyses were completed in the same laboratory using the same calibration procedures. Examples of standard measurements are included in Table A2.

A2.2. Olivine Compositions

All olivine core compositions measured for Kīlauea lavas in this study are reported in Table A3. The core-to-rim traverse of the olivine presented in Figure 2.11 is reported in Table A4. The backscatter electron image of this crystal is Figure A1.

A2.3. Microprobe Glasses

Kīlauea glass compositions were determined using a 15 kV and 10 nA current with a beam diameter of 10 µm. Peak counting times were 50 s for Si, Fe, and K, 40 s for Ti, Al, Mn, Ca, and P, and 30 s for Na. Na was measured in the first round of elements to minimize loss during analyses. Backgrounds for all analyses were measured on both sides of the peak for half the peak counting times. X-ray intensities were converted to concentrations using standard ZAF corrections (Armstrong 1988). Standards for Kīlauea glass analyses include Basaltic Glass from the Juan de Fuca Ridge (Jarosewich et al. 1980; USNM 111240 VG-2) for Si, Al, Fe, Mg, and Ca, Verma Garnet for Mn, Fluor-Apatite (Jarosewich et al. 1980; USNM 104021) for P, Sphene Glass for Ti, Amelia Albite for Na, and Orthoclase for K. Two sigma relative precision for analyses, based on repeated analysis of Juna de Fuca Ridge glass, are 0.5 wt% for SiO_2, 0.25 wt% for Al_2O_3, 0.2 wt% CaO and FeO, and 0.1 wt% for TiO_2, MnO, MgO, Na_2O, K_2O and P_2O_5. Analyses with totals < 99.0 wt% or > 100.5 wt% were rejected. Kīlauea glass data are an average of 10 to 12 replicate analyses. For analytical conditions and procedures for Koʻolau dike glass, see Haskins and Garcia (2004). Glass compositions are reported in Table A5.

Table A1. XRF whole-rock major (wt%) element analyses of Puʻu ʻŌʻō eruption lavas that were re-analyzed to determine Ni (ppm) contents.

Oxide (wt%)	SiO_2	TiO_2	Al_2O_3	Fe_2O_3[a]	MnO	MgO	CaO	Na_2O	K_2O	P_2O_5	Total	Ni[b]
16-Aug-83	50.38	2.622	13.23	12.34	0.19	7.77	10.64	2.24	0.473	0.269	100.15	133
6-Sep-83	50.42	2.657	13.61	12.19	0.18	7.05	10.83	2.51	0.482	0.272	100.20	103
15-Sep-83	50.28	2.630	13.39	12.14	0.18	7.13	10.84	2.19	0.497	0.268	99.55	105
7-Oct-83	49.91	2.498	12.87	12.34	0.19	8.52	10.58	2.06	0.445	0.253	99.67	166
30-Nov-83	50.19	2.542	13.43	12.07	0.18	7.30	10.95	2.17	0.458	0.254	99.54	109
1-Dec-83	50.33	2.535	13.34	12.12	0.18	7.50	10.96	2.30	0.452	0.257	99.97	110
24-Jan-84	50.51	2.539	13.61	12.08	0.18	7.33	11.03	2.16	0.461	2.52	100.15	106
26-Jul-85	50.43	2.457	13.25	12.33	0.18	7.79	10.99	2.01	0.435	0.243	100.12	111
21-Oct-85	50.35	2.450	13.18	12.35	0.19	7.82	10.97	2.07	0.427	0.242	100.05	109
2-Jun-86	50.13	2.449	13.09	12.26	0.19	7.63	10.97	2.09	0.435	0.239	99.48	106
26-Jun-86	50.18	2.440	13.15	12.34	0.19	7.70	10.97	2.09	0.428	0.242	99.73	101
18-Oct-87	50.47	2.376	12.94	12.46	0.20	8.55	10.69	2.00	0.433	0.235	100.35	125
28-Oct-89	50.02	2.354	12.81	12.45	0.17	8.73	10.65	2.26	0.424	0.232	100.1	145
13-Jul-97	50.35	2.333	13.04	12.53	0.19	7.90	10.78	2.03	0.372	0.217	99.74	142
18-Oct-97	49.79	2.260	12.71	12.56	0.19	8.96	10.35	2.08	0.361	0.215	99.48	84
4-Feb-10[c]	51.01	2.347	13.59	12.17	0.18	7.01	10.98	2.12	0.40	0.232	100.04	89
6-Mar-10[c]	50.97	2.318	13.54	12.21	0.19	7.18	10.91	2.20	0.391	0.223	99.46	88

Note(s): [a]Fe_2O_3 is total iron; [b]Ni reported in ppm; [c]New analyses for recent samples

Table A2. XRF whole-rock data for examples of measurements for standard BHVO-2.

Element	Y	Sr	Rb	Nb	Zr	Ni	Cr	V	Zn	Ce	Ba	La
USGS Values	26	389	9.8	18	172	119	280	317	103	38	130	15
±	2	23	1.0	2	11	7	19	11	6	2	13	1
BHVO-2	25.1	387	6.3	18.4	182	113	295	289	110	39	131	17
BHVO-2	25.0	387	6.5	18.3	181	112	295	289	110	37	131	15
BHVO-2	24.9	385	6.7	18.2	180	111	297	287	109	39	133	15
BHVO-2	25.1	388	6.7	18.5	182	112	298	288	110	37	136	16
BHVO-2	25.1	387	6.5	18.2	181	112	294	286	109	41	132	18
BHVO-2	25.1	388	6.7	18.3	182	113	299	290	111	38	129	17
BHVO-2	25.0	388	6.9	18.4	182	112	295	288	110	37	133	18
BHVO-2	25.2	387	6.8	18.4	182	112	295	290	110	38	135	18
BHVO-2	25.2	389	6.4	18.4	183	113	298	290	111	39	131	19

Note(s): XRF analyses were completed at the University of Massachusetts XRF laboratory

Table A3. Microprobe analyses for olivine from Kīlauea lavas. Oxides are in wt%.

Sample Name	SiO_2	FeO	NiO	MnO	MgO	CaO	Total	Fo (%) [1]
Basal Reticulite 1500 C.E. (Summit)	40.06	10.16	0.466	0.134	49.32	0.179	100.3	89.6
	40.05	10.38	0.475	0.141	48.88	0.190	100.1	89.3
	39.87	10.37	0.473	0.140	48.75	0.189	99.8	89.3
	39.99	10.52	0.464	0.138	48.93	0.193	100.2	89.2
	39.66	10.38	0.473	0.144	48.63	0.189	99.5	89.3
	39.86	10.41	0.472	0.139	48.91	0.187	100.0	89.3
	39.71	10.51	0.473	0.144	48.61	0.193	99.6	89.2
	40.03	10.57	0.458	0.143	48.85	0.189	100.2	89.2
	39.62	10.42	0.473	0.140	48.99	0.195	99.8	89.3
	40.09	10.38	0.479	0.142	49.47	0.191	100.7	89.5
1500-1600 C.E. (Summit)	39.90	10.34	0.480	0.136	49.01	0.188	100.1	89.4
	39.91	10.49	0.478	0.139	48.69	0.193	99.9	89.2
	39.05	12.78	0.408	0.174	46.65	0.214	99.3	86.7
	39.43	10.40	0.476	0.140	48.74	0.190	99.4	89.3
	40.03	10.50	0.470	0.140	49.12	0.189	100.5	89.3
	39.54	10.44	0.473	0.142	48.54	0.189	99.3	89.2
	39.72	10.50	0.467	0.142	48.75	0.195	99.8	89.2
	39.34	10.48	0.473	0.139	48.58	0.191	99.2	89.2
	39.56	10.84	0.471	0.145	48.57	0.191	99.8	88.9
	39.48	10.00	0.489	0.130	49.27	0.156	99.5	89.8
1650-1700 C.E. (Summit)	39.47	10.66	0.434	0.143	48.43	0.194	99.3	89.0
	39.18	10.74	0.468	0.141	48.11	0.174	98.8	88.9
	39.30	10.96	0.440	0.147	47.86	0.194	98.9	88.6
	39.41	11.10	0.427	0.150	47.80	0.198	99.1	88.5
	39.25	11.09	0.439	0.146	48.02	0.190	99.1	88.5
	38.93	10.92	0.463	0.145	47.87	0.213	98.5	88.7
	39.16	11.18	0.435	0.148	47.58	0.189	98.7	88.4
	39.59	11.58	0.437	0.159	48.28	0.221	100.3	88.1
	39.38	11.49	0.413	0.155	48.69	0.220	100.4	88.3
	39.58	11.75	0.395	0.161	48.18	0.227	100.3	88.0
Eastern Pumice 1790-1823 C.E. (Summit)	39.39	11.76	0.400	0.160	48.37	0.221	100.3	88.0
	39.77	11.43	0.424	0.151	48.33	0.229	100.3	88.3
	39.93	11.08	0.409	0.150	48.70	0.219	100.5	88.7
	39.52	11.26	0.422	0.154	48.73	0.219	100.3	88.5
	39.76	11.28	0.427	0.153	48.50	0.219	100.3	88.5
	39.32	10.65	0.456	0.140	48.31	0.180	99.1	89.0
	39.26	10.84	0.456	0.144	48.11	0.185	99.0	88.8
	39.51	10.79	0.454	0.142	48.22	0.187	99.3	88.8
Golden Pumice 1790-1823 C.E. (Summit)	39.41	10.82	0.399	0.145	48.33	0.183	99.3	88.8
	39.19	10.55	0.467	0.142	48.36	0.185	98.9	89.1
	39.10	10.45	0.473	0.139	48.46	0.185	98.8	89.2
	39.41	10.47	0.467	0.142	48.29	0.192	99.0	89.2
	39.61	10.48	0.463	0.142	48.66	0.185	99.5	89.2
	39.57	10.29	0.463	0.139	48.68	0.178	99.3	89.4
	39.44	10.79	0.455	0.148	48.21	0.202	99.2	88.8
	39.27	11.50	0.445	0.159	47.66	0.193	99.2	88.1
	39.16	12.28	0.418	0.166	46.82	0.185	99.0	87.2
	39.60	11.00	0.443	0.147	48.32	0.185	99.7	88.7
	39.43	10.93	0.442	0.146	48.21	0.188	99.4	88.7
	39.29	11.02	0.440	0.146	47.86	0.192	98.9	88.6
	39.23	11.51	0.447	0.151	47.70	0.181	99.2	88.1
	39.23	10.97	0.447	0.147	48.33	0.186	99.3	88.7
	39.28	11.02	0.443	0.148	48.11	0.193	99.2	88.6
	39.37	11.43	0.444	0.151	47.74	0.187	99.3	88.2

Sample Name	**SiO_2**	**FeO**	**NiO**	**MnO**	**MgO**	**CaO**	**Total**	**Fo (%)** [1]
	39.56	11.19	0.427	0.155	48.19	0.201	99.7	88.5
	39.35	11.25	0.418	0.148	48.17	0.187	99.5	88.4
	39.74	13.65	0.291	-	45.39	0.219	99.3	85.6
	39.76	14.36	0.302	-	44.58	0.203	99.2	84.7
	39.30	15.30	0.237	-	43.65	0.224	98.7	83.6
14-Oct-68	39.74	13.65	0.291		45.39	0.219	99.3	85.6
(ERZ)	39.76	14.36	0.302		44.58	0.203	99.2	84.7
	39.30	15.30	0.237		43.65	0.224	98.7	83.6
	39.68	13.83	0.291		45.26	0.217	99.3	85.4
	39.62	14.65	0.293		44.26	0.208	99.0	84.3
	39.88	13.76	0.330		45.49	0.200	99.7	85.5
	39.26	16.89	0.210		42.51	0.220	99.1	81.8
	39.85	13.63	0.330		45.57	0.190	99.6	85.6
	39.25	16.31	0.230		43.00	0.230	99.0	82.5
	39.44	15.04	0.280		44.16	0.220	99.1	84.0
13-Jun-69	40.05	13.55	0.322		45.65	0.204	99.8	85.7
(ERZ)	39.86	13.49	0.321		45.56	0.198	99.4	85.8
Mauna Ulu	39.71	13.95	0.295		45.28	0.213	99.4	85.3
	39.80	13.70	0.317		45.43	0.218	99.5	85.5
	39.77	13.60	0.318		45.56	0.220	99.5	85.7
	39.80	13.61	0.316		45.48	0.218	99.4	85.6
	39.65	14.02	0.282		45.15	0.231	99.3	85.2
	39.51	15.22	0.258		44.03	0.229	99.2	83.8
	39.56	14.13	0.289		44.80	0.238	99.0	85.0
	39.72	13.93	0.298		45.20	0.233	99.4	85.3
	39.68	13.38	0.320		45.67	0.216	99.3	85.9
	39.63	14.06	0.285		44.96	0.218	99.2	85.1
	39.77	13.90	0.279		45.20	0.219	99.4	85.3
	39.81	13.99	0.302		45.23	0.215	99.6	85.2
	39.72	14.09	0.294		45.08	0.222	99.4	85.1
	39.76	13.69	0.308		45.38	0.233	99.4	85.5
1970’s	39.41	10.92	0.413	0.146	48.16	0.217	99.3	88.7
(ERZ)	39.21	12.48	0.381	0.159	46.95	0.215	99.4	87.0
Mauna Ulu	38.52	15.51	0.251	0.212	44.27	0.253	99.0	83.6
	38.59	15.99	0.235	0.218	44.15	0.256	99.4	83.1
	38.51	15.20	0.262	0.208	44.46	0.253	98.9	83.9
	39.42	10.72	0.417	0.144	48.24	0.213	99.2	88.9
	39.41	11.36	0.404	0.150	47.92	0.219	99.5	88.3
	39.29	11.30	0.396	0.152	48.14	0.227	99.5	88.4
	39.47	11.09	0.406	0.146	48.21	0.216	99.5	88.6
	38.10	17.84	0.259	0.249	42.40	0.230	99.1	80.9
	38.85	13.00	0.371	0.166	46.32	0.211	98.9	86.4
	37.96	18.44	0.221	0.240	41.90	0.257	99.0	80.2
Aug-71	40.44	11.70	0.383		47.67	0.186	100.4	87.9
(Summit)	40.60	10.93	0.407		48.59	0.185	100.7	88.8
	40.55	11.53	0.403		47.97	0.180	100.6	88.1
	40.21	12.95	0.339		46.57	0.187	100.2	86.5
	40.29	11.96	0.398		47.52	0.180	100.4	87.6
	40.12	13.20	0.305		46.08	0.198	99.9	86.2
	39.84	14.01	0.262		45.44	0.208	99.8	85.3
	40.02	13.32	0.300		45.94	0.206	99.8	86.0
	40.07	13.29	0.307		46.09	0.202	100.0	86.1
	40.01	13.66	0.297		45.58	0.209	99.8	85.6
	40.18	10.80	0.409		48.31	0.183	99.9	88.9
	40.22	10.79	0.409		48.43	0.186	100.0	88.9

Sample Name	**SiO_2**	**FeO**	**NiO**	**MnO**	**MgO**	**CaO**	**Total**	**Fo (%) [1]**
	40.19	11.09	0.409		48.10	0.184	100.0	88.5
	39.87	12.87	0.337		46.40	0.190	99.7	86.5
	40.11	11.77	0.406		47.48	0.176	99.9	87.8
	39.77	13.08	0.307		45.99	0.202	99.4	86.2
	39.60	13.90	0.267		45.30	0.213	99.3	85.3
14-Apr-72	39.93	13.36	0.345		45.98	0.218	99.8	86.0
(ERZ)	39.54	15.06	0.266		44.41	0.218	99.5	84.0
	39.37	15.02	0.249		44.35	0.220	99.2	84.0
	40.19	12.13	0.379		47.27	0.226	100.2	87.4
	39.38	15.38	0.246		44.00	0.216	99.2	83.6
	39.27	15.53	0.283		43.76	0.188	99.0	83.4
	40.11	11.26	0.360		47.84	0.185	99.8	88.3
	39.56	15.36	0.252		44.11	0.214	99.5	83.7
	39.32	16.45	0.215		43.02	0.208	99.2	82.3
	39.96	12.78	0.350		46.54	0.200	99.8	86.7
	39.28	16.84	0.248		42.58	0.210	99.2	81.8
	39.63	14.54	0.330		44.88	0.204	99.6	84.6
	39.67	14.08	0.330		45.06	0.233	99.4	85.1
	39.45	15.58	0.251		43.88	0.212	99.4	83.4
	39.59	14.29	0.323		45.02	0.176	99.4	84.9
	39.27	15.57	0.248		43.76	0.213	99.1	83.4
	39.51	15.16	0.278		44.12	0.192	99.3	83.8
	39.91	12.44	0.345		46.18	0.184	99.1	86.9
3-Jul-83	38.38	17.91	0.239	0.233	42.61	0.246	99.6	80.9
(PO)	38.51	16.64	0.263	0.220	43.61	0.239	99.5	82.4
USGS	39.26	12.18	0.390	0.165	47.15	0.225	99.4	87.3
Ep. 5-139	38.30	17.63	0.254	0.235	42.78	0.226	99.4	81.2
	38.56	16.49	0.267	0.223	43.90	0.166	99.6	82.6
	38.40	16.90	0.258	0.217	43.62	0.243	99.6	82.1
	38.13	18.60	0.239	0.240	41.99	0.235	99.4	80.1
	38.13	18.60	0.243	0.240	41.99	0.237	99.4	80.1
	38.89	14.13	0.376	0.180	45.71	0.226	99.5	85.2
	38.37	17.64	0.258	0.229	43.04	0.221	99.8	81.3
24-Jul-83	39.31	16.22	0.264	0.213	43.94	0.240	100.2	82.8
(PO)	39.35	16.41	0.267	0.214	43.73	0.233	100.2	82.6
USGS	39.16	17.30	0.266	0.229	42.97	0.219	100.1	81.6
Ep. 6-149	39.11	17.34	0.267	0.226	43.01	0.212	100.2	81.6
	38.80	19.11	0.231	0.252	41.52	0.191	100.1	79.5
	39.38	15.47	0.264	0.212	44.51	0.233	100.1	83.7
	39.66	13.43	0.323	0.174	46.29	0.215	100.1	86.0
	39.36	15.87	0.267	0.211	44.42	0.227	100.4	83.3
	39.34	15.12	0.303	0.203	44.83	0.219	100.0	84.1
26-Jul-83	38.24	18.56	0.225	0.243	41.99	0.246	99.5	80.1
(PO)	39.24	12.44	0.372	0.166	47.04	0.246	99.5	87.1
USGS	38.63	15.23	0.270	0.206	44.54	0.248	99.1	83.9
Ep. 6-154	38.80	14.73	0.308	0.200	45.16	0.254	99.5	84.5
	38.50	16.24	0.314	0.204	43.86	0.206	99.3	82.8
	38.39	17.10	0.263	0.234	43.32	0.210	99.5	81.9
	38.42	16.86	0.286	0.216	43.20	0.240	99.2	82.0
	38.64	15.53	0.269	0.206	44.45	0.252	99.3	83.6
	38.24	17.73	0.233	0.234	42.84	0.235	99.5	81.2
	38.12	18.73	0.233	0.249	41.97	0.210	99.5	80.0
	38.53	17.70	0.232	0.239	42.25	0.233	99.2	81.0
	38.92	17.07	0.238	0.228	42.73	0.244	99.4	81.7
	38.97	17.52	0.260	0.233	42.49	0.221	99.7	81.2

Sample Name	**SiO_2**	**FeO**	**NiO**	**MnO**	**MgO**	**CaO**	**Total**	**Fo (%) [1]**
	38.65	18.95	0.231	0.245	41.17	0.219	99.5	79.5
	38.84	16.95	0.238	0.226	42.59	0.240	99.1	81.7
	39.81	11.43	0.395	0.157	47.17	0.217	99.2	88.0
	38.70	17.51	0.255	0.227	42.32	0.192	99.2	81.2
	38.70	18.05	0.246	0.236	42.01	0.225	99.5	80.6
	38.67	18.11	0.238	0.240	42.09	0.232	99.6	80.6
16-Aug-83	37.99	17.73	0.240	0.236	42.52	0.237	99.0	81.0
(PO)	38.63	14.50	0.315	0.192	45.21	0.228	99.1	84.7
USGS	38.47	15.99	0.271	0.211	44.22	0.220	99.4	83.1
Ep. 7-165	38.60	14.34	0.286	0.183	45.50	0.225	99.1	85.0
	38.31	16.58	0.288	0.217	43.70	0.226	99.3	82.4
	38.12	17.76	0.279	0.226	42.70	0.235	99.3	81.1
	38.06	17.73	0.239	0.235	42.78	0.243	99.3	81.1
	37.99	18.09	0.243	0.239	42.43	0.220	99.2	80.7
	38.11	17.37	0.252	0.231	42.89	0.243	99.1	81.5
	38.12	17.47	0.284	0.221	42.75	0.232	99.1	81.3
	38.73	17.87	0.253	0.239	41.95	0.219	99.3	80.7
	38.76	16.98	0.247	0.230	42.63	0.233	99.1	81.7
	38.83	17.23	0.243	0.232	42.51	0.245	99.3	81.5
	38.71	17.64	0.239	0.239	42.04	0.233	99.1	80.9
	39.03	15.32	0.296	0.204	44.02	0.228	99.1	83.7
	39.66	12.88	0.382	0.170	46.19	0.210	99.5	86.5
	39.50	13.01	0.401	0.176	45.84	0.212	99.1	86.3
	38.93	17.27	0.268	0.228	42.61	0.212	99.5	81.5
	39.06	16.87	0.252	0.226	42.85	0.232	99.5	81.9
7-Sep-83	38.52	15.52	0.299	0.203	44.43	0.231	99.2	83.6
(PO)	38.15	17.94	0.248	0.235	42.59	0.234	99.4	80.9
USGS	38.60	15.72	0.287	0.206	44.44	0.241	99.5	83.4
Ep. 8-174	38.81	14.43	0.285	0.195	45.54	0.234	99.5	84.9
	38.40	16.94	0.247	0.223	43.35	0.246	99.4	82.0
	38.62	15.37	0.283	0.202	44.69	0.235	99.4	83.8
	38.66	15.24	0.316	0.196	44.84	0.237	99.5	84.0
	38.41	17.34	0.254	0.222	43.19	0.232	99.7	81.6
	38.31	17.27	0.263	0.224	43.25	0.236	99.5	81.7
	38.68	15.64	0.276	0.206	44.58	0.237	99.6	83.6
	38.97	17.48	0.335	0.225	42.52	0.047	99.6	81.3
	38.89	17.33	0.239	0.229	42.68	0.222	99.6	81.5
	38.81	17.93	0.228	0.238	42.16	0.224	99.6	80.7
	38.95	17.27	0.244	0.230	42.89	0.237	99.8	81.6
	38.83	17.72	0.232	0.237	42.35	0.213	99.6	81.0
	39.42	13.69	0.330	0.185	45.55	0.213	99.4	85.6
	39.20	14.56	0.283	0.199	44.83	0.243	99.3	84.6
	38.97	16.53	0.280	0.218	43.36	0.225	99.6	82.4
	39.08	16.19	0.266	0.216	43.64	0.223	99.6	82.8
17-Sep-83	38.24	16.94	0.270	0.222	43.38	0.240	99.3	82.0
(PO)	39.30	12.52	0.368	0.166	46.98	0.231	99.6	87.0
USGS	38.72	15.09	0.292	0.196	44.97	0.242	99.5	84.2
Ep. 9-178	38.32	17.40	0.270	0.223	43.11	0.225	99.5	81.5
	38.74	15.03	0.292	0.204	45.13	0.265	99.7	84.3
	38.41	16.89	0.253	0.224	43.39	0.239	99.4	82.1
	38.78	15.58	0.289	0.199	44.64	0.248	99.7	83.6
	38.57	17.12	0.257	0.226	43.37	0.229	99.8	81.9
	39.47	12.08	0.363	0.160	47.59	0.227	99.9	87.5
	38.36	17.40	0.247	0.225	43.07	0.233	99.5	81.5
23-Sep-83	39.57	12.12	0.399	0.160	46.90	0.206	99.4	87.3

Sample Name	SiO$_2$	FeO	NiO	MnO	MgO	CaO	Total	Fo (%) [1]
(PO)	39.39	14.33	0.377	0.192	45.27	0.219	99.8	84.9
USGS	39.21	15.69	0.293	0.210	44.30	0.221	99.9	83.4
Ep. 9-178	38.79	17.64	0.264	0.234	42.75	0.191	99.9	81.2
	39.03	16.30	0.265	0.216	43.76	0.233	99.8	82.7
	39.04	16.44	0.278	0.215	43.49	0.214	99.7	82.5
	38.73	18.50	0.242	0.245	42.02	0.216	100.0	80.2
	38.92	16.98	0.253	0.229	43.17	0.233	99.8	81.9
	39.11	15.32	0.299	0.206	44.42	0.226	99.6	83.8
	39.26	15.01	0.318	0.197	44.96	0.211	100.0	84.2
7-Oct-83	38.34	16.42	0.269	0.218	43.47	0.252	99.0	82.5
(PO)	38.39	16.67	0.237	0.223	43.12	0.252	98.9	82.2
USGS	38.32	16.89	0.256	0.225	43.03	0.235	99.0	82.0
Ep. 10-187	38.98	13.66	0.353	0.174	45.73	0.221	99.1	85.7
	39.12	12.86	0.361	0.169	46.50	0.217	99.2	86.6
	38.29	17.47	0.242	0.231	42.85	0.235	99.3	81.4
	38.15	17.73	0.242	0.229	42.66	0.224	99.2	81.1
	39.00	13.20	0.364	0.171	46.24	0.216	99.2	86.2
	38.57	16.02	0.293	0.215	43.94	0.289	99.3	83.0
	38.20	17.17	0.242	0.232	42.86	0.238	98.9	81.6
	39.77	13.66	0.350	0.170	45.73	0.220	99.9	85.7
	39.92	12.86	0.360	0.170	46.50	0.220	100.0	86.6
	39.07	17.47	0.240	0.230	42.85	0.230	100.1	81.4
	38.93	17.73	0.240	0.230	42.66	0.220	100.0	81.1
	39.80	13.20	0.360	0.170	46.24	0.220	100.0	86.2
	39.36	16.02	0.290	0.210	43.94	0.290	100.1	83.0
	38.98	17.17	0.240	0.230	42.86	0.240	99.7	81.7
	39.02	16.17	0.242	0.225	43.53	0.244	99.4	82.8
	39.30	15.28	0.270	0.204	44.39	0.239	99.7	83.8
	39.24	15.02	0.263	0.206	44.46	0.241	99.4	84.1
1-Dec-83	39.02	16.17	0.242	0.225	43.53	0.244	99.4	82.8
(PO)	39.30	15.28	0.270	0.204	44.39	0.239	99.7	83.8
USGS	39.24	15.02	0.263	0.206	44.46	0.241	99.4	84.1
Ep. 12-203	39.35	15.22	0.266	0.211	44.29	0.239	99.6	83.8
	39.02	16.15	0.242	0.221	43.52	0.241	99.4	82.8
	39.16	16.23	0.260	0.219	43.66	0.221	99.7	82.7
	39.06	16.21	0.243	0.224	43.42	0.249	99.4	82.7
	39.06	16.08	0.250	0.221	43.51	0.240	99.4	82.8
	39.17	15.93	0.251	0.223	43.66	0.237	99.5	83.0
	39.00	16.05	0.244	0.223	43.49	0.240	99.2	82.8
11-Jan-87	39.21	16.32	0.209	0.220	43.88	0.242	100.1	82.7
(PO)	39.21	16.97	0.202	0.224	43.50	0.257	100.4	82.0
USGS	39.62	15.04	0.249	0.204	45.04	0.227	100.4	84.2
Ep. 48-685	39.53	14.90	0.249	0.207	44.99	0.226	100.1	84.3
	39.14	17.46	0.203	0.227	43.15	0.262	100.4	81.5
	39.25	17.20	0.196	0.230	43.04	0.260	100.2	81.7
	39.36	17.15	0.200	0.241	43.04	0.232	100.2	81.7
	39.53	15.90	0.239	0.215	44.16	0.212	100.2	83.2
	39.39	17.13	0.199	0.239	43.19	0.229	100.4	81.8
18-Oct-87	39.47	16.25	0.214	0.228	43.76	0.221	100.1	82.8
(PO)	39.64	15.70	0.231	0.221	44.35	0.218	100.4	83.4
Ep. 48	39.42	17.10	0.195	0.240	43.14	0.231	100.3	81.8
	39.33	17.07	0.195	0.242	43.12	0.250	100.2	81.8
	39.28	17.22	0.195	0.241	43.12	0.247	100.3	81.7
	39.32	17.13	0.199	0.241	43.27	0.240	100.4	81.8
	39.27	17.53	0.187	0.248	42.75	0.247	100.2	81.3

Sample Name	SiO_2	FeO	NiO	MnO	MgO	CaO	Total	Fo (%) [1]
	39.31	17.14	0.193	0.235	42.73	0.236	99.8	81.6
	40.06	13.63	0.286	0.191	45.62	0.209	100.0	85.6
	39.38	17.06	0.196	0.237	42.83	0.237	99.9	81.7
28-Oct-89	39.38	17.01	0.197	0.234	42.82	0.236	99.9	81.8
(PO)	39.53	16.15	0.244	0.217	43.69	0.210	100.0	82.8
Ep. 48	39.65	15.83	0.218	0.213	43.79	0.212	99.9	83.1
	39.58	16.50	0.210	0.225	43.36	0.225	100.1	82.4
	39.41	17.06	0.197	0.236	42.87	0.231	100.0	81.8
	39.49	16.51	0.203	0.225	43.19	0.232	99.8	82.3
	39.39	17.21	0.196	0.236	42.77	0.238	100.0	81.6
	39.46	17.07	0.197	0.226	42.77	0.232	100.0	81.7
	39.18	17.22	0.195	0.226	42.82	0.238	99.9	81.6
	39.46	17.04	0.194	0.226	42.78	0.237	99.9	81.7
15-Jun-90	39.37	17.20	0.192	0.224	42.82	0.239	100.0	81.6
(PO)	39.50	17.00	0.197	0.223	42.87	0.226	100.0	81.8
Ep. 48	39.38	16.93	0.207	0.220	43.21	0.222	100.2	82.0
	39.58	15.90	0.239	0.205	43.83	0.205	100.0	83.1
	39.40	16.84	0.211	0.221	43.19	0.222	100.1	82.1
	39.37	17.08	0.205	0.222	42.96	0.223	100.1	81.8
	39.34	17.18	0.195	0.227	42.92	0.241	100.1	81.7
	39.57	17.19	0.197	0.225	43.06	0.228	100.5	81.7
	39.49	16.73	0.217	0.219	43.52	0.220	100.4	82.3
	39.51	16.69	0.224	0.212	43.42	0.212	100.3	82.3
5-Jul-90	39.39	17.08	0.200	0.224	43.15	0.231	100.3	81.8
(PO)	39.37	17.29	0.196	0.227	43.03	0.238	100.3	81.6
Ep. 48	39.42	16.89	0.209	0.218	43.34	0.221	100.3	82.1
	39.35	17.21	0.203	0.227	43.31	0.235	100.5	81.8
	39.43	16.49	0.228	0.213	43.88	0.222	100.5	82.6
	39.38	17.08	0.200	0.223	43.27	0.232	100.4	81.9
	39.21	17.14	0.198	0.240	42.70	0.306	99.8	81.6
	39.27	17.09	0.211	0.237	43.02	0.228	100.1	81.8
	39.16	17.22	0.210	0.242	43.00	0.219	100.0	81.7
	39.17	17.25	0.212	0.237	43.02	0.213	100.1	81.6
20-Jul-90	39.15	17.23	0.204	0.239	43.03	0.223	100.1	81.7
(PO)	39.15	17.27	0.198	0.241	42.79	0.237	99.9	81.5
Ep. 48	39.01	17.10	0.205	0.239	42.89	0.228	99.7	81.7
	39.08	17.15	0.196	0.239	42.79	0.238	99.7	81.6
	39.19	17.07	0.203	0.238	42.87	0.221	99.8	81.7
	39.06	17.29	0.195	0.245	42.80	0.240	99.8	81.5
	39.13	17.17	0.198	0.232	43.01	0.250	100.0	81.7
	39.30	17.35	0.193	0.229	42.95	0.256	100.3	81.5
	39.30	16.62	0.226	0.215	43.53	0.233	100.1	82.4
	39.41	17.22	0.197	0.231	43.12	0.252	100.4	81.7
28-Jul-90	39.22	17.26	0.195	0.227	42.91	0.251	100.1	81.6
(PO)	39.31	17.12	0.202	0.223	43.12	0.241	100.2	81.8
Ep. 48	39.53	15.68	0.244	0.206	44.43	0.233	100.3	83.5
	39.39	17.09	0.200	0.224	43.20	0.254	100.4	81.8
	39.33	16.91	0.214	0.219	43.28	0.236	100.2	82.0
	39.21	17.27	0.195	0.229	42.99	0.251	100.1	81.6
	39.37	17.61	0.188	0.225	42.74	0.236	100.4	81.2
	39.57	17.16	0.195	0.226	43.13	0.236	100.5	81.8
	39.45	16.98	0.199	0.217	43.14	0.226	100.2	81.9
10-Aug-90	39.36	17.12	0.198	0.227	42.95	0.227	100.1	81.7
(PO)	39.34	17.21	0.191	0.228	42.93	0.228	100.1	81.6
Ep. 48	39.32	17.28	0.194	0.232	42.93	0.233	100.2	81.6

Sample Name	SiO_2	FeO	NiO	MnO	MgO	CaO	Total	Fo (%)[1]
	39.34	17.01	0.214	0.223	43.08	0.218	100.1	81.9
	39.23	16.99	0.200	0.219	42.96	0.228	99.8	81.8
	39.36	17.13	0.195	0.226	42.90	0.238	100.0	81.7
	39.27	17.23	0.195	0.227	42.95	0.230	100.1	81.6
	39.08	17.04	0.197	0.224	42.67	0.259	99.5	81.7
	39.14	17.11	0.199	0.224	42.72	0.257	99.6	81.7
	38.92	16.88	0.225	0.219	42.74	0.221	99.2	81.9
24-Feb-91	38.94	16.99	0.202	0.222	42.58	0.258	99.2	81.7
(PO)	38.91	17.00	0.199	0.224	42.47	0.262	99.1	81.7
Ep. 48	38.67	16.87	0.204	0.220	42.54	0.248	98.8	81.8
	39.20	15.46	0.256	0.205	43.75	0.252	99.1	83.5
	39.07	17.14	0.199	0.224	42.61	0.259	99.5	81.6
	39.09	16.88	0.216	0.223	42.92	0.239	99.6	81.9
28-Apr-91	38.95	17.12	0.200	0.226	42.66	0.248	99.4	81.6
(PO)	38.92	17.02	0.199	0.225	42.51	0.254	99.1	81.7
Ep. 48	38.98	16.91	0.201	0.223	42.70	0.254	99.3	81.8
	38.80	16.85	0.206	0.222	42.73	0.248	99.1	81.9
	38.90	16.99	0.201	0.228	42.70	0.252	99.3	81.8
	38.88	17.05	0.201	0.224	42.71	0.255	99.3	81.7
	38.85	17.32	0.209	0.232	42.21	0.245	99.1	81.3
	38.94	17.25	0.209	0.237	42.16	0.250	99.1	81.3
	38.68	18.41	0.202	0.241	41.31	0.250	99.1	80.0
9-Nov-91	39.07	17.90	0.203	0.237	42.55	0.246	100.2	80.9
(PO)	39.09	18.04	0.201	0.236	42.56	0.243	100.4	80.8
Ep. 48	39.21	18.00	0.203	0.235	42.65	0.232	100.5	80.9
5-Oct-92	39.20	18.06	0.204	0.235	42.63	0.233	100.6	80.8
(PO)	39.11	18.06	0.198	0.237	42.50	0.248	100.4	80.7
Ep. 51	39.18	17.81	0.209	0.233	42.73	0.228	100.4	81.0
	39.16	18.05	0.198	0.240	42.55	0.242	100.4	80.8
	38.53	18.21	0.185	0.240	42.00	0.260	99.4	80.4
	38.96	18.11	0.189	0.241	42.23	0.249	100.0	80.6
	38.68	17.99	0.187	0.238	42.08	0.254	99.4	80.7
13-Mar-94	38.53	18.11	0.184	0.242	41.97	0.262	99.3	80.5
(PO)	38.55	18.16	0.186	0.246	42.01	0.256	99.4	80.5
Ep. 53	38.64	18.07	0.188	0.239	42.10	0.253	99.5	80.6
	38.58	18.06	0.179	0.236	42.02	0.261	99.3	80.6
	38.81	18.23	0.187	0.239	42.02	0.255	99.8	80.4
	38.62	17.95	0.184	0.240	42.09	0.250	99.3	80.7
	38.60	17.91	0.194	0.238	42.22	0.251	99.4	80.8
	39.06	17.95	0.204	0.232	42.54	0.245	100.2	80.9
	39.07	17.90	0.200	0.230	42.82	0.243	100.5	81.0
	39.15	18.13	0.185	0.231	42.37	0.250	100.3	80.6
18-May-94	38.88	17.66	0.194	0.224	42.73	0.247	99.9	81.2
(PO)	39.01	17.99	0.189	0.231	42.48	0.246	100.1	80.8
Ep. 53	38.83	18.28	0.179	0.234	42.11	0.249	99.9	80.4
	38.81	18.15	0.186	0.234	42.25	0.244	99.9	80.6
	39.09	17.01	0.215	0.219	43.07	0.225	99.8	81.9
	39.14	17.80	0.195	0.226	42.75	0.234	100.3	81.1
	39.16	17.66	0.181	0.237	41.88	0.249	99.4	80.9
	39.11	17.76	0.179	0.234	41.73	0.257	99.3	80.7
	39.71	15.37	0.239	0.203	44.01	0.212	99.7	83.6
9-Oct-94	39.13	17.72	0.184	0.239	41.79	0.245	99.3	80.8
(PO)	39.55	15.22	0.233	0.206	43.86	0.214	99.3	83.7
Ep. 53	39.20	17.48	0.192	0.230	42.08	0.231	99.4	81.1
	39.19	17.55	0.187	0.232	41.87	0.233	99.3	81.0

Sample Name	**SiO$_2$**	**FeO**	**NiO**	**MnO**	**MgO**	**CaO**	**Total**	**Fo (%) [1]**
	39.32	17.78	0.182	0.235	41.91	0.247	99.7	80.8
	39.16	17.39	0.199	0.226	42.19	0.227	99.4	81.2
	39.20	16.44	0.218	0.217	42.83	0.224	99.1	82.3
	39.01	17.57	0.188	0.230	41.79	0.233	99.0	80.9
	38.99	17.75	0.177	0.234	41.70	0.246	99.1	80.7
14-Jan-95	38.99	17.67	0.183	0.237	41.79	0.249	99.1	80.8
(PO)	39.02	17.82	0.182	0.235	41.80	0.243	99.3	80.7
Ep. 53	39.06	17.80	0.182	0.230	41.77	0.246	99.3	80.7
	38.99	17.67	0.187	0.227	41.79	0.229	99.1	80.8
	38.98	17.50	0.176	0.229	42.54	0.251	99.7	81.2
	39.15	17.43	0.182	0.226	42.80	0.250	100.0	81.4
	39.20	17.37	0.193	0.222	42.95	0.235	100.2	81.5
15-Mar-96	39.09	17.61	0.180	0.230	42.59	0.253	100.0	81.2
(PO)	39.11	17.39	0.181	0.226	42.66	0.252	99.8	81.4
Ep. 53	38.93	17.12	0.204	0.226	42.83	0.225	99.5	81.7
	39.09	17.01	0.206	0.223	42.92	0.222	99.7	81.8
	39.07	17.42	0.181	0.232	42.67	0.252	99.8	81.4
	38.91	17.29	0.182	0.231	42.61	0.246	99.5	81.5
	39.07	17.32	0.181	0.224	42.61	0.250	99.7	81.4
	39.27	17.19	0.180	0.228	42.55	0.251	99.7	81.5
	39.10	17.24	0.179	0.228	42.48	0.248	99.5	81.5
	39.28	17.31	0.180	0.232	42.75	0.241	100.0	81.5
22-Aug-96	39.08	17.58	0.178	0.229	42.40	0.256	99.7	81.1
(PO)	39.24	17.34	0.181	0.232	42.65	0.246	99.9	81.4
Ep. 53	39.12	17.37	0.180	0.232	42.62	0.246	99.8	81.4
	39.20	17.46	0.179	0.237	42.68	0.251	100.0	81.3
	39.15	17.30	0.190	0.224	42.73	0.226	99.8	81.5
	39.02	17.43	0.181	0.228	42.44	0.246	99.5	81.3
	39.12	17.34	0.179	0.233	42.50	0.244	99.6	81.4
	39.18	16.80	0.204	0.218	43.37	0.233	100.0	82.2
	39.01	16.66	0.212	0.222	43.29	0.224	99.6	82.2
	39.24	16.85	0.198	0.218	43.31	0.234	100.1	82.1
13-Feb-99	39.19	17.40	0.191	0.225	42.76	0.260	100.0	81.4
(PO)	39.08	16.74	0.207	0.219	43.28	0.225	99.7	82.2
Ep. 55	39.06	18.29	0.180	0.232	42.09	0.258	100.1	80.4
	39.12	16.89	0.200	0.222	43.26	0.238	99.9	82.0
	39.17	16.80	0.218	0.215	43.56	0.226	100.2	82.2
	39.09	16.84	0.207	0.221	43.37	0.232	100.0	82.1
	38.80	16.91	0.200	0.220	43.02	0.239	99.4	81.9
	38.88	17.38	0.190	0.230	42.24	0.256	99.2	81.2
	39.01	16.82	0.206	0.223	42.87	0.240	99.4	82.0
	39.15	16.75	0.197	0.226	42.82	0.248	99.4	82.0
19-Jun-99	39.01	16.88	0.199	0.222	42.86	0.247	99.4	81.9
(PO)	38.98	17.06	0.194	0.225	42.71	0.243	99.4	81.7
Ep. 55	39.08	16.79	0.199	0.221	42.89	0.237	99.4	82.0
	39.08	16.87	0.195	0.221	42.95	0.243	99.6	81.9
	39.00	16.84	0.201	0.224	42.80	0.245	99.3	81.9
	38.98	16.62	0.215	0.218	42.96	0.226	99.2	82.2
	38.92	16.76	0.204	0.221	42.78	0.241	99.1	82.0
	39.01	17.51	0.210	0.232	42.82	0.244	100.0	81.3
	38.79	17.30	0.207	0.227	42.93	0.232	99.7	81.6
	38.73	17.56	0.185	0.233	42.71	0.245	99.7	81.3
4-Jan-00	39.00	17.55	0.184	0.230	42.68	0.246	99.9	81.3
(PO)	39.02	17.52	0.183	0.234	42.69	0.247	99.9	81.3
Ep. 55	38.94	17.42	0.179	0.231	42.68	0.239	99.7	81.4

Sample Name	SiO_2	FeO	NiO	MnO	MgO	CaO	Total	Fo (%) [1]
	38.84	17.40	0.192	0.228	42.69	0.243	99.6	81.4
	38.69	17.47	0.185	0.232	42.63	0.244	99.5	81.3
	38.86	17.37	0.184	0.229	42.86	0.241	99.7	81.5
	39.01	17.46	0.192	0.226	42.90	0.238	100.0	81.4
	39.13	17.40	0.180	0.239	42.87	0.227	100.0	81.5
	39.07	17.41	0.174	0.240	42.75	0.239	99.9	81.4
	39.23	17.68	0.170	0.237	42.65	0.243	100.2	81.1
4-Aug-00	39.32	17.23	0.179	0.234	43.22	0.227	100.4	81.7
(PO)	39.15	17.55	0.175	0.235	42.91	0.239	100.3	81.3
Ep. 55	38.64	18.75	0.159	0.246	41.87	0.261	99.9	79.9
	39.16	17.58	0.176	0.236	42.89	0.241	100.3	81.3
	39.14	17.17	0.186	0.230	43.33	0.235	100.3	81.8
	39.25	17.58	0.177	0.235	43.11	0.240	100.6	81.4
	39.29	17.39	0.178	0.238	43.14	0.243	100.5	81.6
	39.05	17.52	0.172	0.235	42.56	0.234	99.8	81.2
	38.90	17.31	0.172	0.228	42.44	0.236	99.3	81.4
	39.04	17.09	0.174	0.230	42.58	0.230	99.3	81.6
8-Apr-01	39.17	17.42	0.174	0.228	42.46	0.232	99.7	81.3
(PO)	38.92	17.34	0.175	0.225	42.43	0.230	99.3	81.4
Ep. 55	38.84	17.53	0.171	0.229	42.32	0.231	99.3	81.1
	39.02	17.46	0.171	0.233	42.47	0.228	99.6	81.3
	39.13	17.13	0.191	0.226	42.84	0.223	99.7	81.7
	39.14	16.68	0.197	0.223	43.14	0.219	99.6	82.2
	38.94	17.73	0.167	0.232	42.11	0.236	99.4	80.9
	39.17	16.58	0.176	0.220	43.15	0.208	99.5	82.3
	38.93	17.74	0.169	0.232	42.07	0.233	99.4	80.9
12-Apr-02	38.82	17.66	0.165	0.235	42.15	0.230	99.3	81.0
(PO)	38.88	17.45	0.168	0.235	42.31	0.225	99.3	81.2
Ep. 55	38.87	17.61	0.163	0.236	41.95	0.233	99.1	80.9
	38.92	17.70	0.166	0.230	42.24	0.238	99.5	81.0
	38.78	17.67	0.160	0.229	42.02	0.231	99.1	80.9
20-Aug-02	38.93	17.64	0.175	0.232	42.61	0.216	99.8	81.2
(PO)	39.11	17.81	0.159	0.229	42.55	0.237	100.1	81.0
Ep. 55	39.06	17.82	0.157	0.231	42.45	0.239	99.9	80.9
12-Mar-03	38.65	17.42	0.169	0.231	42.57	0.223	99.3	81.3
(PO)	38.64	17.63	0.163	0.230	42.40	0.231	99.3	81.1
Ep. 55	38.65	17.70	0.163	0.234	42.43	0.231	99.4	81.0
	38.89	17.72	0.162	0.231	42.47	0.240	99.7	81.0
	38.93	17.25	0.164	0.232	42.73	0.230	99.5	81.5
	38.98	17.55	0.169	0.229	42.52	0.223	99.7	81.2
	39.83	14.91	0.258	0.200	44.53	0.234	100.0	84.2
	39.47	15.95	0.215	0.214	43.65	0.232	99.7	83.0
	39.67	15.91	0.213	0.215	43.77	0.234	100.0	83.1
17-Jun-07	39.76	15.96	0.200	0.214	43.55	0.237	99.9	82.9
(PO)	39.58	16.86	0.234	0.229	42.93	0.204	100.0	82.0
Ep. 56	40.12	14.32	0.260	0.200	45.05	0.231	100.2	84.9
	39.79	15.61	0.217	0.212	43.96	0.236	100.0	83.4
	39.96	15.65	0.222	0.211	44.07	0.233	100.3	83.4
	39.98	15.13	0.234	0.201	44.57	0.231	100.3	84.0
	39.85	15.77	0.214	0.210	43.92	0.233	100.2	83.2
	39.99	15.74	0.218	0.211	43.96	0.231	100.3	83.3
	39.47	18.37	0.184	0.234	41.62	0.232	100.1	80.1
	39.41	18.59	0.168	0.238	41.48	0.241	100.1	79.9
	39.42	18.37	0.172	0.238	41.58	0.240	100.0	80.1
24-Aug-07	39.29	18.82	0.165	0.240	41.26	0.253	100.0	79.6

Sample Name	**SiO_2**	**FeO**	**NiO**	**MnO**	**MgO**	**CaO**	**Total**	**Fo (%) [1]**
(PO)	38.71	17.36	0.177	0.233	42.62	0.240	99.3	81.4
Ep. 58	38.76	18.14	0.169	0.233	41.90	0.262	99.5	80.5
	37.69	18.79	0.153	0.258	41.39	0.240	98.5	79.7
23-Sep-08	38.99	17.41	0.176	0.234	42.43	0.247	99.5	81.3
(PO)	39.09	17.34	0.198	0.226	42.44	0.232	99.5	81.4
Ep. 58	39.31	17.92	0.177	0.237	42.12	0.248	100.0	80.7
	39.46	17.75	0.180	0.233	42.27	0.239	100.1	80.9
5-Apr-09	39.20	17.66	0.182	0.230	42.21	0.250	99.7	81.0
(PO)	39.32	17.65	0.178	0.235	42.27	0.248	99.9	81.0
Ep. 58	39.68	15.99	0.236	0.212	43.53	0.224	99.9	82.9
	39.46	17.03	0.208	0.224	42.63	0.226	99.8	81.7
	39.39	17.99	0.170	0.235	41.96	0.258	100.0	80.6
	39.45	17.94	0.191	0.232	41.41	0.212	99.4	80.5
	39.68	18.04	0.169	0.233	41.40	0.267	99.8	80.4
	39.34	19.27	0.152	0.246	39.97	0.299	99.3	78.7
6-Mar-10	39.45	17.94	0.191	0.232	41.41	0.212	99.4	80.5
(PO)	39.68	18.04	0.169	0.233	41.40	0.267	99.8	80.4
Ep. 58	39.34	19.27	0.152	0.246	39.97	0.299	99.3	78.7
	39.71	18.14	0.176	0.235	41.47	0.247	100.0	80.3
	39.74	18.03	0.175	0.234	41.59	0.248	100.0	80.4
	39.56	18.02	0.173	0.235	41.34	0.252	99.6	80.4
	39.48	18.39	0.169	0.238	41.11	0.260	99.6	79.9
	39.72	18.25	0.169	0.236	41.26	0.260	99.9	80.1
	39.74	17.90	0.178	0.231	41.44	0.247	99.7	80.5

Note(s): [a]FeO reported as total iron; [b]Fo (forsterite) = [Mg/(Mg+Fe) x 100]; [c]Mauna Ulu; [d]1971A-2 from Garcia et al. (2003).

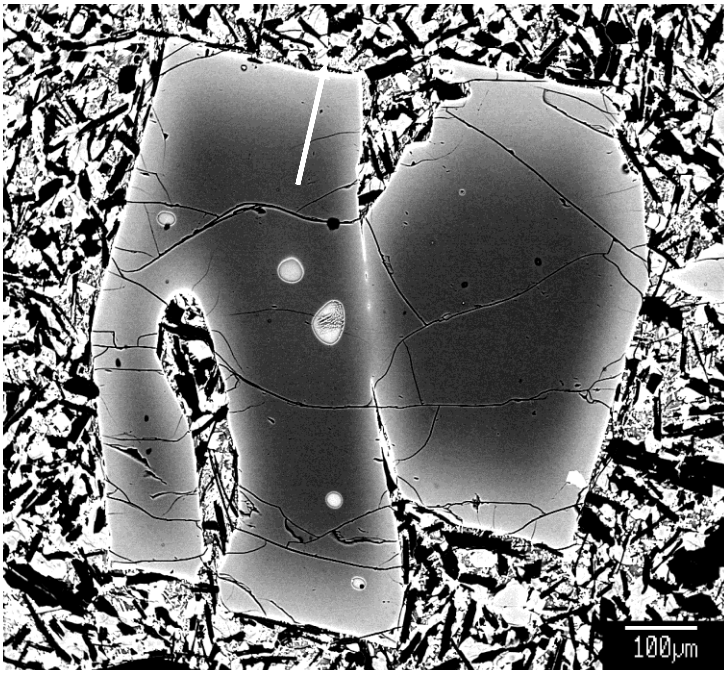

Figure A1. Backscatter electron image of zoned olivine crystal in 1670 Kīlauea lava flow. Core-to-rim traverse (arrow) presented in Table A4.

Table A4. Core (102 μm) to rim (0 μm) traverse through zoned olivine from 1670 lava flow (Figure A1).

SiO_2	MgO	FeO	MnO	NiO	CaO	Total	Distance (μm)	Fo (%)	Xpx
40.70	45.79	12.80	0.160	0.358	0.182	100.0	102	86.4	0.586
40.58	45.85	12.72	0.158	0.364	0.188	99.9	100	86.5	0.529
40.60	45.83	12.70	0.158	0.343	0.187	99.8	98	86.5	0.502
40.67	45.84	12.72	0.149	0.345	0.185	99.9	96	86.5	0.526
40.68	45.75	12.61	0.153	0.362	0.187	99.7	94	86.6	0.520
40.56	45.99	12.74	0.156	0.342	0.192	100.0	92	86.5	0.468
40.81	45.91	12.71	0.160	0.355	0.189	100.1	90	86.5	0.509
40.71	45.82	12.77	0.148	0.354	0.186	100.0	88	86.5	0.544
40.57	45.89	12.72	0.151	0.349	0.184	99.9	86	86.5	0.543
40.64	45.84	12.85	0.150	0.356	0.185	100.0	84	86.4	0.565
40.64	45.84	12.82	0.152	0.357	0.183	100.0	82	86.4	0.576
40.64	45.81	12.70	0.155	0.353	0.184	99.8	80	86.5	0.544
40.59	45.70	12.88	0.155	0.351	0.188	99.9	78	86.3	0.537
40.59	45.85	12.92	0.158	0.347	0.184	100.1	76	86.3	0.568
40.51	45.78	13.01	0.150	0.357	0.187	100.0	74	86.2	0.574
40.66	45.73	12.94	0.158	0.352	0.191	100.0	72	86.3	0.528
40.60	45.67	13.14	0.158	0.346	0.186	100.1	70	86.1	0.590
40.58	45.66	13.16	0.166	0.336	0.183	100.1	68	86.1	0.602
40.41	45.52	13.23	0.156	0.364	0.188	99.9	66	86.0	0.618
40.60	45.44	13.27	0.148	0.353	0.189	100.0	64	85.9	0.595
40.42	45.39	13.44	0.171	0.346	0.190	100.0	62	85.8	0.604
40.52	45.23	13.56	0.158	0.345	0.190	100.0	60	85.6	0.623
40.66	45.39	13.73	0.166	0.345	0.191	100.5	58	85.5	0.639
40.22	44.96	13.72	0.161	0.355	0.185	99.6	56	85.4	0.702
40.41	44.80	13.91	0.179	0.352	0.184	99.8	54	85.2	0.736
40.20	44.76	14.09	0.169	0.356	0.190	99.8	52	85.0	0.720
40.22	44.75	14.39	0.168	0.345	0.191	100.1	50	84.7	0.739
40.21	44.53	14.51	0.177	0.328	0.187	99.9	48	84.5	0.759
40.16	44.34	14.61	0.172	0.341	0.188	99.8	46	84.4	0.791
40.13	44.03	14.78	0.166	0.340	0.191	99.6	44	84.2	0.795
40.22	43.86	15.05	0.189	0.336	0.189	99.8	42	83.9	0.836
39.94	43.73	15.29	0.180	0.336	0.189	99.7	40	83.6	0.865
39.97	43.61	15.55	0.182	0.330	0.196	99.8	38	83.3	0.845
39.88	43.55	15.77	0.183	0.336	0.193	99.9	36	83.1	0.900
40.01	43.21	16.10	0.193	0.323	0.189	100.0	34	82.7	0.950
39.73	42.79	16.24	0.189	0.319	0.207	99.5	32	82.4	0.850
39.83	42.81	16.56	0.200	0.318	0.188	99.9	30	82.2	0.998
39.87	42.64	16.88	0.199	0.305	0.198	100.1	28	81.8	0.950
39.76	42.45	17.16	0.200	0.290	0.200	100.1	26	81.5	0.939
39.63	42.26	17.37	0.215	0.289	0.211	100.0	24	81.3	0.896
39.79	42.03	17.44	0.205	0.278	0.210	100.0	22	81.1	0.888
39.72	41.77	17.67	0.208	0.252	0.217	99.8	20	80.8	0.819
39.60	41.61	17.81	0.200	0.254	0.225	99.7	18	80.6	0.791
39.55	41.71	17.99	0.213	0.252	0.229	99.9	16	80.5	0.782
39.53	41.52	18.20	0.223	0.245	0.230	99.9	14	80.3	0.784
39.55	41.40	18.48	0.215	0.241	0.234	100.1	12	80.0	0.781
39.56	41.36	18.52	0.232	0.235	0.237	100.1	10	79.9	0.760
39.46	41.14	18.68	0.226	0.232	0.240	100.0	8	79.7	0.758
39.55	41.08	18.87	0.226	0.225	0.247	100.2	6	79.5	0.718
39.46	40.69	19.05	0.231	0.228	0.253	99.9	4	79.2	0.714
39.16	40.38	19.44	0.225	0.224	0.257	99.7	2	78.7	0.731
39.04	39.93	19.99	0.236	0.203	0.270	99.7	0	78.1	0.664

Table A5. Microprobe analyses of Kīlauea and Ko‘olau dike glasses with calculations of the effect of silica activity (aSiO2) on nickel diffusivity in olivine.

	Kīlauea Lavas				**Ko‘olau Dikes**								
Oxides (wt%)	**24-Jul-83**	**16-Aug-83**	**28-Oct-89**	**9-Oct-94**	**D-1**	**D-2**	**D-4**	**D-5**	**D-6**	**D-15**	**D-16**	**D-25**	**D-26**
SiO_2	51.02	51.06	51.32	51.81	53.05	53.10	55.05	54.85	53.50	52.90	52.85	52.70	53.75
TiO_2	3.04	3.09	2.54	2.76	2.14	2.12	1.73	1.72	2.00	2.00	1.85	2.26	2.11
Al_2O_3	13.57	13.37	13.74	13.53	14.25	14.34	14.95	14.83	14.52	14.00	13.73	14.13	13.93
FeO	11.78	11.68	10.93	11.50	10.10	10.05	8.80	8.65	9.70	9.95	10.35	10.70	10.35
MnO	0.17	0.17	0.16	0.16	0.17	0.18	0.16	0.14	0.18	0.15	0.16	0.17	0.15
MgO	6.39	6.05	6.92	6.36	6.61	6.59	6.54	6.49	6.78	7.35	7.75	6.25	6.08
CaO	10.33	10.31	11.19	11.01	9.68	9.71	9.40	9.20	9.55	9.65	9.66	10.20	9.64
Na_2O	2.42	2.40	2.25	2.29	2.74	2.72	2.96	2.92	2.72	2.56	2.44	2.55	2.81
K_2O	0.59	0.59	0.44	0.48	0.61	0.58	0.44	0.42	0.40	0.47	0.47	0.48	0.43
P_2O_5	0.29	0.30	0.23	0.25	0.23	0.23	0.17	0.15	0.18	0.22	0.18	0.22	0.20
Total	99.6	99.0	99.7	100.2	99.6	99.6	100.2	99.4	99.5	99.3	99.4	99.7	99.5
T(K)	1442	1447	1434	1436	1443	1442	1449	1451	1450	1450	1450	1445	1441
T(C)	1168	1174	1160	1162	1170	1168	1175	1178	1177	1177	1177	1172	1167
MELTS mol fractions*													
SiO_2	0.449	0.456	0.442	0.452	0.484	0.483	0.510	0.514	0.491	0.481	0.476	0.476	0.496
TiO_2	0.037	0.038	0.031	0.034	0.026	0.025	0.020	0.020	0.024	0.024	0.022	0.027	0.025
Al_2O_3	0.125	0.123	0.128	0.124	0.127	0.128	0.131	0.131	0.131	0.127	0.125	0.128	0.125
Fe_2SiO_4	0.081	0.080	0.075	0.078	0.067	0.067	0.057	0.056	0.064	0.067	0.070	0.071	0.068
$MnSi_{0.5}O_2$	0.002	0.002	0.002	0.002	0.002	0.002	0.002	0.002	0.002	0.002	0.002	0.002	0.002
Mg_2SiO_4	0.078	0.074	0.084	0.077	0.078	0.078	0.075	0.075	0.080	0.088	0.093	0.074	0.071
$CaSiO_3$	0.175	0.175	0.191	0.186	0.160	0.161	0.152	0.149	0.158	0.161	0.163	0.170	0.159
Na_2SiO_3	0.038	0.038	0.036	0.036	0.042	0.042	0.441	0.044	0.416	0.397	0.038	0.039	0.043
$KAlSiO_4$	0.012	0.012	0.009	0.010	0.012	0.012	0.009	0.008	0.008	0.010	0.010	0.010	0.009
$Ca_3(PO_4)_2$	0.002	0.002	0.002	0.002	0.002	0.002	0.001	0.001	0.001	0.001	0.001	0.001	0.001
$aSiO_2$	0.519	0.490	0.442	0.490	0.493	0.493	0.582	0.511	0.536	0.498	0.499	0.495	0.508
log D_{Ni}	-30.68	-30.60	-30.85	-30.80	-30.67	-30.69	-30.53	-30.52	-30.53	-30.55	-30.55	-30.63	-30.70
D_{Ni}	3.424	3.421	3.429	3.427	3.423	3.424	3.419	3.418	3.419	3.419	3.419	3.422	3.424

Note(s): *mol fractions calculated using MELTS supplemental calculator (http://melts.ofm-research.org/CalcForms/) for multicomponent silicate liquids) using T(C) for each sample, f_{O2} QFM-1 (Rhodes and Vollinger, 2005), and a pressure of 850 bars. Kīlauea glass compositions were collected in this study, Ko‘olau glasses from M.O. Garcia (unpublished); for methods see Haskins and Garcia (2004).

A3. Discussion

A3.1. Comparison of Toplis (2005) $Kd_{Fe\text{-}Mg}^{ol/melt}$

Fractional crystallization models of olivine compositions were calculated along a liquid line of descent from each volcano's parental magma composition using the $D_{Ni}^{ol/melt}$ from Matzen et al. (2013), with $D_{Mg}^{ol/melt}$ calculated from Putirka (2008) and a constant $Kd_{Fe\text{-}Mg}^{ol/melt}$ of 0.32 (Putirka et al. 2011). This method was chosen because they recently reviewed the accuracy of previous partitioning approaches (e.g. Hart and Davis 1978, Kinzler et al. 1990, Beattie et al. 1991, Toplis 2005, Li and Ripley 2010, Putirka et al. 2011) when refining their partitioning expression. A comparison of crystallization models with $D_{Ni}^{ol/melt}$ from Matzen et al. (2013) and the melt concentration dependent $Kd_{Fe\text{-}Mg}^{ol/melt}$ of Toplis (2005) showed no difference in olivine compositions > Fo_{88} (Figure A2).

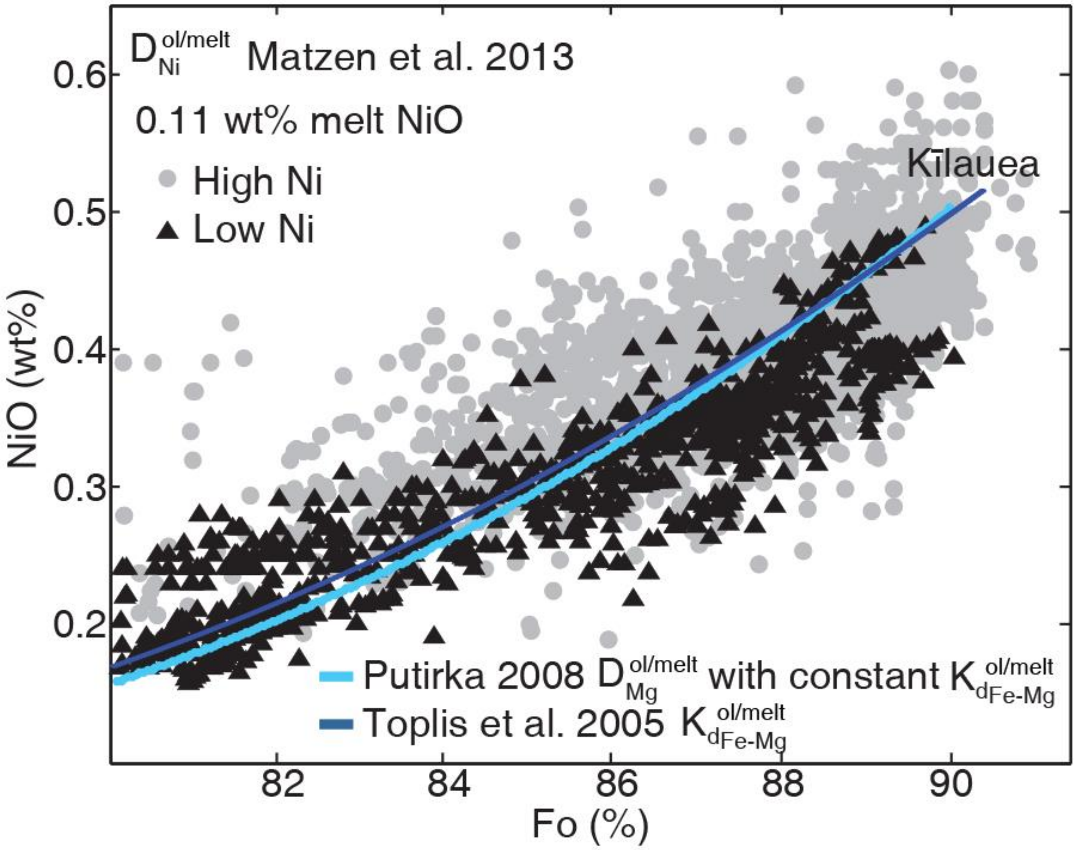

Figure A2. A comparison of fractional crystallization curves along a liquid line of descent for Kīlauea's parental melt composition with 0.11 wt% NiO. At compositions of > Fo_{88}, no differences in Fo-NiO are discernable.

A3.2. Effect of SiO_2 on Ni diffusivity in olivine

Diffusive re-equilibration of Ni in olivine has been shown to be slower in lower SiO_2 magmas (e.g. Kīlauea) compared to higher SiO_2 magmas (e.g. Koʻolau; Zhukova et al. 2014a). To determine whether inter-volcano variations in melt SiO_2 affect the rate of Ni diffusion (and thus different degrees of Fo-NiO decoupling) the activity of silica ($aSiO_2$) was determined in Koʻolau and Kīlauea glasses using a supplemental MELTS calculator (Ghiorso and Sack 1995) and used to calculate Ni diffusivities using the methods of Zhukova et al. (2014a). The 1-5 wt% difference in SiO_2 between the volcanoes has a negligible effect on Ni diffusivity (see Table A5 for glass analyses and diffusivity calculations). Inter-volcano melt SiO_2 variations are unlikely to influence Fo-NiO decoupling, which is therefore chiefly a signature of magma mixing in crustal environments.

A3.3. Numerical diffusion models

Results from sectioning the large and small 3D numerical diffusion models include examples of randomly sliced crystals arranged a numerical “thin section” (Figure A3). Core compositions from each set of slices (both small and large sized crystals) are presented in Table A6.

(a) Numerical “thin section” for large olivine

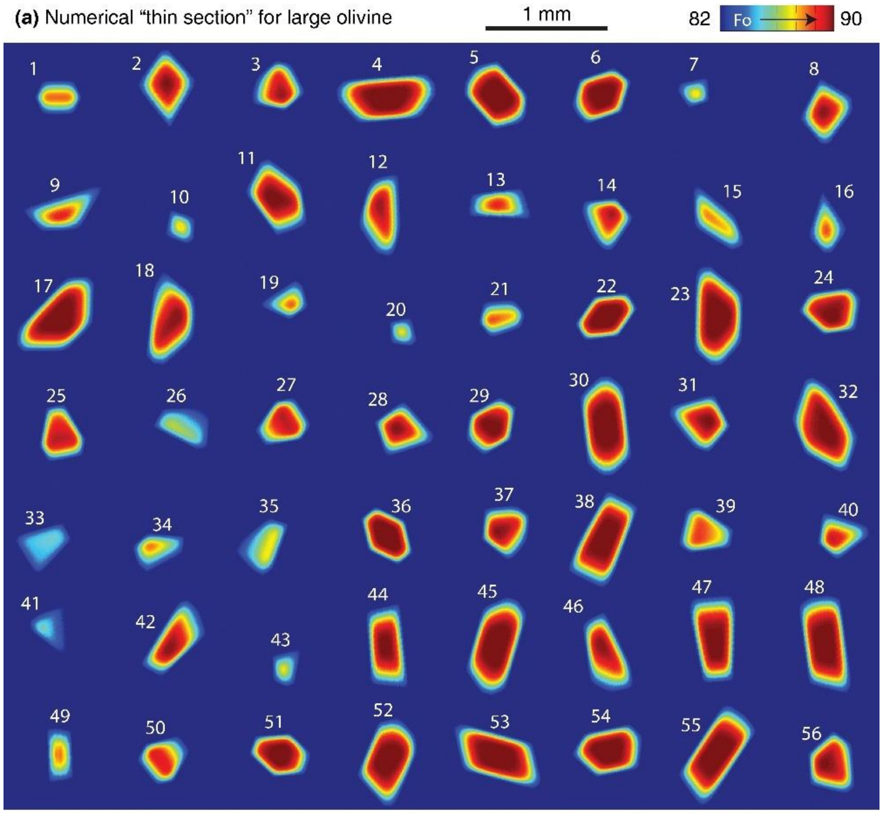

(b) Numerical “thin section” for small olivine

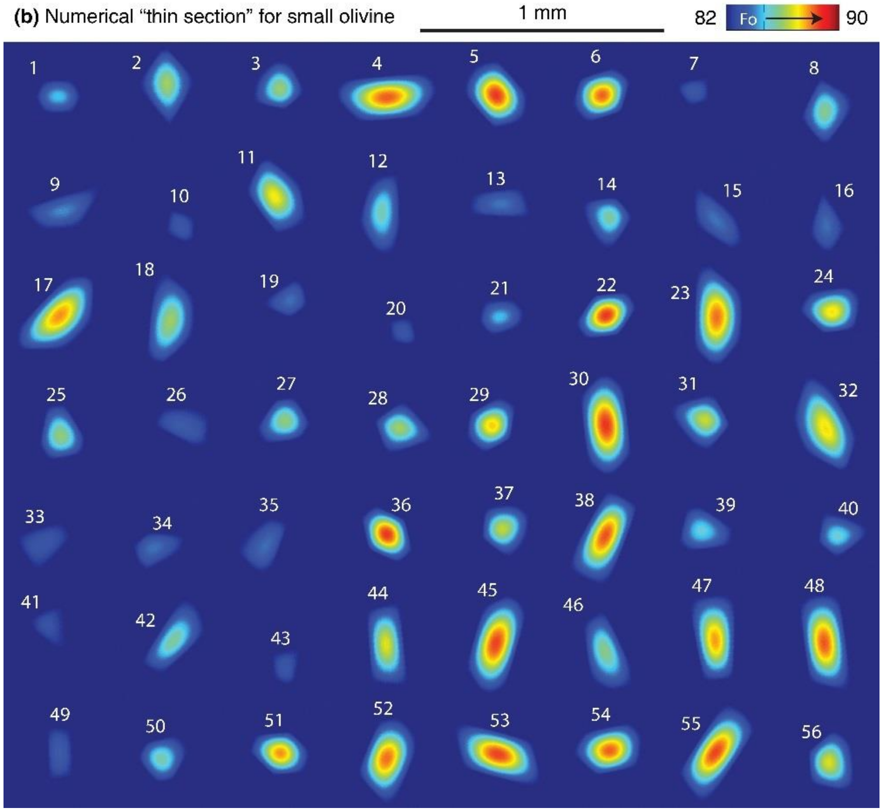

Figure A3. Numerical thin sections for 800 µm **(a)** and 400 µm **(b)** crystal sizes (see scale bars). Compositions and model parameters are the same in both, the crystal size is the only difference.

Table A6. Core compositions for the 56 sections in 800 and 400 µm numerical olivine diffusion models presented in Figure A3. **Additional data do not have section identifiers.**

	800 µm Crystal				**400 µm Crystal**			
Section[a]	**Fo[b]**	**NiO[c]**	**MnO[c]**	**Xpx (%)**	**Fo**	**NiO**	**MnO**	**Xpx (%)**
Initial	**90.0**	**0.600**	**0.130**	**77**	**90.0**	**0.600**	**0.130**	**77**
1	88.1	0.549	0.153	83	84.6	0.404	0.198	83
2	89.9	0.599	0.131	77	86.1	0.487	0.178	87
3	89.5	0.589	0.136	80	85.8	0.464	0.183	86
4	90.0	0.600	0.130	77	88.2	0.564	0.152	84
5	90.0	0.600	0.130	77	88.6	0.573	0.148	83
6	90.0	0.600	0.130	77	88.2	0.562	0.152	84
7	87.2	0.526	0.165	85	83.2	0.338	0.214	78
8	89.8	0.597	0.132	77	85.7	0.467	0.184	87
9	88.9	0.576	0.144	81	84.1	0.393	0.203	83
10	87.2	0.526	0.165	86	83.3	0.339	0.214	78
11	90.0	0.599	0.131	77	86.8	0.514	0.170	87
12	89.6	0.590	0.136	78	85.3	0.451	0.189	86
13	88.9	0.573	0.145	80	84.0	0.386	0.205	83
14	89.3	0.579	0.140	78	85.5	0.455	0.186	86
15	87.7	0.544	0.158	86	83.9	0.375	0.206	81
16	88.5	0.565	0.149	83	83.9	0.374	0.207	81
17	90.0	0.600	0.130	77	87.8	0.549	0.158	85
18	89.8	0.596	0.132	77	86.1	0.483	0.179	87
19	87.9	0.544	0.156	84	83.9	0.373	0.206	81
20	86.7	0.501	0.173	84	83.1	0.329	0.216	76
21	88.0	0.544	0.155	83	84.5	0.399	0.199	82
22	90.0	0.600	0.130	77	88.6	0.574	0.148	83
23	90.0	0.600	0.130	77	88.1	0.559	0.154	85
24	89.9	0.599	0.131	77	87.2	0.525	0.165	86
25	89.3	0.584	0.138	80	86.0	0.473	0.180	86
26	85.2	0.438	0.190	85	83.3	0.335	0.213	76
27	89.5	0.590	0.136	79	85.9	0.470	0.181	86
28	89.9	0.598	0.132	77	86.1	0.485	0.178	87
29	90.0	0.599	0.131	77	87.3	0.531	0.163	86
30	90.0	0.600	0.130	77	88.6	0.574	0.147	83
31	89.9	0.598	0.131	77	86.5	0.502	0.173	87
32	90.0	0.599	0.131	77	87.2	0.528	0.165	86
33	85.0	0.412	0.195	80	83.1	0.318	0.217	74
34	87.4	0.523	0.163	84	83.8	0.370	0.207	81
35	86.2	0.467	0.172	89	83.8	0.361	0.208	79
36	90.0	0.600	0.130	77	88.6	0.574	0.148	83
37	89.7	0.595	0.134	78	86.2	0.486	0.177	86
38	90.0	0.600	0.130	77	88.3	0.566	0.151	84
39	88.3	0.550	0.152	82	85.0	0.425	0.193	84
40	89.2	0.576	0.142	77	85.0	0.433	0.192	85
41	84.4	0.381	0.201	80	83.0	0.312	0.218	74

	800 µm Crystal				400 µm Crystal			
Section[a]	**Fo**	**NiO**	**MnO**	**Xpx (%)**	**Fo**	**NiO**	**MnO**	**Xpx (%)**
42	89.9	0.598	0.132	77	85.7	0.469	0.184	87
43	86.7	0.506	0.171	86	83.2	0.332	0.215	77
44	90.0	0.600	0.130	77	86.8	0.517	0.170	87
45	90.0	0.600	0.130	77	88.5	0.571	0.150	83
46	89.7	0.593	0.134	78	85.8	0.475	0.182	87
47	90.0	0.600	0.130	77	87.8	0.549	0.158	85
48	90.0	0.600	0.130	77	88.3	0.565	0.152	84
49	88.0	0.549	0.155	84	83.4	0.355	0.212	80
50	88.9	0.572	0.144	81	85.5	0.450	0.187	85
51	90.0	0.600	0.130	77	87.8	0.549	0.157	85
52	90.0	0.600	0.130	77	88.1	0.557	0.154	85
53	90.0	0.600	0.130	77	88.5	0.571	0.149	83
54	90.0	0.600	0.130	77	88.2	0.563	0.152	84
55	90.0	0.600	0.130	77	88.4	0.569	0.150	84
56	89.8	0.595	0.133	78	86.6	0.504	0.172	86
	87.3	0.523	0.160	88	83.0	0.323	0.217	76
	89.6	0.591	0.135	78	84.2	0.406	0.200	87
	90.0	0.600	0.130	77	82.2	0.270	0.227	69
	90.0	0.600	0.130	77	85.2	0.446	0.190	86
	86.2	0.477	0.178	85	88.5	0.571	0.149	83
	89.6	0.594	0.140	74	86.4	0.496	0.176	87
	89.7	0.591	0.134	77	88.5	0.570	0.149	84
	90.0	0.600	0.130	77	86.0	0.478	0.181	87
	90.0	0.600	0.130	77	88.5	0.570	0.149	84
	83.9	0.367	0.206	80	85.1	0.436	0.191	85
	90.0	0.600	0.130	77	88.6	0.573	0.148	83
	84.2	0.379	0.203	80	84.5	0.405	0.198	83
	86.0	0.472	0.176	89	87.4	0.534	0.163	86
	84.6	0.397	0.197	81	88.4	0.569	0.150	83
	89.9	0.599	0.132	76	85.5	0.458	0.186	86
	88.4	0.557	0.150	82	82.4	0.279	0.225	70
	90.0	0.600	0.130	77	86.0	0.484	0.180	87
	86.2	0.483	0.178	86	82.9	0.317	0.218	75
	83.7	0.361	0.208	80	84.2	0.401	0.202	84
	90.0	0.600	0.130	77	88.6	0.573	0.148	83
	90.0	0.600	0.130	77	88.5	0.572	0.149	83
	89.9	0.598	0.130	78	88.5	0.572	0.148	83
	89.9	0.599	0.131	77	86.8	0.513	0.170	87
	90.0	0.600	0.130	77	84.4	0.405	0.200	84
	90.0	0.600	0.130	77	82.8	0.311	0.220	74
	85.0	0.422	0.192	84	88.5	0.592	0.149	86
	88.5	0.563	0.149	82	84.2	0.385	0.203	82
	90.0	0.600	0.130	77	88.0	0.555	0.155	85
	83.1	0.324	0.216	76	84.2	0.390	0.203	83

	800 µm Crystal				400 µm Crystal			
Section[a]	**Fo**	**NiO**	**MnO**	**Xpx (%)**	**Fo**	**NiO**	**MnO**	**Xpx (%)**
	90.0	0.600	0.130	77	85.6	0.456	0.185	85
	90.0	0.600	0.130	77	88.4	0.566	0.150	84
	89.9	0.599	0.131	77	86.4	0.492	0.175	86
	89.8	0.597	0.133	77	86.8	0.509	0.171	86
	89.7	0.595	0.133	79	85.8	0.464	0.183	86
	87.5	0.522	0.164	80	87.6	0.541	0.160	86
	90.0	0.600	0.130	77	86.9	0.514	0.169	86
	89.9	0.599	0.131	77	85.0	0.432	0.193	85
	89.9	0.598	0.132	76	88.1	0.559	0.154	84
	90.0	0.600	0.130	77	85.3	0.450	0.189	86
	90.0	0.600	0.130	77	88.1	0.558	0.154	84
	87.9	0.540	0.156	84	82.3	0.273	0.226	69
	88.8	0.570	0.145	81	88.1	0.558	0.154	84
	87.7	0.533	0.159	83	83.2	0.325	0.215	75
	89.0	0.577	0.142	81	87.9	0.550	0.157	85
	90.0	0.600	0.130	77	82.7	0.300	0.222	73
	85.5	0.446	0.186	85	87.4	0.534	0.163	86
	84.5	0.390	0.199	80	86.4	0.496	0.175	87
	90.0	0.600	0.130	77	83.9	0.365	0.207	79
	90.0	0.600	0.130	77	86.5	0.495	0.174	86
	90.0	0.600	0.130	77	85.1	0.438	0.191	85
	89.5	0.589	0.137	78	88.1	0.558	0.154	84
	90.0	0.600	0.130	77	88.6	0.573	0.148	83
	90.0	0.600	0.130	77	87.7	0.545	0.159	86
	87.0	0.509	0.168	84	87.3	0.535	0.164	87
	89.9	0.599	0.131	77	85.5	0.451	0.186	85
	90.0	0.600	0.130	77	84.8	0.418	0.194	84
	90.0	0.600	0.130	77	85.0	0.431	0.193	85
	89.9	0.599	0.130	79	88.5	0.572	0.148	83
	90.0	0.600	0.130	77	84.4	0.408	0.200	84
	90.0	0.600	0.130	77	88.6	0.574	0.148	83
	90.0	0.600	0.130	77	83.1	0.327	0.216	76
	87.9	0.540	0.156	84	88.6	0.573	0.148	83
	90.0	0.600	0.130	77	82.2	0.262	0.228	67
	82.4	0.280	0.225	70	88.4	0.567	0.150	84
	87.2	0.523	0.165	86	86.1	0.481	0.178	86
	90.0	0.600	0.130	77	87.6	0.546	0.161	86
	89.8	0.597	0.132	78	83.1	0.321	0.211	78
	90.0	0.600	0.130	77	86.9	0.520	0.169	87
	84.2	0.387	0.202	82	88.4	0.570	0.150	83
	90.0	0.600	0.130	77	88.5	0.572	0.149	83
	87.4	0.521	0.162	84	83.7	0.355	0.209	79
	90.0	0.600	0.130	77	88.6	0.574	0.148	83
	90.0	0.600	0.130	77	88.3	0.564	0.151	84

	800 µm Crystal				400 µm Crystal			
Section[a]	**Fo**	**NiO**	**MnO**	**Xpx (%)**	**Fo**	**NiO**	**MnO**	**Xpx (%)**
	89.5	0.590	0.136	79	83.7	0.359	0.209	79
	90.0	0.600	0.130	77	85.5	0.451	0.187	85
	87.4	0.525	0.162	85	87.3	0.533	0.164	86
	87.4	0.527	0.163	84	85.9	0.470	0.182	86
	88.5	0.563	0.149	82	87.7	0.545	0.158	85
	90.0	0.600	0.130	77	85.6	0.463	0.185	87
	90.0	0.600	0.130	77	83.2	0.338	0.215	78
	87.6	0.529	0.150	92	84.3	0.390	0.201	82
	85.3	0.441	0.188	85	87.8	0.550	0.157	85
	85.4	0.443	0.188	84	87.5	0.541	0.161	86
	90.0	0.600	0.130	77	82.4	0.281	0.225	70
	90.0	0.600	0.130	77	88.6	0.573	0.148	83
	86.9	0.499	0.169	84	88.1	0.557	0.155	83
	90.0	0.600	0.130	77	87.5	0.538	0.161	85
	86.3	0.484	0.177	86	86.5	0.504	0.174	87
	90.0	0.600	0.130	77	86.7	0.508	0.172	87
	87.1	0.515	0.167	85	88.6	0.573	0.148	83
	90.0	0.600	0.130	77	83.9	0.371	0.206	80
	90.0	0.600	0.130	77	83.4	0.344	0.213	78
	86.2	0.473	0.177	85	87.6	0.542	0.160	85
	90.0	0.600	0.130	77	83.8	0.368	0.208	81
	90.0	0.600	0.130	77	88.4	0.568	0.150	84
	90.0	0.600	0.130	77	86.5	0.497	0.174	86
	89.6	0.593	0.135	78	88.6	0.574	0.148	83
	87.1	0.517	0.167	85	88.4	0.569	0.150	84
	90.0	0.600	0.130	77	88.4	0.566	0.151	84
	90.0	0.600	0.130	77	88.6	0.573	0.148	83
	90.0	0.599	0.131	77	82.3	0.267	0.227	67
	89.9	0.599	0.131	77	83.2	0.337	0.215	77
	90.0	0.600	0.130	77	88.0	0.555	0.155	85
	87.4	0.518	0.163	84	85.1	0.434	0.192	85
	88.4	0.556	0.151	82	87.3	0.533	0.164	86
	90.0	0.600	0.130	77	86.5	0.503	0.174	87
	90.0	0.600	0.130	77	88.1	0.559	0.153	84
	90.0	0.600	0.130	77	84.5	0.401	0.199	83
	90.0	0.600	0.130	77	85.1	0.437	0.190	86
	90.0	0.600	0.130	77	83.7	0.353	0.209	78
	90.0	0.600	0.130	77	88.6	0.573	0.148	83
	89.7	0.595	0.134	78	82.3	0.272	0.226	69
	89.9	0.598	0.132	77	87.3	0.531	0.164	86
	90.0	0.600	0.130	77	84.7	0.420	0.195	85
	86.7	0.494	0.171	84	83.6	0.365	0.210	81
	90.0	0.600	0.130	77	86.5	0.498	0.174	86
	88.7	0.569	0.146	81	88.4	0.568	0.150	84

	800 µm Crystal				400 µm Crystal			
Section[a]	**Fo**	**NiO**	**MnO**	**Xpx (%)**	**Fo**	**NiO**	**MnO**	**Xpx (%)**
	84.8	0.419	0.196	84	86.0	0.481	0.180	87
	86.9	0.513	0.169	86	88.1	0.560	0.154	84
	89.9	0.598	0.132	77	83.4	0.345	0.212	78
	89.9	0.598	0.132	77	85.3	0.457	0.189	87
	90.0	0.600	0.130	77	88.1	0.560	0.154	85
	85.9	0.465	0.182	85	84.2	0.381	0.203	81
	86.2	0.480	0.177	85	84.0	0.374	0.205	81
	83.7	0.356	0.209	79	85.4	0.453	0.187	87
	90.0	0.600	0.130	77	88.5	0.570	0.149	83
	89.8	0.596	0.133	78	82.6	0.290	0.223	71
	90.0	0.600	0.130	77	82.6	0.293	0.223	72
	89.9	0.599	0.131	77	87.4	0.537	0.162	86
	85.5	0.449	0.186	85	88.4	0.569	0.150	84
	89.3	0.584	0.139	80	82.9	0.311	0.219	74
	90.0	0.600	0.131	77	82.6	0.291	0.223	71
	89.8	0.597	0.132	77	84.0	0.375	0.205	81
	89.1	0.579	0.141	80	85.7	0.465	0.184	87
	88.7	0.566	0.147	82	88.6	0.573	0.148	83
	84.2	0.387	0.202	81	86.9	0.515	0.168	86
	89.2	0.583	0.140	80	86.3	0.487	0.177	86
	89.9	0.598	0.132	77	88.5	0.572	0.148	83
	90.0	0.600	0.130	77	82.8	0.303	0.220	73
	87.7	0.541	0.159	84	83.0	0.322	0.217	76
	88.8	0.570	0.145	81	83.2	0.333	0.215	77
	85.1	0.430	0.191	84	88.3	0.563	0.152	84
	90.0	0.600	0.131	77	87.1	0.526	0.166	87
	90.0	0.600	0.130	77	83.8	0.365	0.208	80
	90.0	0.600	0.130	77	82.7	0.295	0.228	68
	90.0	0.600	0.130	77	83.7	0.359	0.209	79
	86.5	0.491	0.173	85	88.2	0.561	0.153	84
	88.1	0.546	0.154	83	84.6	0.403	0.198	83
	89.0	0.575	0.143	81	83.7	0.364	0.209	80
	89.7	0.595	0.133	78	85.4	0.458	0.188	87
	90.0	0.600	0.130	77	84.3	0.407	0.201	85
	88.7	0.570	0.147	82	84.1	0.382	0.204	82
	90.0	0.600	0.130	77	85.4	0.449	0.190	84
	90.0	0.600	0.130	77	88.3	0.564	0.152	84
	90.0	0.600	0.130	77	83.3	0.341	0.214	78
	88.8	0.571	0.145	81	82.4	0.282	0.225	70
	90.0	0.599	0.131	77	85.7	0.463	0.184	86
	90.0	0.600	0.130	77	86.6	0.509	0.173	88
	85.9	0.470	0.181	86	87.0	0.517	0.168	86
	90.0	0.600	0.130	77	82.4	0.279	0.224	70
	87.5	0.528	0.161	84	83.9	0.373	0.206	81

	800 µm Crystal				**400 µm Crystal**			
Section[a]	**Fo**	**NiO**	**MnO**	**Xpx (%)**	**Fo**	**NiO**	**MnO**	**Xpx (%)**
	90.0	0.600	0.130	77	87.1	0.523	0.166	86
	86.0	0.460	0.184	81	83.7	0.359	0.209	79
	89.5	0.589	0.137	79	85.3	0.452	0.189	87
	90.0	0.600	0.130	77	85.7	0.463	0.185	85
	90.0	0.600	0.130	77	86.4	0.498	0.175	87
	90.0	0.600	0.130	77	87.7	0.546	0.158	85
	89.0	0.597	0.142	83	86.0	0.474	0.181	86
	84.7	0.400	0.196	81	84.7	0.413	0.196	83
	89.9	0.598	0.131	77	83.8	0.365	0.208	80
	90.0	0.600	0.130	77	88.0	0.555	0.156	85
	90.0	0.600	0.130	77	86.1	0.489	0.178	87
	88.4	0.562	0.150	83	88.4	0.566	0.151	84
	88.4	0.558	0.150	82	88.4	0.567	0.150	84
	89.0	0.577	0.142	80	84.1	0.386	0.204	81
	89.6	0.593	0.135	78	88.5	0.572	0.148	83
	90.0	0.600	0.130	77	85.5	0.456	0.186	86
	90.0	0.600	0.130	77	88.4	0.569	0.150	84
	85.0	0.413	0.193	82	84.9	0.419	0.194	84
	90.0	0.600	0.130	77	88.3	0.566	0.151	84
	90.0	0.600	0.130	77	84.5	0.416	0.198	85
	89.1	0.581	0.141	80	88.3	0.564	0.152	84
	90.0	0.600	0.131	77	86.4	0.496	0.175	87
	90.0	0.600	0.130	77	86.1	0.488	0.178	87
	88.2	0.559	0.153	84	83.7	0.357	0.209	79
	86.2	0.475	0.177	85	84.8	0.426	0.195	85
	89.8	0.598	0.132	77	86.3	0.492	0.177	87
	84.8	0.409	0.195	82	87.8	0.547	0.158	85
	89.3	0.586	0.138	80	85.8	0.470	0.182	87
	86.8	0.509	0.170	86	82.7	0.306	0.221	74
	90.0	0.600	0.130	77	83.5	0.358	0.211	80
	90.0	0.600	0.130	77	85.3	0.440	0.189	85
	88.5	0.560	0.149	82	88.6	0.573	0.148	83
	90.0	0.600	0.130	77	88.5	0.572	0.148	83
Ave.	**88.7**	**0.559**	**0.146**	**79**	**85.9**	**0.464**	**0.181**	**83**
Min.	**82.4**	**0.280**	**0.130**	**70**	**82.2**	**0.262**	**0.148**	**67**
Max.	**90.0**	**0.600**	**0.225**	**93**	**88.6**	**0.592**	**0.228**	**88**

Note(s): [a] Section numbers are assigned on Figure A3 for the first 56 compositions. [b]Fo is reported as %. [c]NiO and MnO are reported as wt%

APPENDIX B

Supporting Information for

TIMESCALES OF MIXING AND STORAGE FOR KEANAKĀKOʻI TEPHRA MAGMAS (1500-1823 C.E.), KĪLAUEA VOLCANO, HAWAIʻI

B1. Introduction

This supporting file contains all content that appears as Supplementary Material published with Chapter 3: Lynn et al. (in review). All data that appear in the publication's electronic resource are provided below, including olivine core compositions (Table B1), electron microprobe glass methods and analyses (Table B2), and lab procedure for removing adhering glass to document euhedral olivine morphology (Figures B1-B3).

B2. Methods and Results

B2.1. Olivine compositions

All Keanakākoʻi Tephra olivine core compositions are reported in Table B1.

B2.2. Adhering Glass

Major elements were measured on microlite-free glass adhering to olivine from the Basal Reticulite, Unit 7, Unit 11, Unit 20, Golden Pumice, and Eastern Pumice (n=58; Table B2). The adhering groundmass in Layer 6 and Circumferential Lava Flow materials is microlite rich (with plagioclase, clinopyroxene, and oxides), so glass compositions from Mucek (2012) were used for these eruptions. Measurements were made using a five-spectrometer JEOL Hyperprobe JXA-8500F at the University of Hawaiʻi (UH) using a 15 kV accelerating voltage, 10 µm beam, and a 10 nA current. Glass analyses were generally performed > 20 µm away from crystal-glass boundaries to avoid potential boundary layer effects (Shea et al. 2015b). Peak counting times were 60 s for Mg, 50 s for Si, Ti, Fe, and K, 40 s for Al, Mn, and Ca, 35 s for P, and 30 s for Na. Backgrounds for all analyses were measured on both sides of the peak for half of the peak counting times. Na was measured in the first round of elements to minimize loss. X-ray intensities were converted to concentrations using standard ZAF corrections (Armstrong 1988). Standards were Juan de Fuca Ridge Basalt Glass (USNM 111240/52 VG-2; Jarosewich et al. 1980) for Al, Mg, and Ca, Makaopuhi Lava Lake Basalt Glass (USNM 113498/1 A99; Jarosewich et al. 1980) for Si, Ti, and Fe, Verma Garnet for Mn, Fluor-Apatite (USNM 104021; Jarosewich et al. 1980) for P, Amelia Albite for Na, and Adularia Orthoclase (Or-1; Goldich 1967) for K. Reported glass data are averages of 3-5 analyses. Two sigma relative precision, based on repeated analyses of Makaopuhi Lava Lake Basalt Glass, are 0.47 wt% for SiO_2, 0.13 wt% for Al_2O_3, 0.14 wt% for FeO, 0.3 wt% for MgO, 0.29 wt% for TiO_2, 0.01 wt% for MnO, 0.06 wt% for Na_2O, and 0.02 wt% for K_2O and P_2O_5. Analyses with totals < 99.0 wt% or >100.5 wt% were rejected.

B2.3. HF Lab Procedure

Crystals were immersed in a 1 normal HF solution heated on a hotplate at 75 degrees C for 20 minutes. The HF solution was pipetted off and crystals were rinsed three times with quartz distilled water. The sample was then sonicated for several minutes to break down any insoluble fluorides remaining on crystal faces. Crystals were mounted on carbon tape and coated with a 20 nm thick layer of evaporated amorphous C for electron conduction. Secondary electron imaging was completed with the University of Hawai‘i JEOL JXA-8500F microprobe using a 15 kV and 5 nA beam (Figures B1-B3).

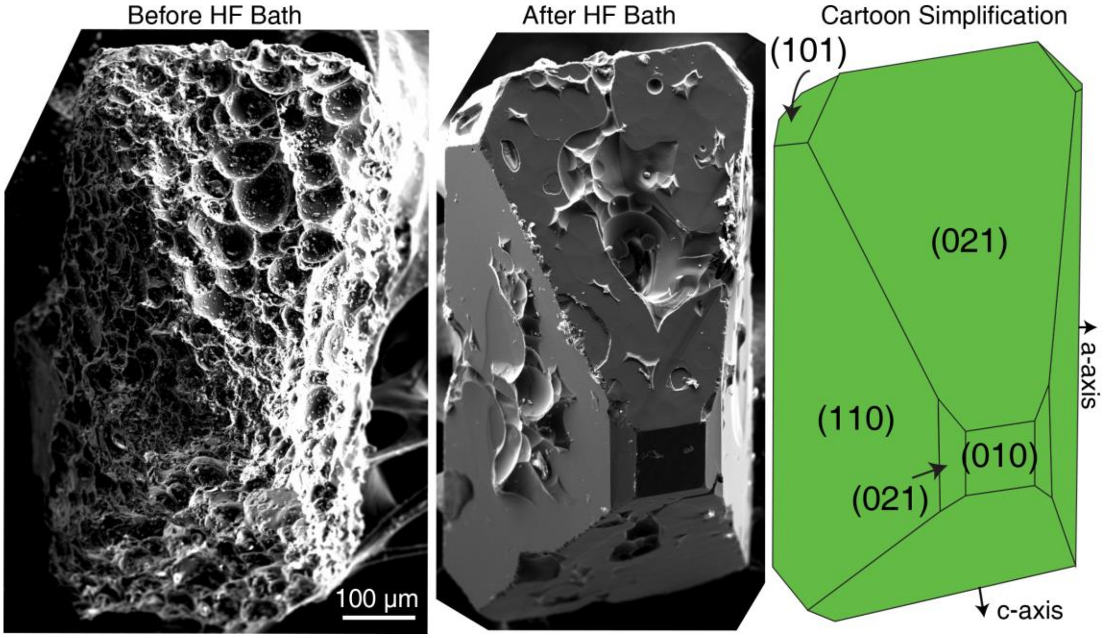

Figure B1. Secondary electron image of the most common morphology found in the Keanakākoʻi Tephra. Note the slight elongation along the *c*-axis but otherwise relatively equant and euhedral morphology.

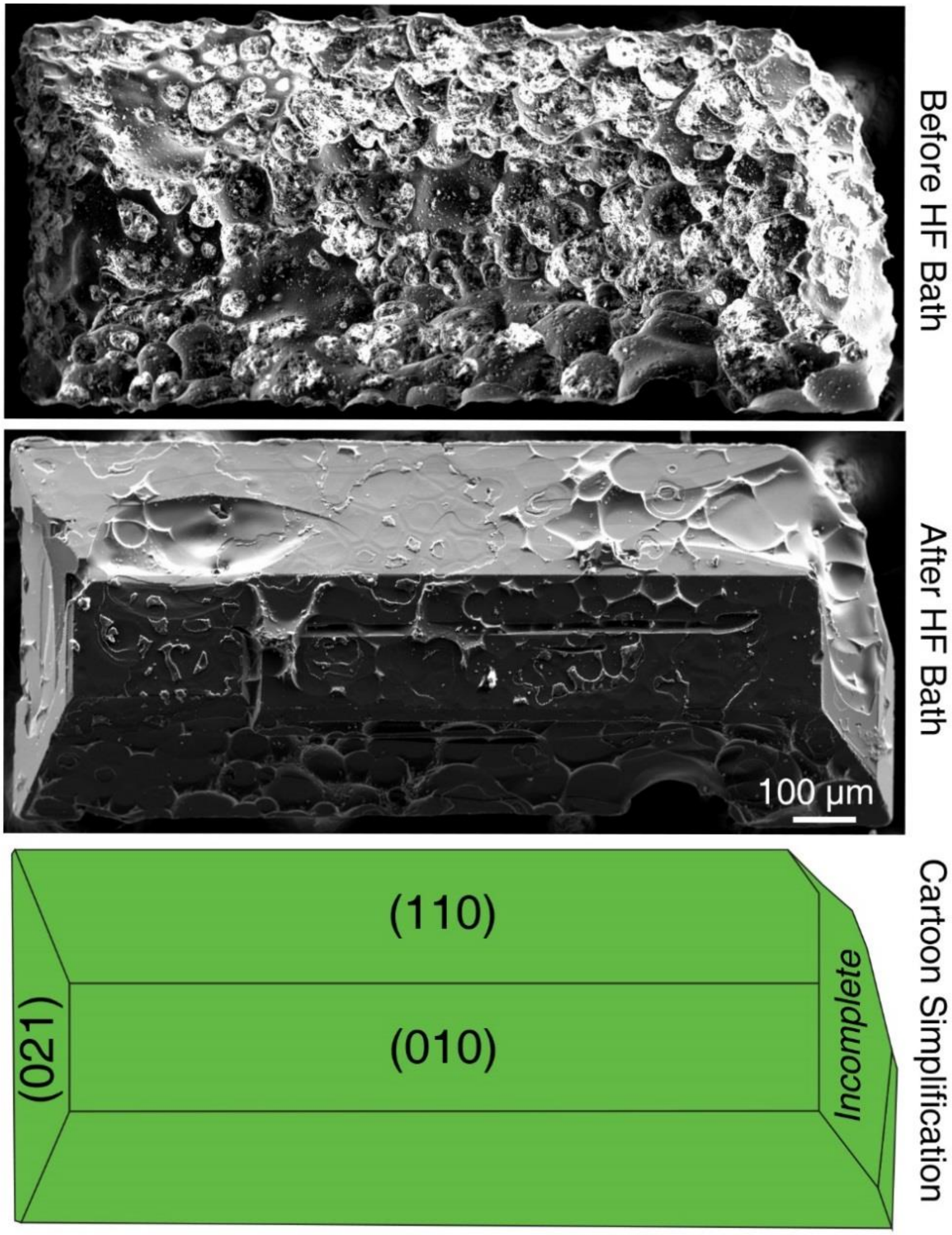

Figure B2. Secondary ion images of a euhedral olivine elongated along the *a*-axis before and after HF acid bath. Despite the natural coating of vesicular glass, crystal faces are still apparent on the crystal (e.g. (021) and (010)). After HF dissolution of the glass, incompletely formed faces are apparent.

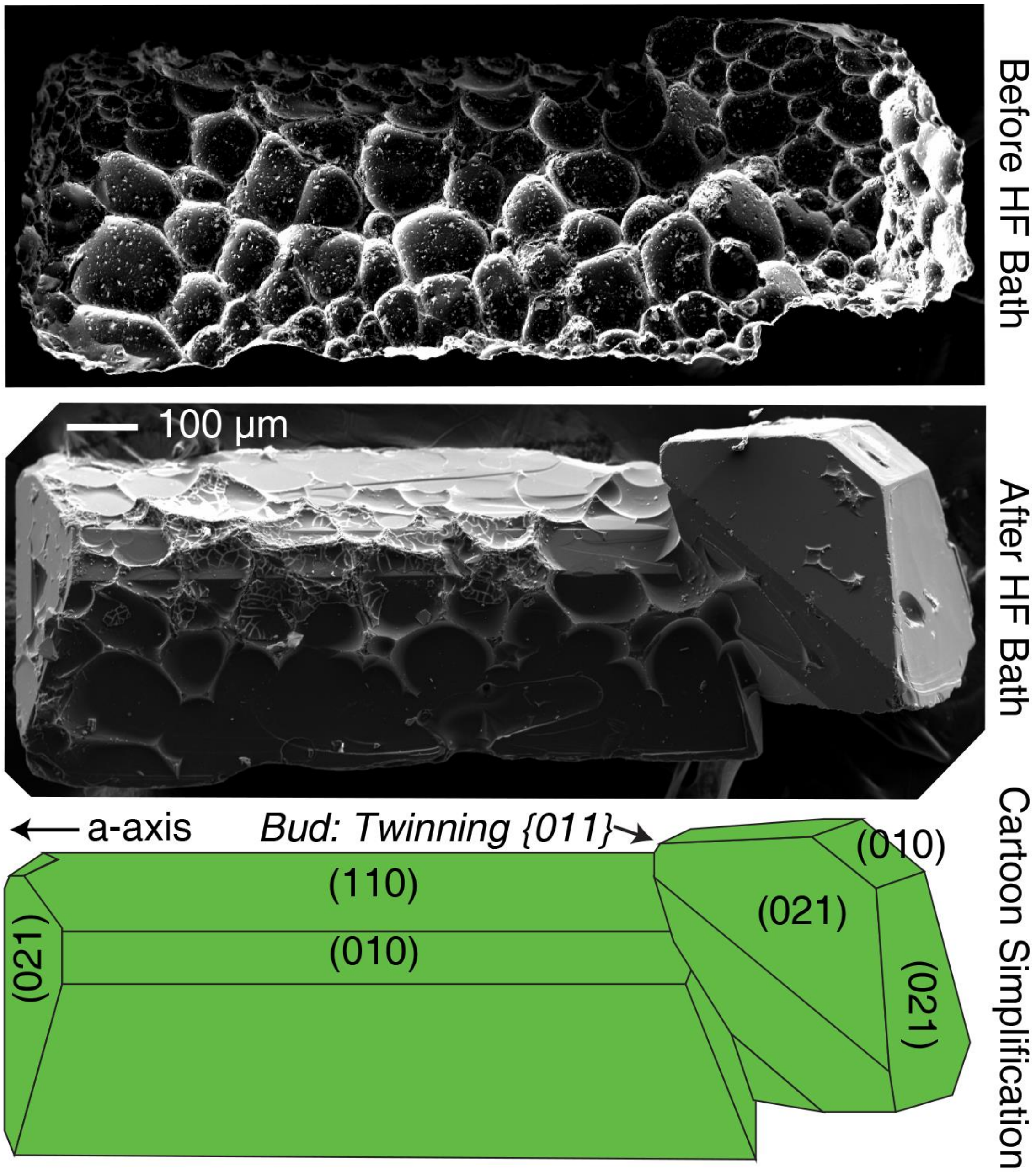

Figure B3. Secondary electron images of euhedral olivine before and after HF acid bath. In this example, a bud formed as a {011} twin on a crystal that is elongated along the *a*-axis.

Table B1. Olivine core compositions for the Keanakākoʻi Tephra.

Sample	SiO$_2$	FeO	MgO	NiO	CaO	Total	Fo*
Basal Reticulite	39.93	10.82	48.14	0.48	0.20	99.6	88.8
	39.56	10.79	48.68	0.51	0.19	99.7	88.9
	39.72	10.68	48.35	0.46	0.21	99.4	89.0
	39.00	16.49	43.98	0.34	0.23	100.0	82.6
	39.75	10.68	48.60	0.47	0.20	99.7	89.0
	38.59	16.41	43.76	0.32	0.25	99.3	82.6
	38.23	17.56	43.01	0.34	0.23	99.4	81.4
	39.66	10.61	48.83	0.47	0.20	99.8	89.1
	39.54	10.51	48.47	0.47	0.20	99.2	89.2
	39.85	10.54	48.52	0.47	0.20	99.6	89.2
	39.37	12.15	47.32	0.43	0.21	99.5	87.4
	39.54	10.97	48.02	0.46	0.21	99.2	88.6
	39.36	12.20	46.96	0.41	0.21	99.1	87.3
	39.65	10.95	47.92	0.45	0.20	99.2	88.7
	39.86	10.62	49.15	0.46	0.20	100.3	89.2
	39.73	10.45	48.61	0.47	0.20	99.5	89.2
	39.71	10.80	48.14	0.46	0.20	99.3	88.8
	39.95	10.48	48.82	0.47	0.20	99.9	89.3
	39.79	10.78	48.26	0.46	0.20	99.5	88.9
	39.86	10.72	48.34	0.47	0.19	99.6	88.9
	39.72	10.24	48.86	0.47	0.19	99.5	89.5
	39.92	10.49	47.98	0.47	0.21	99.1	89.1
	38.06	19.76	41.05	0.29	0.17	99.3	78.8
	39.38	13.17	45.93	0.36	0.21	99.0	86.2
	39.79	10.62	48.64	0.46	0.20	99.7	89.1
	39.84	13.35	45.81	0.37	0.23	99.6	85.9
	39.92	13.01	46.62	0.39	0.20	100.1	86.5
	39.20	15.73	44.12	0.25	0.23	99.5	83.3
	39.59	13.63	45.65	0.34	0.21	99.4	85.7
	39.92	12.10	47.15	0.41	0.20	99.8	87.4
	39.86	11.76	47.56	0.41	0.19	99.8	87.8
	39.69	13.99	45.54	0.29	0.26	99.8	85.3
	39.57	12.94	46.41	0.39	0.22	99.5	86.5
	39.00	16.33	43.58	0.23	0.23	99.4	82.6
	39.70	12.49	46.56	0.41	0.32	99.5	86.9
	39.94	12.88	46.70	0.36	0.27	100.1	86.6
	39.43	13.28	46.02	0.30	0.20	99.2	86.1
	39.23	15.62	44.23	0.29	0.24	99.6	83.5
	39.23	16.25	44.01	0.24	0.22	99.9	82.8
	38.91	16.35	43.48	0.23	0.23	99.2	82.6
	39.79	12.20	46.98	0.40	0.22	99.6	87.3
	39.43	14.32	45.38	0.33	0.22	99.7	85.0
	39.07	15.04	44.46	0.34	0.23	99.1	84.0
	39.23	16.01	43.84	0.24	0.24	99.5	83.0
	39.35	15.85	44.25	0.28	0.24	100.0	83.3
	39.09	16.52	43.62	0.22	0.24	99.7	82.5
	39.22	15.80	44.06	0.24	0.23	99.5	83.3
	38.49	19.39	41.11	0.30	0.20	99.5	79.1
	39.22	16.05	43.86	0.25	0.22	99.6	83.0
	39.52	14.18	45.55	0.37	0.20	99.8	85.1
	39.62	13.05	46.19	0.37	0.20	99.4	86.3
	39.76	13.23	46.13	0.36	0.20	99.7	86.1
	39.42	14.80	45.06	0.39	0.25	99.9	84.4
	39.84	11.63	47.37	0.43	0.19	99.5	87.9

Sample	SiO_2	FeO	MgO	NiO	CaO	Total	Fo*
unit 7	40.26	10.79	48.74	0.46	0.20	100.5	89.0
	39.92	12.76	46.85	0.37	0.20	100.1	86.7
	38.91	17.13	42.83	0.29	0.19	99.4	81.7
	40.03	10.69	48.49	0.46	0.19	99.8	89.0
	39.23	14.77	44.93	0.34	0.22	99.5	84.4
	39.82	10.27	48.44	0.47	0.19	99.2	89.4
	39.94	10.95	47.87	0.45	0.20	99.4	88.6
	39.60	14.95	45.04	0.32	0.21	100.1	84.3
	40.04	12.10	47.35	0.37	0.20	100.1	87.5
	39.94	10.91	47.98	0.41	0.19	99.4	88.7
	39.87	11.23	48.01	0.42	0.19	99.7	88.4
	40.04	10.42	48.53	0.45	0.20	99.6	89.2
	39.52	13.18	46.17	0.35	0.22	99.4	86.2
	39.61	13.22	46.22	0.33	0.20	99.6	86.2
	39.46	14.03	45.70	0.34	0.20	99.7	85.3
	39.43	15.19	44.76	0.22	0.22	99.8	84.0
	40.49	10.88	48.22	0.36	0.19	100.1	88.8
	40.27	10.75	48.19	0.42	0.19	99.8	88.9
	40.09	11.30	47.80	0.35	0.20	99.7	88.3
	40.31	10.19	48.91	0.44	0.19	100.0	89.5
	40.18	10.63	48.32	0.43	0.19	99.8	89.0
	40.37	10.29	48.90	0.43	0.19	100.2	89.4
	40.19	11.32	47.66	0.39	0.19	99.8	88.2
	38.85	14.13	46.07	0.35	0.22	99.6	85.3
	38.37	16.75	43.93	0.31	0.18	99.5	82.4
	39.30	11.24	48.23	0.48	0.20	99.4	88.4
	39.23	11.80	47.84	0.46	0.19	99.5	87.8
	38.53	16.54	44.07	0.21	0.22	99.6	82.6
	39.42	12.16	47.77	0.40	0.20	99.9	87.5
	39.61	11.75	48.22	0.43	0.20	100.2	88.0
	39.01	13.85	46.47	0.32	0.21	99.9	85.7
	39.55	10.53	48.97	0.49	0.19	99.7	89.2
	38.45	17.07	43.79	0.20	0.22	99.7	82.1
	39.74	10.57	49.18	0.48	0.19	100.2	89.2
	39.74	10.68	49.11	0.48	0.19	100.2	89.1
	39.63	10.92	49.04	0.47	0.19	100.3	88.9
	39.25	12.58	47.37	0.34	0.20	99.7	87.0
	38.83	14.99	45.73	0.34	0.22	100.1	84.5
	39.12	12.67	46.96	0.43	0.21	99.4	86.9
	38.89	15.65	44.96	0.30	0.21	100.0	83.7
	39.64	11.00	48.48	0.47	0.19	99.8	88.7
unit 11	40.32	10.93	48.23	0.48	0.20	100.2	88.7
	40.48	10.50	48.82	0.48	0.20	100.5	89.2
	40.47	10.48	48.94	0.46	0.19	100.5	89.3
	40.12	11.19	48.04	0.46	0.19	100.0	88.4
	40.32	11.18	48.36	0.45	0.21	100.5	88.5
	40.19	10.59	48.58	0.46	0.19	100.0	89.1
	40.16	10.52	49.15	0.48	0.18	100.5	89.3
	40.07	10.59	48.59	0.47	0.19	99.9	89.1
	40.38	10.57	48.87	0.46	0.20	100.5	89.2
	39.74	10.57	48.30	0.46	0.20	99.3	89.1
	39.91	10.63	48.64	0.47	0.20	99.8	89.1
	39.82	10.69	48.34	0.46	0.20	99.5	89.0
	39.76	10.90	48.16	0.46	0.19	99.5	88.7
	40.08	10.35	48.72	0.46	0.20	99.8	89.4

Sample	SiO_2	FeO	MgO	NiO	CaO	Total	Fo*
Layer 6	39.42	10.93	48.05	0.43	0.20	99.0	88.7
	39.76	10.52	48.40	0.47	0.20	99.3	89.1
	39.95	10.36	48.69	0.51	0.18	99.7	89.3
	40.53	10.32	48.26	0.50	0.19	99.8	89.3
	40.59	11.69	47.33	0.41	0.21	100.2	87.8
	40.42	10.40	48.20	0.48	0.19	99.7	89.2
	40.27	10.38	48.17	0.48	0.20	99.5	89.2
	39.93	12.75	46.05	0.43	0.20	99.4	86.6
	40.44	10.76	48.02	0.46	0.19	99.9	88.8
	39.32	16.07	43.69	0.31	0.20	99.6	82.9
	40.43	10.30	48.27	0.48	0.19	99.7	89.3
	40.59	10.51	48.44	0.47	0.19	100.2	89.1
	40.48	10.39	48.40	0.48	0.19	99.9	89.2
	39.79	14.17	45.24	0.42	0.21	99.8	85.1
	40.13	10.46	48.31	0.48	0.19	99.6	89.2
	40.26	10.53	48.26	0.48	0.20	99.7	89.1
	40.46	10.38	48.51	0.48	0.19	100.0	89.3
	40.21	10.36	48.35	0.48	0.20	99.6	89.3
	40.30	10.85	47.99	0.47	0.20	99.8	88.7
	40.42	10.70	48.39	0.47	0.19	100.2	89.0
	40.32	10.36	48.44	0.48	0.19	99.8	89.3
	40.02	11.46	47.35	0.45	0.20	99.5	88.0
	40.40	10.48	48.41	0.47	0.20	100.0	89.2
	39.93	11.45	47.26	0.45	0.20	99.3	88.0
	40.16	10.38	48.17	0.48	0.19	99.4	89.2
	40.27	11.04	48.00	0.45	0.20	99.9	88.6
	40.13	10.88	47.95	0.45	0.19	99.6	88.7
	40.52	11.09	48.05	0.51	0.20	100.4	88.5
	40.19	11.04	48.05	0.46	0.19	99.9	88.6
	39.63	14.16	45.77	0.33	0.22	100.1	85.2
	40.39	10.46	48.49	0.47	0.20	100.0	89.2
	40.42	10.44	48.83	0.47	0.19	100.4	89.3
	39.10	17.54	43.13	0.26	0.20	100.2	81.4
	40.26	10.70	48.59	0.45	0.19	100.2	89.0
	39.90	11.07	47.74	0.43	0.19	99.3	88.5
	39.16	15.88	43.93	0.29	0.21	99.5	83.1
	40.06	10.50	48.22	0.46	0.20	99.4	89.1
	39.28	15.39	44.26	0.27	0.23	99.4	83.7
	40.19	10.32	48.50	0.46	0.19	99.7	89.3
	39.99	10.22	48.16	0.47	0.20	99.0	89.4
	39.85	10.31	48.15	0.46	0.20	99.0	89.3
	39.73	10.43	48.16	0.46	0.19	99.0	89.2
	39.74	10.68	48.15	0.46	0.19	99.2	88.9
	39.35	12.59	46.50	0.37	0.21	99.0	86.8
	39.65	10.78	47.97	0.44	0.20	99.0	88.8
	39.64	10.69	48.15	0.46	0.19	99.1	88.9
	39.05	14.40	45.54	0.37	0.22	99.6	84.9
	38.83	14.75	45.27	0.33	0.22	99.4	84.5
	38.62	16.28	43.90	0.29	0.21	99.3	82.8
	39.17	13.78	45.94	0.34	0.21	99.4	85.6
	38.32	17.65	42.62	0.22	0.26	99.1	81.2
	38.51	17.26	43.06	0.27	0.22	99.3	81.6
	38.33	17.90	42.53	0.23	0.25	99.2	80.9
	38.57	17.61	42.76	0.23	0.26	99.4	81.2
	39.16	15.38	44.87	0.29	0.23	99.9	83.9

Sample	SiO_2	FeO	MgO	NiO	CaO	Total	Fo*
	39.07	14.51	45.43	0.40	0.21	99.6	84.8
	38.65	16.06	44.19	0.23	0.22	99.4	83.1
	38.72	15.66	44.45	0.24	0.22	99.3	83.5
	38.89	15.77	44.44	0.24	0.22	99.6	83.4
	38.61	15.92	44.11	0.24	0.22	99.1	83.2
	38.53	17.60	42.78	0.24	0.25	99.4	81.2
	39.66	12.43	47.24	0.37	0.21	99.9	87.1
	39.21	14.72	45.35	0.28	0.21	99.8	84.6
	39.32	12.74	46.86	0.36	0.20	99.5	86.8
	39.48	12.68	47.03	0.37	0.21	99.8	86.9
	38.56	16.83	43.38	0.30	0.22	99.3	82.1
	38.68	15.70	44.16	0.33	0.20	99.1	83.4
	38.70	16.50	43.69	0.28	0.23	99.4	82.5
	39.06	15.01	44.94	0.27	0.21	99.5	84.2
	39.73	11.13	48.08	0.45	0.19	99.6	88.5
	38.93	16.44	44.04	0.24	0.21	99.9	82.7
	39.13	15.02	45.18	0.34	0.22	99.9	84.3
	39.58	11.18	48.02	0.44	0.20	99.4	88.4
	38.82	16.72	43.69	0.26	0.23	99.7	82.3
	38.86	16.17	44.03	0.22	0.23	99.5	82.9
	39.07	15.89	44.58	0.23	0.23	100.0	83.3
	39.21	14.35	45.50	0.33	0.22	99.6	85.0
	40.09	10.37	48.92	0.50	0.19	100.1	89.4
	40.11	10.32	48.91	0.49	0.19	100.0	89.4
	39.20	15.46	44.94	0.28	0.22	100.1	83.8
	38.85	16.09	44.13	0.30	0.21	99.6	83.0
	39.12	15.34	44.81	0.30	0.21	99.8	83.9
	38.59	17.26	43.03	0.25	0.26	99.4	81.6
	39.02	15.50	44.65	0.29	0.23	99.7	83.7
	39.07	13.79	45.55	0.32	0.25	99.0	85.5
	39.48	14.57	45.74	0.31	0.22	100.3	84.8
	39.45	13.56	46.36	0.41	0.19	100.0	85.9
	39.14	16.01	44.35	0.28	0.22	100.0	83.2
	39.24	15.17	45.01	0.32	0.20	99.9	84.1
	39.38	14.08	45.72	0.33	0.21	99.7	85.3
	39.45	13.75	46.13	0.34	0.21	99.9	85.7
	39.14	15.82	44.41	0.25	0.22	99.9	83.3
	38.96	17.75	43.02	0.22	0.25	100.2	81.2
	39.23	15.25	44.86	0.31	0.22	99.9	84.0
	39.32	14.90	45.28	0.25	0.23	100.0	84.4
	39.21	14.98	45.15	0.29	0.21	99.8	84.3
	38.94	17.71	42.86	0.22	0.26	100.0	81.2
	39.47	15.09	45.06	0.30	0.21	100.1	84.2
	39.55	14.34	45.90	0.31	0.21	100.3	85.1
	38.92	17.94	42.71	0.36	0.22	100.1	80.9
	39.43	14.48	45.62	0.29	0.21	100.0	84.9
	39.63	14.41	45.64	0.26	0.22	100.2	85.0
	40.42	10.65	48.91	0.48	0.19	100.7	89.1
	39.33	16.99	43.84	0.26	0.22	100.6	82.1
	39.23	16.92	43.74	0.28	0.22	100.4	82.2
	39.25	16.27	44.08	0.29	0.22	100.1	82.9
	40.20	10.96	48.44	0.44	0.20	100.2	88.7
	38.35	14.74	43.40	0.28	0.22	97.0	84.0
	39.37	16.09	44.22	0.23	0.22	100.1	83.0
	39.43	15.84	44.53	0.29	0.22	100.3	83.4

Sample	SiO_2	FeO	MgO	NiO	CaO	Total	Fo*
	39.39	15.75	44.51	0.31	0.21	100.2	83.4
unit 20	39.61	11.42	48.22	0.41	0.15	99.8	88.3
	38.99	14.94	45.30	0.30	0.21	99.7	84.4
	39.48	10.60	48.27	0.46	0.15	99.0	89.0
	38.99	12.16	47.49	0.42	0.18	99.2	87.4
	40.04	9.96	49.62	0.48	0.15	100.2	89.9
	39.32	11.18	47.86	0.42	0.19	99.0	88.4
	38.42	15.38	44.70	0.30	0.18	99.0	83.8
	39.02	13.31	46.66	0.38	0.21	99.6	86.2
	39.11	13.27	46.71	0.34	0.20	99.6	86.3
	40.76	11.01	48.05	0.45	0.18	100.5	88.6
	41.08	11.63	46.62	0.40	0.20	99.9	87.7
	39.41	10.97	48.59	0.42	0.18	99.6	88.8
	41.07	12.11	46.31	0.41	0.18	100.1	87.2
	39.34	11.28	48.58	0.42	0.18	99.8	88.5
	40.91	12.88	45.57	0.39	0.20	100.0	86.3
	40.79	13.69	45.60	0.36	0.20	100.6	85.6
	40.31	15.92	43.72	0.30	0.19	100.4	83.0
	39.11	21.01	39.38	0.25	0.19	99.9	77.0
	40.45	15.95	43.25	0.38	0.16	100.2	82.9
	40.35	16.40	43.57	0.32	0.17	100.8	82.6
	40.78	11.48	47.24	0.46	0.16	100.1	88.0
	40.82	12.08	47.00	0.40	0.19	100.5	87.4
	38.75	12.77	47.21	0.36	0.21	99.3	86.8
	39.29	10.52	48.53	0.43	0.18	98.9	89.2
	40.61	11.11	47.75	0.43	0.17	100.1	88.5
	38.64	11.36	48.47	0.43	0.17	99.1	88.4
	38.79	11.16	48.86	0.43	0.18	99.4	88.6
	40.21	10.62	48.03	0.50	0.17	99.5	89.0
	40.62	10.66	48.14	0.44	0.17	100.0	89.0
	40.40	11.81	47.36	0.39	0.19	100.1	87.7
	37.78	15.45	45.29	0.30	0.18	99.0	83.9
	40.70	11.68	47.23	0.39	0.19	100.2	87.8
	40.69	11.13	47.72	0.43	0.18	100.1	88.4
	40.32	11.18	48.32	0.43	0.18	100.4	88.5
	39.71	11.31	47.98	0.47	0.20	99.7	88.3
	39.10	14.67	45.42	0.33	0.22	99.7	84.7
	38.70	16.17	43.99	0.31	0.18	99.3	82.9
	39.65	11.41	47.86	0.44	0.19	99.5	88.2
	39.50	12.76	46.93	0.38	0.20	99.8	86.8
	39.57	11.56	47.81	0.43	0.20	99.6	88.1
	39.56	11.98	47.38	0.42	0.20	99.5	87.6
	39.68	11.30	48.06	0.44	0.20	99.7	88.3
	38.64	17.31	43.06	0.33	0.18	99.5	81.6
	39.50	14.11	46.08	0.36	0.18	100.2	85.3
	39.79	11.03	48.35	0.45	0.19	99.8	88.7
	39.71	11.40	47.94	0.44	0.19	99.7	88.2
	39.77	11.22	48.34	0.44	0.19	100.0	88.5
	39.81	11.15	48.11	0.44	0.19	99.7	88.5
	39.44	13.44	46.31	0.38	0.20	99.8	86.0
	39.76	11.34	47.97	0.44	0.19	99.7	88.3
	39.34	13.82	46.02	0.37	0.22	99.8	85.6
	39.57	12.24	47.20	0.41	0.20	99.6	87.3
	38.83	16.28	43.88	0.30	0.20	99.5	82.8
	39.80	11.65	47.79	0.42	0.18	99.9	88.0

Sample	SiO_2	FeO	MgO	NiO	CaO	Total	Fo*
	39.04	15.65	44.44	0.31	0.18	99.6	83.5
	39.76	11.85	47.51	0.38	0.22	99.7	87.7
	39.10	15.90	44.38	0.27	0.23	99.9	83.3
	39.16	14.73	45.12	0.33	0.20	99.5	84.5
	39.72	11.61	47.70	0.42	0.21	99.7	88.0
	39.93	11.22	48.10	0.43	0.19	99.9	88.4
	38.44	19.37	41.41	0.33	0.16	99.7	79.2
	39.82	10.68	48.68	0.47	0.19	99.8	89.0
	39.75	10.64	48.57	0.47	0.21	99.6	89.1
	39.44	12.51	46.78	0.39	0.21	99.3	87.0
	38.87	16.14	44.18	0.39	0.18	99.8	83.0
	39.04	15.20	44.96	0.39	0.21	99.8	84.1
	39.79	11.67	47.80	0.44	0.20	99.9	88.0
CLF	39.44	14.69	45.24	0.29	0.24	99.9	84.6
	39.49	12.90	46.22	0.32	0.21	99.1	86.5
	39.16	15.01	44.56	0.29	0.21	99.2	84.1
	39.13	15.20	44.47	0.27	0.22	99.3	83.9
	39.49	12.82	46.27	0.32	0.21	99.1	86.6
	39.41	13.14	46.38	0.31	0.22	99.5	86.3
	39.01	15.05	44.54	0.27	0.23	99.1	84.1
	38.81	16.63	43.05	0.32	0.19	99.0	82.2
	39.48	13.23	46.15	0.31	0.21	99.4	86.2
	39.18	14.91	44.57	0.29	0.23	99.2	84.2
	39.20	14.72	44.73	0.28	0.23	99.2	84.4
	39.50	12.34	46.79	0.38	0.21	99.2	87.1
	38.16	19.84	40.76	0.21	0.26	99.2	78.6
	39.92	10.71	48.10	0.44	0.21	99.4	88.9
	39.45	12.94	46.35	0.26	0.25	99.2	86.5
	39.48	12.41	46.72	0.35	0.23	99.2	87.0
	39.28	14.01	45.40	0.35	0.23	99.3	85.2
	39.71	11.89	47.22	0.38	0.22	99.4	87.6
	39.40	12.55	46.61	0.34	0.22	99.1	86.9
	38.18	19.94	40.58	0.21	0.26	99.2	78.4
	39.70	11.56	47.54	0.40	0.22	99.4	88.0
	39.61	12.13	46.91	0.39	0.22	99.3	87.3
	39.73	11.94	47.04	0.39	0.23	99.3	87.6
	39.71	11.48	47.50	0.39	0.21	99.3	88.1
	39.72	11.53	47.37	0.40	0.22	99.2	88.0
	39.78	11.32	47.50	0.40	0.22	99.2	88.2
	39.74	11.23	47.55	0.40	0.21	99.1	88.3
	40.28	43.48	15.58	0.25	0.20	99.8	83.3
	40.26	44.28	14.98	0.26	0.19	100.0	84.0
	39.29	39.94	19.96	0.21	0.22	99.6	78.8
	39.30	39.82	20.28	0.18	0.22	99.8	77.8
	40.25	44.08	15.03	0.26	0.19	99.8	83.9
	40.70	45.79	12.80	0.36	0.18	99.8	86.4
	40.57	46.10	12.38	0.36	0.19	99.6	86.9
	40.37	45.33	13.35	0.28	0.18	99.5	85.8
Eastern Pumice	39.68	13.56	46.42	0.35	0.24	100.3	85.9
	40.05	11.64	48.16	0.43	0.23	100.5	88.1
	39.74	12.35	47.70	0.39	0.23	100.4	87.3
	39.76	11.88	47.81	0.37	0.24	100.1	87.8
	39.66	11.91	47.87	0.37	0.24	100.1	87.8
	39.31	14.76	45.74	0.32	0.26	100.4	84.7
	39.40	13.90	46.19	0.32	0.25	100.1	85.6

Sample	SiO_2	FeO	MgO	NiO	CaO	Total	Fo*
	39.65	12.99	47.00	0.35	0.24	100.2	86.6
	39.54	13.22	46.74	0.28	0.25	100.0	86.3
	39.75	11.69	48.16	0.39	0.23	100.2	88.0
	39.43	11.97	47.55	0.37	0.24	99.6	87.6
	39.38	13.06	46.62	0.34	0.24	99.6	86.4
	39.13	13.78	46.03	0.35	0.28	99.6	85.6
	39.89	11.65	48.17	0.39	0.23	100.3	88.1
	39.52	13.06	46.95	0.36	0.24	100.1	86.5
	39.60	12.90	46.85	0.34	0.23	99.9	86.6
	39.80	11.38	48.23	0.41	0.23	100.1	88.3
	38.97	15.94	44.54	0.32	0.23	100.0	83.3
	39.60	12.38	47.38	0.37	0.23	100.0	87.2
	39.89	11.03	48.65	0.40	0.22	100.2	88.7
	39.47	13.19	46.64	0.35	0.34	100.0	86.3
	39.50	12.22	47.61	0.37	0.26	100.0	87.4
	39.80	11.25	48.67	0.41	0.22	100.4	88.5
	39.56	12.72	47.26	0.37	0.26	100.2	86.9
	39.69	12.04	47.82	0.38	0.24	100.2	87.6
	39.50	13.53	46.65	0.35	0.25	100.3	86.0
	39.42	13.29	46.74	0.36	0.28	100.1	86.2
	39.33	14.11	46.42	0.37	0.23	100.5	85.4
	39.39	14.20	46.20	0.33	0.33	100.4	85.3
	40.00	12.16	47.78	0.37	0.24	100.5	87.5
	39.87	11.97	48.09	0.38	0.23	100.5	87.8
	39.71	12.08	48.12	0.38	0.25	100.5	87.7
	39.56	13.74	46.60	0.35	0.24	100.5	85.8
	39.87	12.35	47.63	0.35	0.23	100.4	87.3
	39.76	11.21	48.81	0.42	0.22	100.4	88.6
	39.47	13.74	46.48	0.35	0.24	100.3	85.8
	39.78	12.65	47.32	0.40	0.24	100.4	87.0
	39.56	13.26	47.06	0.35	0.24	100.5	86.3
	39.88	11.56	48.28	0.42	0.22	100.4	88.2
	39.47	14.01	46.20	0.34	0.25	100.3	85.5
	39.41	14.31	45.96	0.27	0.27	100.2	85.1
	39.67	12.31	47.61	0.39	0.22	100.2	87.3
	39.79	11.71	48.37	0.41	0.22	100.5	88.0
	39.53	13.72	46.78	0.32	0.20	100.5	85.9
	39.29	15.50	45.04	0.33	0.27	100.4	83.8
	39.79	12.94	47.04	0.34	0.32	100.4	86.6
	39.81	11.97	48.07	0.38	0.23	100.5	87.7
	39.19	15.75	44.85	0.32	0.23	100.4	83.5
	39.14	14.87	45.38	0.34	0.23	100.0	84.5
	39.52	13.54	46.53	0.36	0.23	100.2	86.0
	39.76	12.34	47.82	0.39	0.22	100.5	87.4
	39.95	11.54	48.35	0.40	0.22	100.5	88.2
	39.84	10.10	49.77	0.49	0.19	100.4	89.8
	39.85	10.07	49.87	0.50	0.19	100.5	89.8
	39.82	12.34	47.76	0.38	0.23	100.5	87.3
	39.01	16.16	44.76	0.33	0.28	100.5	83.2
	39.59	14.04	46.30	0.32	0.27	100.5	85.5
	39.89	12.05	47.95	0.39	0.25	100.5	87.6
	39.75	12.33	47.66	0.38	0.23	100.4	87.3
	39.76	13.20	46.94	0.35	0.24	100.5	86.4
Golden Pumice	39.52	10.88	47.93	0.44	0.19	99.0	88.7
	39.36	11.64	47.51	0.43	0.19	99.1	87.9

Sample	SiO_2	FeO	MgO	NiO	CaO	Total	Fo*
	39.56	10.87	48.12	0.44	0.20	99.2	88.8
	38.95	12.71	46.94	0.40	0.21	99.2	86.8
	39.32	11.11	47.97	0.44	0.20	99.0	88.5
	39.47	10.95	48.34	0.39	0.19	99.3	88.7
	39.68	11.14	47.64	0.39	0.20	99.0	88.4
	39.30	11.80	47.24	0.41	0.21	99.0	87.7
	39.34	11.70	47.24	0.42	0.26	99.0	87.8
	39.64	10.61	48.85	0.45	0.19	99.7	89.2
	39.62	10.40	48.62	0.45	0.18	99.3	89.3
	39.58	11.02	47.77	0.43	0.20	99.0	88.6
	39.49	10.89	48.03	0.44	0.21	99.1	88.7
	39.68	10.89	48.05	0.44	0.19	99.3	88.7
	39.40	11.66	47.68	0.43	0.20	99.4	87.9
	38.99	12.62	46.78	0.40	0.25	99.0	86.9
	39.27	12.46	47.21	0.42	0.19	99.5	87.1
	39.38	11.91	47.53	0.44	0.19	99.5	87.7
	39.24	12.41	46.69	0.40	0.20	98.9	87.0
	39.50	11.54	47.69	0.44	0.20	99.4	88.1
	39.25	11.14	47.82	0.42	0.20	98.8	88.5
	39.36	13.55	46.31	0.35	0.20	99.8	85.9
	39.62	11.31	47.44	0.41	0.20	99.0	88.2
	39.68	11.38	47.93	0.41	0.21	99.6	88.3
	39.01	13.32	46.14	0.39	0.22	99.1	86.1
	39.16	13.68	45.59	0.33	0.23	99.0	85.6
	39.57	11.09	48.08	0.44	0.20	99.4	88.6
	39.65	10.99	47.97	0.45	0.19	99.2	88.6
	39.12	13.81	45.59	0.34	0.20	99.1	85.5
	39.72	11.04	47.90	0.45	0.18	99.3	88.6
	39.70	10.91	47.91	0.45	0.19	99.2	88.7
	39.69	11.68	47.72	0.44	0.19	99.7	87.9
	39.74	10.88	48.21	0.45	0.19	99.5	88.8
	39.64	11.05	47.83	0.45	0.18	99.2	88.5
	39.74	10.47	48.36	0.45	0.18	99.2	89.2
	39.60	12.17	47.18	0.43	0.18	99.6	87.4
	39.70	10.90	48.06	0.47	0.18	99.3	88.7
	39.86	10.84	48.19	0.44	0.18	99.5	88.8
	40.04	10.03	49.12	0.46	0.18	99.8	89.7
	39.58	11.41	47.77	0.45	0.19	99.4	88.2
	39.64	11.50	47.68	0.42	0.19	99.4	88.1
	39.63	12.53	46.84	0.41	0.19	99.6	86.9
	39.87	11.09	48.06	0.45	0.19	99.7	88.5
	39.85	11.00	48.12	0.46	0.19	99.6	88.6
	39.62	11.27	47.59	0.44	0.19	99.1	88.3
	39.77	10.93	47.99	0.46	0.18	99.3	88.7
	39.12	15.38	44.60	0.29	0.19	99.6	83.8
	38.47	18.66	41.80	0.22	0.24	99.4	80.0
	39.51	13.21	46.47	0.40	0.18	99.8	86.2
	39.70	11.97	47.11	0.44	0.18	99.4	87.5
	39.93	11.07	48.20	0.41	0.19	99.8	88.6
	39.70	12.14	47.19	0.42	0.19	99.6	87.4
	39.78	11.59	47.64	0.42	0.19	99.6	88.0
	40.01	10.53	48.55	0.47	0.19	99.8	89.1
	39.88	10.91	48.19	0.45	0.18	99.6	88.7

Note(s): *Fo = forsterite; [(Mg/(Mg+Fe)*100]

Table B2. Compositions of glasses adhering to zoned Keanakāko‘i Tephra olivine used for diffusion modelling.

Oxide (wt%)	BR_5	BR_7	BR_9	BR_12	BR_15	BR_16	BR_17	BR_20	BR_21	BR_28	BR_30
SiO_2	50.83	51.75	50.75	50.67	50.34	50.64	50.91	51.26	50.14	50.71	50.56
TiO_2	2.39	2.54	2.37	2.43	2.41	2.43	2.47	2.42	2.42	2.43	2.44
Al_2O_3	13.49	14.30	13.39	13.53	13.35	13.71	13.63	13.96	13.51	13.85	13.53
FeO	11.06	10.09	11.02	11.02	11.28	11.15	11.16	10.84	11.20	10.97	11.10
MnO	0.17	0.16	0.17	0.18	0.18	0.16	0.18	0.18	0.17	0.17	0.15
MgO	8.16	6.84	8.18	7.43	7.69	7.47	7.45	7.35	7.69	7.18	7.84
CaO	10.78	11.45	10.72	11.40	10.92	10.88	11.17	11.26	10.89	11.27	10.81
Na_2O	2.25	2.12	2.26	2.17	2.21	2.32	2.23	2.25	2.21	2.25	2.22
K_2O	0.42	0.45	0.43	0.42	0.43	0.44	0.42	0.41	0.43	0.41	0.43
P_2O_5	0.21	0.24	0.22	0.21	0.21	0.22	0.23	0.23	0.22	0.23	0.21
Total	99.76	99.94	99.51	99.46	99.02	99.42	99.83	100.18	99.03	99.48	99.30
Mg#	59.4	57.3	59.5	57.2	57.4	57.0	56.9	57.3	57.6	56.4	58.3
T (°C)	1178	1151	1178	1163	1169	1164	1164	1162	1169	1158	1172

Oxide (wt%)	7_1	7_3	7_8	7_12	7_14	7_17	7_20	7_26	7_28	7_29
SiO_2	50.13	50.52	50.29	50.42	50.03	50.22	50.36	50.07	49.86	50.27
TiO_2	2.40	2.46	2.40	2.36	2.46	2.45	2.47	2.43	2.47	2.46
Al_2O_3	13.31	13.53	13.51	13.51	13.35	13.41	13.55	13.41	13.41	13.52
FeO	11.16	11.17	11.11	11.19	11.24	11.15	11.22	11.30	11.10	11.21
MnO	0.16	0.17	0.17	0.15	0.16	0.18	0.17	0.17	0.18	0.16
MgO	8.64	8.59	8.71	8.64	8.71	8.60	8.66	8.76	8.51	8.62
CaO	10.75	10.78	10.76	10.81	10.77	10.73	10.80	10.79	10.81	10.80
Na_2O	2.22	2.25	2.23	2.24	2.24	2.24	2.26	2.23	2.22	2.22
K_2O	0.44	0.43	0.44	0.44	0.45	0.44	0.44	0.44	0.44	0.43
P_2O_5	0.19	0.17	0.21	0.21	0.19	0.19	0.21	0.22	0.19	0.18
Total	99.39	100.08	99.82	99.97	99.60	99.61	100.15	99.82	99.20	99.86
Mg#	60.5	60.4	60.8	60.5	60.5	60.4	60.4	60.5	60.3	60.4
T (°C)	1188	1187	1189	1188	1189	1187	1188	1190	1185	1187

Table B2 (continued). Compositions of glasses adhering to zoned Keanakāko‘i Tephra olivine used for diffusion modeling.

Oxide (wt%)	11_1	11_4	11_6	11_7	11_9	11_14	11_19	11_25	11_34
SiO_2	50.81	50.53	51.11	51.88	50.52	50.96	50.16	50.83	51.75
TiO_2	2.42	2.45	2.37	2.27	2.30	2.42	2.39	2.39	2.54
Al_2O_3	13.57	13.44	13.52	13.58	13.19	13.61	12.95	13.49	14.30
FeO	11.02	11.15	10.96	10.08	11.18	10.97	11.25	11.06	10.09
MnO	0.17	0.17	0.16	0.16	0.17	0.14	0.17	0.17	0.16
MgO	7.65	7.52	8.00	7.34	8.66	7.79	8.62	8.16	6.84
CaO	10.86	10.90	10.75	10.88	10.60	10.79	10.73	10.78	11.45
Na_2O	2.22	2.20	2.26	2.11	2.16	2.26	2.07	2.25	2.12
K_2O	0.45	0.44	0.45	0.37	0.45	0.46	0.42	0.42	0.45
P_2O_5	0.23	0.23	0.22	0.21	0.23	0.26	0.22	0.21	0.24
Total	99.41	99.02	99.79	98.89	99.46	99.66	98.98	99.76	99.94
Mg#	57.9	57.2	59.1	59.0	60.5	58.4	60.3	59.4	57.3
T (°C)	1168	1165	1175	1162	1188	1171	1187	1178	1151

Oxide (wt%)	20_2	20_9	20_17	20_18	20_23	20_29	20_34	20_35	20_36
SiO_2	49.78	50.02	49.82	50.04	49.63	50.14	50.39	50.14	49.61
TiO_2	2.56	2.61	2.62	2.70	2.52	2.51	2.45	2.47	2.29
Al_2O_3	12.80	12.82	12.85	13.22	12.78	12.55	12.75	12.76	12.47
FeO	11.16	11.25	11.26	11.55	11.12	11.26	11.19	11.26	11.30
MnO	0.16	0.17	0.18	0.18	0.16	0.18	0.17	0.18	0.16
MgO	9.62	9.68	9.47	8.64	9.73	10.05	9.51	9.66	10.84
CaO	10.49	10.53	10.57	11.10	10.72	10.36	10.49	10.50	9.86
Na_2O	2.19	2.22	2.13	2.17	2.14	2.13	2.18	2.19	2.23
K_2O	0.45	0.45	0.44	0.44	0.44	0.44	0.45	0.46	0.46
P_2O_5	0.22	0.21	0.21	0.20	0.21	0.21	0.21	0.21	0.25
Total	99.43	99.97	99.56	100.25	99.45	99.83	99.79	99.83	99.48
Mg#	63.1	63.0	62.5	59.7	63.4	63.9	62.7	62.9	65.5
T (°C)	1207	1209	1204	1188	1210	1216	1205	1208	1232

Table B2 (continued). Compositions of glasses adhering to zoned Keanakāko‘i Tephra olivine used for diffusion modeling.

Oxide (wt%)	**EP_3**	**EP_5**	**EP_6**	**EP13**	**EP_15**	**EP_18**	**EP_19**	**EP_23**	**EP_27**	**EP_30**
SiO_2	49.73	49.48	48.99	48.98	49.65	49.49	49.52	49.63	49.96	49.41
TiO_2	2.75	2.75	2.65	2.72	2.70	2.79	2.71	3.14	2.86	2.68
Al_2O_3	13.64	13.18	12.84	13.06	12.83	13.39	13.23	13.76	14.04	13.24
FeO	11.06	10.99	11.24	11.52	10.77	11.26	11.17	11.45	11.24	11.14
MnO	0.17	0.17	0.17	0.17	0.17	0.17	0.17	0.17	0.17	0.17
MgO	6.93	7.82	9.19	8.78	8.27	8.26	8.82	6.62	7.03	8.74
CaO	11.59	11.67	11.21	11.15	11.95	11.40	11.36	11.32	11.67	11.35
Na_2O	2.22	2.20	2.09	2.20	2.12	2.23	2.22	2.44	2.36	2.20
K_2O	0.56	0.54	0.52	0.52	0.53	0.55	0.53	0.63	0.59	0.54
P_2O_5	0.24	0.21	0.23	0.23	0.17	0.24	0.24	0.27	0.26	0.25
Total	98.89	99.01	99.13	99.33	99.15	99.78	99.96	99.43	100.19	99.73
Mg#	55.4	58.5	61.8	60.1	60.3	59.2	61.0	53.4	55.3	60.8
T (°C)	1153	1171	1199	1190	1180	1180	1191	1147	1155	1190

Oxide (wt%)	**GP_6**	**GP_12**	**GP_20**	**GP_22**	**GP_23**	**GP_27**	**GP_31**	**GP_30**	**GP_34**	**GP_36**
SiO_2	51.28	51.52	51.14	51.26	51.42	50.72	50.45	50.69	51.36	50.90
TiO_2	2.41	2.55	2.42	2.45	2.43	2.45	2.44	2.46	2.43	2.44
Al_2O_3	13.08	13.92	13.05	13.21	13.26	12.99	13.07	13.04	13.04	12.99
FeO	11.13	10.79	11.01	11.23	10.89	11.04	11.20	11.06	11.02	10.96
MnO	0.16	0.16	0.16	0.17	0.16	0.16	0.16	0.18	0.17	0.17
MgO	9.09	6.82	8.88	8.46	8.77	8.70	8.45	8.40	8.90	8.45
CaO	10.45	10.65	10.59	10.91	10.64	10.55	10.74	10.71	10.39	10.74
Na_2O	2.09	2.26	2.01	2.03	2.05	2.05	2.01	2.03	2.02	2.00
K_2O	0.42	0.44	0.39	0.40	0.40	0.40	0.40	0.39	0.40	0.40
P_2O_5	0.21	0.22	0.19	0.20	0.24	0.21	0.22	0.20	0.23	0.22
Total	100.32	99.34	99.85	100.32	100.27	99.28	99.14	99.14	99.97	99.27
Mg#	61.8	55.6	61.5	59.9	61.5	60.9	59.9	60.1	61.5	60.4
T (°C)	1197	1151	1192	1184	1190	1189	1184	1183	1193	1184

Note(s): Sample names are unit_olivine# - BR (Basal Reticulite), 7, 11, and 20 (Units 7, 11, and 20, respectively), EP (Eastern Pumice), GP (Golden Pumice). T(°C) is temperature calculated using the Kīlauea glass MgO thermometer of Helz and Thornber (1987). Mg# = [Mg/(Mg+Fe) x 100]

APPENDIX C

Supporting Information for
LITHIUM ZONING IN OLIVINE: DECIPHERING GROWTH VS. DIFFUSION SIGNATURES TO DOCUMENT LATE-STAGE MIXING AT KĪLAUEA VOLCANO, HAWAI‘I

C1. Introduction

This supporting file contains all content that appears as Supplementary Material intended to be published with Chapter 4: Lynn et al. (in prep). All data that will appear in the publication's electron resource are provided below, including laser ablation ICPMS trace element profiles for all crystals presented in the text and appendix (Table C1) and electron microprobe analysis for Fo profiles presented in the text (Table C2). Additional examples of the trace element zoning relationships described in the main text are also provided as supplementary figures with descriptions of the features of interest.

C2. Results

C2.1. Trace element profiles

Laser ablation ICPMS trace element data for all profiles shown in the main text or appendix are reported in Table C1. Appendix figures C1-C4 provide additional examples of the trace element zoning styles presented in the main text. Figure C5 presents P^{5+} against Li^{+} cations per 4 oxygens (molar concentrations) for olivine crystals with contrasting Li zoning behavior: (1) U7 Olivine 12 has diffuse rims and enrichment peaks in the core region and (2) L6 Olivine 24 P and Li are inferred to reflect only growth.

C2.2. Forsterite profiles

Electron probe micro-analysis data for all forsterite profiles shown in the main text are reported in Table C2.

Table C1. Trace element analyses of 1D transects presented in the main text or appendix.

Sample	Li	Na	Al	P	Cr	x (μm)
Unit 20 Olivine 27	1.82	31	122	38	214	11
	1.95	33	119	50	216	22
	2.04	30	112	45	220	33
	2.16	33	101	45	198	44
	2.32	38	97	37	186	55
	2.30	35	95	34	170	66
	2.37	52	103	30	159	77
	2.54	63	107	28	161	88
	2.59	42	101	35	170	99
	2.67	37	99	38	169	110
	2.85	40	96	44	173	121
	2.88	52	117	35	159	132
	2.93	40	91	30	157	143
	3.05	37	92	36	155	154
	3.13	39	92	30	148	165
	3.14	40	92	29	147	176
	3.28	37	88	32	155	187
	3.32	35	93	23	148	198
	3.19	35	89	25	153	209
	3.25	34	90	29	153	220
	3.35	37	89	30	157	231
	3.35	36	98	31	159	242
	3.40	38	93	29	165	253
	3.43	40	99	25	174	264
	3.43	35	96	26	167	275
	3.38	38	95	32	166	286
	3.46	34	96	30	158	297
	3.33	32	96	32	153	308
	3.27	31	96	26	153	319
	3.39	33	93	37	150	330
	3.39	34	92	32	152	341
	3.37	34	98	33	153	352
	3.37	32	95	33	150	363
	3.32	33	99	30	146	374
	3.35	33	95	34	147	385
	3.35	31	95	32	156	396
	3.42	33	101	34	156	407
	3.36	33	101	34	161	418
	3.34	34	100	28	161	429
Unit 7 Olivine 12 *b*-axis	1.70	50	235	26	527	11
	1.57	57	219	45	531	22
	1.44	45	227	26	536	33
	1.43	47	216	29	523	44
	1.40	48	242	172	568	55
	1.50	50	280	326	602	66
	1.34	46	243	58	550	77
	1.34	45	241	37	543	88
	1.34	46	241	28	547	99
	1.37	44	247	66	555	110
	1.43	50	266	246	583	121
	1.37	46	245	56	553	132
	1.38	44	243	56	555	143
	1.34	46	240	61	545	154

Sample	Li	Na	Al	P	Cr	x (μm)
	1.36	46	241	65	550	165
	1.38	47	241	55	551	176
	1.34	46	244	65	548	187
	1.36	45	246	59	553	198
	1.39	46	247	54	551	209
	1.39	46	247	49	552	220
	1.35	44	251	44	558	231
	1.33	46	254	40	554	242
	1.31	44	261	45	560	253
	1.36	44	259	40	558	264
	1.35	46	262	27	564	275
Unit 7 Olivine 12 *c*-axis	1.53	52	263	32	454	11
	1.40	52	268	34	485	22
	1.39	54	274	24	503	33
	1.37	53	268	28	521	44
	1.40	55	320	29	526	55
	1.41	56	298	63	516	66
	1.43	59	371	58	521	77
	1.40	66	474	44	532	88
	1.36	57	360	41	536	99
	1.33	47	247	38	541	110
	1.34	45	240	37	542	121
	1.38	46	247	36	549	132
	1.32	45	255	28	556	143
	1.38	47	248	36	549	154
	1.36	44	246	36	550	165
	1.34	45	251	33	549	176
	1.40	44	245	30	548	187
	1.32	45	262	29	560	198
	1.35	44	257	29	557	209
	1.34	47	239	36	541	220
	1.33	44	264	33	566	231
	1.37	45	253	38	556	242
	1.40	46	242	53	547	253
	1.40	45	242	52	546	264
	1.37	44	243	58	547	275
	1.37	47	240	49	548	286
	1.36	45	247	48	552	297
	1.37	44	254	50	560	308
	1.35	46	256	33	555	319
Layer 6 Olivine 24 *b*-axis	1.57	36	163	77	343	11
	1.55	37	149	94	348	22
	1.62	38	175	117	402	33
	1.56	40	245	172	552	44
	1.52	43	246	182	615	55
	1.53	45	226	181	625	66
	1.50	43	236	220	671	77
	1.47	44	216	210	656	88
	1.50	45	218	226	682	99
	1.51	46	204	244	653	110
	1.54	47	200	225	671	121
	1.52	48	189	202	653	132
	1.60	48	186	206	657	143

Sample	Li	Na	Al	P	Cr	x (µm)
	1.53	49	189	209	659	154
	1.53	46	182	232	631	165
	1.61	48	195	263	682	176
	1.54	49	191	290	676	187
	1.61	48	199	287	676	198
	1.61	49	192	287	686	209
	1.59	49	198	314	681	220
	1.58	48	193	318	683	231
	1.62	49	200	341	692	242
	1.57	48	207	324	674	253
Layer 6 Olivine 24 *c*-axis	1.66	38	149	114	340	11
	1.48	38	144	133	349	22
	1.58	38	152	130	365	33
	1.54	37	146	90	371	44
	1.60	38	154	112	393	55
	1.68	44	181	222	451	66
	1.59	44	199	241	484	77
	1.58	44	210	257	529	88
	1.59	47	209	239	550	99
	1.53	45	205	214	572	110
	1.60	49	216	262	603	121
	1.53	47	208	253	622	132
	1.48	47	206	215	610	143
	1.49	45	204	191	620	154
	1.47	48	203	190	616	165
	1.42	45	208	189	634	176
	1.46	46	209	195	626	187
	1.42	45	204	152	619	198
	1.46	48	198	172	623	209
	1.48	45	206	175	624	220
	1.47	48	212	199	635	231
	1.48	47	208	236	634	242
	1.54	47	207	227	635	253
	1.51	47	219	329	672	264
	1.54	45	217	270	653	275
	1.48	45	211	232	644	286
	1.61	47	218	259	668	297
	1.50	49	217	274	677	308
	1.52	45	207	232	640	319
	1.45	45	215	233	662	330
	1.56	47	221	295	692	341
	1.62	48	226	330	696	352
	1.57	49	225	400	725	363
	1.56	51	229	440	733	374
Eastern Pumice Olivine 15 (Supplement)	1.53	58	161	29	493	11
	1.51	48	159	29	505	22
	1.54	41	169	30	517	33
	1.52	40	164	18	497	44
	1.54	41	164	18	480	55
	1.60	40	165	23	469	66
	1.60	39	174	20	468	77
	1.57	39	168	30	460	88
	1.54	39	170	26	457	99

Sample	Li	Na	Al	P	Cr	x (µm)
	1.58	37	180	28	456	110
	1.51	40	182	26	460	121
	1.55	35	183	26	457	132
	1.57	38	183	31	446	143
	1.56	39	177	29	444	154
	1.65	38	158	26	428	165
	1.62	37	151	26	419	176
	1.58	37	158	26	421	187
	1.54	36	161	23	422	198
	1.61	37	157	47	416	209
	1.60	39	151	70	411	220
	1.62	36	147	55	405	231
	1.62	38	147	51	404	242
	1.65	37	152	55	403	253
	1.62	38	157	83	406	264
	1.62	37	161	96	413	275
	1.67	39	163	110	405	286
	1.62	37	162	129	403	297
	1.63	38	164	116	406	308
	1.65	40	164	107	396	319
	1.58	36	161	92	393	330
	1.60	38	162	99	385	341
	1.67	38	163	89	388	352
	1.60	39	158	92	382	363
	1.60	39	158	94	381	374
	1.66	38	156	85	377	385
	1.59	39	154	86	365	396
	1.63	39	154	91	365	407
	1.65	38	156	86	370	418
	1.60	39	157	84	361	429
	1.65	39	158	78	366	440
Golden Pumice Olivine 27 *a*-axis (Supplement)	1.47	44	245	22	468	11
	1.48	43	227	36	497	22
	1.50	43	221	35	509	33
	1.46	44	219	39	517	44
	1.53	49	227	151	551	55
	1.62	50	232	239	564	66
	1.55	47	205	134	537	77
	1.53	47	195	75	536	88
	1.47	45	198	55	529	99
	1.52	48	200	46	532	110
	1.50	45	201	35	537	121
	1.47	46	196	26	524	132
	1.46	47	199	35	535	143
	1.48	47	195	28	534	154
	1.44	44	186	32	517	165
	1.42	54	217	31	517	176
	1.42	46	195	36	504	187
	1.44	45	204	41	520	198
	1.42	44	188	41	497	209
	1.38	44	190	40	498	220
	1.41	43	190	48	498	231
	1.37	42	192	49	491	242
	1.35	43	208	49	505	253

Sample	Li	Na	Al	P	Cr	x (μm)
	1.40	43	183	46	473	264
	1.37	43	183	49	475	275
	1.41	44	187	48	493	286
	1.40	43	189	52	513	297
	1.41	46	191	46	520	308
	1.43	44	193	40	518	319
	1.38	43	200	41	519	330
Golden Pumice Olivine 27 *c*-axis (Supplement)	1.35	40	253	27	449	11
	1.36	41	257	31	468	22
	1.48	43	241	30	469	33
	1.47	41	227	26	464	44
	1.49	41	215	39	461	55
	1.51	42	208	54	465	66
	1.48	44	217	38	475	77
	1.48	44	220	38	483	88
	1.47	42	231	39	496	99
	1.43	42	237	37	504	110
	1.47	43	240	35	516	121
	1.46	43	243	42	523	132
	1.44	43	245	45	527	143
	1.46	43	250	41	537	154
	1.44	43	248	41	539	165
	1.46	44	248	38	543	176
	1.43	42	251	31	545	187
	1.43	43	248	37	548	198
	1.46	43	251	45	555	209
	1.44	43	252	52	563	220
	1.44	42	254	51	564	231
	1.46	43	255	54	571	242
	1.42	44	256	53	573	253
	1.48	43	256	54	580	264
	1.41	44	255	48	576	275
	1.40	43	258	47	584	286
	1.40	44	258	44	585	297
	1.42	42	257	48	586	308
	1.43	44	258	46	590	319
	1.41	43	258	43	588	330
	1.44	44	264	38	593	341
	1.42	42	264	39	592	352
	1.40	42	264	40	596	363
	1.40	43	262	35	590	374
	1.40	43	261	38	594	385
	1.36	43	259	38	592	396
	1.44	43	261	39	598	407
	1.40	42	257	36	595	418
	1.36	45	261	36	592	429
	1.41	43	260	31	592	440
Basal Reticulite Olivine 10 *a*-axis	1.69	41	261	337	504	374
	1.48	44	223	275	486	363
	1.51	43	201	215	478	352
	1.76	42	180	303	525	341
	1.77	42	192	373	517	330
	1.61	42	199	306	485	319

Sample	Li	Na	Al	P	Cr	x (µm)
	1.57	38	180	113	477	308
	1.50	35	176	58	463	297
	1.55	35	170	32	470	286
	1.67	40	171	152	480	275
	1.70	41	171	114	485	264
	1.68	39	173	118	505	253
	1.64	41	175	96	489	242
	1.61	41	171	75	490	231
	1.73	41	170	152	479	220
	1.72	41	175	176	499	209
	1.67	40	180	152	507	198
	1.65	43	172	104	503	187
	1.68	42	180	91	481	176
	1.66	44	183	92	483	165
	1.64	41	170	53	484	154
	1.55	42	173	40	499	143
	1.56	39	182	23	504	132
	1.67	42	186	46	498	121
	1.58	44	171	49	476	110
	1.51	45	150	46	437	99
	1.57	43	150	52	452	88
	1.66	44	162	55	454	77
	1.63	43	159	66	440	66
	1.61	44	173	55	434	55
	1.61	40	180	60	434	44
	1.61	42	176	81	408	33
	1.76	38	171	77	390	22
	1.74	44	152	69	338	11

Note(s): All trace element abundances are reported in ppm. x is distance from the olivine rim in µm. Average 2σ error on analyses are 0.06 ppm for Li, 2 ppm for Na, 4 ppm for Al, 10 ppm for P, and 8 ppm for Cr.

Table C2. Electron probe micro-analyses for core-to-rim forsterite profiles presented in the main text.

Sample	SiO_2	FeO	MgO	NiO	CaO	Total	Fo*	x (µm)
Layer 6 Olivine 3 *a*-axis	38.96	17.66	42.70	0.21	0.30	99.8	81.2	8
	39.00	17.71	42.55	0.21	0.28	99.7	81.1	16
	38.98	17.68	42.48	0.21	0.27	99.6	81.1	24
	39.05	17.67	42.53	0.21	0.27	99.7	81.1	32
	39.03	17.70	42.55	0.21	0.26	99.8	81.1	40
	39.11	17.71	42.57	0.22	0.27	99.9	81.1	48
	39.13	17.67	42.57	0.22	0.26	99.8	81.1	56
	39.07	17.70	42.59	0.22	0.26	99.8	81.1	64
	39.09	17.66	42.55	0.22	0.26	99.8	81.1	72
	39.13	17.66	42.63	0.22	0.26	99.9	81.2	80
	39.08	17.68	42.68	0.22	0.26	99.9	81.1	88
	39.07	17.66	42.63	0.22	0.25	99.8	81.2	96
	39.10	17.66	42.72	0.23	0.25	100.0	81.2	104
	39.07	17.56	42.78	0.24	0.25	99.9	81.3	112
	39.16	17.56	42.71	0.24	0.24	99.9	81.3	120
	39.10	17.48	42.75	0.24	0.24	99.8	81.4	128
	39.11	17.41	42.83	0.24	0.24	99.8	81.4	136
	39.19	17.45	42.87	0.25	0.23	100.0	81.4	144
	39.19	17.39	42.93	0.25	0.24	100.0	81.5	152
	39.42	17.41	43.33	0.26	0.23	100.7	81.6	160
	39.13	17.15	43.10	0.26	0.23	99.9	81.8	168
	39.19	16.98	43.12	0.27	0.22	99.8	81.9	176
	39.21	16.93	43.26	0.27	0.22	99.9	82.0	184
	39.27	16.92	43.40	0.27	0.22	100.1	82.1	192
	39.21	16.78	43.55	0.28	0.22	100.0	82.2	200
	39.24	16.72	43.61	0.27	0.22	100.1	82.3	208
	39.25	16.61	43.58	0.28	0.22	99.9	82.4	216
	39.50	16.68	43.93	0.29	0.22	100.6	82.4	224
	39.24	16.50	43.73	0.28	0.22	100.0	82.5	232
	39.29	16.47	43.76	0.28	0.22	100.0	82.6	240
	39.27	16.41	43.81	0.28	0.22	100.0	82.6	248
	39.25	16.32	43.84	0.28	0.22	99.9	82.7	256
	39.21	16.31	43.80	0.28	0.22	99.8	82.7	264
	39.34	16.34	43.86	0.29	0.22	100.0	82.7	272
Layer 6 Olivine 24 *b*-axis	40.20	13.85	45.80	0.30	0.22	100.4	85.5	7
	40.07	13.83	45.56	0.30	0.21	100.0	85.5	14
	39.99	13.83	45.73	0.31	0.22	100.1	85.5	21
	39.91	13.71	45.86	0.32	0.21	100.0	85.6	28
	39.99	13.50	46.04	0.33	0.21	100.1	85.9	35
	39.88	13.27	46.04	0.34	0.21	99.7	86.1	42
	39.96	12.93	46.44	0.36	0.21	99.9	86.5	49
	40.04	12.69	46.64	0.37	0.20	99.9	86.8	56
	40.21	12.40	47.02	0.39	0.20	100.2	87.1	63
	40.12	12.10	47.65	0.41	0.20	100.5	87.5	70
	40.27	11.93	47.35	0.41	0.20	100.2	87.6	77
	40.30	11.73	47.52	0.42	0.20	100.2	87.8	84
	40.32	11.64	47.71	0.42	0.20	100.3	88.0	91
	40.31	11.55	47.61	0.43	0.20	100.1	88.0	98
	40.44	11.48	47.91	0.43	0.20	100.5	88.2	105
	40.25	11.43	47.79	0.43	0.20	100.1	88.2	112
	40.30	11.38	47.73	0.43	0.19	100.0	88.2	119
	40.32	11.36	47.86	0.43	0.20	100.2	88.3	126
	40.38	11.36	47.91	0.43	0.20	100.3	88.3	133

Sample	SiO_2	FeO	MgO	NiO	CaO	Total	Fo*	x (μm)
	40.33	11.35	47.86	0.43	0.20	100.2	88.3	140
	40.36	11.35	47.85	0.43	0.20	100.2	88.3	147
	40.23	11.33	47.90	0.43	0.20	100.1	88.3	154
	40.32	11.32	47.88	0.43	0.20	100.1	88.3	161
	40.31	11.28	47.91	0.44	0.20	100.1	88.3	168
	40.16	11.32	47.90	0.44	0.20	100.0	88.3	175
	40.32	11.27	47.99	0.44	0.20	100.2	88.4	182
	40.26	11.27	47.97	0.44	0.20	100.1	88.4	189
	40.23	11.25	47.94	0.44	0.19	100.1	88.4	196
	40.30	11.25	48.09	0.44	0.20	100.3	88.4	203
	40.22	11.24	47.89	0.44	0.20	100.0	88.4	210
	40.21	11.27	47.99	0.44	0.20	100.1	88.4	217
	40.21	11.25	47.90	0.44	0.20	100.0	88.4	224
	40.20	11.23	47.86	0.44	0.20	99.9	88.4	231
	40.19	11.23	48.00	0.44	0.20	100.1	88.4	238
Unit 20 Olivine 27 *c*-axis	40.30	14.13	43.68	0.30	0.56	99.0	90.3	8
	39.34	15.66	44.21	0.27	0.25	99.7	89.4	16
	39.30	16.29	43.71	0.28	0.24	99.8	89.0	24
	39.15	16.47	43.49	0.29	0.22	99.6	88.8	32
	39.16	16.67	43.52	0.30	0.21	99.9	88.7	40
	39.19	16.77	43.54	0.31	0.20	100.0	88.6	48
	39.12	16.82	43.31	0.31	0.20	99.8	88.5	56
	39.13	17.16	43.32	0.32	0.20	100.1	88.3	64
	39.09	17.34	43.09	0.32	0.19	100.0	88.2	72
	38.94	17.54	42.76	0.32	0.18	99.7	88.0	80
	38.97	17.85	42.75	0.33	0.18	100.1	87.8	88
	39.01	18.09	42.54	0.33	0.18	100.1	87.6	96
	38.94	18.36	42.39	0.32	0.17	100.2	87.4	104
	38.85	18.54	42.24	0.32	0.17	100.1	87.2	112
	38.63	18.76	42.03	0.33	0.17	99.9	87.0	120
	38.76	18.89	41.85	0.33	0.16	100.0	86.9	128
	38.73	19.06	41.80	0.33	0.17	100.1	86.8	136
	38.73	19.15	41.62	0.33	0.16	100.0	86.7	144
	38.67	19.34	41.42	0.32	0.16	99.9	86.5	152
	38.63	19.44	41.38	0.32	0.16	99.9	86.5	160
	38.67	19.66	41.31	0.32	0.17	100.1	86.3	168
	38.67	19.77	41.19	0.32	0.16	100.1	86.2	176
	38.59	19.80	41.18	0.32	0.16	100.1	86.2	184
	38.57	19.76	41.04	0.32	0.16	99.8	86.2	192
	38.66	19.96	41.05	0.32	0.16	100.2	86.1	200
	38.53	20.01	40.97	0.33	0.16	100.0	86.0	208
	38.58	20.11	40.94	0.32	0.16	100.1	85.9	216
	38.53	20.12	40.93	0.32	0.16	100.1	85.9	224
	38.56	20.14	40.93	0.32	0.16	100.1	85.9	232
	38.54	20.18	40.83	0.32	0.16	100.0	85.9	240
	38.22	19.95	40.44	0.32	0.16	99.1	85.9	248
	38.46	20.15	40.88	0.32	0.17	100.0	85.9	256
	38.62	20.19	40.88	0.32	0.17	100.2	85.9	264
	38.46	20.21	40.68	0.32	0.16	99.8	85.8	272
	38.52	20.29	40.85	0.32	0.17	100.1	85.8	280
	38.51	20.22	40.70	0.32	0.16	99.9	85.8	288
	38.47	20.25	40.69	0.32	0.16	99.9	85.8	296
	38.46	20.20	40.73	0.32	0.16	99.9	85.8	304
	38.46	20.26	40.76	0.33	0.16	100.0	85.8	312

Sample	SiO_2	FeO	MgO	NiO	CaO	Total	Fo*	x (μm)
	38.50	20.25	40.73	0.32	0.16	100.0	85.8	320
	38.39	20.28	40.69	0.32	0.16	99.8	85.8	328
	38.47	20.28	40.73	0.32	0.16	100.0	85.8	336
	38.45	20.34	40.62	0.32	0.17	99.9	85.7	344
	38.41	20.31	40.75	0.32	0.17	100.0	85.7	352
	38.59	20.36	40.77	0.32	0.17	100.2	85.7	360
	38.48	20.30	40.69	0.33	0.16	100.0	85.7	368
	38.40	20.31	40.67	0.32	0.16	99.9	85.7	376
	38.41	20.32	40.64	0.32	0.16	99.9	85.7	384
	38.45	20.35	40.65	0.32	0.16	99.9	85.7	392
	38.44	20.34	40.74	0.32	0.16	100.0	85.7	400
	38.50	20.36	40.74	0.32	0.17	100.1	85.7	408
	38.46	20.39	40.68	0.32	0.16	100.0	85.7	416
	38.20	20.41	40.60	0.32	0.16	99.7	85.6	424
	38.49	20.34	40.68	0.32	0.16	100.0	85.7	432
	38.48	20.41	40.67	0.33	0.16	100.1	85.7	440
	38.40	20.34	40.58	0.32	0.16	99.8	85.7	448

Note(s): * Fo, forsterite = [Mg/(Mg+Fe) x 100]. x is distance from olivine rim in μm.

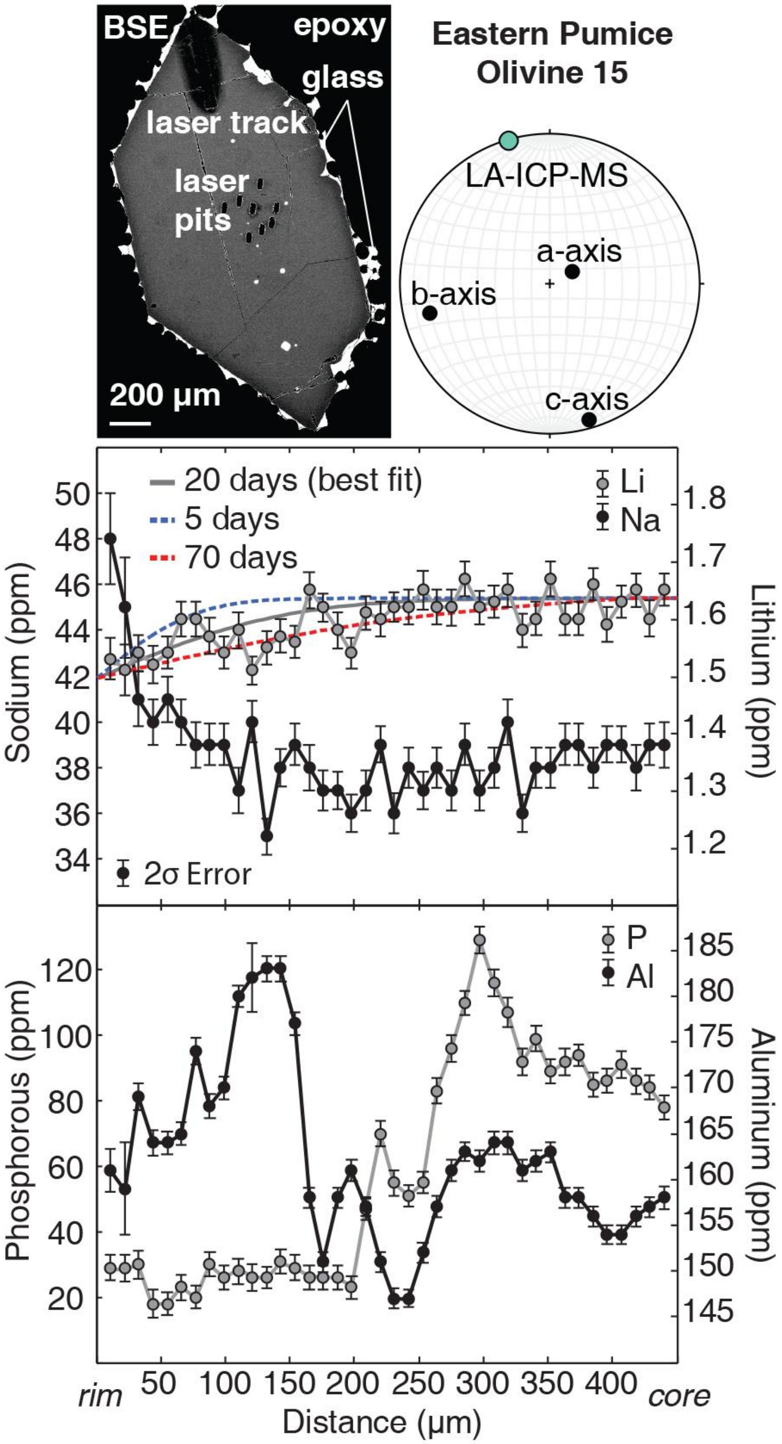

Figure C1. Trace element zoning for an olivine from the Eastern Pumice with reverse zoning of Fe-Mg in backscatter electron (BSE) image. In this transect parallel to the *c*-axis Li and Na show dominantly smooth diffusion profiles inversely zoned to each other. Best-fit Li timescales are presented with minimum and maximum estimates to consider analytical error and noise. P and Al are decoupled and inversely zoned over 100's of μm, characteristic of approximately half of all KT olivine examined in this study.

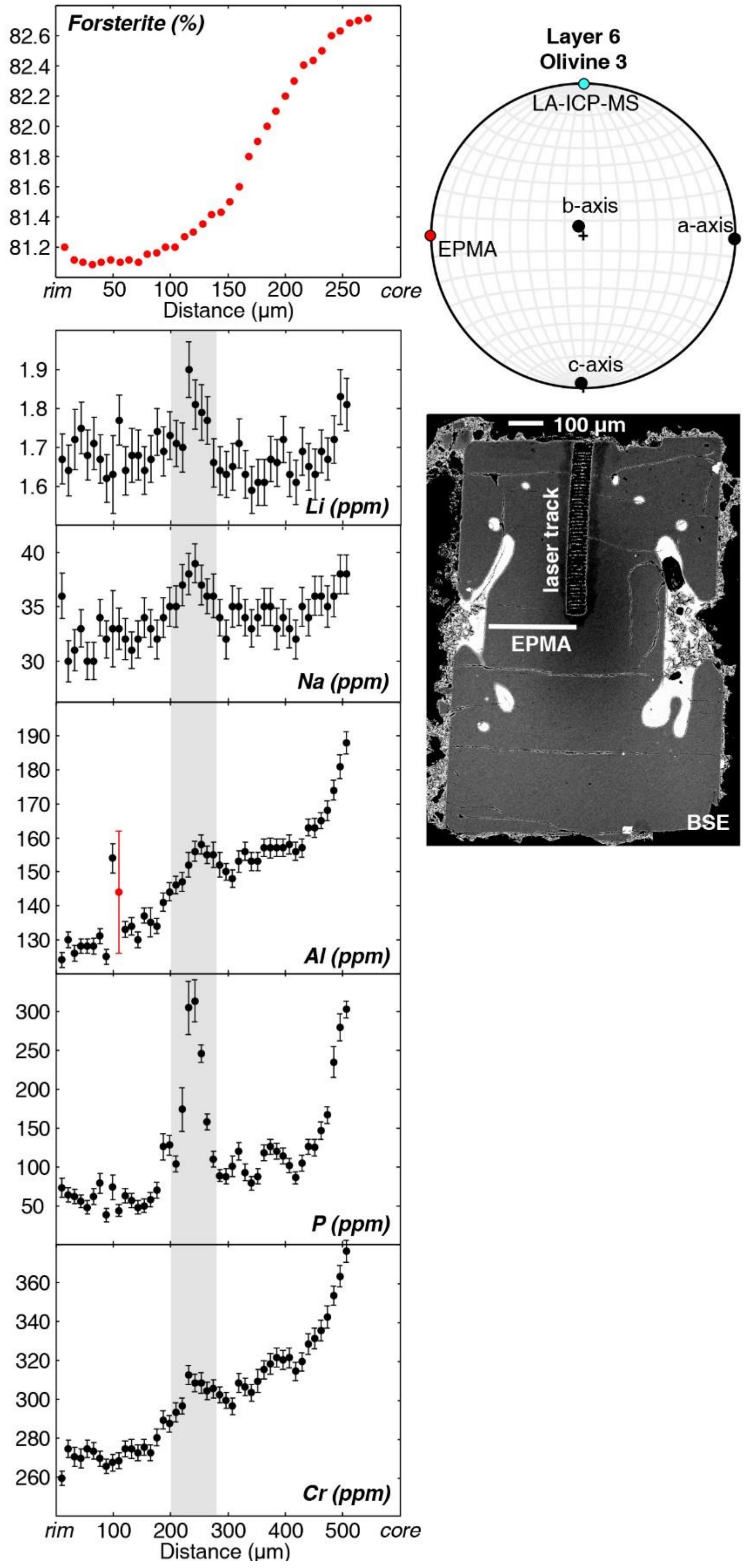

Figure C2. Trace element zoning for a Layer 6 olivine crystal with normal Fo zoning. In this example, all trace elements (Li, Na, P, Al, and Cr) share similar zoning morphologies and preserve enrichment features in the same place.

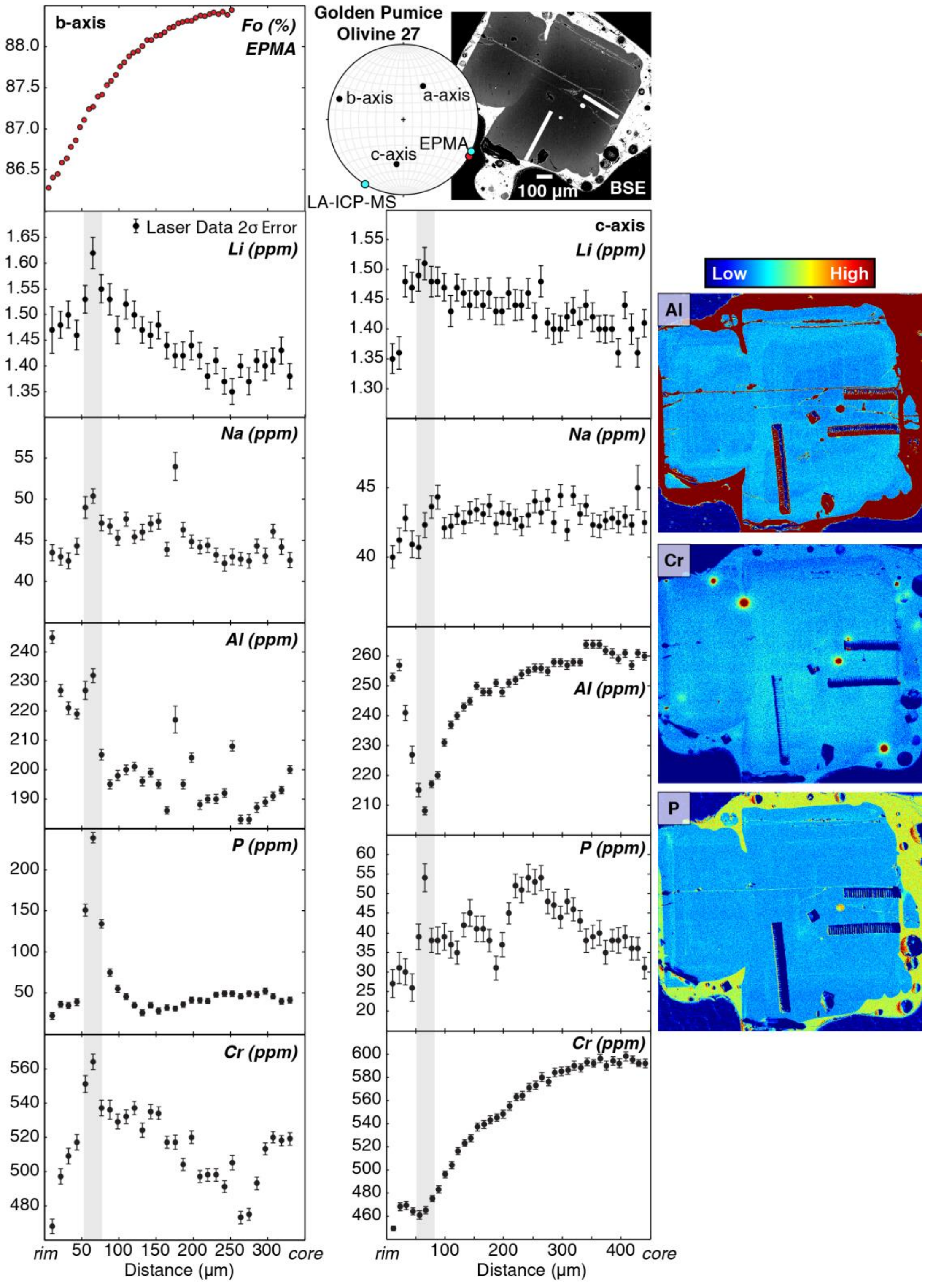

Figure C3. Trace element zoning for two transects from a Golden Pumice olivine that shows no Li diffusion. Lithium zoning mimics P, which is decoupled from Na, Al, and Cr. The *c*-axis transect shows a smooth diffusion profile for Cr. X-Ray maps show complex interior zoning for Al, P, and Cr which do not consistently correlate with each other.

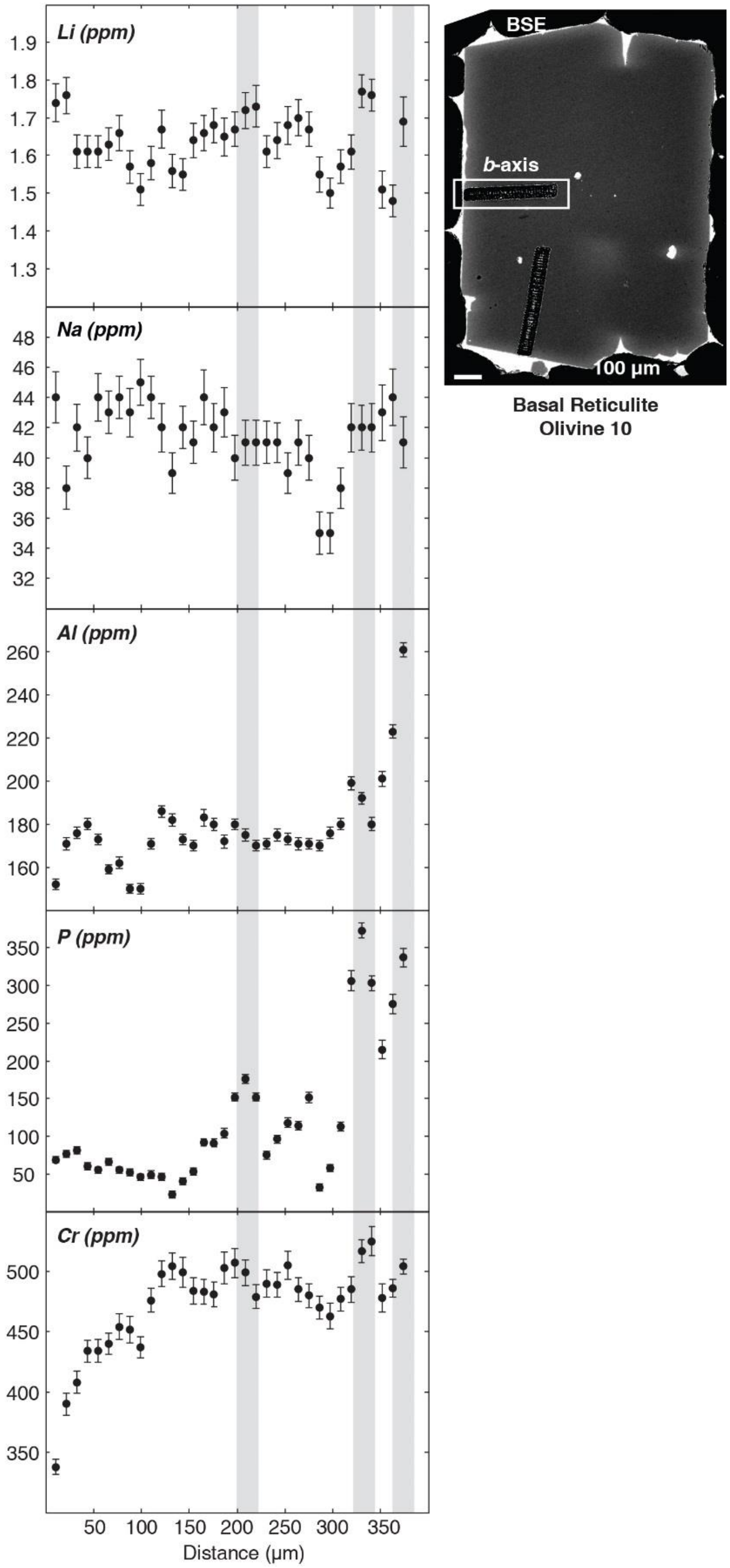

Figure C4. Trace element zoning for the *b*-axis transect from Basal Reticulite Olivine 10. Lithium mimics P in the interior of the crystal (150-400 μm) where P concentrations generally exceed 100 ppm.

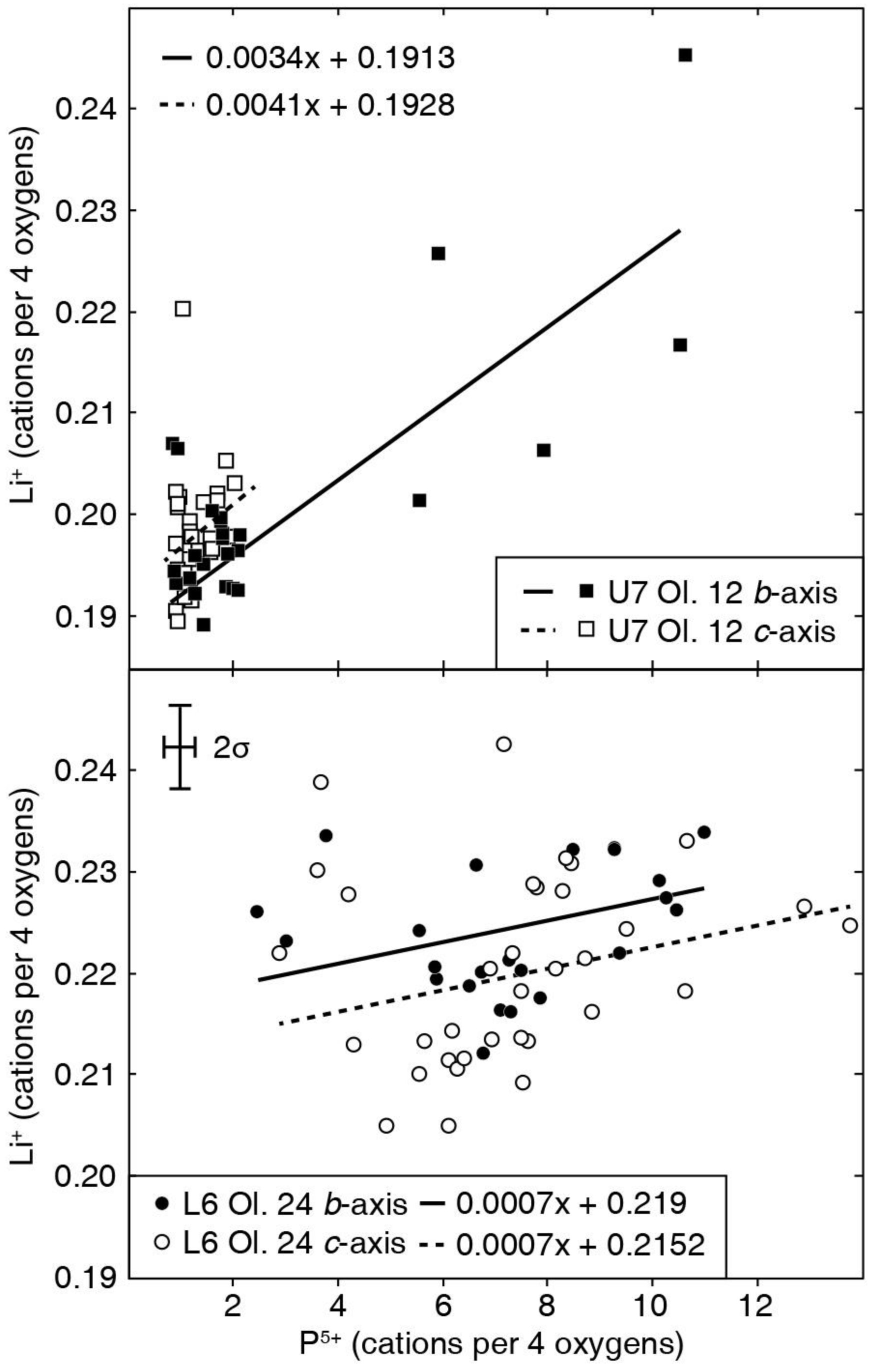

Figure C5. P^{5+} against Li^{+} in olivine, cations per formula unit of four oxygens. Data for Unit 7 Ol. 12 and Layer 6 Ol. 24 are presented because they have growth features (Unit 20 Ol. 27 has enrichment peaks and preserves diffusion). The scatter in the data probably result from the homogenization of high- and low-P (and inferred high- and low-Li) by the 10 x 50 µm spot size during analysis. Analytical error converted to molar concentrations is represented by 2σ error bars. Note that the slopes of the correlations are small (<< 1), indicating that the majority of P incorporated into these olivine crystals must be charge balanced by other mechanisms. This observation is consistent with Li and P relationships documented by Mallmann et al. 2009.

REFERENCES CITED

Anderson, K.R., Poland, M.P., Johnson, J.H., and Miklius, A. (2015) Episodic deflation-inflation events at Kīlauea Volcano and Implications for the shallow magma system. In Geophysical Monograph 208. Carey, Cayol, Poland, and Weis, Eds., Hawaiian Volcanoes: From Source to Surface, p. 229-250, American Geophysical Union, Washington, D.C., USA. doi: 10.1002/9781118872079.ch11

Agrell, S.O., Charnley, N.R., and Ghinner, G.A. (1998) Phosphoran olivine from Pine Canyon, Piute Co., Utah. Mineralogical Magazine, 62, 265-269. doi: 10.1180/002646198547620

Albarede, F., and Bottinga, Y. (1972) Kinetic disequilibrium in trace element partitioning between phenocrysts and host lava. Geochimica et Cosmochimica Acta, 36, 141-156. doi: 10.1016/0016-7037(72)90003-8

Armstrong, J. T. (1988) Quantitative analyses of silicate and oxide materials: Comparison of Monte Carlo, ZAF, and φ(ρz) procedures. In Microbeam Analyses, D.E. Newbury, Ed., San Francisco Press, San Francisco, pp 239-246.

Asimow, F.D., and Ghiorso, M.S. (1998) Algorithmic modifications extending MELTS to calculate subsolidus phase relations. American Mineralogist, 83, 1127-1132. doi: 10.2138/am-1998-9-1022

Ballmer, M.D., Ito, G., and Cheng, C. (2015) Asymmetric dynamical behavior of thermochemical plumes and implications for Hawaiian lava composition. In Geophysical Monograph 208. Carey, Cayol, Poland, and Weis, Eds., Hawaiian Volcanoes: From Source to Surface, p. 35-57, American Geophysical Union, Washington, D.C., USA. doi: 10.1002/9781118872079.ch3

Beattie, P., Ford, C., and Russel, D. (1991) Partition coefficients for olivine-melt and orthopyroxene-melt systems. Contributions to Mineralogy and Petrology, 109, 212-224. doi: 10.1007/BF00306480

Bershov, L.V., Gaite, J-M., Hafner, S.S., and Rager, H. (1983) Electron paramagnetic resonance and ENDOR studies of Cr^{3+} - Al^{3+} pairs in forsterite. Physics and Chemistry of Minerals, 9, 95-101. doi: 10.1007/BF00308364

Boesenberg, J.S., Ebel, D.S., and Hewins, R.H. (2004) An experimental study of phosphoran olivine and its significance in main group pallasites. Lunar and Planetary Science Conference, 1366.

Bouvet de Maisonneuve, C., Costa, F., Huber, C., Vonlanthen, P., Bachmann, O., and Dungan, M.A. (2016) How do olivines record magmatic events? Insights from major and trace element zoning. Contributions to Mineralogy and Petrology, 171, 1-20. doi: 10.1007/s00410-016-1264-6

Brenan, J.M., Neroda, E., Lundstrom, C.C., Shaw, H.F., Ryerson, F.J., and Phinney, D.L. (1998) Behaviour of boron, beryllium, and lithium during melting and crystallization: Constraints from mineral-melt partitioning experiments. Geochimica et Cosmochimica Acta, 62, 2129-2141. doi: 10.1016/S0016-7037(98)00131-8

Buening, D.K., and Buseck, P.R. (1973) Fe-Mg lattice diffusion in olivine. Journal of Geophysical Research, 78, 6852-6862. doi: 10.1029/JB078i029p06852

Byers, C.D., Garcia, M.O., and Muenow, D.W. (1985) Volatiles in pillow rim glasses from Loihi and Kilauea volcanoes, Hawaii. Geochimica et Cosmochimica Acta, 49, 1887-1896. doi: 10.1016/0016-7037(85)90083-3

Cardozo, N., and Allmendinger, R.W. (2013) Spherical projections with OSXStereonet. Computers and Geosciences, 51, 193-205. doi: 10.1016/j.cageo/2012.07.021

Cayol, V., Dieterich, J.H., Okamura, A.T., and Miklius, A. (2000) High magma storage rates before the 1983 eruption of Kilauea, Hawaii. Science, 288, 2343-2346. doi: 10.1126/science.288.5475.2343

Cervelli, P.F., and Miklius, A. (2003) The shallow magmatic system of Kilauea Volcano. U.S. Geological Survey Professional Paper, 1676, 149-163.

Chakraborty, S. (1997) Rates and mechanisms of Fe-Mg interdiffusion in olivine at 980°-1300°C. Journal of Geophysical Research, 102, 12317-12331. doi: 10.1029/97JB00208

Chakraborty, S. (2010) Diffusion coefficients in olivine, wadsleyite and ringwoodite. In Diffusion in Minerals and Melts, Zhang, Y., and Cherniak, D.J., Eds., Reviews in Mineralogy and Gochemistry, 72, pp 603-639. doi: 10.2138/mg.2010.72.13

Charlier, B.L.A., Morgan, D.J., Wilson, C.J.N., Wooden, J.L., Allan, A.S.R., and Baker, J.A. (2012) Lithium concentration gradients in feldspar and quartz record the final minutes of magma ascent in an explosive supereruption. Earth and Planetary Science Letters, 319-320, 218-227. doi: 10.1016/j.epsl.2011.12.016

Chemtob, S.M., Jolliff, B.L., Rossman, G.R., Eiler, J.M., and Arvidson, R.E. (2010) Silica coatings in the Ka‘u Desert, Hawaii, a Mars analog terrain: A micromorphological, spectral, chemical, and isotopic study. Journal of Geophysical Research (Planets), 115, E04001. doi: 10.10298/2009JE003473.

Cherniak, D.J., and Liang, Y. (2014) Titanium diffusion in olivine. Geochimica et Cosmochimica Acta, 147, 43-57. doi: 10.1016/j.gca.2014.10.016

Clague, D.A., and Dalrymple, G.B. (1987) The Hawaiian-Emperor volcanic chain: Part I, Geologic Evolution. In Volcanism in Hawaii, v. 1. Decker, Wright, and Stauffer, Eds., U.S. Geological Survey Professional Paper, 1350, 5-54.

Clague, D.A., and Denlinger, R.P. (1994) Role of olivine cumulates in destabilizing the flanks of Hawaiian volcanoes. Bulletin of Volcanology, 56, 425-434. doi: 10.1007/BF00302824

Clauge, D.A., Moore, J.G., Dixon, J.E., and Friesen, W.B. (1995) Petrology of submarine lavas from Kilaueas Puna Ridge, Hawaii. Journal of Petrology, 36, 229-349. doi: 10.1093/petrology/36.2.299

Coogan, L.A., Hain, A., Stahl, S., and Chakraborty, S. (2005) Experimental determination of the diffusion coefficient for calcium in olivine between 900°C and 1500°C. Geochimica et Cosmochimica Acta, 369, 3683-3694. doi: 10.1016/j.gca.2005.03.002

Cooper, K.M., and Kent, A.J.R. (2014) Rapid remobilization of magmatic crystals kept in cold storage. Nature, 506, 480-483. doi:10.1038/nature12991

Corbi, F., Rivalta, E., Pinel, V., Maccaferri, F., Bagnardi, M., and Acocella, V. (2015) How caldera collapse shapes the shallow emplacement and transfer of magma in active volcanoes. Earth and Planetary Science Letters, 431, 287-293. doi: 10.1016/j.epsl.2015.09.028

Costa, F., and Chakraborty, S. (2004) Decadal time gaps between mafic intrusion and silicic eruption obtained from chemical zoning patterns in olivine. Earth and Planetary Science Letters, 224, 517-530. doi: 10.1016/.j.epsl.2004.08.011

Costa, F., and Dungan, M. (2005) Short time scales of magmatic assimilation from diffusion modeling of multiple elements in olivine. Geology, 33, 837-840. doi: 10.1130/G21675.1

Costa, F., Dohmen, R., and Chakraborty, S. (2008) Time scales of magmatic processes from modeling the zoning patterns of crystals. Reviews in Mineralogy and Geochemistry, 69, 545-594. doi: 10.2138/rmg.2008.69.14

Crank, J. (1975) The Mathematics of Diffusion, 2nd edition, 414 p. Oxford Science Publication, Oxford.

Davis, F.A., Cottrell, E., Birner, S.K., Warren, J., and Lopez, O.G. (2017) Revisiting the electron microprobe method of spinel-olivine-orthopyroxene oxybarometry applied to spinel peridotites. American Mineralogist, 102, 421-435. doi: 10.2138/am-2017-5823.

Decker, R.W., and Christiansen, R.L. (1984) Explosive eruptions of Kilauea Volcano, Hawaii. In Explosive Volcanism: Inception, Evolution, and Hazards, 122-132, National Academy Press, Washington, D.C., USA.

Decker, R.W., Okamura, A., Miklius, A., and Poland, M. (2008) Evolution of deformation studies on active Hawaiian volcanoes. U.S. Geological Survey Scientific Investigations Report, 2008-5090, 23 p.

Denlinger, R.P. (1997) A dynamic balance between magma supply and eruption rate at Kilauea volcano, Hawaii. Journal of Geophysical Research, 102, 18091-18100. doi: 10.1029/97JB01071

Dohmen, R., and Chakraborty, S. (2007a) Fe-Mg diffusion in olivine II: point defect chemistry, change of diffusion mechanisms and a model for calculation of diffusion coefficients in natural olivine. Physics and Chemistry of Minerals, 34, 409-430. doi: 10.1007/s00269-007-0158-6

Dohmen, R., and Chakraborty, S. (2007b) Erratum on “Fe-Mg diffusion in olivine II: Point defect chemistry, change of diffusion mechanisms and a model for calculation of diffusion coefficients in natural olivine." Physics and Chemistry of Minerals, 34, 597-598. doi: 10.1007/s00269-007-0185-3

Dohmen, R., Kasemann, S.A., Coogan, L., and Chakraborty, S. (2010) Diffusion of Li in olivine. Part I: Experimental observations and a multi-species diffusion model. Geochimica et Cosmochimica Acta, 74, 274-292. doi: 10.1016/j.gca.2009.10.016

Donaldson, C.H. (1976) An experimental investigation of olivine morphology. Contributions to Mineralogy and Petrology, 57, 187-213. doi: 10.1007/BF00405225

Donovan, J.J., and Tingle, T.N. (1996) An improved mean atomic number correction for quantitative microanalysis. Journal of Microscopy, 2, 1-7. doi: 10.1017/S1431927696210013

Dvorak, J.J., and Dzurisin, D. (1993) Variations in magma supply rate at Kilauea Volcano, Hawaii. Journal of Geophysical Research, 98, 22255-22268. doi: 10.1029/93JB02765

Dzurisin, D., Lockwood, J., Casadevall, T.J., and Rubin, M. (1995) The Uwekahuna Ash Member of the Puna Basalt: product of violent phreatomagmatic eruptions at Kilauea volcano, Hawaii, between 2800 and 2100 ^{14}C years ago. Journal of Volcanology and Geothermal Research, 66, 163-184. doi: 10.1016/0377-0273(94)00062-L

Easton, M.E. (1987) Stratigraphy of Kilauea Volcano. In Volcanism in Hawaii v. 1. Decker, Wright, and Stauffer, Eds., U.S. Geological Survey Professional Paper, 1350, 243-260.

Easton, R.M., and Garcia, M.O. (1980) Petrology of the Hilina Formation, Kilauea Volcano, Hawaii. Bulletin of Volcanology, 43, 657-673. doi: 10.1007/BF02600364

Edmonds, M. (2015) Partitioning of light lithophile elements during basalt eruptions on Earth and application to Martian shergottites. Earth and Planetary Science Letters, 411, 142-150. doi: http//dx.doi.org/10.1016/j.epsl.2014.11.034.

Edmonds, M., Sides, I.R., Swanson, D.A., Werner, C., Martin, R.S., Mather, T.A., Herd, R.A., Jones, R.L., Mead, M.I., Sawyer, G., Roberts, T.J., Sutton, A.J., and Elias, T. (2013) Magma storage, transport and degassing during the 2008-2010 summit eruption at Kīlauea Volcano, Hawaiʻi. Geochimica et Cosmochimica Acta, 123, 284-301. doi: 10.1016/j.gca.2013.05.038

Eggins, S.M. (1991) Petrogenesis of Hawaiian tholeiites: 1, phase equilibria constants. Contributions to Mineralogy and Petrology, 110, 387-397. doi: 10.1007/BF00310752

Ellis, W. (1827) Narrative of a tour through Hawaii, or, Owhyhee; with observations on the natural history of the Sandwich Islands, and remarks on the manners, customs, traditions, history, and language of their inhabitants. 2nd edition, Fisher Son and Jackson, London, 480 p.

Faure, F., Trolliard, G., Nicollet, C., and Montel, J-M. (2003a) A developmental model of olivine morphology as a function of the cooling rate and degree of undercooling. Contributions to Mineralogy and Petrology, 145, 251-263. doi: 10.1007/s00410-003-0449-y

Faure, F., Trolliard, G., and Soulestin, B. (2003b) TEM investigations of forsterite dendrites. American Mineralogist, 88, 1241-1250. doi: 10.2138/am-2003-8-907

Faure, F., and Schiano, P. (2005) Experimental investigation of equilibration conditions during forsterite growth and melt inclusion formation. Earth and Planetary Science Letters, 236, 882-898. doi: 10.1016/j.epsl.2005.04.050

Ferguson, D.J., Gonnermann, H.M., Ruprecht, P., Plank, T., Hauri, E.H., Houghton, B.F., and Swanson, D.A. (2016) Magma decompression rates during explosive eruptions of Kīlauea volcano, Hawaii, recorded by melt embayments. Bulletin of Volcanology, 78, 1-12. doi: 10.1007/s00445-016-1064-x

Fiske, R.S., Rose, T.R., Swanson, D.A., Champion, D.E., and McGeehin, J.P. (2009) Kulanaokuaiki Tephra (ca. A.D. 400-1000): Newly recognized evidence for highly explosive eruptions at Kīlauea Volcano, Hawaiʻi. Geological Society of America Bulletin, 121, 712-728. doi: 10.1130/B26327.1

Frey, F.A., Garcia, M.O., and Roden, M.F. (1994) Geochemical characteristics of Koolau volcano: Implications of intershield geochemical differences among Hawaiian volcanoes. Geochimica et Cosmochimica Acta, 58, 1441-1462. doi: 10.1016/0016-7037(94)90547-7

Gaister, A.V., Konovalov, A.A., Shakurov, G.S., Subbotin, K.A., Tarasov, V.F., and Zharikov, E.V. (2003) High-frequency two-dimensional spectroscopy of Cr^{3+} and Ho^{3+} dimers in synthetic forsterite. Proceedings of SPIE – The International Society for Optical Engineering, 5478, 46-54. doi: 10.1117/12.558454

Garcia, M.O. (1996) Petrography and olivine and glass chemistry of lavas from the Hawaii Scientific Drilling Project. Journal of Geophysical Research, 101, 11701-11713. doi: 10.1029/95JB03846

Garcia, M.O. (2002) Submarine picritic basalts from Ko‘olau volcano, Hawaii: Implications for parental magma compositions and mantle source. In Geophysical Monograph 128. Takahashi, Lipman, Garcia, Naka, and Aramaki, Eds., Hawaiian Volcanoes: Deep Underwater Perspectives, p. 391-401. American Geophysical Union, Washington, D.C., USA. doi: 10.1029/GM128p0391

Garcia, M.O. (2015) How and why Hawaiian volcanism has become pivotal to our understanding of volcanoes from their source to the surface. In Geophysical Monograph 208. Carey, Cayol, Poland, and Weis, Eds., Hawaiian Volcanoes: From Source to Surface, p. 1-18, American Geophysical Union, Washington, D.C., USA. doi: 10.1002/9781118872079.ch1

Garcia, M.O., and Wolfe, E.W. (1988) Petrology of the erupted lava. In The Puu Oo eruption of Kilauea Volcano, Hawaii: Episodes 1 through 20, January 3, 1983, through June 8, 1984. Wolfe, Ed., U.S. Geological Survey Professional Paper, 1463, 127-143.

Garcia, M.O., Ho, R.A., Rhodes, J.M., and Wolfe, E.W. (1989) Petrologic constraints on rift-zone processes. Bulletin of Volcanology, 52, 81-96. doi: 10.1007/BF00301548

Garcia, M.O., Rhodes, J.M., Wolfe, E.W., Ulrich, G.E., and Ho, R.A. (1992). Petrology of lavas from episodes 2-47 of the Puu Oo eruption of Kilauea Volcano, Hawaii: Evaluation of magmatic processes. Bulletin of Volcanology, 55, 1-16. doi: 10.1007/BF0030115

Garcia, M.O., Jorgenson, B.A., Mahoney, J.J., Ito, E., and Irving, A.J. (1993) An evaluation of temporal geochemical evolution of Loihi summit lavas: Results from *Alvin* submersible dives. Journal of Geophysical Research Solid Earth, 98, 537-550. doi: 10.1029/92JB01707

Garcia, M.O., Hulseboch, T.P., and Rhodes, J.M. (1995) Olivine-rich submarine basalts from the southwest rift zone of Mauna Loa Volcano: Implications for magmatic processes and geochemical evolution. In Geophysical Monograph 92. Rhodes, J.M. and Lockwood, J.P., Eds., Mauna Loa Revealed: Structure, Composition, History, and Hazards, p. 219-239, American Geophysical Union, Washington, D.C., USA. doi: 10.1029/GM092p0219

Garcia, M.O., Rhodes, J.M., Trusdell, F.A., and Pietruszka, A.J. (1996) Petrology of lavas from the Puʻu ʻŌʻō eruption of Kīlauea Volcano: III. The Kupaianaha episode (1986-1992). Bulletin of Volcanology, 58, 359-379. doi: 10.1007/s004450050145

Garcia, M.O., Ito, E., Eiler, J.M., and Pietruszka, A.J. (1998) Crustal contamination of Kilauea Volcano magmas revealed by oxygen isotope analyses of glass and olivine from Puu Oo eruption lavas. Journal of Petrology, 39, 803-817. doi: 10.1093/petroj/39.5.803

Garcia, M.O., Pietruszka, A.J., Rhodes, J.M., and Swanson, K.J. (2000) Magmatic processes during the prolonged Puʻu ʻOʻo eruption of Kilauea Volcano, Hawaii. Journal of Petrology, 41, 967-990. doi: 10.1093/petrology/41.7.967

Garcia, M.O., Pietruszka, A.J., and Rhodes, J.M. (2003) A petrologic perspective of Kīlauea volcano’s summit magma reservoir. Journal of Petrology, 44, 2313-2339. doi: 10.1093/petrology/egg079

Garcia, M.O., Ito, E., and Eiler, J.M. (2008) Oxygen isotope evidence for chemical interaction of Kīlauea historical magmas with basement rocks. Journal of Petrology, 49, 757-769. doi: 10.1093/petrology/egm034

Gavrilenko, M., Ozerov, A., Kyle, P.R., Carr, M.J., Nikulin, A., Vidito, C., and Danyushevsky, L. (2016) Abrupt transition from fractional crystallization to magma mixing at Gorely volcano (Kamchatka) after caldera collapse. Bulletin of Volcanology, 78, 1-47.

Gerlach, T.M., McGee, K.A., Elias, T., Sutton, A.J., and Doukas, M.P. (2002) Carbon dioxide emission rate of Kīlauea Volcano: Implications for primary magma and the summit reservoir. Journal of Geophysical Research, 107, 2189-2204. doi: 10.1007/s00445-016-1038-z

Ghiorso, M.S., and Sack, R.O. (1995) Chemical mass transfer in magmatic processes IV. A revised and internally consistent thermodynamic model for the interpretation and extrapolation of liquid-solid equilibria in magmatic systems at elevated temperatures and pressures. Contributions to Mineralogy and Petrology, 119, 197-212. doi: 10.1007/BF00307281

Ghiorso, M.S., and Gualda, G.A.R. (2015) An H_2O-CO_2 mixed fluid saturation model compatible with rhyolite-MELTS. Contributions to Mineralogy and Petrology, 169, 1-30. doi: 10.1007/s00410-015-1141-8

Girona, T., and Costa, F. (2013) DIPRA: A user friendly program to model multi-element diffusion in olivine with applications to timescales of magmatic processes. Geochemistry, Geophysics, Geosystems, 14, 422-431. doi: 10.1029/2012GC004427

Goldich, S.S., Ingamells, C.O., Suhr, N.H., and Anderson, D.H. (1967) Analyses of silicate rock and mineral standards. Canadian Journal of Earth Science, 4, 747-755. doi: 10.1139/e67-052

Grant, K.J., and Wood, B.J. (2010) Experimental study of the incorporation of Li, Sc, Al, and other trace elements into olivine. Geochimica et Cosmochimica Acta, 74, 2412-2428. doi: 10.1016/j.gca.2010.01.015

Green, D.H., and Ringwood, A.E., (1967) The genesis of basaltic magmas. Contributions to Mineralogy and Petrology, 15, 103-190. doi: 10.1007/BF00372052

Greene, A.R., Garcia, M.O., Pietruszka, A.J., Weis, D., Marske, J.P., Vollinger, M.J., and Eiler, J. (2013) Temporal geochemical variations in lavas from Kīlauea’s Pu’u ‘Ō’ō eruption (1983-2010): Cyclic variations from melting of source heterogeneities. Geochemistry, Geophysics, Geosystems, 14, 4849-4873. doi: 10.1002/ggge.20285

Greenland, L.P. (1988) Gases from the 1983-1984 east-rift eruption. In The Puu Oo eruption of Kilauea Volcano, Hawaii: Episodes 1 through 20, January 3, 1983, through June 8, 1984. Wolfe, Ed., U.S. Geological Survey Professional Paper, 1463, 145-153.

Gualda, G.A.R., Ghiorso, M.S., Lemons, R.V., and Carley, T. (2012) Rhyolite MELTS: A modified calibration of MELTS optimized for silica-rich, fluid bearing magmatic systems. Journal of Petrology, 53, 875-890. doi: 10.1093/petrology/egr080

Gurenko, A.A., Hoernle, K.A., Sobolev, A.V., Hauff, F., and Schmincke, H-U. (2010) Source components of the Gran Canaria (Canary Islands) shield stage magmas: evidence from olivine composition and Sr-Nd-Pb isotopes. Contributions to Mineralogy and Petrology, 159, 689-702. doi: 10.1007/s00410-009-0448-8

Hammer, J., Jacob, S., Welsch, B., Hellebrand, E., and Sinton, J. (2015) Clinopyroxene in postshield Haleakala ankaramite: 1. Efficacy of thermobarometry. Contributions to Mineralogy and Petrology, 171, 7. doi: 10.1007/s00410-015-1212-x

Hart, S.R., and Davis, K.E. (1978) Nickel partitioning between olivine and silicate melt. Earth and Planetary Science Letters, 40, 203-219. doi: 10.1016/0012-821X(78)90091-2

Hartley, M.E., Morgan, D.J., Maclennan, J., Edmonds, E., and Thordarson, T. (2016) Tracking timescales of short-term precursors to large basaltic fissure eruptions through Fe-Mg diffusion in olivine. Earth and Planetary Science Letters, 439, 58-70. doi: 10.1016/j.epsl.2016.01.018

Haskins, E.H., and Garcia, M.O. (2004) Scientific drilling reveals geochemical heterogeneity within the Koʻolau shield, Hawaiʻi. Contributions to Mineralogy and Petrology, 147, 162-188. doi: 10.1007/s00410-003-0546-y

Helz, R.T. (1987) Diverse olivine types in lavas of the 1959 eruption of Kilauea Volcano and their bearing on eruption dynamics. In: Volcanism in Hawaii. Decker, Wright, and Stauffer, Eds., U.S. Geological Survey Professional Paper, 1350, 691-722.

Helz, R.T., and Thornber, C.R. (1987) Geothermometry of Kilauea Iki lava lake, Hawaii. Bulletin of Volcanology, 49, 651-668. doi: 10.1007/BF01080357

Helz, R.T., Clague, D.A., Sisson, T.W., and Thornber, C.R. (2014) Petrologic insights into basaltic volcanism at historically active Hawaiian volcanoes. In:

Characteristics of Hawaiian Volcanoes. Poland, Takahashi, and Landowski, Eds. U.S. Geological Survey Professional Paper, 1801, 237-292. doi: 10.3133/pp18016

Helz, R.T., Clague, D.A., Mastin, L.G., and Rose, T.R. (2015) Evidence for large compositions ranges in coeval melts erupted from Kīlauea's summit reservoir. In Geophysical Monograph 208. Carey, Cayol, Poland, and Weis, Eds., Hawaiian Volcanoes: From Source to Surface, p. 125-145, American Geophysical Union, Washington, D.C., USA. doi: 10.1002/9781118872079.ch7

Helz, R.T., Cottrell, E., Brounce, M.N., and Kelley, K.A. (2017) Olivine-melt relationships and syneruptive redox variations in the 1959 eruption of Kīlauea Volcano as revealed by XANES. Journal of Volcanology and Geothermal Research, (in press). doi: 10.1016/j.jvolgeores.2016.12.006

Herzberg, C. (2006) Petrology and thermal structure of the Hawaiian plume from Mauna Kea volcano. Nature, 444, 605-609. doi: 10.1038/nature05254

Herzberg, C., Asimow, P.D., Ionov, D.A., Vidito, C., Jackson, M.G., and Geist, D. (2013) Nickel and helium evidence for melt above the core-mantle boundary. Nature, 493, 393-397. doi: 10.1038/nature11771

Herzberg, C., Cabral, R.A., Jackson, M.G., Vidito, C., Day, J.M.D., and Hauri, E.H. (2014) Phantom Archean crust in Mangaia hotspot lavas and the meaning of heterogeneous mantle. Earth and Planetary Science Letters, 396, 97-106. doi: 10.1016/j.epsl.2014.03.065

Herzberg, C., Vidito, C., and Starkey, N.A. (2016) Nickel-Cobalt contents of olivine record origins of mantle peridotite and related rocks. American Mineralogist, 101, 1952-1966. doi: 10.2138/am-2016-5538

Hill, D.P., and Zucca, J.J. (1987) Geophysical constraints on the structure of Kilauea and Mauna Loa volcanoes and some implications for seismomagmatic processes. In: Volcanism in Hawaii v. 2. Decker, Wright, and Stauffer, Eds., U.S. Geological Survey Professional Paper, 1350, 903-917.

Holcomb, R.T. (1987) Eruptive history and long-term behavior of Kilauea Volcano. In Volcanism in Hawaii v. 1. Decker, Wright, and Stauffer, Eds., U.S. Geological Survey Professional Paper, 1350, 261-350.

Holzapfel, C., Chakraborty, S., Rubie, D.C., and Frost, D.J. (2007) Effect of pressure on Fe-Mg, Ni, and Mn diffusion in $(Fe_xMg_{1-x})_2SiO_4$ olivine. Physics of the Earth and Planetary Interiors, 162, 186-198. doi: 10.1016/j.pepi.2007.04.009

Humphreys, M.C.S., Menand, T., Blundy, J.D., and Klimm, K. (2008) Magma ascent rates in explosive eruptions: Constraints from H_2O diffusion in melt inclusions. Earth and Planetary Science Letters, 270, 25-40. doi: 10.1016/j.epsl.2008.02.041

Ito, M., and Ganguly, J. (2006) Diffusion kinetics of Cr in olivine and ^{53}Mn-^{53}Cr thermochronology of early solar system objects. Geochimica et Cosmochimica Acta, 70, 799-809. doi: 10.1016/j.gca.2005.09.020

Jackson, M.C., Frey, F.A., Garcia, M.O., and Wilmoth, R.A. (1999) Geology and geochemistry of basaltic lava flows and dikes from the Trans-Koolau tunnel, Oahu, Hawaii. Bulletin of Volcanology, 60, 381-401. doi: 10.1007/s004450050239

Jambon, A., Lussiez, P., Clocchiatti, R., Weisz, J., and Hernandez, J. (1992) Olivine growth rates in a tholeiitic basalt: An experimental study of melt inclusions in plagioclase. Chemical Geology, 96, 277-287. doi: 10.1016/0009-2541(92)90059-E.

Jarosewich, E., Nelen, J.A., and Norberg, J.A. (1980) Reference samples for electron microprobe analysis. Geostandards Newsletters, 4, 43-47. doi: 10.1111/j.1751-908X.1980.tb00273.x

Jochum, K.P., Weis, U., Stoll, B., Kuzmin, D., Qichao, Y., Raczek, I., Jacob, D.E., Stracke, A., Birbaum, K., Frick, D.A., Günther, D., and Enzweiler, J. (2011) Determination of reference values for NIST SRM 610-617 glasses following ISO guidelines. Geostandards in Geoanalytical Research, 35, 397-429. doi: 10.1111/j.1751-908X.2011.00120.x

Jochum, K.P., Weis, U., Schwager, B., Stoll, B., Wilson, S.A., Haug, G.H., Andreae, M.O., and Enzweiler, J. (2016) Reference values following ISO guidelines for frequently requested rock reference materials. Geostandards in Geoanalytical Research, 40, 333-350. doi: 10.1111/j.1751-908X.2015.00392.x

Jollands, M.C., Burnham, A.D., O'Neill, H.S.C., Hermann, J., and Qian, Q. (2016a) Beryllium diffusion in olivine: A new tool to investigate timescales of magmatic processes. Earth and Planetary Science Letters, 450, 71-82. doi: 10.1016/j.epsl.2016.06.028

Jollands, M.C., Padrón-Navarta, J.A., Hermann, J., and O'Neill, H.S.C. (2016b) Hydrogen diffusion in Ti-doped forsterite and the preservation of metastable point defects. American Mineralogist, 101, 1571-1583. doi: 10.2138/am-2016-5568

Jollands, M.C., Hermann, J., O'Neill, H.S.C., Spandler, C., and Padrón-Navarta, J.A. (2016c) Diffusion of Ti and some divalent cations in olivine as a function of temperature, oxygen fugacity, chemical potentials and crystal orientation. Journal of Petrology, 57, 1983-2010. doi: 10.1093/petrology/egw067

Kahl, M., Chakraborty, S., Costa, F., and Pompilio, M. (2011) Dynamic plumbing system beneath volcanoes revealed by kinetic modeling, and the connection to monitoring data: An example from Mt. Etna. Earth and Planetary Science Letters, 308, 11-22. doi: 10.1016/j.epsl.2011.05.008

Kahl, M., Chakraborty, S., Costa, F., Pompilio, M., Liuzzo, M., and Viccaro, M. (2013) Compositionally zoned crystals and real-time degassing data reveal changes in magma transfer dynamics during the 2006 summit eruptive episodes of Mt. Etna. Bulletin of Volcanology, 75, 1-14. doi: 10.1007/s00445-013-0692-7

Kauahikaua, J., and Poland, M. (2012) One hundred years of volcano monitoring in Hawaii. EOS Transactions, 93, 29-40. doi: 10.1029/2012EO030001

Keller, R.A., Fiske, M.R., and Duncan, R.A. (1995) Geochemistry and ^{40}Ar/^{39}Ar geochronology of basalts from ODP Leg 145 (North Pacific Transect). Rea, Basov, Scholl, and Allan, Eds. Proceedings of the Ocean Drilling Program: Scientific Results, 145, 333-344. doi: 10.2973/odp.proc.sr.145.131.1995

Kilburn, C.R.J. (2015) Lava flow hazards and modeling. In: The Encyclopedia of Volcanoes. Sigurdsson, Houghton, McNutt, Rymer, and Stix, eds. Elsevier, p. 957-934.

Kinzler, R.J., Grove, T.L., and Recca, S.J. (1990) An experimental study on the effect of temperature and melt composition on the partition of nickel between olivine and silicate melt. Geochimica et Cosmochimica Acta, 54, 1255-1265. doi: 10.1016/0016-7037(90)90151-A

Koyanagi, R.Y., Tanigawa, W.R., and Nakata, J.S. (1988) Seismicity associated with the eruption. In The Puu Oo eruption of Kilauea Volcano, Hawaii: Episodes 1 through 20, January 3, 1983, through June 8, 1984. Wolfe, Ed., U.S. Geological Survey Professional Paper, 1463, 183-235.

Lasaga, A.C. (1979) Multicomponent exchange and diffusion in silicates. Geochimica et Cosmochimica Acta, 43, 455-469. doi: 10.1016/0016-7037(79)90158-3

Li, C., and Ripley, E.M. (2010) The relative effects of composition and temperature on olivine-liquid Ni partitioning: Statistical deconvolution and implications for petrological modeling. Chemical Geology, 275, 99-104. doi: 10.1016/j.chemgeo.2010.05.001

Li, X., Kind, R., Yuan, X., Wölbern, I., and Hanka, W. (2004) Rejuvenation of the lithosphere by the Hawaiian plume. Nature, 427, 827-829. doi: 10.1038/nature02349

Lin, G., Amelung, F., Lavallée, Y., and Okubo, P.G. (2014) Seismic evidence for a crustal magma reservoir beneath the upper east rift zone of Kilauea volcano, Hawaii. Geology, 42, 187-190. doi: 10.1130/G35001.1

Linde, A.T., and Sacks, I.S. (1995) Continuous monitoring of volcanoes with borehole strainmeters. In Geophysical Monograph 92. Rhodes and Lockwood, Eds., Mauna Loa Revealed: Structure, Composition, History, and Hazards, p. 171-185, American Geophysical Union, Washington, D.C., USA. doi: 10.1029/GM092p0171

Lloyd, A.S., Ruprecht, P., Hauri, E.H., Rose, W., Gonnermann, H.M., and Plank, T. (2014) NanoSIMS results from olivine-hosted melt embayments: Magma ascent rate during explosive basaltic eruptions. Journal of Volcanology and Geothermal Research, 283, 1-18. doi: 10.1016/j.jvolgeores.2014.06.002

Lynn, K.J., Shea, T., and Garcia, M.O. (2017) Nickel variability in Hawaiian olivine: Evaluating the relative contributions from mantle and crustal processes. American Mineralogist, 102, 507-518. doi: 10.2138/am-2017-5763.

Lynn, K.J., Garcia, M.O., Shea, T., and Costa, F. (in review) Timescales of mixing and storage for Keanakākoʻi Tephra magmas (1500-1823 C.E.), Kīlauea Volcano, Hawaiʻi. Submitted to Contributions to Mineralogy and Petrology.

Maaløe, S., Pederson, R.B., and James, D. (1988) Delayed fractionation of basaltic lavas. Contributions to Mineralogy and Petrology, 98, 401-407. doi: 10.1007/BF00372360

Macdonald, G.A., Abbott, A.T., and Peterson, F.L. (1983). Volcanoes in the Sea. University of Hawaii Press, Honolulu, USA, 517 p.

Mallmann, G., O'Neill, H.S.C., and Klemme, S. (2009) Heterogeneous distribution of phosphorus in olivine from otherwise well-equilibrated spinel peridotite xenoliths and its implications for the mantle geochemistry of lithium. Contributions to Mineralogy and Petrology, 158, 485-504. doi: 10.1007/s00410-009-0393-6

Marlow, J.J., Martins, Z., and Sephton, M.A. (2008) Mars on Earth: soil analogues for future Mars missions. News and Reviews in Astronomy and Geophysics, 49, 2.20-2.23. doi: 10.1111/j.1468-4004.2008.49220.x

Marske, J.P., Pietruszka, A.J., Weis, D., Garcia, M.O., and Rhodes, J.M. (2007) Rapid passage of a small-scale mantle heterogeneity through the melting regions of Kilauea and Mauna Loa volcanoes. Earth and Planetary Science Letters, 259, 34-50. doi: 10.1016/j.epsl.2007.04.026

Marske, J.P., Garcia, M.O., Pietruszka, A.J., Rhodes, J.M., and Norman, M.D. (2008) Geochemical variations during Kīlauea's Pu‘u ‘Ō‘ō eruption reveal a fine-scale mixture of mantle heterogeneities within the Hawaiian plume. Journal of Petrology, 49, 1297-1318. doi: 10.1093/petrology/egn025

Mass, J.L., Burlitch, J.M., Budil, D.E., Freed, J.H., Barber, D.B., Pollock, C.R., Higuchi, M., and Dieckmann, R. (1995) Quenching of the fluorescence from chromium (III) ions in chromium-doped forsterite by an aluminum codopant. Chemistry of Materials, 7, 1008-1014. doi: 10.1021/cm00053a030

Mastin, L.G. (1997) Evidence for water influx from a caldera lake during the explosive hydromagmatic eruption of 1790, Kilauea volcano, Hawaii. Journal of Geophysical Research, 102, 20093-20109. doi: 10.1029/97JB01426

Mastin, L.G., Christiansen, R.L., Thornber, C., Lowenstern, J., and Beeson, M. (2004) What makes hydromagmatic eruptions so violent? Some insights from the Keanakāko‘i Ash, Kīlauea Volcano, Hawai‘i. Journal of Volcanology and Geothermal Research, 137, 15-31. doi: 10.1016/j/volgeores.2004.05.015

Matzen, A.K., Baker, M.B., Beckett, J.R., and Stolper, E.M. (2011) Fe-Mg partitioning between olivine and high-magnesian melts and the nature of Hawaiian parental liquids. Journal of Petrology, 52, 1243-1263.

Matzen, A.K., Baker, M.B., Beckett, J.R., and Stolper, E.M. (2013) The temperature and pressure dependence of Nickel partitioning between olivine and silicate melt. Journal of Petrology, 54, 2521-2545. doi: 10.1093/petrology/egq089

May, M., Carey, R.J., Swanson, D.A., and Houghton, B.F. (2015) Reticulite-producing fountains from ring fractures in Kīlauea Caldera ca. 1500 CE. In Geophysical Monograph 208. Carey, Cayol, Poland, and Weis, Eds., Hawaiian Volcanoes: From Source to Surface, p. 351-367, American Geophysical Union, Washington, D.C., USA. 10.1002/9781118872079.ch16

McCanta, M.C., Beckett, J.R., and Stolper, E.M. (2008) Zoning of phosphorus in olivine: Dynamic crystallization experiments and a study of chondrule olivine in unequilibrated ordinary chondrites. Lunar and Planetary Science Conference, 1807.

McCarty, R.J., and Stebbins, J.F. (2017) Constraints on aluminum and scandium substitution mechanisms in forsterite, periclase, and larnite: High resolution NMR. American Mineralogist, in press. doi: 10.2138/am-2017-5976

McDade, P., Blundy, J.D., and Wood, B.J. (2003) Trace element partitioning on the Tinaquillo Lherzolite solidus at 1.5 GPa. Physics of the Earth and Planetary Interiors, 139, 129-147. doi:10.1016/S0031-9201(03)00149-3

McPhie, J., Walker, G.P.L., and Christiansen, R.L. (1990) Phreatomagmatic and phreatic fall and surge deposits from explosions at Kilauea Volcano, Hawaii, 1790 A.D.: Keanakakoi Ash Member. Bulletin of Volcanology, 52, 334-354. doi: 10.1007/BF00302047

Milman-Barris, M.S., Beckett, J.R., Baker, M.B., Hofmann, A.E., Morgan, Z., Crowley, M.R., Vielzeuf, D., and Stolper, E. (2008) Zoning of phosphorus in igneous olivine. Contributions to Mineralogy and Petrology, 155, 739-765. doi: 10.1007/s00410-007-0268-7

Misener, D.J. (1974) Cationic diffusion in olivine to 1400 °C and 35 kbar. In Geochemical Transport and Kinetics. Hofmann, Giletti, Yoder, and Yund, Eds., Carnegie Institution of Washington, Washington D.C., p 117-129.

Montgomery-Brown, E.K., Poland, M.P., and Miklius, A. (2015) Delicate balance of magmatic-tectonic interaction at Kīlauea Volcano, Hawai‘i, revealed from slow slip events. In: Geophysical Monograph 208. Carey, Cayol, Poland, and Weis, eds., Hawaiian Volcanoes: From Source to Surface, p. 269-288, American Geophysical Union, Washington, D.C., USA. doi: 10.1002/9781118872079.ch13

Montierth, C., Johnston, D.A., and Cashman, K.V. (1995) An empirical glass-composition-based geothermometer for Mauna Loa lavas. In Geophysical Monograph 92. Rhodes and Lockwood, Eds., Mauna Loa Revealed: Structure, Composition, History, and Hazards, p. 207-217, American Geophysical Union, Washington, D.C., USA. doi: 10.1029/GM092p0207

Moore, J.G., and Ault, W.U. (1965) Historic littoral cones in Hawai‘i. Pacific Science, 19, 3-11.

Moussallam, Y., Edmonds, M., Scaillet, B., Peters, N., Gennaro, E., Sides, I., and Oppenheimer, C. (2016) The impact of degassing on the oxidation state of basaltic magmas: A case study of Kīlauea volcano. Earth and Planetary Science Letters, 450, 317-325. doi: 10.1016/j.epsl.2016.06.031

Mucek, A. (2012) Geochemistry of glasses from the Keanakāko‘i Tephra. Bachelor of Science Senior Thesis, submitted to the University of Hawai‘i at Mānoa.

Müller, R.D., Sdrolias, M., Gaina, C., and Roest, W.R. (2008) Age, spreading rates, and spreading asymmetry of the world’s ocean crust. Geochemistry, Geophysics, Geosystems, 9, DOI: 10.1029/2007GC001743.

Mysen, B., Virgo, D., and Seifert, F.A. (1985) Relationships between properties and structure of aluminosilicate melts. American Mineralogist, 70, 88-105.

Nakamura, M. (1995) Residence time and crystallization history of nickeliferous olivine phenocrysts from the northern Yatsugatake volcanoes, Central Japan: Application of a growth and diffusion model in the system Mg-Fe-Ni. Journal of Volcanology and Geothermal Research, 66, 81-100. doi: 10.1016/0377-0273(94)00054-K

National Geophysical Data Center (2006) 2-minute Gridded Global Relief Data (ETOPO2) v2. National Geophysical Data Center, NOAA. [accessed 2 January 2017] doi: 10.7289/V5J1012Q

Neal, C.A., Duggan, T.J., Wolfe, E.W., and Brandt, E.L. (1988) Lava samples, temperatures, and compositions. In The Puu Oo eruption of Kilauea Volcano, Hawaii: Episodes 1 through 20, January 3, 1983, through June 8, 1984. Wolfe, Ed., U.S. Geological Survey Professional Paper, 1463, 99-126.

Neal, C.A., and Lockwood, J.P. (2003) Geologic map of the summit region of Kīlauea Volcano, Hawaii. U.S. Geological Survey Geologic Investigations Series, I-2759, 1-14.

Norman, M.D., and Garcia, M.O. (1999) Primitive magmas and source characteristics of the Hawaiian plume: Petrology and geochemistry of shield picrites. Earth and Planetary Science Letters, 168, 27-44. doi: 10.1016/S0012-821X(99)00043-6

Okamura, A.T., Dvorak, J.J., Koyanagi, R.Y., and Tanigawa, W.R. (1988) Surface deformation during dike propagation. In The Puu Oo eruption of Kilauea Volcano, Hawaii: Episodes 1 through 20, January 3, 1983, through June 8, 1984. Wolfe, Ed., U.S. Geological Survey Professional Paper, 1463, 165-181.

Okubo, P.G. (1995) A seismological framework for Mauna Loa Volcano, Hawaii. In Geophysical Monograph 92. Rhodes and Lockwood, Eds., Mauna Loa Revealed: Structure, Composition, History, and Hazards, p. 187-197, American Geophysical Union, Washington, D.C., USA. doi: 10.1029/GM092p0187

Oldenburg, C.M., Spera, F.J., Yuen, D.A., and Sewell, G. (1989) Dynamic mixing in magma bodies: Theory, simulations, and implications. Journal of Geophysical Research Solid Earth, 94, 9215-9236. doi: 10.1029/JB094iB07p09215

Ort, M.H., Di Muro, A., Michon, L., and Bachèlery, P. (2016) Explosive eruptions from the interaction of magmatic and hydrothermal systems during flank extension: the Bellecombe Tephra of Piton de La Fournaise (La Réunion Island). Bulletin of Volcanology, 78, 5. doi: 10.1007/s00445-015-0998-8

Pack, A., and Palme, H. (2003) Partitioning of Ca and Al between forsterite and silicate melt in dynamic systems with implications for the origin of Ca, Al-rich forsterites in primitive meteorites. Meteoritics and Planetary Science, 38, 1263-1281. doi: 10.1111/j.1945-5100.2003.tb00312.x

Papike, J.J., Karner, J.M., and Shearer, C.K. (2005) Comparative planetary mineralogy: valence state partitioning of Cr, Fe, Ti, and V among crystallographic sites in olivine, pyroxene, and spinel from planetary basalts. American Mineralogist, 90, 277-290. doi: 10.2138/am.2005.1779

Parsons, B., and Sclater, J.G. (1977) An analysis of the variation of ocean floor bathymetry and heat flow with age. Journal of Geophysical Research, 82, 803-827. doi: 10.1029/JB082i005p00803

Pearce, T.H. (1984) The analysis of zoning in magmatic crystals with emphasis on olivine. Contributions to Mineralogy and Petrology, 86, 149-154. doi: 10.1007/BF00381841

Peltier, A., Poland, M.P., and Staudacher, T. (2015) Are Piton de la Fournaise (La Réunion) and Kīlauea (Hawai‘i) really “analog volcanoes”? In Geophysical Monograph 208. Carey, Cayol, Poland, and Weis, Eds., Hawaiian Volcanoes: From Source to Surface, p. 507-531, American Geophysical Union, Washington, D.C., USA. doi: 10.1002/9781118872079.ch23

Petry, C., Chakraborty, S., and Palme, H. (2004) Experimental determination of Ni diffusion coefficients in olivine and their dependence on temperature, composition, oxygen fugacity, and crystallographic orientation. Geochimica et Cosmochimica Acta, 68, 4179-4188. doi: 10.1016/j.gca.2004.02.024

Pietruszka, A.J., and Garcia, M.O. (1999) A rapid fluctuation in the mantle source and melting history of Kilauea volcano inferred from the geochemistry of its historical summit lavas (1790-1982). Journal of Petrology, 40, 1321-1342. doi: 10.1093/petroj/40.8.1321

Pietruszka, A.J., Norman, M.D., Garcia, M.O., Marske, J.P., and Burns, D.H. (2013) Chemical heterogeneity in the Hawaiian mantle plume from the alteration and dehydration of recycled oceanic crust. Earth and Planetary Science Letters 361, 298-309. doi: 10.1016/j.epsl.2012.10.030

Pietruszka, A.J., Heaton, D.E., Marske, J.P., and Garcia, M.O. (2015) Two magma bodies beneath the summit of Kīlauea Volcano unveiled by isotopically distinct melt deliveries from the mantle. Earth and Planetary Science Letters, 413, 90-100. doi: 10.1016/j.epsl.2014.12.040

Poland, M.P. (2015) "Points requiring elucidation" about Hawaiian volcanism. In Geophysical Monograph 208. Carey, Cayol, Poland, and Weis, Eds., Hawaiian Volcanism: From Source to Surface, p. 533-562, American Geophysical Union, Washington, D.C., USA. doi: 10.1002/9781118872079.ch24

Poland, M.P., Miklius, A., Sutton, A.J., and Thornber, C.R. (2012) A mantle-driven surge in magma supply to Kīlauea Volcano during 2003-2007. Nature Geoscience, 5, 295-300. doi: 10.1038/ngeo1426

Poland, M.P., Miklius, A., and Montgomery-Brown, E.K. (2014) Magma supply, storage, and transport at shield-stage Hawaiian volcanoes. In Characteristics of Hawaiian Volcanoes, Poland, M.P., Takahashi, T.J., and Landowski, C.M. eds., U.S. Geological Survey Professional Paper 1801, 179-234. doi: 10.3133/pp18015

Poland, M.P., Orr, T.R., Kauahikaua, J.P., Brantley, S.R., Babb, J.L., Patrick, M.R., Neal, C.A., Anderson, K.R., Antolik, L., Burgess, M., Elias, T., Fuke, S., Fukunaga, P., Johanson, I.A., Kagimoto, M., Kamibayashi, K., Lee, L., Miklius, A., Million, W., Moniz, C., Okubo, P.G., Sutton, J.A., Takahashi, J., Thelen, W.A., Tollett, W., and Trusdell, F. (2016) The 2014-2015 Pāhoa lava flow crisis at Kīlauea Volcano, Hawai‘i: Disaster avoided and lessons learned. GSA Today, 26, 4-10. doi: 10.1130/GSATG262A.1

Powers, S. (1916) Explosive ejectamenta of Kilauea. American Journal of Science, 41, 227-244. doi: 10.2475/ajs.s4-41.243.227

Powers, H.A. (1948) A chronology of the explosive eruptions of Kilauea. Pacific Science, 2, 278-292.

Powers, H.A. (1955) Composition and origin of basaltic magma of the Hawaiian Islands. Geochimica et Cosmochimica Acta, 7, 77-107. doi: 10.1016/0016-7037(55)90047-8

Prior, D.J., Boyle, A.P., Brenker, F., Cheadle, M.C., Day, A., Lopez, G., Peruzzo, L., Potts, G.J., Reddy, S., Speiss, R., Timms, N.E., Trimby, P., Wheeler, J., and Zetterström, L. (1999) The application of electron backscatter diffraction and orientation contrast imaging in the SEM to textural problems in rocks. American Mineralogist, 84, 1741-1759. doi: 10.2138/am-1999-11-1204

Putirka, K.D. (2008) Thermometers and barometers for volcanic systems. Reviews in Mineralogy and Geochemistry, 69, 61-120. doi: 10.2138/rmg.2008.69.3

Putirka, K., Ryerson, F.J., Perfit, J., and Ridley, W.I. (2011) Mineralogy and composition of the oceanic mantle. Journal of Petrology, 52, 279-313. doi: 10.1093/petrology/egq080

Rae, A.S.P., Edmonds, M., Maclennan, J., Morgan, D., Houghton, B., Hartley, M.E., and Sides, I. (2016) Time scales of magma transport and mixing at Kīlauea Volcano, Hawaiʻi. Geology, 44, 463-466. doi: 10.1130/G37800.1

Rhodes, J.M. (1995) The 1852 and 1868 Mauna Loa picrite eruptions: Clues to parental magma compositions and the magmatic plumbing system. In Geophysical Monograph 92. Rhodes and Lockwood, Eds., Mauna Loa Revealed: Structure, Composition, History, and Hazards, p. 241-262. American Geophysical Union, Washington, D.C., USA. doi: 10.1029/GM092p0241

Rhodes, J.M. (2015) Major-element and isotopic variations in Mauna Loa magmas over 600 ka: Implications for magma generation and source lithology as Mauna Loa transits the Hawaiian plume. In Geophysical Monograph 208. Carey, Cayol, Poland, and Weis, Eds., Hawaiian Volcanoes: From Source to Surface, p. 59-78. American Geophysical Union, Washington, D.C., USA. doi: 10.1002/9781118872079.ch4

Rhodes, J.M., Wenz, K.P., Neal, C.A., Sparks, S.W., and Lockwood, J.P. (1989) Geochemical evidence for invasion of Kilauea’s plumbing system by Mauna Loa magma. Nature, 337, 257-260. doi: 10.1038/337257a0

Rhodes, J.M., and Hart, S.R. (1995) Episodic trace element and isotopic variations in historical Mauna Loa lavas: Implications for magma and plume dynamics. In Geophysical Monograph 92. Rhodes and Lockwood, Eds., Mauna Loa Revealed: Structure, Composition, History, and Hazards, p. 263-288. American Geophysical Union, Washington, D.C., USA. doi: 10.1029/GM092p0263

Rhodes, J.M., and Vollinger, M.J. (2004) Composition of basaltic lavas sampled by phase-2 of the Hawaii Scientific Drilling Project: Geochemical stratigraphy and magma types. Geochemistry Geophysics Geosystems, 5, doi: 10.1029/2002GC000434.

Rhodes, J.M., and Vollinger, M.J. (2005) Ferric/ferrous ratios in 1984 Mauna Loa lavas: a contribution to understanding the oxidation state of Hawaiian magmas. Contributions to Mineralogy and Petrology, 149, 666-674. doi: 10.1007/s00410-005-0662-y

Rhodes, J.M., Huang, S., Frey, F.A., Pringle, M., and Xu, G. (2012) Compositional diversity of Mauna Kea shield lavas recovered by the Hawaii Scientific Drilling Project: Inferences on source lithology, magma supply, and the role of multiple volcanoes. Geochemistry Geophysics Geosystems, 13, doi: 10.1029/2011GC003812.

Rosen, J. (2016) Crystal clocks: How smudged crystals offer windows into a volcano's explosive past. Science, 354, 822-825.

Ruprecht, P., and Plank, T. (2013) Feeding andesite eruptions with a high-speed connection from the mantle. Nature, 500, 68-72. doi: 10.1038/nature12342

Ryan, M.P. (1987) Elasticity and contractancy of Hawaiian olivine tholeiite and its role in the stability and structural evolution of subcaldera magma reservoirs and rift systems. In Volcanism in Hawaii v. 2. Decker, Wright, and Stauffer, Eds., U.S. Geological Survey Professional Paper, 1350, 1395-1447.

Ryan, M.P. (1988) The mechanics and three-dimensional internal structure of active magmatic systems: Kilauea Volcano, Hawaii. Journal of Geophysical Research, 93, 4213-4248. doi: 10.1029/JB093iB05p04213

Ryan, J.G., and Langmuir, C.H. (1987) The systematics of lithium abundances in young volcanic rocks. Geochimica et Cosmochimica Acta, 51, 1727-1741. doi: 10.1016/0016-7037(87)90351-6.

Seelos, K.D., Arvidson, R.E., Jolliff, B.L., Chemtob, S.M., Morris, R.V., Ming, D.W., and Swayze, G.A. (2010) Silica in a Mars analog environment: Ka‘u Desert, Kilauea Volcano, Hawaii. Journal of Geophysical Research (Planets), 115, E00D15, doi:10.1029/2009JE003347.

Shamberger, P.J., and Garcia, M.O. (2007) Geochemical modeling of magma mixing and magma reservoir volumes during early episodes and Kilauea volcano’s Puu Oo eruption. Bulletin of Volcanology, 69, 345-352. doi: 10.1007/s00445-006-0074-5

Sharp, R.P., Dzurisin, D., and Malin, M.C. (1987) An early 19th century reticulite pumice from Kilauea Volcano. In: Volcanism in Hawaii v. 1. Decker, Wright, and Stauffer, Eds., U.S. Geological Survey Professional Paper, 1350, 395-404.

Shea, T., Costa, F., Krimer, D., and Hammer, J.E. (2015a) Accuracy of timescales retrieved from diffusion modeling in olivine: A 3D perspective. American Mineralogist, 100, 2026-2042. doi: 10.2138/am-2015-5163

Shea, T., Lynn, K.J., and Garcia, M.O. (2015b) Cracking the olivine zoning code: Distinguishing between crystal growth and diffusion. Geology, 43, 935-938. doi: 10.1130/G37082.1

Shorttle, O., and Maclennan, J. (2011) Compositional trends of Icelandic basalts: Implications for short-length scale lithological heterogeneity in mantle plumes. Geochemistry, Geophysics, Geosystems, 12, doi:10.1029/2011/GC003748.

Sides, I.R., Edmonds, M., Maclennan, J., Swanson, D.A., and Houghton, B.F. (2014) Eruption style at Kīlauea Volcano in Hawaiʻi linked to primary melt composition. Nature Geoscience, 7, 464-469. doi: 10.1038/ngeo2140

Sleep, N.H. (1990) Hotspots and mantle plumes: Some phenomenology. Journal of Geophysical Research, 95, 6715-6736. doi: 10.1029/JB095iB05p06715

Sobolev, A.V., Hofmann, A.W., Sobolev, S.V., and Nikogosian, I.K. (2005) An olivine-free mantle source of Hawaiian shield basalts. Nature, 434, 590-597. doi: 10.1038/nature03411

Sobolev, A.V., Hofmann, A.W., Kuzmin, D.V., Yaxley, G.M., Arndt, N.T., Chung, S-L., Danyushevsky, L.V., Elliott, T., Frey, F.A., Garcia, M.O., Gurenko, A.A., Kamenetsky, V.S., Kerr, A.C., Krivolutskaya, N.A., Matvienkov, V.V., Nikogosian, I.K., Rocholl, A., Suschevskaya, N.M., and Teklay, M. (2007) Estimating the amount of recycled crust in sources of mantle derived melts. Science, 316, 412-417. doi: 10.1126/science.1138113

Spandler, C., and O’Neill, H.S.C. (2010) Diffusion and partition coefficients of minor and trace elements in San Carlos olivine at 1,300°C with some geochemical implications. Contributions to Mineralogy and Petrology, 159, 791-818. doi: 10.1007/s00410-009-0456-8

Stolper, E., Sherman, S., Garcia, M.O., Baker, M., and Seaman, C. (2004) Glass in the submarine section of the HSDP2 drill core, Hilo, Hawaii. Geochemistry, Geophysics, Geosystems, 5, doi: 10.10292003GC000553.

Swanson, D.A. (2008) Hawaiian oral tradition describes 400 years of volcanic activity at Kīlauea. Journal of Volcanology and Geothermal Research, 176, 427-431. doi: 10.1016/j.jvolgeores.2008.01.033

Swanson, D.A., Rose, T.R., Fiske, R.S., and McGeehin, J. (2012a) Keanakākoʻi Tephra produced by 300 years of explosive eruptions following collapse of Kīlauea's caldera in about 1500 CE. Journal of Volcanology and Geothermal Research, 215-216, 8-25. doi: 10.1016/j.volgeores.2011.11.009

Swanson, D.A., Zolkos, S.P., and Haravitch, B. (2012b). Ballistic blocks around Kīlauea Caldera: Their vent locations and number of eruptions in the late 18th century. Journal of Volcanology and Geothermal Research, 231-232, 1-11. doi: 10.1016/j.jvolgeores.2012.04.008

Swanson, D.A., Rose, T.R., Mucek, A.E., Garcia, M.O., Fiske, R.S., and Mastin, L.S. (2014) Cycles of explosive and effusive eruptions at Kīlauea Volcano, Hawaiʻi. Geology, 42, 631-634. doi: 10.1130/G35701.1

Takahashi, E., and Nakajima, K. (2002) Melting processes in the Hawaiian plume: An experimental study. In Geophysical Monograph 128. Takahashi, Lipman, Garcia, Naka, and Aramaki, Eds., Hawaiian Volcanoes: Deep Underwater Perspectives, p. 403-418, American Geophysical Union, Washington, D.C., USA. doi: 10.1029/GM129p0403

Thomson, A., and Maclennan, J. (2013) The distribution of olivine compositions in Icelandic basalts and picrites. Journal of Petrology, 54, 745-768. doi: 10.1093/petrology/egs083

Thornber, C.R., Heliker, C., Sherrod, D.R., Kauahikaua, J.P., Miklius, A., Okubo, P.G., Trusdell, F.A., Budahn, J.R., Ridley, W.I., and Meeker, G.P. (2003) Kilauea east rift zone magmatism: An episode 54 perspective. Journal of Petrology, 44, 1525-1559. doi: 10.1093/petrology/egg048

Tilling, R.I., and Dvorak, J.J. (1993) Anatomy of a basaltic volcano. Nature, 363, 125-133. doi: 10.1038/363125a0

Tilling, R.I., Kauahikaua, J.P., Brantley, S.R., and Neal, C.A. (2014) The Hawaiian Volcano Observatory – A natural laboratory for studying basaltic volcanism. In Characteristics of Hawaiian Volcanoes, Poland, Takahashi, and Landowski, Eds., U.S. Geological Survey Professional Paper, 1801, 3-64. doi: 10.3133/pp18011

Tomascak, P.B., Magna, T., and Dohmen, R. (2016) Advances in lithium isotope geochemistry. Springer International Publishing, Switzerland, 195 p.

Toplis, M.J. (2005) The thermodynamics of iron and magnesium partitioning between olivine and liquid: Criteria for assessing and predicting equilibrium in natural and experimental systems. Contributions to Mineralogy and Petrology, 149, 22-39. doi: 10.1007/s00410-004-0629-4

Trusdell, F.A. (1995) Lava flow hazards and risk assessment on Mauna Loa Volcano, Hawaii. In Geophysical Monograph 92. Rhodes and Lockwood, Eds., Mauna Loa Revealed: Structure, Composition, History, and Hazards, p. 327-336, American Geophysical Union, Washington, D.C., USA. doi: 10.1029/GM092p0327

Vinet, N., and Higgins, M.D. (2011) What can crystal size distributions and olivine compositions tell us about magma solidification processes inside Kilauea Iki lava lake, Hawaii? Journal of Volcanology and Geothermal Research, 208, 136-162. doi: 10.1016/j.jvolgeores.2011.09.006

Wagner, T.P., and Grove, T.L. (1998) Melt/harzburgite reaction in the petrogenesis of tholeiitic magma from Kilauea volcano, Hawaii. Contributions to Mineralogy Petrology, 131, 1-12. doi: 10.1007/s004100050374

Wang, Z., and Gaetani, G.A. (2008) Partitioning of Ni between olivine and siliceous eclogite partial melt: experimental constraints on the mantle source of Hawaiian basalts. Contributions to Mineralogy and Petrology, 156, 661-678. doi: 10.1007/s00410-008-0308-y

Watson, E.B., and Müller, T. (2009) Non-equilibrium isotopic and elemental fractionation during diffusion-controlled crystal growth under static and dynamic conditions. Chemical Geology, 267, 111-124. doi: 10.1016/j.chemgeo.2008.10.036

Watson, E.B., Cherniak, D.J., and Holycross, M.E. (2015) Diffusion of phosphorus in olivine and molten basalt. American Mineralogist, 100, 2053-2065. doi: 10.2138/am-2015-5416

Weis, D., Garcia, M.O., Rhodes, J.M., Jellinek, M., and Scoates, J.S. (2011) Role of the deep mantle in generating the compositional asymmetry in the Hawaiian mantle plume. Nature Geoscience, 4, 831-838. doi: 10.1038/ngeo1328

Welsch, B., Faure, F., Famin, V., Baronnet, A., and Bachèlery, P. (2013) Dendritic crystallization: A single process for all textures of olivine in basalts? Journal of Petrology, 54, 539-574. doi: 10.1093/petrology/egs077

Welsch, B., Hammer, J.E., and Hellebrand, E. (2014) Phosphorus reveals dendritic architecture of olivine. Geology, 42, 867-870. doi: 10.1130/G35691.1

Wilson, D., Elias, T., Orr, T., Patrick, M., Sutton, J., and Swanson, D. (2008) Small explosion from new vent at Kilauea's summit. Eos Transections AGU, 89, 203-203. doi: 10.1029/2008EO220003

Wolfe, C.J., Solomon, S.C., Laske, G., Collins, J.A., Detrick, R.S., Orcutt, J.A., Bercovici, D., and Hauri, E.H. (2009) Mantle shear-wave velocity structure beneath the Hawaiian hot spot. Science, 326, 1388-1390. doi: 10.1126/science.1180165

Woodland, A.B., Seitz, H.M., and Yaxley, G.M. (2004) Varying behavior of Li in metasomatised spinel peridotite xenoliths from western Victoria, Australia. Lithos, 75, 55-66. doi: 10.1016/j.lithos.2003.12.014

Wright, T.L. (1971) Chemistry of Kilauea and Mauna Loa lavas in space and time. U.S. Geological Survey Professional Paper, 735, 40 p.

Wright, T.L., and Fiske, R.S. (1971) Origin of the differentiated and hybrid lavas of Kilauea volcano, Hawaii. Journal of Petrology, 12, 1-65. doi: 10.1093/petrology/12.1.1

Wright, T.L., and Pierson, T.C. (1992) Living with Volcanoes: The U.S. Geological Survey's Volcano Hazards Program. U.S. Geological Survey Circular, 1073, 57 pp.

Wright, T.L., and Helz, R.T. (1996) Differentiation and magma mixing on Kilauea's east rift zone: A further look at the eruptions of 1955 and 1960. Part II. The 1960 lavas. Bulletin of Volcanology, 57, 602-630. doi: 10.1007/s004450050115

Wright, T.L., and Klein, F.W. (2008) Dynamics of magma supply to Kīlauea volcano, Hawai'i: Integrating seismic, geodetic, and eruption data. Geological Society, London, Special Publications, 304, 83-116. doi: 10.1144/SP304.5

Wright, T.L., and Klein, F.W. (2014) Two hundred years of magma transport and storage at Kīlauea Volcano, Hawai'i, 1790-2008. U.S. Geological Survey Professional Paper, 1806, 240 p. doi: 10.3133/pp1806

Yang, H., Frey, F.A., Clague, D.A., and Garcia, M.O. (1999) Mineral chemistry of submarine lavas from Hilo Ridge, Hawaii: implications for magmatic processes within Hawaiian rift zones. Contributions to Mineralogy and Petrology, 135, 355-372. doi: 10.1007/s004100050517

Yoder, H.S., and Tilley, CE (1962) Origin of basaltic magmas: An experimental study of natural and synthetic rock systems. Journal of Petrology, 3, 342-532. doi: 10.1093/petrology/3.3.342

Zhang, Y (2010) Diffusion in minerals and melts: Theoretical background. Reviews in Mineralogy and Geochemistry, 72, 5-59. doi: 10.2138/rmg.2010.72.2

Zhukova, I., O'Neill, H. StC., Cambell, I.H., and Kilburn, M.R. (2014a) The effect of silica activity on the diffusion of Ni and Co in olivine. Contributions to Mineralogy and Petrology, 168, 1029. doi: 10.1007/s00410-014-1029-z

Zhukova, I., O'Neill, H., and Campbell, I. (2014b) The effect of mineral paragenesis on Al diffusion in olivine. EGU General Assembly Conference Abstracts, 16, 573.